D 2023

U.PORTO
FEUP FACULDADE DE ENGENHARIA
UNIVERSIDADE DO PORTO

MEMBRANES PROCESSES FOR TERTIARY TREATMENT OF URBAN WASTEWATERS: PHOTOCATALYTIC MEMBRANE REACTOR AND OZONE MEMBRANE REACTOR

PEDRO HENRIQUE PRESUMIDO

TESE DE DOUTORAMENTO APRESENTADA
À FACULDADE DE ENGENHARIA DA UNIVERSIDADE DO PORTO EM
PROGRAMA DOUTORAL EM ENGENHARIA DO AMBIENTE

Membranes Processes for Tertiary Treatment of Urban Wastewaters: Photocatalytic Membrane Reactor and Ozone Membrane Reactor

Thesis submitted in partial fulfilment of the requirements for the degree of Doctor of Philosophy in Environmental Engineering at the Faculty of Engineering, University of Porto

Pedro Henrique Presumido

Supervisor: Vítor Jorge Pais Vilar, Ph.D.
Co-Supervisors: Manuel Joaquim Sabença Feliciano, Ph.D.
Ana Isabel de Emílio Gomes, Ph.D.

Associate Laboratory in Chemical Engineering (ALiCE)
Laboratory of Separation and Reaction Engineering – Laboratory of Catalysis and Materials (LSRE-LCM)
Department of Chemical Engineering
Faculty of Engineering
University of Porto
July 2023

This work was financially supported by: (i) LA/P/0045/2020 (ALiCE), UIDB/50020/2020 and UIDP/50020/2020 (LSRE-LCM), funded by national funds through FCT/MCTES (PIDDAC); (ii) NOR-WATER project, with reference 0725_NOR_WATER_1_P, funded by INTERREG VA Spain-Portugal cooperation programme, Cross-Border North Portugal/Galizia Spain Cooperation Program (POCTEP); (iii) OZONE4WATER project, with reference PTDC/EAM-AMB/4702/2020, funded by national funds through the FCT/MCTES (PIDDAC); (iv) Healthy Waters project, with reference NORTE-01-0145-FEDER-000069, supported by Norte Portugal Regional Operational Programme (NORTE 2020), under the PORTUGAL 2020 Partnership Agreement, through the European Regional Development Fund (ERDF); and (v) Fundação para a Ciência e a Tecnologia (FCT) through the scholarships SFRH/BD/138756/2018 and COVID/BD/152947/2022.

FEUP - LSRE - LCM - Universidade do Porto

FCT Fundação para a Ciência e a Tecnologia
REPÚBLICA PORTUGUESA
CIÊNCIA, TECNOLOGIA E ENSINO SUPERIOR
UNIÃO EUROPEIA
Fundo Social Europeu

Acknowledgments

After four years of this doctoral program, it would not be entirely fair do not express my sincere thanks to all of those who, directly or indirectly, have contributed to the concretisation of this work.

First of all, I would like to sincerely acknowledge my supervisor, Dr. Vítor Vilar, for the opportunity to perform this thesis under his guidance, as well as his assiduous and enriching presence in the discussion and resolution of the difficulties encountered. I am also thankful to my co-supervisors, Dr. Manuel Joaquim Sabença Feliciano and Dr. Ana Isabel de Emílio Gomes, for all the support and encouragement. Without your assistance and valuable knowledge would not have been possible to meet all the objectives.

I am very grateful to Dr. Hermenegildo García, for receiving me so well in his laboratory and always being so supportive and helpful, and Dr. Ana Primo for all the help and partnership.

A mention must be made to the following institutions that supported this work: the Foundation for Science and Technology (FCT) for the doctoral grant (SFRH/BD/138756/2018 and COVID/BD/152947/2022); the Associate Laboratory in Chemical Engineering (ALiCE), the Laboratory of Separation and Reaction Engineering and Laboratory of Catalysis and Materials (LSRE-LCM), financially supported by LA/P/0045/2020 (ALiCE), UIDB/50020/2020 and UIDP/50020/2020 (LSRE-LCM), funded by national funds through FCT/MCTES (PIDDAC). Financial support for this work was also provided by: NOR-WATER project, with reference 0725_NOR_WATER_1_P, funded by INTERREG VA Spain-Portugal cooperation programme, Cross-Border North Portugal/Galizia Spain Cooperation Program (POCTEP); OZONE4WATER project, with reference PTDC/EAM-AMB/4702/2020, funded by national funds through the FCT/MCTES (PIDDAC); and Healthy Waters project, with reference NORTE-01-0145-FEDER-000069, supported by Norte Portugal Regional Operational Programme (NORTE 2020), under the PORTUGAL 2020 Partnership Agreement, through the European Regional Development Fund (ERDF).

I am also very grateful to the technicians, MSc. Esther Domínguez Torres (ITQ), MSc. Amparo Forneli Rubio (ITQ) and Dr. Luís Carlos Matos (FEUP) for the help provided.

I would like to thank all my colleagues at LSRE-LCM for the partnership and good work environment over the last few years. A special thanks to those who somehow helped me, contributing to the accomplishment of my work or sharing good moments in the laboratory routine: Agustina de Oliveira, Bruna Castanheira, Bruna Porto, Carla Santos, Daniela Morais, Fabiane Lira, Inalmar Segundo, Inês Rodrigues, Inês Rodrigues, Jéssica Xavier, Joana Monteiro, João Miller, Jonathan Espíndola, Karyn

Silva, Leonardo Delgado, Lúa Vazquez, Lúcio Gomes, Lucrécio Santos, Maria Prada, Mateus Caixeta, Mateus Pituco, Paula Remor, Paulo Marrocos, Reynel Castellanos, Sandra Miranda, Sara Santos, Sara Soares.

I would like to express my genuine acknowledgment to the persons that I left in Brazil: my family, especially my parents, Ana Cláudia and Márcio, brother Márcio Júnior and his wife Nathalia, grandmother Iracema, Ivanete and also my friends. Thank you for all unconditional support, love and patience.

I would want to convey my sincere appreciation to my loving wife, Larissa, for being my partner and family, for your unwavering commitment to helping us achieve our goals, and for being my unending source of love and affection. This accomplishment is also yours. To my beloved son, Miguel Henrique, who, despite being small, I can already feel the size of his heart. When you were born, a love grew capable of facing the world. I love you very much.

Finally, I am thankful to God for giving me the perseverance and strength to get here and for putting all these outstanding people in my way.

With love to my wife and son

At the beginning of an innovation,

there is always fundamental research.

Professor Dr. Ernst C. Wit

Abstract

Urban wastewater treatment plants (UWWTPs) are major hotspots for contaminants of emerging concern (CECs) (e.g., pharmaceutically active compounds, pesticides, industrial chemicals), antibiotic-resistant bacteria (ARB) and antibiotic-resistance genes (ARGs), release to water compartments, and, consequently, new approaches are required to reduce CECs&ARB&ARGs mass fluxes into the environment. Moreover, water scarcity and quality are contemporary issues in many parts of the world. The use of alternative water sources to conventional ones, such as the reuse of urban wastewater (UWW), arises as an option that can contribute to solving the problem of water scarcity. However, the reclaimed UWW must follow quality guidelines for its use and be adequate in terms of public health and environmental protection, particularly for the removal of CECs and ARB&ARGs and the reduction of toxicity. Hence, advanced treatment methods for UWW are critical nowadays.

The present thesis aimed to design and evaluate two membrane reactors using functionalised membranes for water purification. The two experimental units of membrane reactors were distinguished by their modes of operation: (i) Pressure-driven membrane process (PMP; the membrane acts as a filter medium and catalyst support) and (ii) Membrane contactor (MC; the membrane acts as an ozone injector and catalyst support). Ultrapure water (UPW), demineralised water (DW) and UWW after secondary treatment were fortified with several CECs with different characteristics. The PMP system combines membrane filtration with heterogeneous photocatalysis within a single unit. The MC integrates ozonation and photocatalytic ozonation processes. The quality of treated effluents was evaluated in terms of CECs removal, disinfection and toxicity using zebrafish embryo bioassay.

First, a new concept for the preparation of large-area membranes, based on site formation of multilayer defective graphene (G), was investigated for water desalination and UWW treatment using the PMP. The desalination membrane was prepared using a continuous film of multilayer boron nitrite (BN)-codoped defective G on a porous (100 nm) α-Al_2O_3 membrane as support. The thermal stability of the ceramic α-Al_2O_3 makes possible the preparation of defective multilayer (B,N)G by pyrolysis of chitosan (CS) containing adsorbed $(NH_4)_3BO_3$. The partial removal of B and N dopant atoms by H_2 during the pyrolysis causes the generation of subnanometric pores due to atom vacancy, as determined by control experiments in the absence of this gas. NaCl and KCl removal efficiency from brackish water greater than 95% was obtained for a permeate flux of 24.3 L m^{-2} h^{-1} at 10 bar. Due to the excellent rejection rate of NaCl and KCl from brackish water and high permeate flux at lower transmembrane pressure, as well

as the large area, the membrane reported herein appears to be easy to implement in water desalination and other membrane filtration applications.

Following this, a continuous multilayer defective G-TiO_2 thin films over the ceramic microfiltration membrane shell-side were prepared *in situ* using the same procedure as the desalination membrane. The functionalisation of the microfiltration membranes was optimised using two different methods to verify the best option regarding permeate quality (CECs removal) and quantity. Membrane A (MA): TiO_2-P25 incorporated in the G preparation stage (1% [MA-1], 2% [MA-2] and 3% [MA-3] [w/v]); and membrane B (MB): TiO_2-P25 thin-film uniformly coated over the G film surface (coating layers: 3 [MB-1], 6 [MB-2], and 9 [MB-3]). After the catalyst deposition and before the pyrolysis step, the air was forced to pass through the membranes pores (inside-outside mode), providing a porous film. The membranes coated with MA-3 and MB-2 catalyst films, irradiated by UVA light, showed the highest ability for CECs removal. Furthermore, the relative flux reduction ratio (*RFR*) decreased by around 45% in the absence of UVA light, owing to membrane fouling. The combination of filtration and oxidation (G-TiO_2-UVA) provided a permeate with higher quality and minimised membrane fouling. Although MB allowed for a permeate with higher quality, MA provided a higher permeate flux.

Subsequently, a tubular porous borosilicate membrane contactor was investigated as a MC for ozone gas/water mass transfer and the removal of CECs in DW. Ozone gas/water contact occurs on the membrane shell-side, as the ozone gas stream is fed from the lumen side and permeates through the pores generating micro-sized ozone bubbles pseudo-uniformly delivered to the annular reaction zone where the contaminated water to be treated flows. The water swirls around the membrane and drags the generated O_3 microbubbles. The membrane is also coated with TiO_2-P25 and radiation can be externally supplied via four UV lamps. The performance of the MC was evaluated by measuring the volumetric mass transfer coefficient (K_La) in continuous mode from a mass balance for O_3 in the gas and the liquid phases, considering the water pH and temperature (T), the O_3 concentration in the gas phase ($[O_3]_{G,inlet}$), the liquid (Q_L) and gas (Q_G) flow rates. The K_La ranged from 3.5 to 9.0 min^{-1} (comparable to a Venturi injection system) for water with a pH of 3.0 and a temperature of 20 ºC and improved with the increase of Q_G (1.5-fold from 0.15 to 1.0 Ndm^3 min^{-1}) and Q_L (2.0-fold from 20 to 50 L h^{-1}), due to enhanced turbulence on the membrane shell-side and annular zone. In terms of mass transfer resistance, the water phase boundary layer ($1/k_L$) is the main resistance to ozone transfer providing 53–76% of the total mass transfer resistance, while the contribution of the membrane phase varies between 24% and 47%. The ozonation showed satisfactory degradation (>80% for 13 out of the 19 CECs spiked in demineralised

water; 10 µg L^{-1}) applying an ozone dose of 12 g m^{-3} ($D_{T\text{-}O_3}$ = 4.3 g m^{-3}) and a Q_L of 150 L h^{-1}. Photocatalytic ozonation (O_3/UVC/TiO_2) did not significantly improve the treatment performance due to the low residence time (3.9 s) and UVC fluence (50 mJ cm^{-2}) applied inside the contactor.

Finally, the same ozone MC described above was applied to promote the tertiary treatment of UWW, targeting the removal of CECs, bacterial disinfection and toxicity reduction. The ozonation tests were carried out under continuous mode and short residence time (5.8 s) with secondary-treated UWW collected in different seasons (winter and summer) and spiked with a mix of 19 CECs (10 µg L^{-1} each). For an O_3 dose of 18 g m^{-3}, the best performance was obtained by increasing the O_3 concentration (maximum $[O_3]_{G,inlet}$ of 200 g Nm^{-3}) and decreasing the gas flow rate (minimum Q_G of 0.15 Ndm^3 min^{-1}), providing the highest ozone transfer yield (88%) and, thus higher specific ozone dose (g O_3 per g dissolved organic carbon). Under these conditions, removals >80% or concentrations below the limit of quantification were obtained for 13 of the 19 CECs and reductions up to 5 log units for total heterotrophs and below the limit of detection for enterobacteria and enterococci. Tests including a UVC dose of 0.10 kJ L^{-1} enhanced disinfection ability but had no impact on CECs oxidation. After ozonation, the abundance of ARB was reduced but not eliminated and microbial regrowth after 3-day storage was observed. No toxic effect was detected on zebrafish embryos using a dilution factor of 4 for the ozonised UWW and if granular activated carbon adsorption is subsequently applied the dilution factor decreases to 2.

Resumo

As estações de tratamento de águas residuais urbanas (ETAR) são um dos principais focos de contaminantes de preocupação emergente (CECs – *Contaminants of Emerging Concern*) (por exemplo, compostos farmacêuticos, pesticidas, produtos químicos industriais, entre outros), bactérias resistentes a antibióticos (ARB – *Antibiotic Resistance Bacteria*) e genes resistentes a antibióticos (ARGs – *Antibiotic Resistant Genes*), através das descargas nos compartimentos aquáticos e, consequentemente, novas abordagens são necessárias para reduzir os fluxos de massa de CECs&ARB&ARGs no ambiente. Além disso, a escassez e a qualidade da água são questões atuais em muitas partes do mundo. A utilização de fontes de água alternativas às convencionais, como o reuso de águas residuais urbanas (ARU), surge como uma opção que pode contribuir para solucionar o problema da escassez hídrica. No entanto, a ARU reutilizada deve seguir as diretrizes de qualidade para seu uso e ser adequado em termos de saúde pública e proteção ambiental, principalmente para a remoção de CECs e ARGs&ARB e redução da toxicidade. Portanto, métodos avançados de tratamento para ARU são fundamentais atualmente.

A presente tese teve como principal objetivo projetar e avaliar dois reatores de membrana utilizando membranas funcionalizadas para tratamento de água. As duas unidades experimentais de reatores de membrana apresentam modos de operação distintos: (i) processo de membrana acionados por pressão (PMP; a membrana atua como meio filtrante e suporte para catalisador) e (ii) contatores de membrana (CMs; a membrana atua como um injetor de ozono e suporte para catalisador). Água ultrapura, desmineralizada e ARU após tratamento secundário foram fortificados com vários CECs com diferentes características. O sistema PMP combina filtração por membrana com fotocatálise heterogénea em uma única unidade. O MC integra os processos de ozonização e ozonização fotocatalítica. A qualidade dos efluentes tratados foi avaliada em termos de remoção de CECs, desinfeção e toxicidade usando bioensaio de embrião de peixe-zebra.

Primeiramente, um novo conceito para a preparação de membranas de grande área com base na formação *in situ* de grafeno defeituoso multicamadas (G) foi investigado para dessalinização de água e tratamento de ARU usando o PMP. A membrana de dessalinização foi preparada usando um filme contínuo de nitrito de boro (BN) multicamada-codopado com G defeituoso em uma membrana porosa (100 nm) α-Al_2O_3 utilizada como suporte. A estabilidade térmica da cerâmica α-Al_2O_3 possibilita a preparação de multicamadas defeituosas (B,N)G por pirólise de quitosana (QS) contendo $(NH_4)_3BO_3$ adsorvido. A remoção parcial dos átomos dopantes de B e N pelo H_2 durante a pirólise gera poros subnanométricos

devido à lacuna atómica, conforme determinado por experiências de controlo na ausência deste gás. Foi obtida uma eficiência de remoção de NaCl e KCl da água salobra superior a 95% para um fluxo de permeado de 24,3 L m^{-2} h^{-1} a 10 bar de pressão. Devido à excelente taxa de rejeição de NaCl e KCl da água salobra e alto fluxo de permeado em baixa pressão transmembrana, bem como a sua extensa área, a membrana aqui relatada parece ser fácil de implementar em tecnologias de dessalinização e em outras aplicações de filtração por membrana.

Em seguida, filmes finos de G-TiO_2 defeituosos em multicamadas contínuas sobre o lado externo da membrana de microfiltração de cerâmica foram preparados *in situ* usando o mesmo procedimento da membrana de dessalinização. A funcionalização das membranas de microfiltração foi otimizada usando dois métodos diferentes para verificar qual a melhor opção em relação à qualidade (remoção de CECs) e quantidade do permeado: membrana A (MA): TiO_2-P25 incorporado na etapa de preparação G (1% [MA-1], 2% [MA-2] e 3% [MA-3] [p/v]), e membrana B (MB): filme fino de TiO_2-P25 revestido uniformemente sobre o superfície do filme G (camadas de revestimento: 3 [MB-1], 6 [MB-2] e 9 [MB-3]). Após a deposição do catalisador e antes da etapa de pirólise, ar sintético foi forçado a passar pelos poros das membranas (de dentro para fora), formando um filme poroso. As membranas revestidas com filmes catalisadores MA-3 e MB-2, irradiadas com luz UVA, apresentaram a maior capacidade de remoção de CECs. Além disso, a taxa de redução do fluxo relativo (*RFR*) diminuiu em cerca de 45% na ausência de luz UVA, devido à incrustação da membrana. A combinação de filtração e oxidação (G-TiO_2-UVA) proporcionou um permeado com maior qualidade e minimizou a incrustação da membrana. Embora a MB permitisse um permeado com maior qualidade, a MA forneceu um fluxo de permeado maior.

Posteriormente, um contator de membrana tubular porosa de borossilicato foi investigado como um CM para transferência de massa de gás ozono/água e remoção de CECs em água desmineralizada. O contato do gás ozono/água ocorre no lado externo da membrana, pois a corrente de ozono é alimentada pelo interior e permeia através dos poros, gerando microbolhas de ozono entregue de forma pseudo-uniforme à zona de reação anular onde circula a água contaminada a ser tratada. A água flui em torno da membrana e arrasta as microbolhas de O_3 geradas. A membrana também é revestida com TiO_2-P25 e a radiação pode ser fornecida externamente através de quatro lâmpadas UV. O desempenho do CM foi avaliado medindo o coeficiente volumétrico de transferência de massa (K_La) em modo contínuo a partir de um balanço de massa para O_3 nas fases gasosa e líquida, considerando o pH e a temperatura (T) da água, a concentração de O_3 no gás ($[O_3]_{G,entrada}$), e os caudais de líquido (Q_L) e gás (Q_G). O K_La variou de 3,5 a

9,0 min^{-1} (comparável a um sistema de injeção Venturi) para água com pH de 3,0 e temperatura de 20 ºC e melhorou com o aumento do caudal de gás (1,5 vezes quando o Q_G aumentou de 0,15 para 1,0 Ndm^3 min^{-1}) e de líquido (2,0 vezes quando o Q_L aumentou de 20 para 50 L h^{-1}), devido ao aumento da turbulência no lado externo da membrana e na zona anular. Em termos de resistência à transferência de massa, a camada limite da fase aquosa ($1/k_L$) é a principal resistência fornecendo entre 53 e 76% da resistência total à transferência de massa, enquanto a contribuição da fase de membrana varia entre 24 e 47%. A ozonização apresentou degradação satisfatória (>80% para 13 dos 19 CECs adicionados em água desmineralizada com concentração de 10 µg L^{-1}) aplicando uma dose de ozono de 12 g m^{-3} ($D_{T\text{-}O_3}$ = 4,3 g m^{-3}) e um Q_L de 150 L h^{-1}. A ozonização fotocatalítica (O_3/UVC/TiO_2) não melhorou significativamente o desempenho do tratamento devido ao baixo tempo de residência (3,9 s) e fluência de UVC (50 mJ cm^{-2}) aplicado.

Finalmente, o mesmo CM de ozono descrito acima foi aplicado para promover o tratamento terciário de ARU visando a remoção de CECs, desinfeção bacteriana e redução de toxicidade. Os testes de ozonização foram realizados em modo contínuo e curto tempo de residência (5,8 s) com amostras de ARU após tratamento secundário recolhido em diferentes estações do ano (inverno e verão) acrescida de uma mistura de 19 CECs (concentração inicial: 10 µg L^{-1} cada). Para uma dose de O_3 de 18 g m^{-3}, o melhor desempenho foi obtido aumentando a concentração de O_3 ($[O_3]_{G,inlet}$ máxima de 200 g Nm^{-3}) e diminuindo o caudal de gás (Q_G mínima de 0,15 Ndm^3 min^{-1}), proporcionando o maior rendimento de transferência de ozono (88%) e, portanto, maior dose específica (g O_3 por g de carbono orgânico dissolvido). Nessas condições, foram obtidas remoções >80% ou concentrações abaixo do limite de quantificação para 13 dos 19 CECs e reduções de até 5 unidades logarítmicas para bactérias heterotróficas totais e abaixo do limite de deteção para enterobactérias e enterococos. Testes incluindo uma dose de UVC de 0,10 kJ L^{-1} melhoraram a capacidade de desinfeção, mas não tiveram impacto na oxidação dos CECs. Após a ozonização, a abundância de bactérias resistentes a antibióticos foi reduzida, mas não eliminada, e foi observado crescimento microbiano após 3 dias de armazenamento. Nenhum efeito tóxico foi detetado em embriões de peixe-zebra usando um fator de diluição de 4 para a ARU ozonizada e se for aplicada uma etapa de adsorção com carvão ativado granular posteriormente, o fator de diluição diminui para 2.

Table of Contents

List of Figures

List of Tables

Notation

Acronyms

(B,N)G	Boron and nitrogen-codoped defective graphene
2NB	2-Nitrobenzaldehyde
AFM	Atomic force microscopy
AOPs	Advanced oxidation processes
ARB	Antibiotic-resistant bacteria
ARGs	Antibiotic-resistance genes
ARZ	Annular reaction zone
BET	Brunauer-Emmett-Teller adsorption-desorption isotherms
BN	Boron nitrite
BPR	Back pressure regulator
C	Column
CB	Conduction band
C_{bulk}	Solute concentration in the bulk
CECs	Contaminants of emerging concern
CFU	Colony forming units
CPC	Compound parabolic collector
CS	Chitosan
$C_{surface}$	Solute concentration on membrane surfaces
CVD	Chemical vapor deposition
D	Discard
DAD	Diode array detector
DEH	Dehumidifier
DFT	Density functional theory
DRS	UV–Visible diffuse reflectance spectra
DW	Demineralised water
EDS	Energy dispersive X-ray analysis
ESI	Electrospray interface
FET	Fish Embryo Acute Toxicity
FIB	Fast ion bombardment
FT	Feed tank

FTIR	Fourier transform infrared spectra
G	Graphene
GAC	Granular activated carbon
GEN	Ozone generator
GLMC	Gas/liquid membrane contactor
GO	Graphene oxide
GP	Gear pump
H-CAT	Heat catalyst
hpf	Hour post-fertilization
$J_{Convection}$	Bulk crossflow by convective transport
$J_{diffusion}$	Bulk stream due to diffusion
LLMC	Liquid/liquid membrane contactor
LSD	Fisher's least significant difference
MBR	Membrane bioreactor
MC	Membrane contactors
MF	Microfiltration
MFC	Mass flow controller
MFR	Membrane filtration reactor
MRM	Multiple-reaction monitoring
MS	Magnetic stirrer
MSB	Magnetic stirrer bar
MW	Molecular weight
MWCO	Molecular weight cut-off
NEM	Nano-enhanced membranes
NF	Nanofiltration
NOM	Natural organic matter
O_3AN	Ozone analyser
OMC	Ozone measuring cells
PA	Polyamide
PAN	Polyacrylonitrile
PC	Computer
PES	Polyethersulfone
PES	Poly(ether sulfones)
PFAS	Short-chain perfluoroalkylated substances

PMP	Pressure-driven membrane process
PMR	Photocatalytic membrane reactor
PP	Peristaltic pump
PS	Power supply
PSF	Polysulfone
PTFE	Polytetrafluoroethylene
PVDF	Polyvinylidene fluoride
Q	Quantifier transition
q	Qualifier transition
RO	Reverse osmosis
ROS	Reactive oxygen species
SC	Synthetic wastewater
SCR	System controller
SEM	Scanning electron microscopy
SP	Sampling point
SPG	Shirasu porous glass
TC	Temperature controller
TEM	Transmission electron microscopy
TM	Temperature meter
UF	Ultrafiltration
UPW	Ultrapure water
UWW	Urban wastewater
UWWTD	Urban wastewater treatment directive
UWWTP	Wastewater treatment plant
VB	Valence band
XPS	X-ray photoelectron spectroscopy
XRD	X-ray powder diffraction

Symbols

$\frac{d[O_3]}{dt}$	Variation of dissolved O_3 concentration in water as a function of time (g m^{-3} min^{-1})
n_i	Number of bubbles of diameter d_{eq}
$[CEC]_t$	CECs concentration after a certain time (μg dm^{-3})
$[CECs]_0$	CECs concentration in the feed liquid stream (μg dm^{-3})

$[O_3^*]$	Ozone concentration in the liquid phase at saturation (g m^{-3})
$[O_3]$	Dissolved ozone concentration at time t (g m^{-3})
$[O_3]_{G,inlet}$	Ozone concentration in the inlet gas stream (g Nm^{-3})
$[O_3]_{G,outlet}$	Ozone concentration in the outlet gas stream (g Nm^{-3})
$[O_3]_L$	Ozone concentration in the aqueous phase (g m^{-3})
$1/(k_G H)$	Mass transfer resistance in the gas boundary layer (s m^{-1})
$1/K_L$	Overall mass transfer resistance (s m^{-1})
$1/k_L$	Mass transfer resistance in the liquid boundary layer (s m^{-1})
$1/k_M$	Mass transfer resistance in the membrane matrix (s m^{-1})
a	Gas–water interfacial area per unit water volume (m^{-1})
A	Effective membrane area (m^2)
A_p	Projected bubble area (mm^2)
B	Form factor of the pore
C	Ozone concentration (mg L^{-1})
CE	Collision energy (V)
C_f	Salt concentration of the feed (µS cm^{-1})
CFV	Cross-flow velocity (cm s^{-1})
C_p	Salt concentration of the permeate (µS cm^{-1})
C_{thi}	Nominal concentration of thiosulfate (mol L^{-1})
CV	Cone voltage (V)
d_{32}	Sauter mean diameter (mm)
$D_{A\text{-}O_3}$	Inlet ozone dose (g m^{-3})
$D_{C\text{-}O_3}$	Consumed ozone dose (g m^{-3})
d_{eq}	Equivalent spherical bubble diameter (mm)
D_K	Knudsen diffusion coefficient (m^2 s^{-1})
D_M	Effective diffusion coefficient of ozone in the membrane (m^2 s^{-1})
D_{O_3}	Diffusion coefficient of ozone in the gas phase (m^2 s^{-1})
d_p	Diameter of the largest pore (m)
d_{pore}	Mean pore diameter (m)
$D_{T\text{-}O_3}$	Transferred ozone dose (g m^{-3})
Dw_{O_3}	Diffusion coefficient of ozone in water (m^2 s^{-1})
f	Correction factor for thiosulfate
FRR	Flux recovery ratio (%)

h	Liquid height to corresponding level (mm)
H	Henry's constant
h_0	Liquid height without the presence of gas (mm)
Ha	Hatta number
J	Permeate flux (L m^{-2} h^{-1})
J_0	Permeate flux for ultrapure water filtration (L m^{-2} h^{-1})
J_{210}	Permeate flux after 210 min of reaction (L m^{-2} h^{-1})
J_{CECs}	Permeate flux with CECs (L m^{-2} h^{-1})
J_{CM}	Permeate flux of the membrane after cleaning (L m^{-2} h^{-1})
k_{CEC}	Pseudo-first-order kinetic constant (min^{-1})
k_d	Self-decomposition constant of ozone (s^{-1} or min^{-1})
k_G	Mass transfer coefficients for the gaseous phase (m s^{-1})
K_L	Overall mass transfer coefficient based on water phase (m s^{-1})
k_L	Mass transfer coefficient in the water phase (m s^{-1})
K_La	Volumetric mass transfer coefficient based on water phase (s^{-1} or min^{-1})
k_M	Mass transfer coefficient in the membrane (m s^{-1})
k_{O_3}	Rate constant of the direct reaction between O_3 and the pollutant (M^{-1} s^{-1})
LEP	Liquid entry pressure (kPa)
LOD	Limit of detection (CFU mL^{-1})
LOQ	Limit of quantification (µg L^{-1})
m	Mass of ozone (mg)
M	Molar mass of ozone (g mol^{-1})
M_{O_3}	Molar mass of ozone (g mol^{-1})
MTE	Mass transfer efficiency (%)
pH_{pzc}	Point of zero charge
Q_G	Gas flow rate (Ndm^3 min^{-1})
Q_L	Volumetric water flow rate (L h^{-1})
R	Ideal gas constant (J K^{-1} mol^{-1})
R (%)	Salt rejection (%)
R^2	Coefficient of determination (%)
Rc	Cake layer height (mm)
Re	Reynolds number
RFR	Relative flux reduction ratio (%)

Rir	Irreversible fouling ratio (%)
Rr	Reversible fouling ratio (%)
RSD	Relative standard deviation (%)
RSM	Roughness surface morphology (nm)
S^2_R	Residual variance ($\mu g^2\ L^{-2}$)
T	Temperature (ºC)
t	Experiment time (h)
TMP	Transmembrane pressure (bar)
V	Volume of the ozonised water sample (mL)
V_{thi}	Sodium thiosulfate volume (mL)
Z_i	Maximum vertical distance between the highest and lowest data points in the image (nm)
ΔpH	Difference between final and initial pH value
Δx	Membrane thickness (mm)
ε	Porosity of the membrane (%)
ε_G	Gas holdup (%)
τ	Hydraulic residence time (s)
τ_p	Pore tortuosity
Φ_T	Overall quantum yield
n	Number of samples

Chemical names

$(NH_4)_3BO_3$	Ammonium borate
Al	Aluminium
Cu	Copper
H_2O_2	Hydrogen peroxide
H_2SO_4	Sulfuric acid
H_3BO_3	Boric acid
KCl	Potassium chloride
KI	Potassium iodide
Mg	Magnesium
N_2	Nitrogen
$Na_2S_2O_3$	Sodium thiosulfate
NaCl	Sodium chloride

NaOH	Sodium hydroxide
O_2	Oxygen
O_3	Ozone
PDS	Peroxydisulfate
TiO_2	Titanium dioxide

1 Introduction

This first chapter provides an overview of the occurrence of contaminants of emerging concern (CECs) in the environment, as well as treatment technologies focusing on membrane reactors. An exhaustive review of the technological advances and applicability of membrane photocatalytic reactor (PMR) and membrane contactor (MC) is given, where several studies were compared regarding their efficiency in the removal of CECs. The objectives and the thesis outline are also provided at the end of the chapter.

1.1 General context

Urban wastewater treatment plants (UWWTPs) are the major hotspots for contaminants of emerging concern (CECs). CECs are chemical and biological substances that have been shown to negatively impact human health and/or environmental parameters but are not currently subject to EU water quality regulations. CECs may have harmful effects even at trace concentrations when they come into contact with organisms. For instance, disruption of the endocrine system may reduce fish reproduction, sublethal toxicity may reduce the abundance of invertebrates, and proliferation of antibiotic-resistant bacteria (ARB) and antibiotic-resistance genes (ARGs). Consequently, new approaches are required towards the One Water-One Health approach to reduce CECs&ARB&ARGs mass fluxes into the environment [1].

Water authorities are creating policy guidelines to encourage the use of new tertiary treatment technologies for urban wastewater (UWW) and to prevent the discharge of hazardous compounds to the aquatic environment to meet the world's limited freshwater supply and growing water demand. In order to comply with human health and environmental protection requirements, the European Directive 2013/39/EU of August 12, 2013, amends Directives 2000/60/EC and 2008/105/EC, established guidelines for the monitoring and treatment of a group of 45 priority compounds. Likewise, in Decision 2015/495 of March 20, 2015, the first watch list of 10 compounds or groups of substances of environmental concern for monitoring by the European Union was established. Furthermore, the European Parliament recently approved for the first time the minimum requirements at the European level for reclaimed water (i.e., UWW that has been treated in a reclamation plant) to be used for agricultural purposes, safely protecting people and the environment [2]. It is important to mention recent CEC-related publications in the Official Journal of the European Union, such as European Directive 2013/39 (August 12, 2013) [3], European Decision 2018/840 (June 5, 2018) [4], and European Decision 2020/1161 (August 4, 2020) [5]. In this sense, and in line with the circular economy action plan, the European Commission recently published a proposal for the new UWW treatment directive (UWWTD) [6] targeting new standards and limit values, including new requirements for CECs abatement in UWWTPs, and focusing on promoting the widespread reuse of treated UWW.

In this context, several governments across the globe are investing more in upgrading UWWTPs with advanced treatment technologies [7]. The intrinsic poor biodegradability of many CECs places a cap on how well they can be removed using standard biological treatments [8]. As a result, advanced treatment technologies are needed, such as advanced oxidation processes (AOPs), ozonation, membrane filtration, and adsorption using activated carbon [9]. In order to maximize prospects for the removal of the broadest range of CECs, the current trend entails merging or integrating technologies. This is done by utilising

the advantages of each technology while minimizing the drawbacks of each one. It has been demonstrated that the simultaneous application of AOPs (e.g., H_2O_2/UV, O_3/UV, O_3/UV/H_2O_2, UV/H_2O_2/TiO_2, persulfate AOPs, photo-Fenton, electrolysis/Fenton, electro-oxidation) is effective against bacteria and other microorganisms, toxic and persistent organic compounds [10-16]. In that same line, the most frequently integrated or combined technical methods for CECs removal at full/commercial scale are: (i) ozonation + adsorption with granular activated carbon; (ii) ozonation and biological active filters; (iii) membrane filtration (nanofiltration, reverse osmosis); and (iv) adsorption/ion-exchange [9]. While many CECs are successfully removed or degraded using these methods, it is also necessary to address the generation, behaviour, and end-of-life of the by-products produced by advanced oxidation technologies [17]. In some cases, the by-products generated are more harmful than the primary compounds. Another important point to highlight is the operating cost of the treatment technology. For example, the removal of CECs using membrane technology is effective, but it has significant operating costs (1.37–2.16 \$ m^{-3}), mainly associated with high energy consumption (0.8–1 kWh m^{-3}) [18, 19]. Additionally, the retentate stream, where contaminants are concentrated, also needs to be treated. Hence, there is a growing need to develop and integrate water/wastewater treatment methods and datasets to better address the complexity of the water cycle and water resources management.

1.2 Review framework

This research drew data from works published in international journals regarding membrane processes used to remove CECs and their degradation products from water/wastewater. Membrane processes applied for the removal of the CECs are classified into three main categories: (i) pressure-driven membrane process (PMP); (ii) membrane contactor (MC); and (iii) membrane bioreactor (MBR). Since the first two were employed in this thesis, only they will be covered. The data were presented through tables and figures, and the main results were highlighted and discussed.

Figure 1.1a presents the publications related to the various types of treatment techniques that have been studied for CECs removal. Membrane and adsorption technologies have received the highest attention compared to other techniques over the past 10 years. Moreover, works employing membrane technologies were also classified into three categories. The results show that a large majority of studies focused on PMP (79.3%) compared to the other categories (Figure 1.1b).

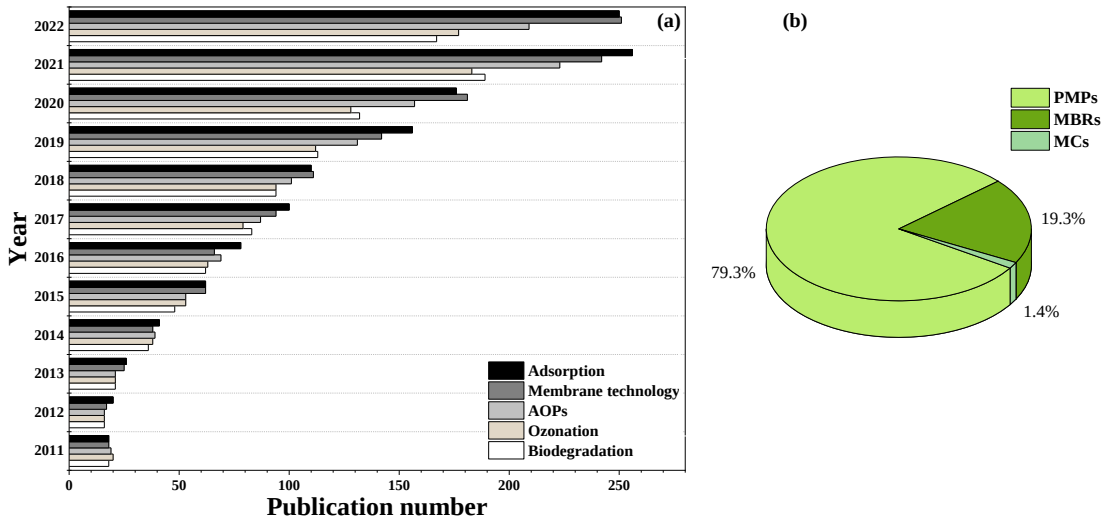

Figure 1.1. Publications related to different techniques used for the CECs removal by year in the period 2011–2021 (a) and distribution of processes used in membrane technologies for the same period (b). Note: The results were obtained from the Scopus database using as keywords (abstract, title, keywords): "membrane" or "adsorption" or "biodegradation" or "AOPs" or "ozonation" and "wastewater", or "water treatment", and "contaminants of emerging concern", or "emerging pollutants" and limited to the document type as research article. Whenever one of the categories was selected (membrane, adsorption, biodegradation, AOPs, ozonation), the others were set to "and not" to avoid overlapping papers. PMP – Pressure-driven membrane process; MBR – Membrane bioreactor; MC – Membrane contactor; AOPs – Advanced oxidation processes.

1.3 Pressure-driven membrane process (PMP)

Pressure-driven membrane process (PMP) is a separation technique widely applied in water and wastewater treatment. In PMP, water and low molecular weight (MW) solutes permeate through the membrane pores by applying a driving force (i.e., applied pressure), while suspended solids and high molecular weight solutes are rejected by the membrane [20]. The main advantages of PMP are: (i) high separation efficiency in a single stage; (ii) production of high-quality treated water; (iii) low or no chemical consumption; (iv) process with the automatic and continuous application; and (v) possibility of expansion by increasing the size of the system or by connecting membrane modules [20, 21].

The processes are commonly divided into four overlapping categories of increasing selectivity: microfiltration (MF), ultrafiltration (UF), nanofiltration (NF), and reverse osmosis (RO). As the MW or size of the molecules of the compounds decreases, the membrane's pore size should be smaller, following the trend from MF through UF to NF/RO (Figure 1.2). As a result, the membranes become more resistant to mass transfer and consequently increasing the applied pressure (driving force) is required in order to maintain the same flow [22]. Therefore, the required transmembrane pressure (*TMP*) must be increased (MF: 0.1–5 μm, 1–10 bar; UF: 1–100 nm, 1–10 bar; NF: 0.5–10 nm, 10–30 bar; RO: <0.5 nm, 35–100 bar) to provide the same flux [23]. Currently, each membrane type is used for a specific industrial application, such as MF and UF, which are typically used over a wide range of applications, such as pharmaceutical, food, and dairy industries, usually to separate high molecular components from low

molecular ones [24, 25]. NF and RO processes are often used for desalination and pure water production [26].

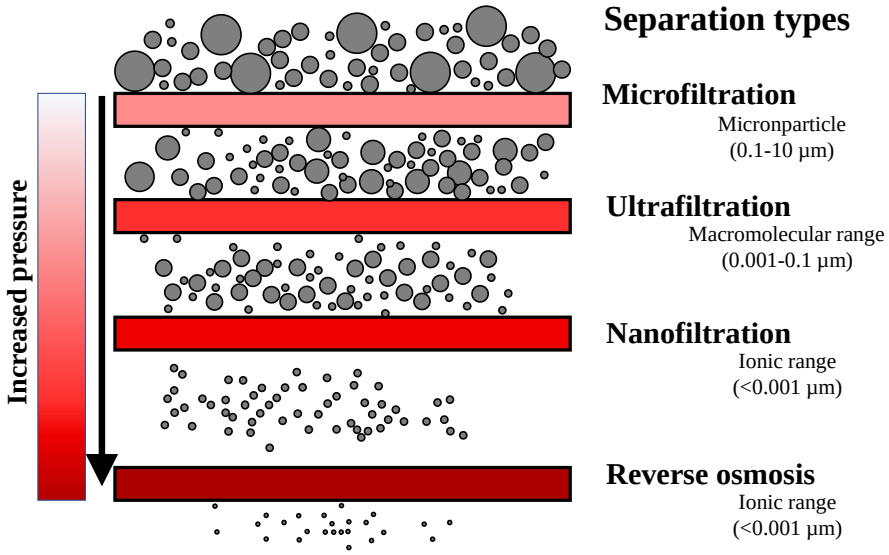

Figure 1.2. The applicability ranges of different membrane separation processes. Adapted from Madsen [27].

The membrane separation procedure can be carried out in either a cross-flow mode or a dead-end mode [23] (Figure 1.3). When operating in dead-end mode, the whole feed is processed by a membrane to create a filtrate (permeate). As a result, the concentration of the separated substances increases, eventually leading to the formation of a filter cake on the membrane surface, decreasing the filtration performance. Consequently, the dead-end method is inappropriate for most large-scale industrial applications [23]. On the other hand, in the cross-flow mode, the flow is applied tangentially across the membrane surface. As the feed flows across the membrane surface, filtrate passes through the membrane pores while concentrate accumulates at the opposite end of the membrane. Hence, the retained fraction, the fraction of the feed that has not been filtered, may be discarded or partially recycled into the feed tank. The major benefit of the cross-flow configuration is that it limits the deposition of fouling on the membrane surface since the feed flowing tangentially to the membrane partially eliminates the molecules and particles that have been deposited [28].

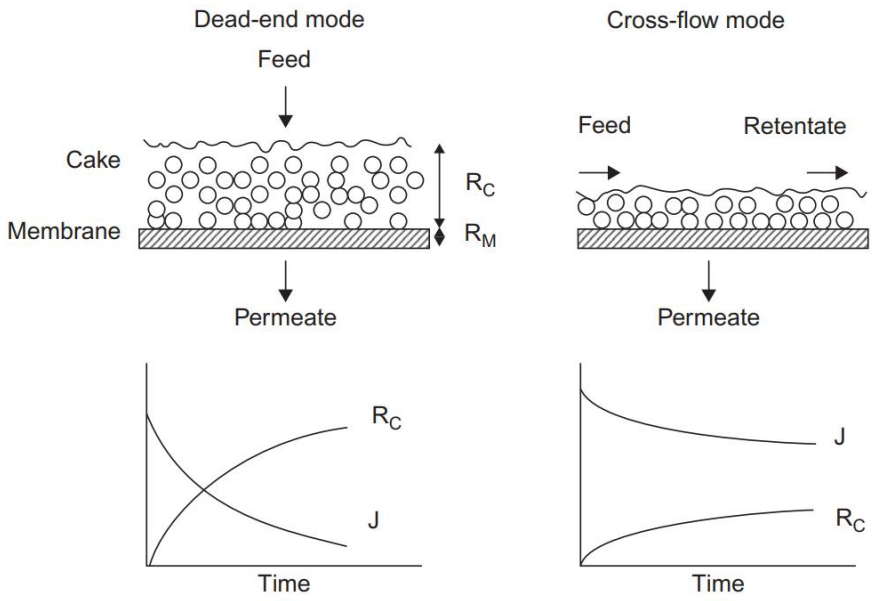

Figure 1.3. Schematic representations of the cross-flow and dead-end modes and their impacts on the permeate flux (J) and cake layer height (R_C). Note: RM – membrane resistance. Reprinted from Cui et al. [23].

Several lab-scale studies have been conducted to evaluate the removal of CECs using membrane methods [29-33]. Furthermore, this technique has already been implemented for the CECs rejection on a real scale, for instance, in water reclamation facilities and drinking water treatment plants [34, 35].

The membrane pore size plays an important role in CECs removal efficiency. For example, comparison research with UF and NF membranes focused on removing 38 different organic emerging contaminants from wastewater (pharmaceuticals, endocrine-disrupting chemicals, benzotriazoles, benzothiazoles, and perfluorinated compounds) showed that the greater removal of CECs by NF was mainly associated with its smaller pore size [36]. Furthermore, the removal efficiency of each compound depends on the molecular size (i.e., molecular weight or Stokes radius), charge, and hydrophobicity [37]. Kiso et al. [38] reported that hydrophobicity and solute molecular shape were essential factors for rejecting aromatic pesticides by NF membranes.

Similarly, the removal efficiency for emerging contaminants is also highly dependent on the membrane material. For example, the removal of bisphenol A (BPA) from synthetic wastewater presented a much better performance using a polyamide-based membrane (≥98%) when compared to a cellulose acetate membrane (10–40%) [39]. This result was attributed to the structure of membrane skin and the nonpolar and hydrophobic character of many endocrine-disrupting compounds, which make them adsorbed by polymers. The same results were found for the retention of the pesticide dichloroaniline in NF membranes. The polyamide-based membrane showed better removals when compared to the cellulose acetate membrane [40].

The matrix also strongly influences membrane rejection of CECs, especially due to possible interactions between CECs, water components, and membranes. Dolar et al. [41] investigated the effect of water matrixes (ultrapure water, model water, tap water, and real pharmaceutical wastewater) on the removal of sulfamethoxazole, trimethoprim, ciprofloxacin, dexamethasone and febantel using NF membranes. In general, the rejection of CECs was higher in model and tap water than in ultrapure water, but the water flux was lower. These results were assigned to the ion adsorption inside the membranes pores and the influence of natural organic matter (NOM). Espíndola et al. [42] also evaluated the effect of a UWW matrix for the removal of oxytetracycline (OTC) in a MF membrane doped with TiO_2. The UWW matrix negatively affected the permeate flux and the removal of OTC, and this effect was attributed to (i) the existing contaminants (organic and inorganic matter) in the UWW matrix that is capable of inhibiting the rate of CECs removal; and (ii) the deposited/adsorbed pollutants onto the membrane surface. On the other hand, Sanches et al. [43] found that the rejection percentage obtained for hormones and pesticides tested (except for pentachlorophenol) were independent of the water matrix composition, even though the two natural water matrices evaluated (groundwater and surface water) were very different in terms of organic and inorganic composition. These results are consistent with data obtained by Nikbakht Fini et al. [44], who studied the effect of the water matrix on pesticide removal. By using different water matrices as the feed, the authors slightly enhanced pesticide rejection (from ~93.5% to 95.9%). According to them, this was associated with a higher pore-blocking effect due to the higher amounts of ions in the real groundwater samples, leading to a shortage of passageways for pesticide molecules. Furthermore, the electrostatic interaction between cations and negatively charged phenoxy acid herbicides could contribute to the formation of complexes with bigger molecular sizes, leading to higher observed rejection values. Consistent with the literature, a complete understanding of rejection mechanisms must be achieved, as real water matrices are very complex, and simultaneous effects on the removal of target compounds can occur. In addition to the parameters described above, the CECs removal in PMP is also influenced by other factors such as solution pH and concentration of contaminants [14, 15].

In wastewater recovery/reuse and drinking water treatment, membrane filtration processes can be used alone or as a combination of membranes in series to remove CECs. Table 1.1 shows an overview of several published studies and the following findings can be highlighted:

1. The studies addressed the retention of different groups of CECs, such as pharmaceuticals, hormones, insecticides, herbicides, pesticides, heavy metals, and their possible metabolites in aquatic environments;

2. CECs concentrations varied from high values (mg L^{-1}) [39] to more realistic values (ng L^{-1} or µg L^{-1}) [45]. Studies that use high concentrations justify doing so to better assess the retention of compounds and the limiting effects of the filtration process [46];
3. NF has been the most used filtration process due to its ability to reject CECs;
4. Flat sheet has been the most commonly applied membrane configuration;
5. Different water matrices were used for the filtration processes;
6. Although several membrane materials were investigated, polymeric membranes were the most evaluated;
7. Some works highlighted that the UF was not able to eliminate the CECs completely; however, in other cases, removal efficiencies of more than 80% were observed for the UF process;
8. In processes using NF membranes, the removal efficiencies are within a wide range (between 1.8% and ≥99%) [38, 43];
9. In most studies, RO membrane showed rejection values above 80% for CECs, regardless of membrane material.

Table 1.1. An overview of a pressure-driven membrane process (PMP) applied to remove different contaminants of emerging concern (CECs).

CECs	Treatment			Membrane				Ref.
	Initial concentration	Source*	Removal range	Material	Configuration	Pore size/MWCO**	Separation type***	
Atenolol, trimethoprim, sulfamethoxazole, carbamazepine, chloramphenicol	1 mg L^{-1}	SW/SC	23.6–83.2%	Polyvinylidene difluoride (PVDF)	Flat sheet	0.42 nm	NF	[47]
Acetaminophen, caffeine, carbamazepine, ibuprofen, naproxen, phenacetine, phenazone, fenoprofen, gemfibrozil, ketoprofen, metronidazole, sulfamethoxazole, 17β estradiol, estrone, bisphenol A, 1,4-dioxane, 17α ethynilestradiol	5–18 μg L^{-1}	SW	22–96%	Aromatic polyamide	Flat sheet	1 nm	NF	[48]
4-Amino-antipiryne, antipyrine, atenolol, benzafibrate, carbamazepine, ciprofloxacin, codeine, diclofenac, fenofibric acid, furosemide, gemfibrozil, hydrochlorothiazide, ibuprofen, iopamidol, iopromide, ketoprofen, metronidazole, n-acetyl-4-amino-antipiryne, naproxen, n-formyl-4-amino-antipiryne, nicotine, ofloxacin, pravastatin, primidone, ranitidine, sulfamethoxazole, trimethoprim, velafaxime	0.12–5.8 μg L^{-1}	UWW	11–95%	Polyethersulfone/polyamide	Flat sheet	150–300 Da	UF/NF	[45]
Atenolol, carbamazepine, ciprofloxacin, citalopram, diclofenac, estrone, fluconazole, ibuprofen, imidacloprid, ketoconazole, losartan, metoprolol, naproxen, oxazepam, paracetamol, propranolol, sertraline sulfamethoxazole, tramadol, trimethoprim, venlafaxine	0.01–37 μg L^{-1}	UWW	>93%	Polysulfone	Flat sheet	10 kDa	UF	[49]
Acesulfame, 4-Methyl-1H-benzotriazole, 5-Methyl-1H-benzotriazole, acesulfame, AMPA, carbamazepine, clarithromycin, diclofenac, EDTA, glyphosate, iomeprol, iopromide, metoprolol, sulfamethoxazol, TMDD	0.2–13 μg L^{-1}	UWW	>99%	Polyethersulphone	Tubular	20 nm	UF	[50]

Table 1.1. An overview of a pressure-driven membrane process (PMP) applied to remove different contaminants of emerging concern (CECs) (continued).

CECs	Treatment			Membrane				Ref.
	Initial concentration	Source*	Removal range	Material	Configuration	Pore size/MWCO**	Separation type***	
Fenobucarb, propyzamide, chlorothalonil, isoxathion, tricyclazole, carbaryl, mefenacet, methyldymron, chloroneb, esprocarb, propiconazole	0.5–1.5 mg L^{-1}	SC	1.8–99%	Poly(vinyl alcohol)/polyamide and Sulfonated polyethersulfone	Flat sheet	-	NF	[38]
Bisphenol A	50 mg L^{-1}	SC	10–40% and >98%	Polyamide and cellulose acetate	Flat sheet	200–300 Da	NF/RO	[39]
Dichloroaniline	1–10 µg L^{-1}	SC	10–95%	Polyamide and cellulose acetate	Flat sheet	0.8–1 nm	NF	[40]
Sulfamethoxazole, trimethoprim, ciprofloxacin, dexamethasone, febantel	10 mg L^{-1}	SC/TW/UWW	50–99.9%	Polyamide	Tubular	0.7–1.6 nm	NF/RO	[41]
Atrazine, alachlor, pentachlorophenol, estrone, 17β-estradiol, 17α-ethinylestradiol, progesterone, estriol	75–150 µg L^{-1}	SW/GW	67.4–99.9%	Polysulfone	Flat sheet	150–300 Da	NF	[43]
2-methyl-4-chlorophenoxy acetic acid, 2-methyl-4-chlorophenoxy propionic acid, 2,6-dichlorobenzamide	1 mg L^{-1}	GW	30–99%	Polyamide	Flat sheet	100–400 Da	NF/RO	[44]
Amoxicillin	30 mg L^{-1}	SC	66–90%	Polysulfone	Flat sheet	30–50 nm	UF	[51]
Atenolol, trimethoprim, sulpiride, primidone, carbamazepine, nalidixic acid, sulfamethoxazole, indomethacin	50 µg L^{-1}	SC	80–98%	Polysulfone	Flat sheet	0.4–0.5 nm	NF	[37]
Diethyl phthalate, di-(2-ethylhexyl) phthalate, 2-methyl-1-propanol, 2-butenal, 2-ethyl-1-hexanol, 1,3-dioxolane, 1-butanol, 3-methyl-3-buten-1-ol, naphthalene, 2-methylphenol	0.8 mg L^{-1}	UWW	>82.5%	Polyamide	Flat sheet	100–400 Da	NF/RO	[52]
Diclofenac, ibuprofen, zinc sulphate, zinc nitrate	20 mg L^{-1}	SC	40–98%	Polyamide	Tubular	80–400 Da	NF	[46]

Note: *UWW – Wastewater; SC – Synthetic wastewater; TW – Tap water; SW – surface water; GW – groundwater; ** MWCO – Molecular weight cut-off; *** MF – microfiltration, UF – ultrafiltration, NF – nanofiltration, RO – reverse osmosis.

Despite all the advantages presented above for the PMP system, membrane fouling is the major barrier to the use of membrane separation technology. During the filtration process, particles, colloidal particles, or solute molecules from the wastewater deposit on the membrane surface and pores, which causes a decrease in membrane performance [20]. Membrane fouling is a serious problem in all PMPs, and pore blockage can be classified as reversible and irreversible [51]. Reversible fouling, which can be removed by rewashing, results from rejected contaminant molecules adhering to or depositing on the membrane's surface. Irreversible fouling is produced by a variety of substances that have a significant affinity for the membrane and is mostly eliminated by chemical washing or enzymatic degradation. Problems caused by fouling range from limiting membrane performance to reducing membrane life and even increasing cleaning costs [53]. Furthermore, it is worth noticing that PMPs are merely separation procedures, thus the contaminant is rejected and enriched towards a retentate stream. To enhance the quality and decrease the amount of retentate, the concentrate can be treated or hybrid systems like photocatalytic membrane reactors can be used [54].

1.3.1 Photocatalytic membrane reactor (PMR)

The heterogeneous photocatalytic process involves photo-exciting a semiconductor catalyst by absorbing photons with energy equal to or greater than its bandgap, resulting in the creation of an electron-hole pair. Photocatalytic oxidation of CECs is initiated by reactive species such as $O_2^{-\bullet}$, h^+, and $OH^\bullet$. Basically, when the TiO_2 film, for example, is exposed to light, the electrons located in the valence band (VB) of TiO_2 were excited (e^-_{CB}) to the conduction band (CB) with the formation of positive holes (h^+_{VB}) (Equation (1.1)).

$$TiO_2 + h_\nu \rightarrow TiO_2(e^-_{CB}) + TiO_2(h^+_{VB}) \quad (1.1)$$

Furthermore, h^+_{VB} is able to react with hydroxide (or water) to form hydroxyl radicals, which are powerful reactive oxygen species able to degrade CEC molecules (Equation (1.2)). Simultaneously, reactive h^+_{VB} also oxidizes CEC directly.

$$TiO_2(h^+_{VB}) + H_2O \rightarrow H^+ + OH^\bullet \quad (1.2)$$

Photocatalytic membrane reactor (PMR) are hybrid reactors that combine membrane filtration and photocatalytic oxidation [55]. In PMR, the photocatalyst can be deposited on the membrane (nano-engineered membranes - NEM) or suspended in the reaction water. In both configurations, the membrane serves as a barrier to contaminants, allowing only the permeation of small molecules and water through its pores. The NEM, in the coated-catalyst configuration, is tasked with effecting *in-situ* oxidation/reduction of contaminants, thereby elevating the antifouling characteristics of the membrane

and the quality of the permeate and retentate. On the other hand, in the suspended catalyst configuration, the membrane serves as a physical barrier against photocatalyst particles and organic molecules. Hence, the PMR enable the slurry-type reactor to operate continuously without losing any photocatalyst particles and to control the water residence time [56]. It is noteworthy that slurry systems generally have a greater catalyst surface area available for the adsorption and oxidation of CECs, resulting in higher rates of contaminant degradation. However, these systems also experience a greater decline in permeate flux. In summary, in the first configuration, oxidation by hydroxyl radicals occurs on the outer surface or within the membrane's pores, while contaminants permeate in a one-pass stream. In the second configuration, the oxidation process usually takes place in the feed tank.

The literature has already extensively addressed the photocatalytic oxidation of organic molecules in water and wastewater [57-63]. In the same sense, the generation of highly reactive species on the membrane surface is able to: (i) enhance membrane permeability and hydrophilicity; and (ii) improve the antifouling membrane properties through oxidation of organic molecules and microbiota adsorbed onto the membrane surface and blocking the membrane pores, leading to a higher and more constant permeate flux and a concentrate with higher quality [64-67]. Additionally, CECs are forced toward the membrane surface, increasing their concentration near the liquid/catalyst interface and boosting the reaction rate.

1.3.1.1 Effect of photocatalyst type and characteristics of CECs on their removal

Several studies already reported the combination of photocatalysis with different categories of PMP, such as MF [42, 68-70], UF [71-75], NF [76-79], and RO [80-82]. Furthermore, different semiconducting metal oxides (ZnO [83], CeO_2 [84], SnO_2 [85], WO_3 [86], ZrO_2 [75], Fe_2O_3 [87], and TiO_2 [42]) can be used to oxidize the organic compounds present in the wastewater and eventually mineralize them into carbon dioxide, water and mineral acids (Table 1.2). Due to its great oxidizing capacity (3.2 eV), straightforward and inexpensive production, chemical and photochemical stability, and non-toxicity, TiO_2 is the most investigated photocatalytic material, either alone or in codoping with another semiconductor [88]. Photocatalysts can be deposited on the membrane surface to create photocatalytic membranes. This can be done using a variety of processes, including electrospinning [89], electrospraying [90], magnetron sputtering [79], dip-coating [14], and chemical vapor deposition (CVD) [91]. The main deposition techniques used in the preparation of photocatalytic membranes are summarized in Table 1.2.

Liu et al. [92] proposed a method that involves depositing $ZnIn_2S$ on the membrane surface in order to simultaneously increase photocatalytic activity and decrease membrane fouling (Figure 1.4). The

removal efficiencies for fluvastatin (97.19%) and TOC (53.29%) were much higher than those of the pure PVDF membrane, demonstrating the superior photocatalytic activity of $ZnIn_2S$ membrane and antifouling properties.

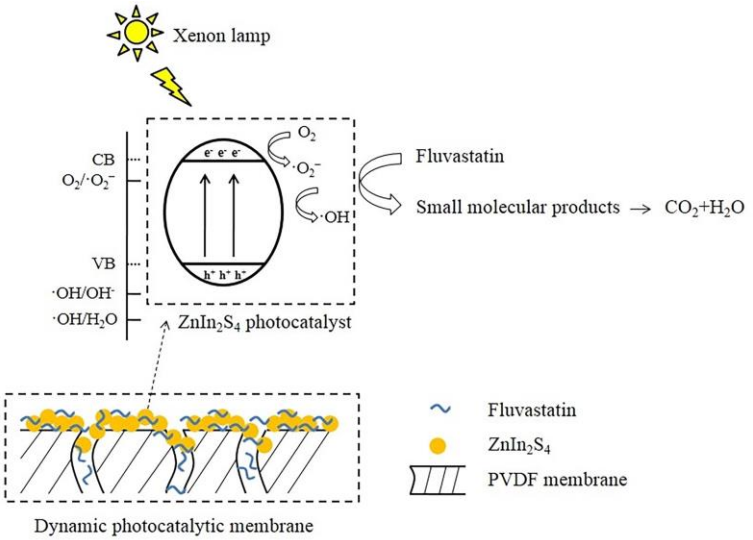

Figure 1.4. Fluvastatin removal mechanism by a dynamic photocatalytic membrane under irradiation. Reprinted from Liu et al. [92].

Lv et al. [93] created a simple biomimetic mineralization technique to construct a self-cleaning photocatalytic NF membrane for wastewater treatment. In this process, a polydopamine/polyethyleneimine intermediate layer is fabricated on an UF membrane using a co-deposition method followed by biomimetic mineralization of a photocatalytic layer composed of β-FeOOH nanorods. Under visible light, the β-FeOOH layer showed effective photocatalytic activity for the degradation of organic dyes through the photo-Fenton reaction with hydrogen peroxide. The photocatalytic membrane showed effective filtration performance and self-cleaning ability.

In general, as catalyst loading is increased, the catalyst's surface area grows. This improves the catalyst's adsorption capacity and degradation efficiency, which reduces membrane fouling. Alem et al. [94] examined the photocatalytic efficiency of membranes made from $TiO_2/\alpha\text{-}Al_2O_3$ using the sol-gel method. According to the researchers, a multi-layered membrane has much more photoactivity than a single-layer membrane. Based on methyl orange removal, the photoactivity of the TiO_2 membrane was assessed at 41.9% for the multilayer membrane and 27.1% for the single-layer membrane after 9 hours of UV exposure. In contrast, Ahmad et al. [95] demonstrated that adding more layers of TiO_2 coating to membrane support reduces water permeability and increases fouling rates even when exposed to UV radiation (Figure 1.5). The authors explain that this result may be associated with several factors, including the rise in internal recombination of the TiO_2 layer and the aggregation of photocatalyst particles that prevent light penetration.

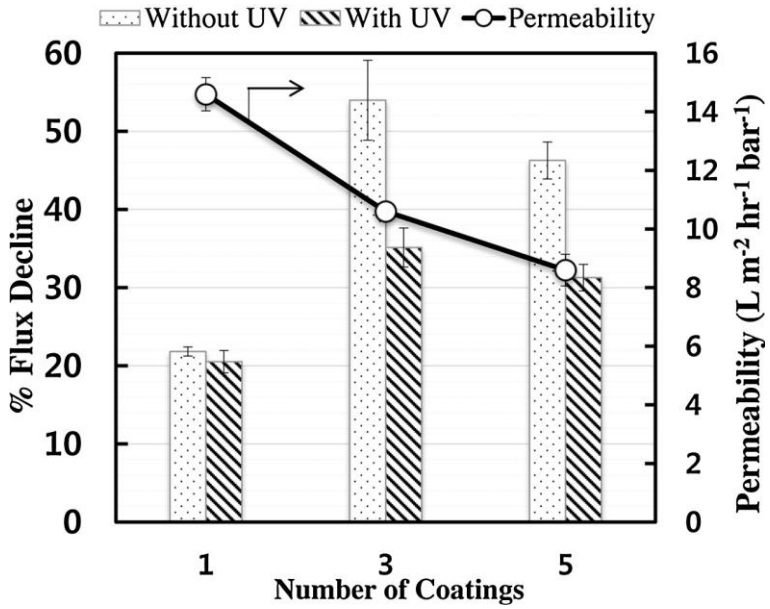

Figure 1.5. Effect of multilayer coatings on membrane fouling. Reprinted from Ahmad et al. [95].

Although semiconductors, such as TiO_2-P25, can be anchored on membranes to improve their performance (NEM) [42, 96], the high recombination rate of photogenerated e^-/h^+ is a significant drawback [97]. Graphene (G) is a single layer of a hexagonal carbon network showing a high surface area with delocalization of π electrons, boosting the charge carrier's separation in photocatalytic reactions. Furthermore, due to their superior adsorptive and photocatalytic capabilities, which allow for the removal and destruction of hazardous CECs, nanomaterials like G and metal-based nanoparticles in water treatment have shown promise [98]. The recombination of e^-_{CB} and h^+_{VB} would occur immediately without an acceptor. Therefore, the suppression of recombination of charge carriers is the key to enhancing the photocatalytic activity of semiconductor photocatalysts [99]. Nanomaterials that combine carbon and semiconductor photocatalysts could potentially offer desirable efficiency for separating electron-hole pairs. Because the Fermi energy of G is lower than the CB of TiO_2, the G can act as a sink for the photogenerated electrons.

The formation of C-Ti bond improves the transfer efficiency of e^-_{CB} from TiO_2 to graphene, inhibiting the recombination and prolonging the life times of separated carriers (Equation (1.3)).

$$G\text{-}TiO_2(e^-_{CB}) \rightarrow G(e^-_{CB})\text{-}TiO_2 \quad (1.3)$$

The electrons in the CB of TiO_2 would react with the dissolved oxygen in the aqueous medium to produce a large number of $O_2^{\bullet -}$ to degrade the CECs (Equation (1.4)).

$$G(e^-_{CB}) + O_2 \rightarrow G + O_2^{\bullet -} \quad (1.4)$$

G-based TiO_2 membrane for CECs removal has recently been reported elsewhere [100-102]. Almeida et al. [103] reported TiO_2/graphene oxide (GO) nanocomposite immobilized into poly(vinylidene difluoride-co-trifluoroethylene) (P(VDF-TrFE)) fibres, showing high oxidation rates for methylene blue. Rao et al. [87] fabricated a flat membrane interconnecting TiO_2 nanowires, Fe_2O_3 nanoparticles, and GO sheets for the removal of humic acids from water. The impregnation of GO-TiO_2 in ceramic membranes was able to remove 5 different organic compounds from 32 to 99% [104].

It is important to note that the mechanisms of CECs removal during treatment with photocatalytic membranes may be due to (Figure 1.6): (i) size exclusion; (ii) adsorption; (iii) hydrophobic interactions; (iv) electrostatic interactions; and (v) photocatalytic oxidation under irradiation [55, 105].

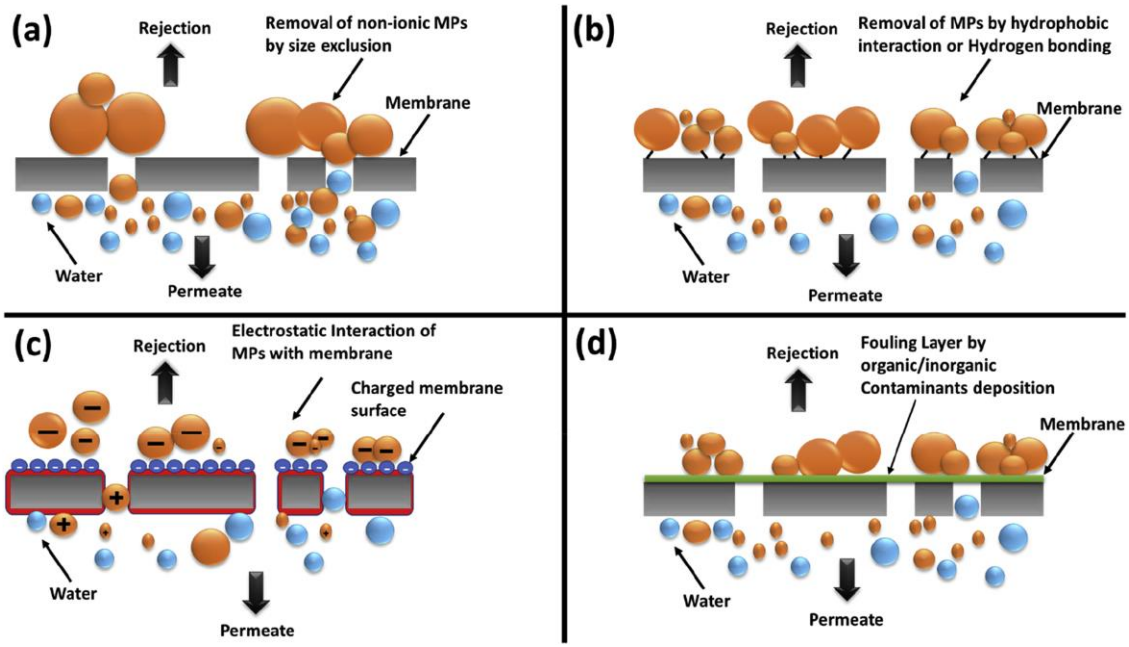

Figure 1.6. Removal mechanism of CECs removal during membrane separation. (a) Size exclusion; (b) Hydrophobic interaction; (c) Electrostatic interaction; (d) Adsorption. Note: MPs – organic micropollutants. Reprinted from Khanzada et al. [106].

Some authors report that adsorption and size exclusion are the main removal mechanisms for PMR [55, 106]. According to Rani et al. [55], the initial removals of CECs in photocatalytic UF membranes are linked to adsorption, and after equilibrium is reached, other mechanisms will act for the removal of CECs. Moreover, it is further noted that for size exclusion, the size of CECs is not only based on their molecular weight but also on molecular length and width, and this mechanism was also observed in uncharged CECs [107].

The adsorption and size exclusion phenomena are further impacted by the hydrophobic and hydrophilic interaction of CECs with the membrane surface, which are a log K_{ow} function [107]. For example, CECs

with log K_{ow} > 2.5 are highly hydrophobic [55]. Furthermore, due to electrostatic interactions, the charge of CECs also influences their adsorption on the membrane surface.

Fernández et al. [108] studied the photocatalytic degradation of 33 trace organics contaminants (including drugs, analgesics, antibiotics, surfactants, or herbicides). According to the findings of this study, 14 CECs showed 50-88% degradation after 1 h of reaction, while 18 compounds disappeared utterly. The flame-retardant tris(2-chloroethyl) phosphate (TCEP) was not removed. In general, the higher log K_{ow} value resulted in a higher level of adsorption on the PVDF membrane, where highly retained compounds are hydrophobic (log K_{ow} > 4), while hydrophilic compounds were less or not retained.

As with PMPs, PMRs are also influenced by the water matrix. Sarasidis et al. [71] explored diclofenac removal on a laboratory scale employing a hybrid TiO_2/UVA catalysis UF process. The results show excellent system performance (maximum diclofenac removal of ~99.5% and mineralization of ~69%). Nonetheless, the variation in removal efficiencies found for the different water matrices (ultrapure water, tap water, and groundwater) highlights the significance of feedwater properties.

1.3.1.2 Effect of membrane properties on CECs removal

Another important factor for PMR is the selection of the most suitable substrate support (membrane), which must include high specific surface area, high abrasion, chemical resistance, high stability against photolysis and reactivity with reactive oxygen species (ROS) [109]. The substrate materials must have a physical structure that facilitates liquid-solid separation and junctions between the substrate and photocatalyst, which must be able to withstand the strain from interactions between particles and fluid mechanics. Other factors to consider when selecting the best membrane substrate are pore size or molecular weight cut-off (MWCO), zeta potential, contact angle, and roughness [55]. Materials such as alumina, polyvinylidene fluoride (PVDF), poly(sulfone) (PSF), poly(ethersulfone) (PES), poly(acrylonitrile) (PAN), and stainless steel are used as substrate materials to prepare photocatalytic membranes to be used in PMR [110-114].

Polymeric membranes have been extensively employed in PMR because they are readily accessible, generally inexpensive, and come in a variety of pore diameters. For example, Lotfi et al. [115] showed good results in the removal of steroid hormones in a continuous polyethersulfone–titanium dioxide (PES–TiO_2) photocatalytic membrane reactor. This efficiency is a result of the nanoscale size of the membrane, which offers a large surface area and enhances the interaction between the radicals and CECs molecules. However, the majority of polymeric membranes are constrained by one or more working parameters (such as pH, temperature, pressure, and chlorine tolerance), which limits the range of their

potential uses [23]. Rani et al. [55] also cited in their review a low resistance to UV light and the destruction of membrane structure due to hydroxyl radicals. Dzinun et al. [116] suggested that UV irradiation has some effect on the stability of the TiO_2/PVDF membrane after 30 days of exposure due to the appearance of cracks. On the other hand, inorganic membranes, including those made of γ-alumina/α-alumina, borosilicate glass, pyrolyzed carbon, zirconia, or stainless steel, are very resistant to even the most severe working conditions (chemical resistance, thermal stability, low chemical demand, low cleaning frequency, and longer lifetime) [117-119]. This technology is crucial for photocatalytic membranes because membranes manufactured from these materials are stable at the elevated temperatures required for CVD, fixing semiconductors by heat treatment and transforming the amorphous TiO_2 precursor into the anatase phase [91].

Starr et al. [120] evaluated two different deposition methods, layer-by-layer and plasma-enhanced CVD, for coating TiO_2 nanoparticles on the ceramic membrane surface. A comparison of the photocatalytic efficiency of the two types of coating shows that the layer-by-layer coated membrane has significantly greater photocatalytic activity than the plasma-enhanced CVD membrane. The type of membrane material was a key factor as both impregnation methodologies employed heat treatment with temperatures between 300 and 500 °C. Other studies also presented works with ceramic membranes [117-119].

In turn, due to the possibility of working as filters and anodes, photoelectrocatalytic membranes have arisen as a promising approach for wastewater remediation without the need to add chemicals. Diverse inorganic membrane materials have been endowed with electrical conductivity by their doping with composites such as ZnO, TiO_2, either alone or mixed with carbon, sulphur or boron [87, 121, 122]. Once the membrane anode is electrified, the generated charge carriers promote the electrochemical generation of reactive oxygen species able to degrade the CECs and, at the same time, results in the decomposition of H_2O into O_2 and H_2, which induce gas and liquid microflows reducing concentration polarization and membrane fouling. Although the synthesis of photo-catalytic/electrocatalytic membranes is still at a primitive stage, it appears to be a promising approach for wastewater remediation. Kumari et al. [123] proposed a macroporous photoelectrocatalytic membrane prepared using stainless steel metallic membrane coated with TiO_2 and ZnO via atomic layer deposition. In cross-flow reactors, the photoelectrocatalytic efficacy of membranes has been proven for the degradation of methylene blue, phenol, paracetamol, and atrazine. These membranes offered higher degradation kinetic factors of 2.9 and 2.3 compared to photocatalysis and electrocatalysis, respectively.

1.3.1.3 Self-cleaning property of PMR

Fouling is a process that causes a membrane to lose performance due to the deposition of suspended or dissolved materials onto its filtration surface [124]. Simply pausing filtration will not eliminate scale and is often the main limitation for the application of membranes in wastewater treatment. In general, according to Cui et al. [23], fouling mechanisms for porous membranes can be divided into four categories: (i) complete pore blocking; (ii) internal pore blocking; (iii) partial pore blocking; and (iv) cake filtration. Moreover, as seen in *Section 1.3*, fouling can be classified into reversible and irreversible.

In PMR, the action of the photocatalyst with UV irradiation decreases membrane fouling and increases the permeate flux. According to Ma et al. [122], the Si-doped TiO_2/Al_2O_3 composite membrane had higher permeability to pure water than the membrane that had not been exposed to UV irradiation. Moreover, in experiments containing dye wastewater, the membrane flux with UV illumination was increased by approximately 30% after 4 h running, compared with that without UV (Figure 1.7).

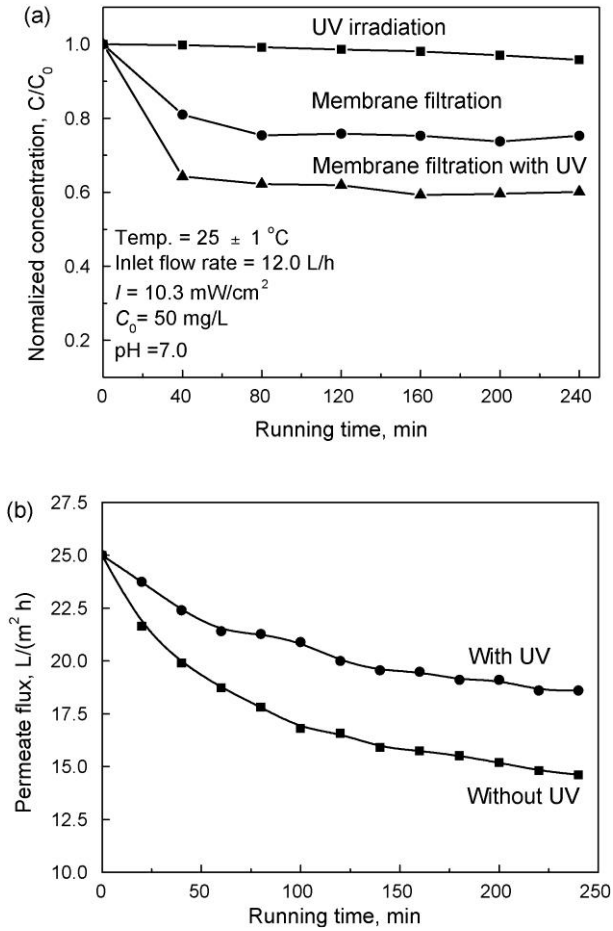

Figure 1.7. (a) Water purification experiment for Reactive Red ED-2B solution flow treatment with inlet concentration of 50 mg L^{-1}; (b) antifouling properties of Si-doped TiO_2 composite membrane. Reprinted from Ma et al. [122].

Similarly, Song et al. [125] studied membranes composed of polyvinylidene fluoride–PVDF doped with polyethylene glycol–PEG and TiO_2 in the presence of UV irradiation. The authors reported a flux decline

of 61% on PVDF–PEG membrane (without TiO_2), 56% without UV irradiation (PVDF–PEG–TiO_2), and only 28% with UV irradiation (PVDF–PEG–TiO_2) after 100 min of filtration. The flow of the PVDF–PEG–TiO_2 membrane, which was exposed to UV light, stabilized after a 20-minute filtering trial.

Therefore, an efficient UV or solar radiation design must be used to scale up and execute integrated photocatalytic membrane processes. This is shown by the fact that membrane fouling was decreased when adequate irradiation was provided to the photocatalyst [55].

Table 1.2. Studies on photocatalytic membrane reactor (PMR) identifying CECs or dye removed considering treatment and membrane characteristics.

CECs	Treatment				Membrane				Ref.
	Initial concentration	Source*	Removal range	Photocatalyst	Fabrication method	Material	Configuration	Separation type	
Di-n-butyl phthalate, di(2-ethylhexyl) phthalate, cephalexin, sulfamethoxazole, caffeine	-	UWW	4–99%	G-TiO_2	Dip-coating	Alumina	Tubular	MF	[104]
Ibuprofen	-	SC	20–50%	ZnO	Phase Inversion Method	Polyvinylidene fluoride (PVDF)	Flat	UF	[83]
Tetracycline and humic acid	20 mg L^{-1}	SC	>80%	Bi_2WO_6/CeO_2	Phase inversion method	Polyvinylidene fluoride (PVDF) and nanocomposite were grafted	Flat	UF	[84]
Pharmaceutical wastewater	-	UWW	90%	ZrO_2–SnO_2	Sol–gel method	Polysulfone (PSF)	Flat	-	[85]
Rhodamine B	7 mg L^{-1}	SC	70.8%	Ti_3C_2/WO_3	Directly vacuum filtration	Polyvinylidene fluoride (PVDF)	Flat	UF	[86]
Oxytetracycline	5 mg L^{-1}	UWW/SC	>90%	TiO_2	Dip-coating	Alumina	Tubular	MF	[42]
Methyl blue, methyl orange, Congo red, and rhodamine B	20 mg L^{-1}	SC	31–99.6%	β-FeOOH	Co-deposition method followed by mineralization of a photocatalytic layer	Polyacrylonitrile (PAN)	Flat	UF/NF	[93]
Fluvastatin	10 mg L^{-1}	SC	60–97.19%	$ZnIn_2S_4$	Phase inversion method and dead-end filtration	Polyvinylidene fluoride (PVDF)	Flat	UF	[92]
Methyl orange	5 mg L^{-1}	SC	27.1–41.9	TiO_2	Sol-gel preparation and dip-coating	α-Alumina	Flat	UF	[94]
Methylene blue, phenol, paracetamol and atrazine	5–25 mg L^{-1}	SC	>90%	TiO_2/ZnO	Atomic layer deposition	Stainless steel	Flat	MF	[123]

Table 1.2. Studies on photocatalytic membrane reactor (PMR) identifying CECs or dye removed considering treatment and membrane characteristics (continued).

CECs	Treatment				Membrane				Ref.
	Initial concentration	Source*	Removal range	Photocatalyst	Fabrication method	Material	Configuration	Separation type	
Methylene blue and methyl orange	2–6.4 mg L^{-1}	SC	2–57%	GO-TiO_2	Dip-coating	γ-Alumina	Tubular	UF	[118]
Cimetidine, sulfamethoxazole, propranolol, acetaminophen	10 µM	SC	40–90%	TiO_2	Electrospinning	Polyvinylidene fluoride (PVDF)	Flat	UF	[126]
Carbamazepine, diclofenac, iopromide, gemfibrozil, metoprolol, sulfamethoxazole, trimethoprim and warfarin	0.2–0.4 mg L^{-1}	GW/UWW	70–90%	TiO_2	Co-extrusion technique	Polyvinylidene fluoride (PVDF)	Tubular	UF	[127]
Congo red	0.1 g L^{-1}	SC	~95%	TiO_2	Spin-coated	Alumina	Flat	UF	[95]
Carbamazepine	1 mg L^{-1}	SC/SW	~75%	N-doped TiO_2	Sol-gel method	α-Alumina	Flat	MF	[128]
Ciprofloxacin	10 mg L^{-1}	SC	26.26–59.95%	Reduced graphene oxide – Bi_2WO_6	Double-layer coating method	Polyvinylidene fluoride (PVDF)	Flat	MF	[129]
Carbamazepine, venlafaxine, fluoxetine, atenolol, sulfamethoxazole, ibuprofen, atorvastatin, naproxen, triclosan, triclocarban, carbamazepine-10,11-epoxide, norfluoxetine, p-hydroxy atorvastatin, o-hydroxy atorvastatin	2 µg L^{-1}	SC	15–72%	TiO_2	Dip-coating and thermal-chemical oxidation	Quartz fibre filters and porous titanium sheets	Flat	MF	[130]
Oestradiol, oestrone, progesterone and testosterone	50 ng L^{-1}– 1 mg L^{-1}	SC	33–80%	TiO_2	Dip-coating	Polyethersulfone (PES)	Flat	MF	[115]

Table 1.2. Studies on photocatalytic membrane reactor (PMR) identifying CECs or dye removed considering treatment and membrane characteristics (continued).

CECs	Treatment				Membrane				Ref.
	Initial concentration	Source*	Removal range	Photocatalyst	Fabrication method	Material	Configuration	Separation type	
Estrone, 17β-estradiol, progesterone, testosterone	50 ng L^{-1}	SC	5–80%	Pd(II)-porphyrin	Adsorption	Polyvinylidene fluoride (PVDF)	Flat	MF	[131]
Rhodamine B	10 μM	SC	~90%	Poly(phenylene butadiynylene)	Phase inversion	Polysulfone (PSF)	Flat	NF	[78]
Bisphenol A	10 mg L^{-1}	SC	~90%	Fe-doped TiO_2	Interfacial polymerization	Polysulfone (PSF)	Flat	UF	[105]
Methylene blue and chlorhexidine digluconate	35–1000 mg L^{-1}	SC	30–40%	TiO_2	Sol-gel method	Polyethersulfone (PES) and polyvinyl-chloride/polyacrylonitile (PVC/PAN)	Hollow fibre	UF	[132]
Ibuprofen	10 mg L^{-1}	SC	~86%	TiO_2	Electrodeposition	Polysulfone (PSF)	Flat	UF	[133]
17β-estradiol, estrone, testosterone and progesterone	100 ng L^{-1}	SC	15–90%	Pd, Zn, Mn-porphyrins	Impregnation	Polyvinylidene fluoride (PVDF)	Flat	UF	[134]

Note: *UWW – Wastewater; SC – Synthetic wastewater; SW – surface water; GW – groundwater.

1.3.2 Pressure-driven membrane process and graphene film for water desalination

Another application for PMP is in water desalination. Technologies aimed at the desalination of sea and brackish water are crucial for meeting future demand and improving drinking water quality. In this context, among the various technologies employed, continuous G films together with PMP can serve to develop the ultimate membranes for water desalination since the one-atom thickness represents the physical zero-depth limit for any membrane [135, 136]. The major advantages of continuous G as a membrane that would be used as a disruptive technology are its high mechanical strength, high elasticity and wide range of chemical stability. Adequate porosity on the G sheet should allow to combine a high flux due to the zero depth and high solute removal [137, 138]. On the other hand, the main barriers that limit the general application of desalination technologies to produce fresh water are the high pressures required to overcome osmotic pressure and low permeate fluxes, resulting in a high energy consumption. These limitations are closely related to the development of more efficient strong continuous membranes that withstands high pressures and exhibits a high salt rejection rate.

Kim et al. [139] deposited GO nanosheets followed by amino GO nanosheets on the surface of amino polyethersulfone (PES) membrane. The obtained membrane exhibits a good salt rejection of 98% for a water flux of 28 L m^{-2} h^{-1} at a pressure of 55 bar. Also, Cohen-Tanugi et al. [140] reported theoretical studies based on classical molecular dynamics simulations on the behaviour of multilayer graphene membrane for desalination. Their study on models varying the number of overlapped holey graphene layers concluded that a ~ 200 nm thick nanoporous multilayer graphene membrane should have rejection efficiency and permeate flux like those of a single-layer graphene membrane.

1.4 Membrane contactor (MC)

Membrane contactor (MC) are suitable modules that can aid in the transfer of a constituent between gas/liquid (GLMC) or liquid/liquid (LLMC) phases and are often used in environmental processes [141] (Figure 1.8). Contrary to the basic principles of separation membranes, MCs do not offer any selectivity, working just as a convenient barrier between the two phases, keeping them separated and allowing their contact in a large (as compared to volume) and well-defined interfacial area [142]. As with any technology, MCs have both advantages and disadvantages [141, 143]. The advantages are: (i) higher interfacial area; (ii) higher mass transfer; (iii) operating flexibility; (iv) scale-up simplicity; (v) compact structure; (vi) operation with low-pressure drops; (vii) overall higher efficiency. On the other hand, the disadvantages are: (i) mass-transfer resistance from the membrane itself; (ii) the membrane lifespan.

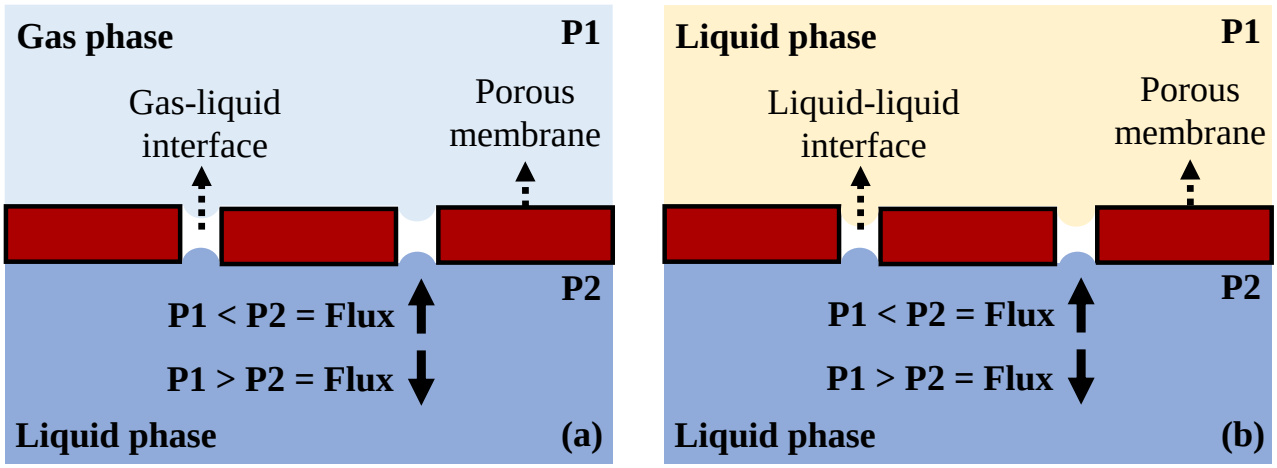

Figure 1.8. Schematic diagram of (a) gas/liquid membrane contactor (GLMC) and (b) liquid/liquid membrane contactor (LLMC). Note: P – Pressure. Modified from Bazhenov et al. [144].

1.4.1 Gas/liquid membrane contactor (GLMC)

A reliable technology called a gas-liquid membrane contactor (GLMC) has long been used in post-combustion plants and the petrochemical industry to remove acid gases, mainly CO_2 [144, 145]. Recently, a particularly intriguing approach for treating water has also been the use of GLMC for ozone diffusion [146-148]. The focus of this dissertation is to evaluate GLMC in ozonation processes. Therefore, only this category of contactors will be discussed in this section.

Ozonation is a technique most successfully applied in several fields of water/wastewater treatment [149], such as disinfection [150, 151], oxidation of CECs [152-155], and removal of colour, odour, and taste [156]. A major obstacle to the broader use of O_3 technology is the relatively high energy consumption (around 7.2 to 12.3 kW/kg O_3) [149], rather large footprint treatment unit, and operational issues related to the dispersion of ozone gas in water. GLMC is an emerging alternative to traditional O_3 injection methods, such as fine bubble diffusers, for which O_3-liquid transport is a rate-limiting factor due to the size and distribution of O_3 bubbles. While the principles of direct gas-liquid mass transfer of O_3 into the aqueous phase are well understood, bubbling methods bear several disadvantages, such as locally inaccurate O_3 dosages due to short-circuiting, low ozone mass transfer rates from gas to liquid phase, foam formation in treatment reactors, bubble coalescence and uneconomic off-gas recovery (mainly O_2) [149]. Moreover, conventional ozonation systems result in the need to use deeper tanks to obtain a higher dissolution efficiency of ozone gas into the water, as also as unconsumed/unreacted ozone losses and, consequently, higher operational costs and footprints.

Compared to traditional contactors, GLMC has the following advantages [157-161]: (i) the specific surface area of MC is much higher than in conventional contactors and may result in a higher volumetric mass transfer coefficient (K_La); (ii) microscale bubble operation that prevents foaming phenomena; (iii)

greater control on the dosing of ozone to the water; (iv) reduced losses of unreacted ozone; (v) scale-up to almost any size is easily possible by adding modules of the same type and size without losing transfer efficiency since a constant O_3 concentration can be established at the gas/liquid interface. Also, no changes in the specific energy dissipation are caused, which is crucial in the scale-up of direct gas reactors, and membrane reactors have a small footprint. Table 1.3 compares the characteristics between the GLMC and some conventional contactors. The membranes can be used in small cross-section contactors with high linear flow rates, resulting in compact units with good plug-flow characteristics. Ozone membrane contactors offer potential economic benefits such as increased ozone transfer efficiencies and reduced energy requirements when compared to traditional processes.

Table 1.3. Comparison of some traditional contactors versus membrane contactor (MC) [162].

Contactor type	Surface area (m^2/m^3)	Mass transfer coefficient (K_La) (min^{-1})	Gas/liquid flow ratio (%)
Bubble column	50 – 600	0.3 – 7.2	60 – 98
Packed column	10 – 350	0.02 – 4.2	2 – 25
Venturi	150 – 2500	4.8 – 15	5 – 30
Membrane contactor (MC)	1000 – 10000	3 – 30	1 – 99

The GLMC may be operated in several different configurations, including flat sheet [148, 163], hollow fibre [164, 165], and tubular [166] membrane modules. Membrane resistance to ozone is one important point to be considered in the selection of the membrane material. Mori et al. [167] studied ozone resistance of various organic materials for hollow fibre membranes, for example, polyethylene (PE), polyvinylidene fluoride (PVDF), and polytetrafluorethylene (PTFE), and reported that the ozone resistance was in the following order: PTFE > PVDF > PE. In this same sense, for the ozonation of dye wastewater, Bamperng et al. [168] compared the efficiency of a MC with a PVDF or PTFE membrane. The findings showed that PTFE had higher stability since its performance was only slightly reduced. On the other hand, a 30% reduction in the performance was observed for the PVDF membrane. Other studies also demonstrated the applicability of ceramic, borosilicate glass, and stainless-steel membranes in ozonation [169, 170].

1.4.1.1 Mass transfer in GLMC

Gas-liquid mass transfer in a GLMC is divided into various steps, as described by Bamperng et al. [168] (Figure 1.9). Firstly, there is the gas diffusion from the bulk to the interface between the gas phase and the membrane surface. Secondly, the transport of gas through the membrane pores. And finally, the dissolution of a gas component into a liquid with or without the reaction.

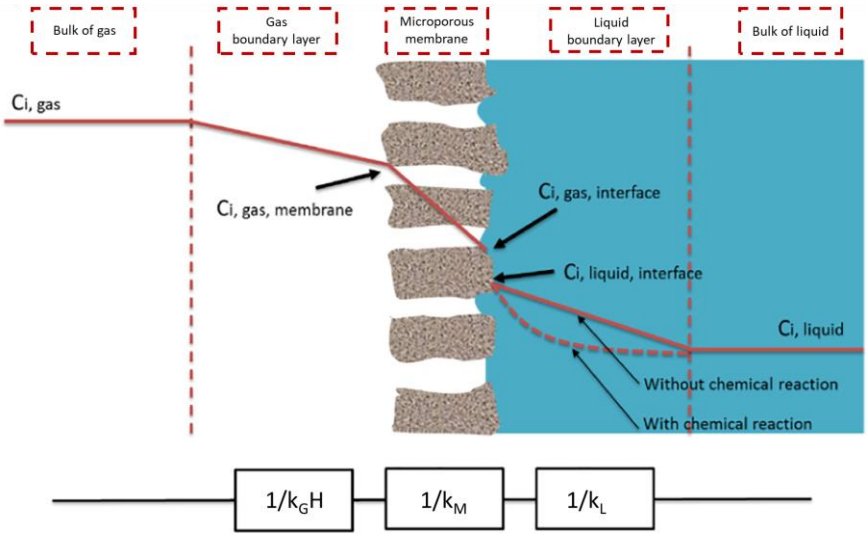

Figure 1.9. Mass transfer regions and resistance-in-series in gas/liquid membrane contactor. Note: Ci – dissolved gases concentrations; $1/(k_G H)$, $1/k_M$, and $1/k_L$ are the mass transfer resistances in the gas boundary layer, membrane matrix, and liquid boundary layer, respectively. Adapted from Schmitt et al. [161].

Utilizing the resistance-in-series model, the mass transfer mechanism in the GLMC process can also be stated as Equation (1.5):

$$\frac{1}{K_L} = \frac{1}{k_G H} + \frac{1}{k_M} + \frac{1}{k_L} \tag{1.5}$$

where K_L is the overall mass transfer coefficient based liquid phase (m/s); k_G, k_M, and k_L are the individual mass transfer coefficients of the gas phase, membrane, and liquid phase, respectively. $1/(k_G H)$, $1/k_M$, and $1/k_L$ are the mass transfer resistances in the gas boundary layer, membrane matrix, and liquid boundary layer, respectively. H represents Henry's constant. It is important to highlight that there are a number of notations and variants in studies to characterize series resistances in GLMC, depending on the assumptions used, such as neglecting gas-side resistance [168], neglecting gas-side and membrane resistance [171, 172], or accounting for all contributions [173].

It's also crucial to remember that while the passage of gas through dry pores has a minimal impact on the membrane resistance, the entry of water into the pores causes this resistance to grow [172, 174]. Hence, an additional resistance for wet pores can be optionally included in Equation (1.5). Consequently, the *TMP* must be higher to overcome this resistance created by a stagnant film that interferes with transfer [161]. Ozone transfer is encouraged when the gas/liquid contact is kept near the membrane surface because ozone diffusivity is better within the gas (2×10^{-5} m^2 s^{-1} [168]) than inside the liquid (1.76×10^{-9} m^2 s^{-1} [175]). Furthermore, the k_M for porous membranes depends on the gas diffusion via the pores or its obstruction by the membrane walls and may be roughly estimated with regard to membrane specificities (pore size, membrane thickness, and hydrophobicity) using Equation (1.6).

$$k_M = \frac{D_M \times \varepsilon}{\tau_p \times \Delta x} \tag{1.6}$$

where D_M is the effective diffusion coefficient of ozone in the membrane ($m^2\ s^{-1}$), ε is the porosity of the membrane, τ_p is the pore tortuosity, and Δx is the membrane thickness (m). D_M is characterized by molecular diffusion and Knudsen diffusion (D_K) and can be expressed as Equation (1.7) [176].

$$D_M = \frac{1}{\frac{1}{D_{O_3}} + \frac{1}{D_K}} \tag{1.7}$$

Typically, membrane contactors are better suited for use with hydrophobic porous membranes. Kukuzaki et al. [172] investigated hydrophilic and hydrophobized Shirasu porous glass (SPG) tubular membranes to better understand the membrane's role in ozone transfer. They concluded that, due to the presence of water in the pores, the mass transfer resistance ($1/k_M$) in the hydrophilic membrane was higher than in the hydrophobic membrane under identical circumstances. A breakthrough pressure, also known as a liquid entry pressure (*LEP*, kPa), is typically used to describe a membrane's capacity to resist wetting and is controlled by the Young-Laplace equation (Equation (1.8)).

$$LEP = -\frac{B\gamma_L}{d_p} \tag{1.8}$$

where B is the form factor of the pore ($B = 1$ is for cylindrical pores, while $0 < B < 1$ is for irregular pores), γ_L is the liquid surface tension ($N\ m^{-1}$), and d_p is the diameter of the largest pore (m). In GLMC systems that aim to generate a contactor bubbleless, the liquid pressure must be greater than the gas pressure, but less than the rupture transmembrane pressure [161]. Microporous membranes, for instance, are only suitable for low transmembrane pressure applications since bubble formation is possible at higher pressures (>3 psi) [177].

Furthermore, in studies carried out by Vladisavljević [178], the k_M was obtained from the "Wilson plot", where the values of $1/K_L$ were plotted against $1/Q_L$. Thus, the mass transfer resistance in the membrane ($1/k_M$) was determined by extrapolating the linear fit of the data to $1/Q_L = 0$, implying $Q_L \rightarrow \infty$ and thus $1/k_L \approx 0$ (Equation (1.5)).

1.4.1.2 Effect of different parameters on mass transfer

The gas-liquid mass transfer can be affected by several factors, and they can influence positively or negatively (Table 1.4). This section will summarize the main effects and discuss the main parameters already reported in the literature.

Table 1.4. Effect of different parameters on mass transfer. Modified from Schmitt et al. [161].

Parameters	Influence on the ozone mass transfer when the parameter increases	Reference
Initial pH	–	[168, 179, 180]
Water temperature	–	[181-183]
Liquid flow rate	+	[182, 184]
Inlet ozone gas flow rate	+	[183, 185]
Applied ozone concentration	=	[172, 183, 184]
Operating gas pressure	+	[183, 186]
Chemical reaction	+	[180, 187, 188]

Water pH and temperature

Several studies have revealed that the pH of the liquid phase has a significant impact on ozonation and, consequently, on mass transfer [146, 168, 189]. With an increase in pH, free radical processes are accelerated, and the presence of hydroxide anions speeds up the breakdown of ozone (Equations (1.9) and (1.10)) [189]. Consequently, leading to lower concentrations of dissolved ozone in ozonated effluents.

$$O_3 + OH^- \rightarrow HO_2^- + O_2 \quad (1.9)$$

$$O_3 + HO_2^- \rightarrow OH^\bullet + O_2 + O_2^- \quad (1.10)$$

The increase in O_3 decomposition can be a negative point for mass transfer, but the ozonation of resistant compounds has positive points, as they can react by indirect reaction thanks to the formation of hydroxyl radicals, which are non-selective oxidants.

The temperature of the liquid can also directly impact the solubility and half-life of the O_3 molecule, according to Henry's law. Therefore, increasing temperature causes two things to happen: (i) the decomposition of O_3 is accelerated, and the stability of O_3 in water is decreased [181]; and (ii) certain properties of the liquid are changed, such as lower surface tension and viscosity [182]. Huang et al. [183] investigated the effects of different temperatures on ozone concentration and $OH^\bullet$ concentration in the liquid phase (Figure 1.10). The results confirmed that the ozone concentration in the liquid phase decreases significantly with increasing temperature. On the one hand, an increase in temperature accelerates ozone decomposition and thus decreases ozone stability in the water, resulting in lower concentrations of dissolved ozone in the liquid phase. On the other hand, the concentration of $OH^\bullet$ in water increases with temperature when the temperature is between 20 and 35 °C.

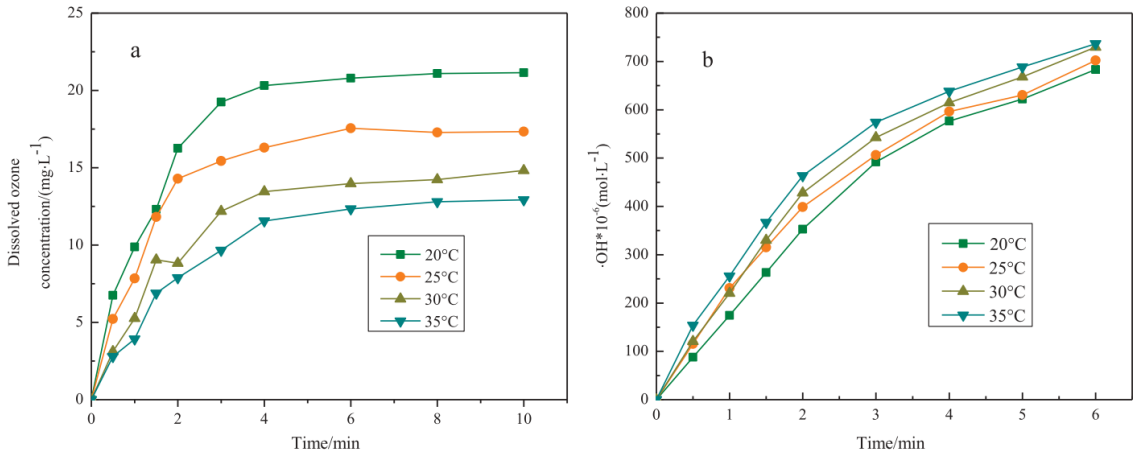

Figure 1.10. Effect of liquid phase temperature on the concentration of O_3 (a) and $OH^{\bullet}$ (b) in water. Reprinted from Huang et al. [183].

Liquid flow rate

The liquid flow rate is regarded as a key design factor for GLMCs, since it significantly impacts mass transfer, dissolved ozone concentration, and pressure drop in the system. Increasing the liquid flow rate results in a higher ozone mass transfer [179, 182, 184]. This phenomenon may be explained by the fact that as Q_L increases, there is more liquid turbulence, or a higher Reynolds number, which leads to the formation of smaller gas bubbles or thinner liquid films, increasing the interfacial area and decreasing the resistance to O_3 transfer in the water phase boundary layer. This statement is supported by Zoumpouli et al. [190], in which the authors reported that liquid flow rate is the most important factor in ozone mass transfer, followed by membrane thickness and ozone gas concentration.

It is highly recommended to implement a high liquid velocity in wastewater treatment applications in order to have a high mass transfer and significant shear stress on the membrane surface that might reduce potential fouling. Nevertheless, higher liquid flow rates indicate lower residence time. It's noteworthy to note that a particular amount of dissolved ozone concentration is necessary for many applications to achieve a satisfactory degree of disinfection or a sufficient kinetic response. Therefore, it is necessary to find a balance between high liquid velocity, i.e., high mass transfer, and high dissolved ozone content.

Applied ozone concentration

The relationship between O_3 in the gas-phase ($[O_3]_{G,inlet}$) and soluble O_3 in the liquid-phase ($[O_3]_L$) can be represented by Henry's law. The equilibrium concentration (solubility) of ozone in water ($[O_3^*]$) increases with the enhancement of equilibrium pressure and O_3 gas concentration due to the higher O_3 diffusion rate (Equation (1.11)). Figure 1.11 presents the results obtained by Kukuzaki et al. [172] with tubular hydrophilic and hydrophobized SPG membranes. The authors made experiments for different ozone concentrations in the gas phase (1.1–3.8 mol m^{-3}). The dissolved ozone concentration, as

measured at the contactor output in the liquid phase, rises in proportion to the amount of ozone in the gas phase (Figure 1.11a), associated with a higher driving force. This is mainly caused by an increase in the amount of imported ozone, which raises the mass transfer driving force from the gas phase into the liquid phase and enhances ozone concentration in the liquid phase [183]. In contrast, the overall mass transfer coefficient based on the water phase was virtually independent of the amount of ozone in the gas phase (Figure 1.11b) [172, 184].

$$[O_3^*] = \frac{[O_3]_{G,inlet}}{H} \tag{1.11}$$

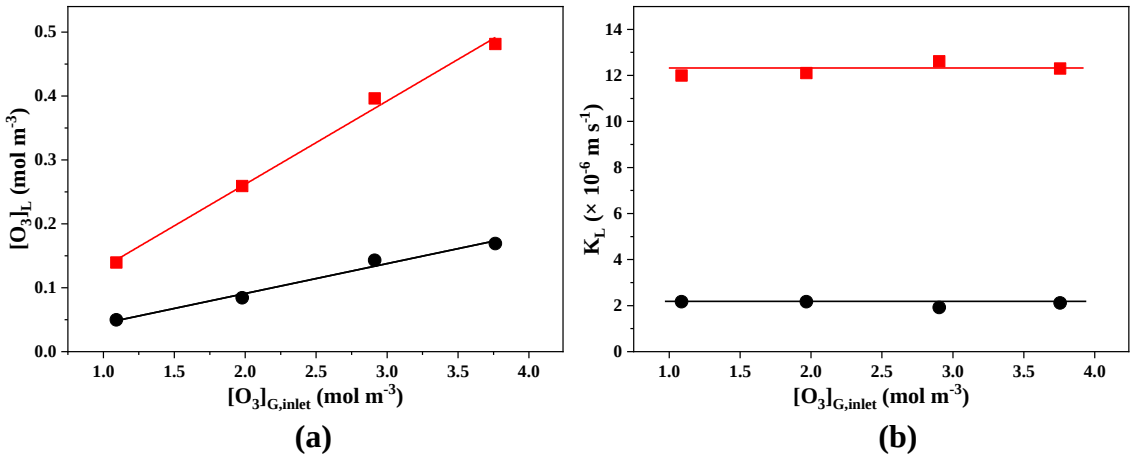

Figure 1.11. (a) Concentration of ozone dissolved in water at the steady state as a function of ozone concentration in the gas phase for (●) the hydrophilic and (■) hydrophobized SPG membranes; (b) Overall mass transfer coefficient for ozone dissolution as a function of ozone concentration in the gas phase for (●) the hydrophilic and (■) hydrophobized SPG membranes. The volumetric water flow rate inside the membrane was kept at 8 dm^3 min^{-1}. Adapted from Kukuzaki et al. [172].

Inlet ozone gas flow rate

The mass transfer and the ozone concentration in the water are positively influenced by the increase in the inlet ozone gas flow rate. According to several studies, the mass transfer results indicate that a higher ozone gas flow rate decreases the required time to reach the dissolved O_3 equilibrium in the reactor and slightly improves the equilibrium concentration [183, 185]. The amount of O_3 injected per unit of time increases with an increase in ozone gas flow rate, speeding up the rate at which O_3 dissolves until equilibrium. Additionally, a greater gas flow rate improves the turbulence at the gas-liquid interface, increasing the number and velocity of the produced bubbles and dispersing the liquid more effectively [172]. This results in a higher gas-liquid interface area and increases the mass transfer resistance.

1.4.1.3 Application of the GLMC in the removal of CECs

Gas-liquid contact systems can be an excellent strategy to increase the effectiveness of ozone-based treatment methods for CECs removal. The homogeneous distribution of the O_3 gas stream into the liquid phase through virtually unlimited dosing points along the membrane length can raise the transformation rate of target contaminants [191], reducing O_3 consumption and avoiding bromate formation [169]. Furthermore, due to its operational benefits of high interphase surface and independent gas/liquid management, membrane contactors make it easier to deliver the required ozone dose to achieve treatment efficiency [172, 180]. Several studies have investigated the removal of CECs through membrane contactors using ozonation processes (Table 1.5). Most of these works have focused on the following:

- Treatment of synthetic effluents contaminated with dyes [146, 147, 164, 191];
- Using high initial contaminant concentrations (mg L^{-1}) [146-148, 160, 164, 165, 168, 191];
- Using a single model pollutant [147, 148, 152, 160, 164, 165, 190, 191];
- Using polymer hollow fibre membranes, such as polytetrafluoroethylene (PTFE) [148, 152, 160, 165, 191], polyvinylidene fluoride (PVDF) [146, 147, 164], polydimethylsiloxane (PDMS) [190].

PVDF membranes can get entirely or partially wet, which causes their pores to fill with liquid and lower the mass-transfer efficiency (as seen in *Section 1.4.1.1*). Hence, hydrophobic membranes are necessary for ozonation in order to prevent this wetness. Hanh Le et al. [164] prepared PVDF membranes modified by pulse inductively coupled plasma and grafting by chloroalkylsilanes for hydrophobicity enhancement and applied in the treatment of dye wastewater using ozonation (Figure 1.12). In comparison to the original membrane, the modified membrane had a greater and more consistent ozone flux. After 90 minutes, Direct Blue 71 (DB 71) removal by ozonation with the membrane contactor showed values above 90%. Removals of COD and TOC were 63% and 20%, respectively.

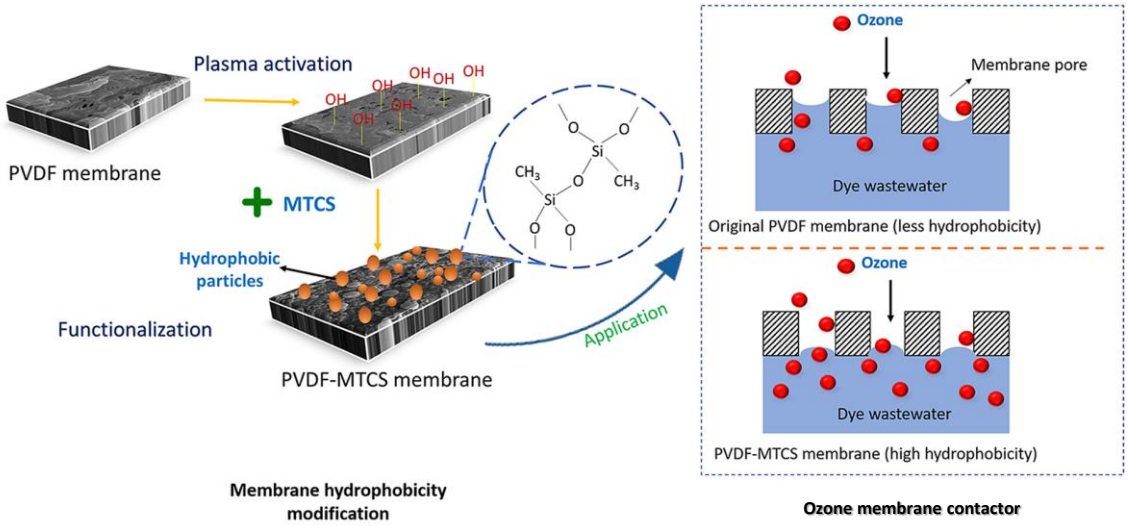

Figure 1.12. Schematic of a modified hydrophobic PVDF hollow fibre membrane for dye effluent treatment by ozonation membrane contactor. Note: MTCS – methyltrichlorosilane; PVDF – polyvinylidene fluoride. Modified from Hanh Le et al. [164].

In a ceramic tubular membrane contactor with gas on the shell side, Stylianou et al. [169] investigated the removal of carbamazepine (CBZ), benzotriazole (BZT), p-chlorobenzoic acid (pCBA), atrazine (ATZ), as well as bromate formation. At 0.4 mg O_3 mg DOC^{-1}, the carbamazepine concentration was reduced to below 0.1 M, removing >90%. On the other hand, BZT, pCBA, and ATZ were eliminated at 70, 57, and 49%, respectively. The authors emphasized that the sequence of the compounds' reactivity with O_3 reflected the removal effectiveness.

Merle et al. [152] studied the use of a membrane contactor in conjunction with an advanced oxidation process (presence of H_2O_2) to reduce bromate generation and decrease CECs. The authors used the reactor "MEMBRO_3X", in which ozone is transferred to the water through the pores of polytetrafluoroethylene (PTFE) hollow fibre membranes (Figure 1.13). Compared to the conventional peroxone process (O_3/H_2O_2), the MEMBRO_3X procedure performs better in terms of CECs abatement (95% removal for pCBA) and bromate reduction (<0.5 μg/L BrO_3^-) for the treatment of groundwater and surface water.

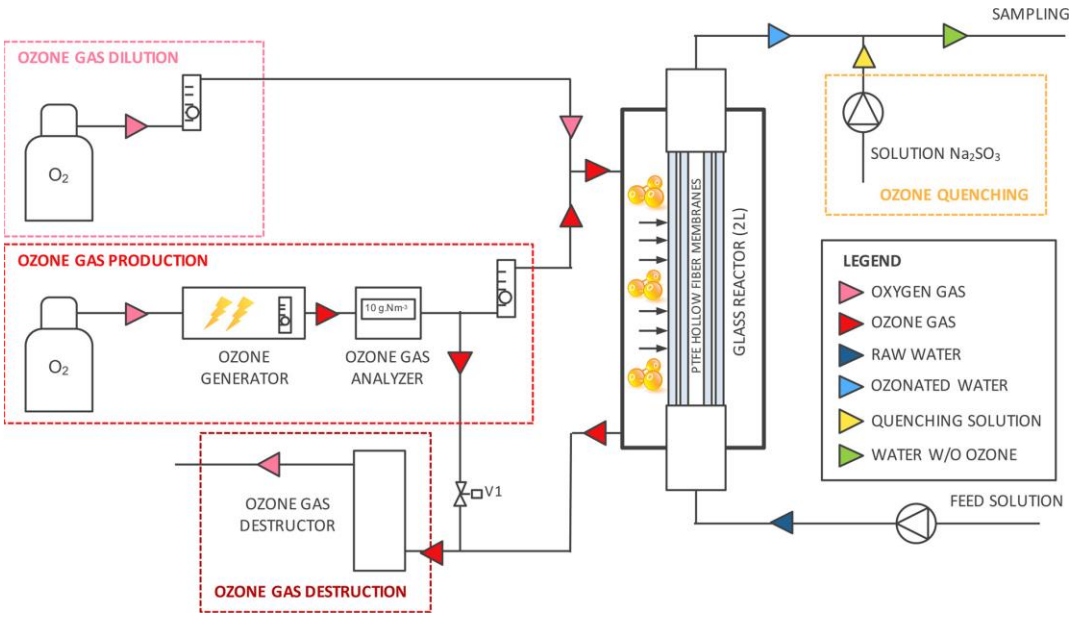

Figure 1.13. Scheme of the MEMBRO$_3$X process at laboratory scale. PTFE hollow fibre membranes were placed in a glass reactor fed with an ozone/oxygen gas mixture. The water flows inside the fibres without permeation through the membranes, while ozone gas diffuses through the membranes by a chemically driven transfer. Downstream from the reactor, residual ozone is quenched with SO_3^{2-}.

In addition, membranes can be functionalised with nanoparticles or catalysts to improve membrane performance (nano-enhanced membranes – NEM) and the removal of water contaminants by catalytic ozonation [148, 160, 192]. This approach has proved successful in recent research, e.g., Mansas et al. [193] demonstrated the enhanced catalytic ozonation activity of a commercial NF ceramic membrane functionalized with mesoporous maghemite (γ-Fe_2O_3). Also, Liu et al. [194] applied a $CuMn_2O_4$/g-C_3N_4 catalytic ceramic membrane that increased more than 3-fold the degradation rate of benzophenone-4 when compared to O_3-only, and Lee et al. [195] developed a Ce-doped TiOx ceramic membrane that proved to be effective in degrading and mineralizing a mixture of micropollutants with low specific O_3 consumption.

Table 1.5. Studies on GLMCs in ozonation processes identifying CECs or dyes removed considering treatment, membrane characteristics, and evaluated parameters.

CECs	Initial concentration	Source*	Removal range	Type of membrane	Evaluated parameters	Ref.
Carbamazepine, benzotriazole, p-chlorobenzoic acid, atrazine	1 µM	SW	49–90%	Tubular α-Al_2O_3	• Impact of hydrogen peroxide (peroxide treatment)	[169]
p-chlorobenzoic acid	0.5 µM	SW	>90%	Polytetrafluoroethylene (PTFE) hollow fibre	• Ozone dose • Inlet ozone concentration in the gas stream • Hydrogen peroxide dose	[152]
Direct Blue 71 and reactive Red 239	100 mg L^{-1}	SC	>90%	Polyvinylidene fluoride (PVDF) hollow fibre	• Dye concentration • Comparison of different membranes • Effect of dye types	[146]
Direct blue 71	100 mg L^{-1}	UWW	>90%	Polyvinylidene fluoride (PVDF) hollow fibre	• Ozone fluxes • Ozone dose • Hydrophobicity	[164]
Reactive blue 19	75 mg L^{-1}	SC	65–97%	Polyvinylidene fluoride (PVDF) hollow fibre	• Influence of Fenton reagents • Initial pH • Dye concentration • Gas flow rate • Liquid flow rate • Ozone concentration	[147]
Nitrobenzene	30 mg L^{-1}	SC	~80%	Polytetrafluoroethylene (PTFE) flat sheet	• Ozone concentration • Gas flow rate • Initial pH value • Membrane matrix • Presence of current	[148, 160]
p-chlorobenzoic acid	10 µM	SC/UWW	15–80%	Non-porous tubular polydimethylsiloxane (PDMS)	• Ozone concentration • Membrane size • Liquid flow rate • Presence of H_2O_2	[190]

Table 1.5. Studies on GLMCs in ozonation processes identifying CECs or dyes removed considering treatment, membrane characteristics, and evaluated parameters (continued).

CECs	Initial concentration	Source*	Removal range	Type of membrane	Evaluated parameters	Ref.
Direct red 23, acid blue 113, reactive red 120	100 mg L^{-1}	SC	72–97%	Polyvinylidene fluoride (PVDF) and polytetrafluoroethylene (PTFE) hollow fibre	• Liquid flow rate • Gas flow rate • Operating temperature	[168]
Acid orange 7	5 mg L^{-1}	SC	34%	Polytetrafluoroethylene (PTFE) hollow fibre	• Ozone concentration • Liquid flow rate • Gas flow rate	[191]
Sulfolane	200 mg L^{-1}	SC	96.5%	Polytetrafluoroethylene (PTFE) hollow fibre	• Ozone concentration • Liquid flow rate • Temperature • Ultrasonic power • Presence of sodium chloride	[165]

Note: *UWW – Wastewater; SC – Synthetic wastewater; SW – surface water.

1.4.2 Liquid/Liquid membrane contactor (LLMC)

Liquid/Liquid membrane contactor (LLMC) is a device that brings two liquid fluids into contact at the entrance of pores and has been studied as a potential technology for wastewater treatment. LLMCs generally utilise hydrophobic hollow fibre membranes to transfer species, particularly ammonia, across the membrane from the feed side to the permeate side. This enables the concentration and recovery of nutrients from wastewater [196].

LLMC has also been studied for injecting liquid oxidants such as hydrogen peroxide (H_2O_2), peroxydisulfate (PDS), and iron (photo-Fenton) combined with radiation (UVA/UVC) for wastewater treatment with the main focus on CECs removal [10-12, 14, 197-199]. Commonly, the oxidant is typically delivered upstream of the photoreactor intake with the use of static mixers, which can enhance the in-line mixing of the chemical product with the effluent to be treated [200, 201]. The homolytic cleavage of the oxidant by UV photons and its subsequent breakdown with the organic and inorganic species present in the effluent cause the oxidant concentration to drop throughout the length of the reactor. This triggers an inhomogeneous reaction rate within the photoreactor and limits the length of reactors that can be utilized in full-scale applications. An oxidant concentration profile is therefore seen along the length of the reactor. Hence, higher dosages of oxidant are needed in the feed stream in order to reduce the radial and axial concentration gradients within the annular reaction zone and so maximize the effectiveness of the photochemical process. Nevertheless, a high concentration of oxidants can function as a radical scavenger mainly at the reactor intake [202], and increasing levels of residual oxidants constitute waste and need to be removed before discharging the treated water into the environment [203].

Membrane technology can be also used to deliver the bare minimum of oxidant required for the reaction. Vilar et al. [10] proposed an LLMC for UVC/H_2O_2 photochemical reactions where the chemical is injected radially for more uniform distribution along the length of the reactor. Cui et al. [204] proposed a theoretical analysis indicating the validity and promise of a continuous LLMC for the catalytic N-oxidation of alkylpyridines with hydrogen peroxide. For real-scale applications, a single LLMC model and a multiunit reactor bundle utilising a ceramic membrane for segregated H_2O_2 feeding were presented. Likewise, Buba et al. [205] used a liquid-liquid tube-in-tube semipermeable membrane microreactor to synthesize N-Methylated amino acids. In this experiment, a Teflon AF 2400 membrane was employed as a better mixing method, with the solvent being injected via a syringe pump in the reactor's annulus.

1.4.2.1 Application of the LLMC in the removal of CECs

Vilar and co-workers presented an LLMC, also called a tube-in-tube membrane reactor, for photochemical UVC-UVA/Oxidant (H_2O_2; PDS; Fe^{2+}), in a continuous-mode operation (Table 1.6; Figure 1.14). This reactor comprises an inner UF membrane and an outer quartz tube that receives UVC or UVA light from four lamps. The primary innovation of this technology is the radial insertion of an oxidant along the whole porous membrane length. According to the authors, the water's helical motion around the membrane shell-side improved the oxidant radial mixing, promoting a more uniform distribution of the oxidant in the annular reaction zone of the membrane microreactor. The suggested new reactor demonstrated performance that warrants further study, with oxytetracycline (OTC) removal efficiencies of roughly 36% and 7% in a single-pass mode ($[OTC]_0$ = 2 mg L^{-1}, $[H_2O_2]_0$ = 15.8 mg L^{-1}) utilizing ultrapure (SC) and UWW as solution matrices, respectively [10].

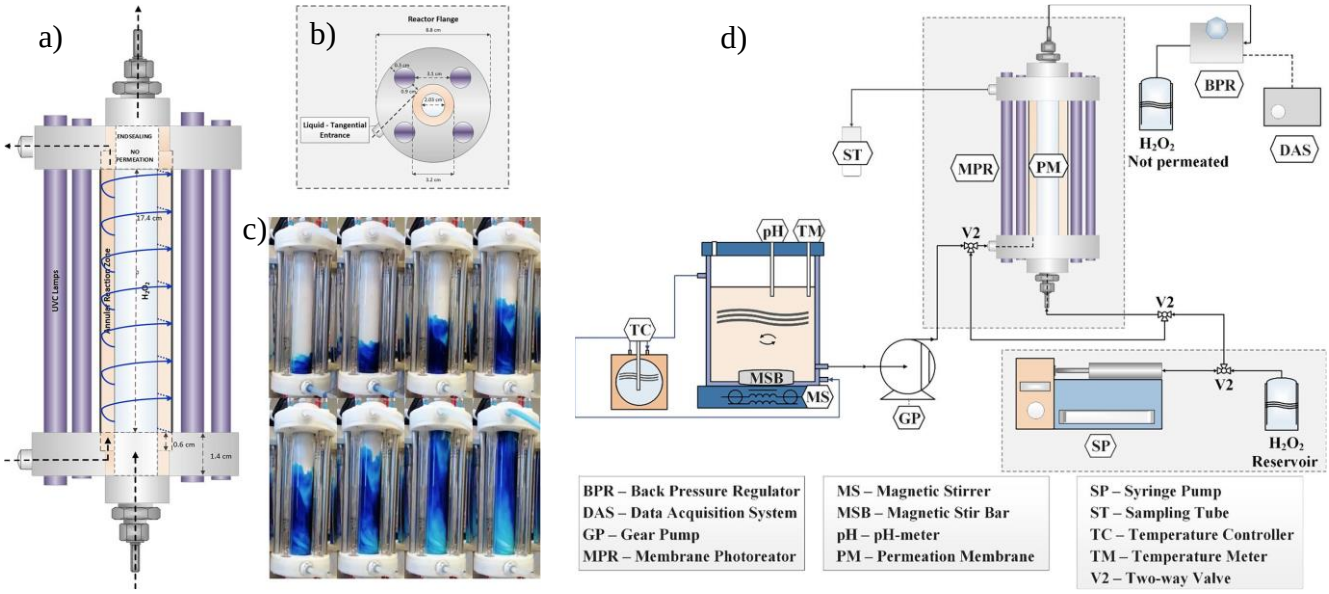

Figure 1.14. a) Reactor scheme; b) reactor flanges design; c) images of the helical motion of the tracer solution (methylene blue dye solution) in the annular reaction zone; d) sketch of the proposed setup. Reprinted from Vilar et al. [10].

To improve the removal of CECs, Castellanos et al. [11] proposed the use of a tube-in-tube membrane reactor for continuous dosing of small amounts of H_2O_2 to the active catalyst sites immobilized in the membrane shell-side (heterogeneous H_2O_2/TiO_2 photocatalysis), improving its contact with the catalytic sites and pollutants to be oxidized, also avoiding catalyst deactivation. In SC and UWW, tests were conducted using 100 µg L^{-1} of 17-estradiol (E2) and 17-ethinylestradiol (EE2). The UVC/H_2O_2/TiO_2 system demonstrated the maximum oxidation capacity with radial H_2O_2 addition, which led to E2 and EE2 elimination percentages of 51/32% and 48/30%, respectively, for the SC/UWW. In the same sense, Diório et al. [197] evaluated the effect of several parameters in the removal of a CEC target molecule,

amoxicillin (AMX), using SC and UWW ($[AMX]_{inlet}$ = 2.0 mg L^{-1}). The UVC/H_2O_2/TiO_2 system with radial addition of H_2O_2 (20 mg L^{-1}) and 9-TiO_2-P25 layers provided the highest AMX removal efficiency (72.2 ± 0.5%) with a UV fluence of 45 mJ cm^{-2} (residence time of 4.6 s). The authors also report that due to the presence of ROS scavengers and light-filtering species, the UWW matrix demonstrated a detrimental influence on AMX removal (~44%). Likewise, the oxidation of four pharmaceuticals, paracetamol (PCT), furosemide (FRS), nimesulide (NMD), and diazepam (DZP) (200 µg L^{-1} each), was performed using photochemical and photocatalytic processes, driven by UVA or UVC photons [198]. At steady state regime, the UVC/H_2O_2/TiO_2 system, with radial H_2O_2 addition (20 mg L^{-1}), showed the highest pharmaceuticals removal percentage, PCT (27.4%), FRS (35.0%), NMD (24.2%) and DZP (30.0%) in SC.

Díaz-Angulo et al. [12] presented the same tube-in-tube membrane reactor to promote a highly efficient photo-Fenton process at neutral pH under continuous mode operation. The membrane's lumen side supplies an acidic ferrous ion (Fe^{2+}) solution that is dosed and evenly distributed to the membrane shell side by permeating through the membrane pores (inside-out mode). In the reactor annulus, contaminated water that contains the antibiotic AMX and the oxidant H_2O_2 flows continually (space between the membrane shell-side and an outer quartz tube). With a residence time of only 4.6 seconds, the photo-Fenton reaction with Fe^{2+} radial addition, powered by UVC light, demonstrated the maximum AMX elimination for SC (65%; using $[Fe^{2+}]$ = 2 mg L^{-1} and $[H_2O_2]$ = 10 mg L^{-1}) and UWW (45%; using $[Fe^{2+}]$ = 5 mg L^{-1} and $[H_2O_2]$ = 40 mg L^{-1}).

Castellanos et al. [14] studied the performance of the UF ceramic membrane as photocatalyst support and oxidant-catalyst/water contactor to promote sulphate radical advanced oxidation processes by activation of peroxydisulfate (PDS). The PDS stock solution is supplied by the membrane's lumen side, permeates the membranes pores and reaches the annular reaction zone, where the catalyst and PDS are activated by UV light. For two endocrine-disrupting substances, E2 and EE2, spiked (100 µg L^{-1} each) in SC and UWW, the UVC/PDS/TiO_2 system demonstrated the highest removal efficiency. Similar results were also found by Lumbaque et al. [199] but for the removal of 4 pharmaceuticals (PCT, FRS, NMD, DZP; 200 µg L^{-1} of each).

Table 1.6. Summary of the main studies on LLMC for injection of different oxidants in the removal of CECs.

CECs	Initial concentration	Source[a]	Removal range	Oxidant[b] – Catalyst	Oxidant concentration	Ref.
Oxytetracycline	2 mg L^{-1}	SC/UWW	~36%	H_2O_2	7.9–63 mg L^{-1}	[10]
17β-estradiol, 17α-ethinylestradiol	100 µg L^{-1}	SC/UWW	30–51%	H_2O_2 – TiO_2	5–80 mg L^{-1}	[11]
Amoxicillin	2 mg L^{-1}	SC/UWW	18–72%	H_2O_2 – TiO_2	5–80 mg L^{-1}	[197]
Paracetamol, furosemide, nimesulide, diazepam	200 µg L^{-1}	SC/UWW	~35%	H_2O_2 – TiO_2	5–80 mg L^{-1}	[198]
Amoxicillin	2 mg L^{-1}	SC/UWW	~90%	H_2O_2 – Fe^{2+}	0.5–5 mg L^{-1}/ 2–40 mg L^{-1}	[12]
Paracetamol, furosemide, nimesulide, diazepam	200 µg L^{-1}	SC/UWW	2–43%	$S_2O_8^{2-}$ – TiO_2	0.15–2.36 mM	[199]
17β-estradiol, 17α-ethinylestradiol	100 µg L^{-1}	SC/UWW	8–46%	$S_2O_8^{2-}$ – TiO_2	0.15–2.35 mM	[14]

Note: [a]UWW – Urban wastewater; SC – Synthetic wastewater; [b]H_2O_2 – Hydrogen peroxide; Fe^{2+} – Ferrous ion; $S_2O_8^{2-}$ – Peroxydisulfate;

1.5 Overview and future outlook

By 2050, the rate of urbanization in Europe is projected to rise from its current level of 75% to approximately 84% [206]. This growth will increase the demand for water in quantity and quality and, consequently, increase pollution concentration if new and effective environmental measures are not implemented. Therefore, as part of the European Green Deal's Zero Pollution Action Plan [207], the EU 2030 Biodiversity Strategy [208], and the EU Urban Agenda [209], a substantial emphasis on water is needed to progress toward zero pollution. The best approach to conserve our water resources is to take immediate action to combat pollution from urban runoff and to address emerging issues like plastics (particularly plastic littering and uncontrolled discharge of microplastics), dangerous chemicals, bacteria, diseases, viruses, and other CECs. This calls for a systemic perspective that results in the creation of long-term projects to redesign society as a whole in a circular and resilient mode, which is reflected in the creation of new technologies, solutions, business models, and governance structures.

In this introductory section, some new treatment technologies that employed membranes were discussed based on the removal of CECs in the environment. Additionally, an overview of the main advantages and disadvantages of the application of membrane reactors was described, in which the membrane was used either as a filtering medium or as a means to dose oxidants (gaseous/liquid) combined with AOPs processes. The following can be highlighted based on the information provided:

i) Membrane filtration is one of the most efficient methods for removing CECs from water and wastewater because it may reject CECs in multiple ways depending on the chemistry of the input water, the membranes, and the characteristics of the solute. However, the main challenges in

using this technology are membrane fouling and the production of retentate. Combining membrane separation with AOPs not only removes resistant CECs, but also integrates their positive properties with each other.

ii) MCs are an interesting alternative to intensify wastewater treatment. Using MC, the oxidant is added uniformly to the water to be treated through many dosing points and with a high mass transfer surface area. It leads to a better transformation rate of CECs than with conventional processes. For example, many parameters influence mass transfer during ozonation using MCs. Consequently, when appropriately selected, the process efficiency may be considerably increased. On the other hand, the development of more effective membrane materials with hydrophobic properties is extremely relevant to enhance mass transfer.

1.6 Aim of the work and thesis outline

The present thesis focuses on the design and evaluation of two membrane reactors using innovative functionalized membranes for use in treatment processes. The two experimental units of membrane reactors were distinguished by their modes of operation: (i) filtration mode (the membrane acts as a filter medium and catalyst support) and (ii) dosing mode (the membrane acts as an ozone injector and catalyst support). DW and UWW, after secondary treatment, were fortified with several CECs with different characteristics.

The main objectives addressed in this thesis were:

i) Assessment of the efficiency of two membrane reactors (PMR and MC) for tertiary treatment of UWW, regarding the elimination of a mixture of CECs, towards wastewater reuse and, consequently, to have a positive effect on human health.
ii) Assessment of the influence of several operational variables on the efficiency of reactor systems, including the initial concentration of pollutants, *TMP*, liquid flow (hydraulic residence time, Reynolds), pH, temperature, oxidant dosage, amount of photocatalyst, radiation source (UVA/UVC), among others.

In addition, other objectives were covered, such as:

a) Preparation of a large area graphene membrane with subnanometric porosity for application in water desalination and in other membrane filtration applications.
b) Development of ceramic or borosilicate NEM through functionalization with TiO_2 and graphene codoped with TiO_2 (G-TiO_2) to promote their photocatalytic properties.

c) Minimization of membrane fouling by two mechanisms: photo-induced hydrophilicity of membranes, which may facilitate the adsorption of water on the membrane surface rather than fouling, and *in situ* degradation of contaminants on the membrane surface.
d) Evaluation of the PMR/MC efficiency for the removal of CECs from synthetic and real aqueous matrixes and optimization of the operational variables.
e) Quality assessment of treated effluents with toxicity tests using zebrafish embryo bioassay and microbiological inactivation efficiency.

The present thesis is structured into 7 chapters:

Chapter 1 corresponds to the present introductory section, wherein the water pollution problem by CECs and the treatment technologies that use membrane reactors are addressed. An exhaustive review of the most varied membrane reactors with different configurations and photocatalysts is presented, focusing mainly on the removal efficiency of CECs and their applicability/viability of the process.

Chapter 2 describes all chemical reagents, modelling of degradation kinetics, experimental units, and procedures, as well as the employed analytical determinations used within this thesis.

Chapter 3 focuses on the study of a continuous multilayer graphene prepared on ceramic microporous support with an area over 80 cm^2, 10^9 larger area than the previous reports. Subnanometric pores in the membrane have been formed by B and N doping and subsequent removal of the dopant elements creating vacancies. These pores can allow the translocation of H_2O molecules but no hydrated Na^+ or K^+ cations. The membrane exhibits over 95% removal for NaCl and KCl in high concentrations and high permeation flow.

Chapter 4 discloses the fabrication of a continuous multilayer graphene-TiO_2 nanocomposite prepared on ceramic microporous support using two different methods. The membrane exhibits a high permeate flux and CECs rejection, associated with size exclusion, Donnan exclusion, and reactivity towards hydroxyl radicals. The combination of filtration and oxidation (G-TiO_2-UVA) provided a higher-quality permeation and minimized membrane fouling.

Chapter 5 proposes a novel ozone membrane contactor to intensify ozone gas/water mass transfer and, simultaneously, allow the use of light and catalyst to activate ozone in a single unit. In this tubular porous borosilicate membrane distributor, the O_3 stream is fed by the lumen side and quickly delivered to the liquid through "virtually" unlimited dosing points along the membrane length. This technological approach enables a more homogeneous distribution of the injected gas, generating O_3 microbubbles in

the water and increasing the rate of ozone mass transfer, thus improving the reaction with the pollutants and reducing O_3 consumption.

Chapter 6 presents a disruptive ozone membrane contactor to promote highly efficient tertiary treatment of UWW, targeting disinfection and CECs removal under continuous mode operation. The effects of ozone dose, ozone inlet concentrations, O_3/UVC/TiO_2 process, and hydraulic residence time were investigated. Wastewater toxicity after treatment was also assessed.

Finally, Chapter 7 displays a discussion of the most relevant results and conclusions of this thesis, as well as some suggestions for future work.

1.7 References

[1] J.P. Meador, A. Yeh, G. Young, E.P. Gallagher, Contaminants of emerging concern in a large temperate estuary, Environmental Pollution 213 (2016) 254-267. https://doi.org/10.1016/j.envpol.2016.01.088.

[2] European Commission, Regulation (EU) 2020/741 of the European Parliament and of the Council of 25 May 2020 on minimum requirements for water reuse, Official Journal of the European Communities L 177/32 (2020).

[3] European Commission, Directive 2013/39/EU of the European Parliament and of the Council of 12 August 2013 amending Directives 2000/60/EC and 2008/105/EC as regards priority substances in the field of water policy, Official Journal of the European Union L 226/1 (2013).

[4] European Commission, Commission Implementing Decision (EU) 2018/840 of 5 June 2018 establishing a watch list of substances for Union-wide monitoring in the field of water policy pursuant to Directive 2008/105/EC of the European Parliament and of the Council and repealing Commission Implementing Decision (EU) 2015/495, Official Journal of the European Union L 141/9 (2018).

[5] European Commission, Commission Implementing Decision (EU) 2020/1161 of 4 August 2020 establishing a watch list of substances for Union-wide monitoring in the field of water policy pursuant to Directive 2008/105/EC of the European Parliament and of the Council Official Journal of the European Union, Official Journal of the European Union L 257/32 (2020).

[6] European Commission, Proposal for a revised Urban Wastewater Treatment Directive, 2022. https://environment.ec.europa.eu/publications/proposal-revised-urban-wastewater-treatment-directive_en.

[7] R.I.L. Eggen, J. Hollender, A. Joss, M. Schärer, C. Stamm, Reducing the Discharge of Micropollutants in the Aquatic Environment: The Benefits of Upgrading Wastewater Treatment Plants, Environmental Science & Technology 48 (14) (2014) 7683-7689. https://doi.org/10.1021/es500907n.

[8] P. Krzeminski, M.C. Tomei, P. Karaolia, A. Langenhoff, C.M.R. Almeida, E. Felis, F. Gritten, H.R. Andersen, T. Fernandes, C.M. Manaia, L. Rizzo, D. Fatta-Kassinos, Performance of secondary wastewater treatment methods for the removal of contaminants of emerging concern implicated in crop uptake and antibiotic resistance spread: A review, Science of The Total Environment 648 (2019) 1052-1081. https://doi.org/10.1016/j.scitotenv.2018.08.130.

[9] L. Rizzo, S. Malato, D. Antakyali, V.G. Beretsou, M.B. Đolić, W. Gernjak, E. Heath, I. Ivancev-Tumbas, P. Karaolia, A.R. Lado Ribeiro, G. Mascolo, C.S. McArdell, H. Schaar, A.M.T. Silva, D. Fatta-Kassinos, Consolidated vs new advanced treatment methods for the removal of contaminants of emerging concern from urban wastewater, Science of The Total Environment 655 (2019) 986-1008. https://doi.org/10.1016/j.scitotenv.2018.11.265.

[10] V.J.P. Vilar, P. Alfonso-Muniozguren, J.P. Monteiro, J. Lee, S.M. Miranda, R.A.R. Boaventura, Tube-in-tube membrane microreactor for photochemical UVC/H_2O_2 processes: A proof of concept, Chemical Engineering Journal 379 (2020) 122341. https://doi.org/10.1016/j.cej.2019.122341.

[11] R.M. Castellanos, J. Paulo Bassin, M. Dezotti, R.A.R. Boaventura, V.J.P. Vilar, Tube-in-tube membrane reactor for heterogeneous TiO_2 photocatalysis with radial addition of H_2O_2, Chemical Engineering Journal 395 (2020) 124998. https://doi.org/10.1016/j.cej.2020.124998.

[12] J. Díaz-Angulo, S. Cotillas, A.I. Gomes, S.M. Miranda, M. Mueses, F. Machuca-Martínez, M.A. Rodrigo, R.A.R. Boaventura, V.J.P. Vilar, A tube-in-tube membrane microreactor for tertiary treatment of urban wastewaters by photo-Fenton at neutral pH: A proof of concept, Chemosphere 263 (2021) 128049. https://doi.org/10.1016/j.chemosphere.2020.128049.

[13] P. Alfonso-Muniozguren, A.I. Gomes, D. Saroj, V.J.P. Vilar, J. Lee, The role of ozone combined with UVC/H_2O_2 process for the tertiary treatment of a real slaughterhouse wastewater, Journal of Environmental Management 289 (2021) 112480. https://doi.org/10.1016/j.jenvman.2021.112480.

[14] R.M. Castellanos, P.H. Presumido, M. Dezotti, V.J.P. Vilar, Ultrafiltration ceramic membrane as oxidant-catalyst/water contactor to promote sulfate radical AOPs: a case study on 17β-estradiol and 17α-ethinylestradiol removal, Environmental Science and Pollution Research 29 (28) (2022) 42157-42167. https://doi.org/10.1007/s11356-021-14806-5.

[15] D. Seibert, C.F. Zorzo, F.H. Borba, R.M. de Souza, H.B. Quesada, R. Bergamasco, A.T. Baptista, J.J. Inticher, Occurrence, statutory guideline values and removal of contaminants of emerging concern by Electrochemical Advanced Oxidation Processes: A review, Science of The Total Environment 748 (2020) 141527. https://doi.org/10.1016/j.scitotenv.2020.141527.

[16] E.M. Cuerda-Correa, M.F. Alexandre-Franco, C. Fernández-González, Advanced Oxidation Processes for the Removal of Antibiotics from Water. An Overview, Water 12 (1) (2020) 102. https://doi.org/10.3390/w12010102.

[17] C. Christophoridis, M.-C. Nika, R. Aalizadeh, N.S. Thomaidis, Ozonation of ranitidine: Effect of experimental parameters and identification of transformation products, Science of The Total Environment 557-558 (2016) 170-182. https://doi.org/10.1016/j.scitotenv.2016.03.026.

[18] G.K. Pearce, UF/MF pre-treatment to RO in seawater and wastewater reuse applications: a comparison of energy costs, Desalination 222 (1) (2008) 66-73. https://doi.org/10.1016/j.desal.2007.05.029.

[19] I. Vergili, Y. Kaya, U. Sen, Z.B. Gönder, C. Aydiner, Techno-economic analysis of textile dye bath wastewater treatment by integrated membrane processes under the zero liquid discharge approach, Resources, Conservation and Recycling 58 (2012) 25-35. https://doi.org/10.1016/j.resconrec.2011.10.005.

[20] S. Mozia, Photocatalytic membrane reactors (PMRs) in water and wastewater treatment. A review, Separation and Purification Technology 73 (2) (2010) 71-91. https://doi.org/10.1016/j.seppur.2010.03.021.

[21] R. Zhang, Y. Huang, C. Sun, L. Xiaozhen, X. Bentian, Z. Wang, Study on ultrasonic techniques for enhancing the separation process of membrane, Ultrasonics Sonochemistry (2018). https://doi.org/10.1016/j.ultsonch.2018.12.041.

[22] M. Mulder, Basic principles of membrane technology, 2nd ed., Springer Dordrecht 1996. https://doi.org/10.1007/978-94-009-1766-8.

[23] Z.F. Cui, Y. Jiang, R.W. Field, Fundamentals of Pressure-Driven Membrane Separation Processes, in: Z.F. Cui, H.S. Muralidhara (Eds.), Membrane Technology, Butterworth-Heinemann, Oxford, 2010, pp. 1-18. https://doi.org/10.1016/B978-1-85617-632-3.00001-X.

[24] V.B. Brião, A.L. Sbeghen, L.M. Colla, V. Castoldi, B. Seguenka, G.d.O. Schimidt, J.A.V. Costa, Is downstream ultrafiltration enough for production of food-grade phycocyanin from Arthrospira platensis?, Journal of Applied Phycology 32 (2) (2020) 1129-1140. https://doi.org/10.1007/s10811-019-02006-1.

[25] B.F. Jirjis, S. Luque, Chapter 9 - Practical Aspects of Membrane System Design in Food and Bioprocessing Applications, in: Z.F. Cui, H.S. Muralidhara (Eds.), Membrane Technology, Butterworth-Heinemann, Oxford, 2010, pp. 179-212. https://doi.org/10.1016/B978-1-85617-632-3.00009-4.

[26] J.R. Du, X. Zhang, X. Feng, Y. Wu, F. Cheng, M.E.A. Ali, Desalination of high salinity brackish water by an NF-RO hybrid system, Desalination 491 (2020) 114445. https://doi.org/10.1016/j.desal.2020.114445.

[27] H.T. Madsen, Chapter 6 - Membrane Filtration in Water Treatment – Removal of Micropollutants, in: E.G. Søgaard (Ed.), Chemistry of Advanced Environmental Purification Processes of Water, Elsevier, Amsterdam, 2014, pp. 199-248. https://doi.org/10.1016/B978-0-444-53178-0.00006-7.

[28] C. Bhattacharjee, V.K. Saxena, S. Dutta, Static turbulence promoters in cross-flow membrane filtration: a review, Chemical Engineering Communications 207 (3) (2020) 413-433. https://doi.org/10.1080/00986445.2019.1587610.

[29] J.L. Acero, F.J. Benitez, F. Teva, A.I. Leal, Retention of emerging micropollutants from UP water and a municipal secondary effluent by ultrafiltration and nanofiltration, Chemical Engineering Journal 163 (3) (2010) 264-272. https://doi.org/10.1016/j.cej.2010.07.060.

[30] L. Malaeb, G.M. Ayoub, Reverse osmosis technology for water treatment: State of the art review, Desalination 267 (1) (2011) 1-8. https://doi.org/10.1016/j.desal.2010.09.001.

[31] Y. Yoon, P. Westerhoff, S.A. Snyder, E.C. Wert, Nanofiltration and ultrafiltration of endocrine disrupting compounds, pharmaceuticals and personal care products, Journal of Membrane Science 270 (1) (2006) 88-100. https://doi.org/10.1016/j.memsci.2005.06.045.

[32] M.A. Al-Obaidi, J.P. Li, C. Kara-Zaïtri, I.M. Mujtaba, Optimisation of reverse osmosis based wastewater treatment system for the removal of chlorophenol using genetic algorithms, Chemical Engineering Journal 316 (2017) 91-100. https://doi.org/10.1016/j.cej.2016.12.096.

[33] S. Ge, L. Feng, L. Zhang, Q. Xu, Y. Yang, Z. Wang, K.-H. Kim, Rejection rate and mechanisms of drugs in drinking water by nanofiltration technology, Environmental Engineering Research 22 (3) (2017) 329-338. https://doi.org/10.4491/eer.2016.157.

[34] R. Iglesias, E. Ortega, G. Batanero, L. Quintas, Water reuse in Spain: Data overview and costs estimation of suitable treatment trains, Desalination 263 (1) (2010) 1-10. https://doi.org/10.1016/j.desal.2010.06.038.

[35] J. Radjenović, M. Petrović, F. Ventura, D. Barceló, Rejection of pharmaceuticals in nanofiltration and reverse osmosis membrane drinking water treatment, Water Research 42 (14) (2008) 3601-3610. https://doi.org/10.1016/j.watres.2008.05.020.

[36] O.S. Arvaniti, M.E. Dasenaki, A.G. Asimakopoulos, N.C. Maragou, V.G. Samaras, K. Antoniou, G. Gatidou, D. Mamais, C. Noutsopoulos, Z. Frontistis, N.S. Thomaidis, A.S. Stasinakis, Effectiveness of tertiary treatment processes in removing different classes of emerging contaminants from domestic

wastewater, Frontiers of Environmental Science & Engineering 16 (11) (2022) 148. https://doi.org/10.1007/s11783-022-1583-y.

[37] Y.-l. Liu, Y.-y. Zhao, X.-m. Wang, X.-h. Wen, X. Huang, Y.F. Xie, Effect of varying piperazine concentration and post-modification on prepared nanofiltration membranes in selectively rejecting organic micropollutants and salts, Journal of Membrane Science 582 (2019) 274-283. https://doi.org/10.1016/j.memsci.2019.04.018.

[38] Y. Kiso, Y. Sugiura, T. Kitao, K. Nishimura, Effects of hydrophobicity and molecular size on rejection of aromatic pesticides with nanofiltration membranes, Journal of Membrane Science 192 (1) (2001) 1-10. https://doi.org/10.1016/S0376-7388(01)00411-2.

[39] S. Yüksel, N. Kabay, M. Yüksel, Removal of bisphenol A (BPA) from water by various nanofiltration (NF) and reverse osmosis (RO) membranes, Journal of Hazardous Materials 263 (2013) 307-310. https://doi.org/10.1016/j.jhazmat.2013.05.020.

[40] C. Causserand, P. Aimar, J.P. Cravedi, E. Singlande, Dichloroaniline retention by nanofiltration membranes, Water Research 39 (8) (2005) 1594-1600. https://doi.org/10.1016/j.watres.2004.12.039.

[41] D. Dolar, A. Vuković, D. Ašperger, K. Košutić, Effect of water matrices on removal of veterinary pharmaceuticals by nanofiltration and reverse osmosis membranes, Journal of Environmental Sciences 23 (8) (2011) 1299-1307. https://doi.org/10.1016/S1001-0742(10)60545-1.

[42] J.C. Espíndola, R.O. Cristóvão, A. Mendes, R.A.R. Boaventura, V.J.P. Vilar, Photocatalytic membrane reactor performance towards oxytetracycline removal from synthetic and real matrices: Suspended vs immobilized TiO_2-P25, Chemical Engineering Journal 378 (2019) 122114. https://doi.org/10.1016/j.cej.2019.122114.

[43] S. Sanches, A. Penetra, A. Rodrigues, E. Ferreira, V.V. Cardoso, M.J. Benoliel, M.T. Barreto Crespo, V.J. Pereira, J.G. Crespo, Nanofiltration of hormones and pesticides in different real drinking water sources, Separation and Purification Technology 94 (2012) 44-53. https://doi.org/10.1016/j.seppur.2012.04.003.

[44] M. Nikbakht Fini, H.T. Madsen, J. Muff, The effect of water matrix, feed concentration and recovery on the rejection of pesticides using NF/RO membranes in water treatment, Separation and Purification Technology 215 (2019) 521-527. https://doi.org/10.1016/j.seppur.2019.01.047.

[45] J.L. Acero, F.J. Benitez, A.I. Leal, F.J. Real, F. Teva, Membrane filtration technologies applied to municipal secondary effluents for potential reuse, Journal of Hazardous Materials 177 (1) (2010) 390-398. https://doi.org/10.1016/j.jhazmat.2009.12.045.

[46] J. Cuhorka, E. Wallace, P. Mikulášek, Removal of micropollutants from water by commercially available nanofiltration membranes, Science of The Total Environment 720 (2020) 137474. https://doi.org/10.1016/j.scitotenv.2020.137474.

[47] Y. Song, X. Li, Y. Wang, S. Ma, T. Li, X. Chen, Y. Li, K. Jiang, Adsorption and fouling behaviors of customized nanocomposite membrane to trace pharmaceutically active compounds under multiple influent matrices, Water Research 206 (2021) 117762. https://doi.org/10.1016/j.watres.2021.117762.

[48] V. Yangali-Quintanilla, S.K. Maeng, T. Fujioka, M. Kennedy, G. Amy, Proposing nanofiltration as acceptable barrier for organic contaminants in water reuse, Journal of Membrane Science 362 (1) (2010) 334-345. https://doi.org/10.1016/j.memsci.2010.06.058.

[49] S. Gidstedt, A. Betsholtz, M. Cimbritz, Å. Davidsson, M. Hagman, S. Karlsson, M. Takman, O. Svahn, F. Micolucci, Chemically enhanced primary treatment, microsieving, direct membrane filtration and GAC filtration of municipal wastewater: a pilot-scale study, Environmental Technology (2022) 1-12. https://doi.org/10.1080/09593330.2022.2099307.

[50] A. Nahrstedt, A. Gaba, B. Zimmermann, T. Jentzsch, K. Kroemer, Y. Tiemann, L. Harsanyi, P. Buchta, U. Doelchow, J. Lipnizki, K. Mende, T. Koch, A. Rohn, Reuse of municipal wastewater for different purposes based on a modular treatment concept, Journal of Water Reuse and Desalination 10 (4) (2020) 301-316. https://doi.org/10.2166/wrd.2020.040.

[51] M. Shakak, R. Rezaee, A. Maleki, A. Jafari, M. Safari, B. Shahmoradi, H. Daraei, S.-M. Lee, Synthesis and characterization of nanocomposite ultrafiltration membrane (PSF/PVP/SiO_2) and performance evaluation for the removal of amoxicillin from aqueous solutions, Environmental Technology & Innovation 17 (2020) 100529. https://doi.org/10.1016/j.eti.2019.100529.

[52] Y. Ozay, O. Canli, B.O. Unal, B. Keskinler, N. Dizge, Investigation of plasticizer production industry wastewater treatability using pressure-driven membrane process, Water Supply 21 (5) (2020) 1994-2007. https://doi.org/10.2166/ws.2020.268.

[53] W. Guo, H.-H. Ngo, J. Li, A mini-review on membrane fouling, Bioresource Technology 122 (2012) 27-34. https://doi.org/10.1016/j.biortech.2012.04.089.

[54] S.H. Joo, B. Tansel, Novel technologies for reverse osmosis concentrate treatment: A review, Journal of Environmental Management 150 (2015) 322-335. https://doi.org/10.1016/j.jenvman.2014.10.027.

[55] C.N. Rani, S. Karthikeyan, S. Prince Arockia Doss, Photocatalytic ultrafiltration membrane reactors in water and wastewater treatment - A review, Chemical Engineering and Processing - Process Intensification 165 (2021) 108445. https://doi.org/10.1016/j.cep.2021.108445.

[56] V. Augugliaro, M. Litter, L. Palmisano, J. Soria, The combination of heterogeneous photocatalysis with chemical and physical operations: A tool for improving the photoprocess performance, Journal of Photochemistry and Photobiology C: Photochemistry Reviews 7 (4) (2006) 127-144. https://doi.org/10.1016/j.jphotochemrev.2006.12.001.

[57] M. Skoumal, P.-L. Cabot, F. Centellas, C. Arias, R.M. Rodríguez, J.A. Garrido, E. Brillas, Mineralization of paracetamol by ozonation catalyzed with Fe^{2+}, Cu^{2+} and UVA light, Applied Catalysis B: Environmental 66 (3) (2006) 228-240. https://doi.org/10.1016/j.apcatb.2006.03.016.

[58] E.J. Rosenfeldt, P.J. Chen, S. Kullman, K.G. Linden, Destruction of estrogenic activity in water using UV advanced oxidation, Science of The Total Environment 377 (1) (2007) 105-113. https://doi.org/10.1016/j.scitotenv.2007.01.096.

[59] G. Pérez-Lucas, A. El Aatik, M. Aliste, V. Hernández, J. Fenoll, S. Navarro, Reclamation of aqueous waste solutions polluted with pharmaceutical and pesticide residues by biological-photocatalytic (solar) coupling in situ for agricultural reuse, Chemical Engineering Journal 448 (2022) 137616. https://doi.org/10.1016/j.cej.2022.137616.

[60] B. Gupta, A.K. Gupta, C.S. Tiwary, P.S. Ghosal, A multivariate modeling and experimental realization of photocatalytic system of engineered S–C_3N_4/ZnO hybrid for ciprofloxacin removal: Influencing factors and degradation pathways, Environmental Research 196 (2021) 110390. https://doi.org/10.1016/j.envres.2020.110390.

[61] Y. Sun, L. Xu, P. Jin, X. Bai, X. Jin, X. Shi, Simultaneous removal of colorless micropollutants and hexavalent chromium by pristine TiO_2 under visible light: An electron transfer mechanism, Chemical Engineering Journal 405 (2021) 126968. https://doi.org/10.1016/j.cej.2020.126968.

[62] D.B. Silva, G. Buttiglieri, B. Babić, D. Ašperger, S. Babić, Performance of TiO_2/UV-LED-Based Processes for Degradation of Pharmaceuticals: Effect of Matrix Composition and Process Variables, Nanomaterials 12 (2) (2022). https://doi.org/10.3390/nano12020295.

[63] E. Baştürk, M. Karataş, Removal of pharmaceuticals by advanced treatment methods, Journal of Environmental Management 300 (2021) 113808. https://doi.org/10.1016/j.jenvman.2021.113808.

[64] O.K. Dalrymple, D.H. Yeh, M.A. Trotz, Removing pharmaceuticals and endocrine-disrupting compounds from wastewater by photocatalysis, Journal of Chemical Technology & Biotechnology 82 (2) (2007) 121-134. https://doi.org/10.1002/jctb.1657.

[65] D. Kanakaraju, B.D. Glass, M. Oelgemöller, Advanced oxidation process-mediated removal of pharmaceuticals from water: A review, Journal of Environmental Management 219 (2018) 189-207. https://doi.org/10.1016/j.jenvman.2018.04.103.

[66] T. Sun, Y. Liu, L. Shen, Y. Xu, R. Li, L. Huang, H. Lin, Magnetic field assisted arrangement of photocatalytic TiO_2 particles on membrane surface to enhance membrane antifouling performance for water treatment, Journal of Colloid and Interface Science 570 (2020) 273-285. https://doi.org/10.1016/j.jcis.2020.03.008.

[67] W. Zhang, L. Ding, J. Luo, M.Y. Jaffrin, B. Tang, Membrane fouling in photocatalytic membrane reactors (PMRs) for water and wastewater treatment: A critical review, Chemical Engineering Journal 302 (2016) 446-458. https://doi.org/10.1016/j.cej.2016.05.071.

[68] H.K. Shon, S. Phuntsho, S. Vigneswaran, Effect of photocatalysis on the membrane hybrid system for wastewater treatment, Desalination 225 (1) (2008) 235-248. https://doi.org/10.1016/j.desal.2007.05.032.

[69] M.J. Rivero, S.A. Parsons, P. Jeffrey, M. Pidou, B. Jefferson, Membrane chemical reactor (MCR) combining photocatalysis and microfiltration for grey water treatment, Water Science and Technology 53 (3) (2006) 173-180. https://doi.org/10.2166/wst.2006.090.

[70] R.C. Asha, M. Kumar, Sulfamethoxazole in poultry wastewater: Identification, treatability and degradation pathway determination in a membrane-photocatalytic slurry reactor, Journal of Environmental Science and Health, Part A 50 (10) (2015) 1011-1019. https://doi.org/10.1080/10934529.2015.1038161.

[71] V.C. Sarasidis, K.V. Plakas, S.I. Patsios, A.J. Karabelas, Investigation of diclofenac degradation in a continuous photo-catalytic membrane reactor. Influence of operating parameters, Chemical Engineering Journal 239 (2014) 299-311. https://doi.org/10.1016/j.cej.2013.11.026.

[72] D. Deemter, F.E.B. Coelho, I. Oller, S. Malato, A.M. Amat, Assessment of a Novel Photocatalytic TiO_2-Zirconia Ultrafiltration Membrane and Combination with Solar Photo-Fenton Tertiary Treatment of Urban Wastewater, Catalysts 12 (5) (2022) 552. https://doi.org/10.3390/catal12050552.

[73] N. Sreedhar, M. Kumar, S. Al Jitan, N. Thomas, G. Palmisano, H.A. Arafat, 3D printed photocatalytic feed spacers functionalized with β-FeOOH nanorods inducing pollutant degradation and

membrane cleaning capabilities in water treatment, Applied Catalysis B: Environmental 300 (2022) 120318. https://doi.org/10.1016/j.apcatb.2021.120318.

[74] R. Yue, B. Raisi, J. Rahmatinejad, Z. Ye, B. Barbeau, M.S. Rahaman, A photo-Fenton nanocomposite ultrafiltration membrane for enhanced dye removal with self-cleaning properties, Journal of Colloid and Interface Science 604 (2021) 458-468. https://doi.org/10.1016/j.jcis.2021.06.157.

[75] F.E. Bortot Coelho, D. Deemter, V.M. Candelario, V. Boffa, S. Malato, G. Magnacca, Development of a photocatalytic zirconia-titania ultrafiltration membrane with anti-fouling and self-cleaning properties, Journal of Environmental Chemical Engineering 9 (6) (2021) 106671. https://doi.org/10.1016/j.jece.2021.106671.

[76] L. Zhu, M. Wu, B. Van der Bruggen, L. Lei, L. Zhu, Effect of TiO_2 content on the properties of polysulfone nanofiltration membranes modified with a layer of TiO_2–graphene oxide, Separation and Purification Technology 242 (2020) 116770. https://doi.org/10.1016/j.seppur.2020.116770.

[77] D.A.B. Sidik, N.H.H. Hairom, A.W. Mohammad, Performance and fouling assessment of different membrane types in a hybrid photocatalytic membrane reactor (PMR) for palm oil mill secondary effluent (POMSE) treatment, Process Safety and Environmental Protection 130 (2019) 265-274. https://doi.org/10.1016/j.psep.2019.08.018.

[78] A.K. Holda, S. Perera, E.A. Emanuelsson Patterson, Photocatalytic membranes containing homocoupled conjugated microporous poly(phenylene butadiynylene) for chemical-free degradation of organic micropollutants, Catalysis Communications 168 (2022) 106463. https://doi.org/10.1016/j.catcom.2022.106463.

[79] S. Sanches, C. Nunes, P.C. Passarinho, F.C. Ferreira, V.J. Pereira, J.G. Crespo, Development of photocatalytic titanium dioxide membranes for degradation of recalcitrant compounds, Journal of Chemical Technology & Biotechnology 92 (7) (2017) 1727-1737. https://doi.org/10.1002/jctb.5172.

[80] I.R. Bellobono, F. Morazzoni, P.M. Tozzi, Photocatalytic membrane modules for drinking water purification in domestic and community appliances, International Journal of Photoenergy 7 (2005) 365386. https://doi.org/10.1155/S1110662X05000164.

[81] C. Zhou, D. Ye, H. Jia, S. Yu, M. Liu, C. Gao, Surface mineralization of commercial thin-film composite polyamide membrane by depositing barium sulfate for improved reverse osmosis performance and antifouling property, Desalination 351 (2014) 228-235. https://doi.org/10.1016/j.desal.2014.07.040.

[82] V.-H. Nguyen, Q.B. Tran, X.C. Nguyen, L.T. Hai, T.T.T. Ho, M. Shokouhimehr, D.-V.N. Vo, S.S. Lam, H.P. Nguyen, C.T. Hoang, Q.V. Ly, W. Peng, S.Y. Kim, T.V. Tung, Q. Van Le, Submerged photocatalytic membrane reactor with suspended and immobilized N-doped TiO_2 under visible irradiation for diclofenac removal from wastewater, Process Safety and Environmental Protection 142 (2020) 229-237. https://doi.org/10.1016/j.psep.2020.05.041.

[83] N. Rosman, W.N.W. Salleh, J. Jaafar, Z. Harun, F. Aziz, A.F. Ismail, Photocatalytic Filtration of Zinc Oxide-Based Membrane with Enhanced Visible Light Responsiveness for Ibuprofen Removal, Catalysts 12 (2) (2022). https://doi.org/10.3390/catal12020209.

[84] S.A.G. Krishnan, S. Abinaya, G. Arthanareeswaran, S. Govindaraju, K. Yun, Surface-constructing of visible-light Bi_2WO_6/CeO_2 nanophotocatalyst grafted PVDF membrane for degradation of

tetracycline and humic acid, Journal of Hazardous Materials 421 (2022) 126747. https://doi.org/10.1016/j.jhazmat.2021.126747.

[85] S.F. Zakeritabar, M. Jahanshahi, M. Peyravi, Photocatalytic Behavior of Induced Membrane by ZrO_2–SnO_2 Nanocomposite for Pharmaceutical Wastewater Treatment, Catalysis Letters 148 (3) (2018) 882-893. https://doi.org/10.1007/s10562-018-2303-x.

[86] X. Pang, S. Xue, T. Zhou, Q. Xu, W. Lei, 2D/2D nanohybrid of Ti_3C_2 MXene/WO_3 photocatalytic membranes for efficient water purification, Ceramics International 48 (3) (2022) 3659-3668. https://doi.org/10.1016/j.ceramint.2021.10.147.

[87] G. Rao, Q. Zhang, H. Zhao, J. Chen, Y. Li, Novel titanium dioxide/iron (III) oxide/graphene oxide photocatalytic membrane for enhanced humic acid removal from water, Chemical Engineering Journal 302 (2016) 633-640. https://doi.org/10.1016/j.cej.2016.05.095.

[88] I. Horovitz, V. Gitis, D. Avisar, H. Mamane, Ceramic-based photocatalytic membrane reactors for water treatment – where to next?, Reviews in Chemical Engineering 36 (5) (2020) 593-622. https://doi.org/10.1515/revce-2018-0036.

[89] H. Piao, J. Zhao, M. Liu, S. Zhang, Q. Huang, Y. Liu, C. Xiao, Ultra-low power light driven lycopodium-like nanofiber membrane reinforced by PET braid tube with robust pollutants removal and regeneration capacity based on photo-Fenton catalysis, Chemical Engineering Journal 450 (2022) 138204. https://doi.org/10.1016/j.cej.2022.138204.

[90] C.I. Covaliu-Mierlă, E. Matei, O. Stoian, L. Covaliu, A.C. Constandache, H. Iovu, G. Paraschiv, TiO_2–Based Nanofibrous Membranes for Environmental Protection, Membranes 12 (2) (2022). https://doi.org/10.3390/membranes12020236.

[91] G.E. Romanos, C.P. Athanasekou, V. Likodimos, P. Aloupogiannis, P. Falaras, Hybrid Ultrafiltration/Photocatalytic Membranes for Efficient Water Treatment, Industrial & Engineering Chemistry Research 52 (39) (2013) 13938-13947. https://doi.org/10.1021/ie303475b.

[92] T. Liu, L. Wang, X. Liu, C. Sun, Y. Lv, R. Miao, X. Wang, Dynamic photocatalytic membrane coated with $ZnIn_2S_4$ for enhanced photocatalytic performance and antifouling property, Chemical Engineering Journal 379 (2020) 122379. https://doi.org/10.1016/j.cej.2019.122379.

[93] Y. Lv, C. Zhang, A. He, S.-J. Yang, G.-P. Wu, S.B. Darling, Z.-K. Xu, Photocatalytic Nanofiltration Membranes with Self-Cleaning Property for Wastewater Treatment, Advanced Functional Materials 27 (27) (2017) 1700251. https://doi.org/10.1002/adfm.201700251.

[94] A. Alem, H. Sarpoolaky, M. Keshmiri, Sol–gel preparation of titania multilayer membrane for photocatalytic applications, Ceramics International 35 (5) (2009) 1837-1843. https://doi.org/10.1016/j.ceramint.2008.10.034.

[95] R. Ahmad, J.K. Kim, J.H. Kim, J. Kim, Well-organized, mesoporous nanocrystalline TiO_2 on alumina membranes with hierarchical architecture: Antifouling and photocatalytic activities, Catalysis Today 282 (2017) 2-12. https://doi.org/10.1016/j.cattod.2016.03.051.

[96] X. Zhang, T. Zhang, J. Ng, D.D. Sun, High-Performance Multifunctional TiO_2 Nanowire Ultrafiltration Membrane with a Hierarchical Layer Structure for Water Treatment, Advanced Functional Materials 19 (23) (2009) 3731-3736. https://doi.org/10.1002/adfm.200901435.

[97] R. Qian, H. Zong, J. Schneider, G. Zhou, T. Zhao, Y. Li, J. Yang, D.W. Bahnemann, J.H. Pan, Charge carrier trapping, recombination and transfer during TiO_2 photocatalysis: An overview, Catalysis Today 335 (2019) 78-90. https://doi.org/10.1016/j.cattod.2018.10.053.

[98] S.K. Fanourakis, J. Peña-Bahamonde, P.C. Bandara, D.F. Rodrigues, Nano-based adsorbent and photocatalyst use for pharmaceutical contaminant removal during indirect potable water reuse, npj Clean Water 3 (1) (2020) 1. https://doi.org/10.1038/s41545-019-0048-8.

[99] P. Gao, Z. Liu, M. Tai, D.D. Sun, W. Ng, Multifunctional graphene oxide–TiO_2 microsphere hierarchical membrane for clean water production, Applied Catalysis B: Environmental 138-139 (2013) 17-25. https://doi.org/10.1016/j.apcatb.2013.01.014.

[100] A.M. Chávez, R.R. Solís, F.J. Beltrán, Magnetic graphene TiO_2-based photocatalyst for the removal of pollutants of emerging concern in water by simulated sunlight aided photocatalytic ozonation, Applied Catalysis B: Environmental 262 (2020) 118275. https://doi.org/10.1016/j.apcatb.2019.118275.

[101] L. Yang, L. Xu, X. Bai, P. Jin, Enhanced visible-light activation of persulfate by Ti^{3+} self-doped TiO_2/graphene nanocomposite for the rapid and efficient degradation of micropollutants in water, Journal of Hazardous Materials 365 (2019) 107-117. https://doi.org/10.1016/j.jhazmat.2018.10.090.

[102] Z. Zhou, Z. Shen, Z. Cheng, G. Zhang, M. Li, Y. Li, S. Zhan, J.C. Crittenden, Mechanistic insights for efficient inactivation of antibiotic resistance genes: a synergistic interfacial adsorption and photocatalytic-oxidation process, Science Bulletin 65 (24) (2020) 2107-2119. https://doi.org/10.1016/j.scib.2020.07.015.

[103] N.A. Almeida, P.M. Martins, S. Teixeira, J.A. Lopes da Silva, V. Sencadas, K. Kühn, G. Cuniberti, S. Lanceros-Mendez, P.A.A.P. Marques, TiO_2/graphene oxide immobilized in P(VDF-TrFE) electrospun membranes with enhanced visible-light-induced photocatalytic performance, Journal of Materials Science 51 (14) (2016) 6974-6986. https://doi.org/10.1007/s10853-016-9986-4.

[104] G.C.C. Yang, Y.-C. Chen, H.-X. Yang, C.-H. Yen, Performance and mechanisms for the removal of phthalates and pharmaceuticals from aqueous solution by graphene-containing ceramic composite tubular membrane coupled with the simultaneous electrocoagulation and electrofiltration process, Chemosphere 155 (2016) 274-282. https://doi.org/10.1016/j.chemosphere.2016.04.060.

[105] Q. Wang, C. Yang, G. Zhang, L. Hu, P. Wang, Photocatalytic Fe-doped TiO_2/PSF composite UF membranes: Characterization and performance on BPA removal under visible-light irradiation, Chemical Engineering Journal 319 (2017) 39-47. https://doi.org/10.1016/j.cej.2017.02.145.

[106] N.K. Khanzada, M.U. Farid, J.A. Kharraz, J. Choi, C.Y. Tang, L.D. Nghiem, A. Jang, A.K. An, Removal of organic micropollutants using advanced membrane-based water and wastewater treatment: A review, Journal of Membrane Science 598 (2020) 117672. https://doi.org/10.1016/j.memsci.2019.117672.

[107] O. Ojajuni, D. Saroj, G. Cavalli, Removal of organic micropollutants using membrane-assisted processes: a review of recent progress, Environmental Technology Reviews 4 (1) (2015) 17-37. https://doi.org/10.1080/21622515.2015.1036788.

[108] R.L. Fernández, J.A. McDonald, S.J. Khan, P. Le-Clech, Removal of pharmaceuticals and endocrine disrupting chemicals by a submerged membrane photocatalysis reactor (MPR), Separation and Purification Technology 127 (2014) 131-139. https://doi.org/10.1016/j.seppur.2014.02.031.

[109] A. Fernández, G. Lassaletta, V.M. Jiménez, A. Justo, A.R. González-Elipe, J.M. Herrmann, H. Tahiri, Y. Ait-Ichou, Preparation and characterization of TiO_2 photocatalysts supported on various rigid supports (glass, quartz and stainless steel). Comparative studies of photocatalytic activity in water purification, Applied Catalysis B: Environmental 7 (1) (1995) 49-63. https://doi.org/10.1016/0926-3373(95)00026-7.

[110] E. Erusappan, S. Thiripuranthagan, R. Radhakrishnan, M. Durai, S. Kumaravel, T. Vembuli, N.J. Kaleekkal, Fabrication of mesoporous TiO_2/PVDF photocatalytic membranes for efficient photocatalytic degradation of synthetic dyes, Journal of Environmental Chemical Engineering 9 (4) (2021) 105776. https://doi.org/10.1016/j.jece.2021.105776.

[111] A. Singh, S.K. Ramachandran, M.B. Gumpu, L. Zsuzsanna, G. Veréb, S. Kertész, A. Gangasalam, Titanium dioxide doped hydroxyapatite incorporated photocatalytic membranes for the degradation of chloramphenicol antibiotic in water, Journal of Chemical Technology & Biotechnology 96 (4) (2021) 1057-1066. https://doi.org/10.1002/jctb.6617.

[112] C. Ding, X. Qin, Y. Tian, B. Cheng, PES membrane surface modification via layer-by-layer self-assembly of GO@TiO_2 for improved photocatalytic performance, Journal of Membrane Science 659 (2022) 120789. https://doi.org/10.1016/j.memsci.2022.120789.

[113] X. Zhang, K. Fu, Z. Su, Fabrication of 3D MoS_2-TiO_2@PAN electro-spun membrane for efficient and recyclable photocatalytic degradation of organic dyes, Materials Science and Engineering: B 269 (2021) 115179. https://doi.org/10.1016/j.mseb.2021.115179.

[114] L. Bobirică, C. Bobirică, G.I. Lupu, C. Orbeci, Influence of operating parameters on photocatalytic oxidation of 2,4-dichlorofenol in aqueous solution by TiO_2 /stainless steel photocatalytic membrane, Applied Sciences (Switzerland) 11 (24) (2021). https://doi.org/10.3390/app112411664.

[115] S. Lotfi, K. Fischer, A. Schulze, A.I. Schäfer, Photocatalytic degradation of steroid hormone micropollutants by TiO2-coated polyethersulfone membranes in a continuous flow-through process, Nature Nanotechnology 17 (4) (2022) 417-423. https://doi.org/10.1038/s41565-022-01074-8.

[116] H. Dzinun, M.H.D. Othman, A.F. Ismail, M.H. Puteh, M.A. Rahman, J. Jaafar, Stability study of PVDF/TiO_2 dual layer hollow fibre membranes under long-term UV irradiation exposure, Journal of Water Process Engineering 15 (2017) 78-82. https://doi.org/10.1016/j.jwpe.2016.05.009.

[117] C.P. Athanasekou, S. Morales-Torres, V. Likodimos, G.E. Romanos, L.M. Pastrana-Martinez, P. Falaras, D.D. Dionysiou, J.L. Faria, J.L. Figueiredo, A.M.T. Silva, Prototype composite membranes of partially reduced graphene oxide/TiO_2 for photocatalytic ultrafiltration water treatment under visible light, Applied Catalysis B: Environmental 158-159 (2014) 361-372. https://doi.org/10.1016/j.apcatb.2014.04.012.

[118] C.P. Athanasekou, N.G. Moustakas, S. Morales-Torres, L.M. Pastrana-Martínez, J.L. Figueiredo, J.L. Faria, A.M.T. Silva, J.M. Dona-Rodriguez, G.E. Romanos, P. Falaras, Ceramic photocatalytic membranes for water filtration under UV and visible light, Applied Catalysis B: Environmental 178 (2015) 12-19. https://doi.org/10.1016/j.apcatb.2014.11.021.

[119] W. Li, J. Li, N. Wang, X. Li, Y. Zhang, Q. Ye, S. Ji, Q.-F. An, Recovery of bio-butanol from aqueous solution with ZIF-8 modified graphene oxide composite membrane, Journal of Membrane Science 598 (2020) 117671. https://doi.org/10.1016/j.memsci.2019.117671.

[120] B.J. Starr, V.V. Tarabara, M. Herrera-Robledo, M. Zhou, S. Roualdès, A. Ayral, Coating porous membranes with a photocatalyst: Comparison of LbL self-assembly and plasma-enhanced CVD techniques, Journal of Membrane Science 514 (2016) 340-349. https://doi.org/10.1016/j.memsci.2016.04.050.

[121] H. Zhao, H. Li, H. Yu, H. Chang, X. Quan, S. Chen, CNTs–TiO2/Al2O3 composite membrane with a photocatalytic function: Fabrication and energetic performance in water treatment, Separation and Purification Technology 116 (2013) 360-365. https://doi.org/10.1016/j.seppur.2013.06.007.

[122] N. Ma, X. Quan, Y. Zhang, S. Chen, H. Zhao, Integration of separation and photocatalysis using an inorganic membrane modified with Si-doped TiO_2 for water purification, Journal of Membrane Science 335 (1) (2009) 58-67. https://doi.org/10.1016/j.memsci.2009.02.040.

[123] P. Kumari, N. Bahadur, X.A. Conlan, M. Laleh, L. Kong, L.A. O'Dell, L.F. Dumée, A. Merenda, Atomically-thin Schottky-like photo-electrocatalytic cross-flow membrane reactors for ultrafast remediation of persistent organic pollutants, Water Research 218 (2022) 118519. https://doi.org/10.1016/j.watres.2022.118519.

[124] F. Saffarimiandoab, B.Y. Gul, R.S. Tasdemir, S.E. Ilter, S. Unal, B. Tunaboylu, Y.Z. Menceloglu, İ. Koyuncu, A review on membrane fouling: Membrane modification, Desalination and Water Treatment 216 (2021) 47-70. http://doi.org/10.5004/dwt.2021.26815.

[125] H. Song, J. Shao, Y. He, B. Liu, X. Zhong, Natural organic matter removal and flux decline with PEG–TiO_2-doped PVDF membranes by integration of ultrafiltration with photocatalysis, Journal of Membrane Science 405-406 (2012) 48-56. https://doi.org/10.1016/j.memsci.2012.02.063.

[126] S. Ramasundaram, H.N. Yoo, K.G. Song, J. Lee, K.J. Choi, S.W. Hong, Titanium dioxide nanofibers integrated stainless steel filter for photocatalytic degradation of pharmaceutical compounds, Journal of Hazardous Materials 258-259 (2013) 124-132. https://doi.org/10.1016/j.jhazmat.2013.04.047.

[127] L. Paredes, S. Murgolo, H. Dzinun, M.H. Dzarfan Othman, A.F. Ismail, M. Carballa, G. Mascolo, Application of immobilized TiO_2 on PVDF dual layer hollow fibre membrane to improve the photocatalytic removal of pharmaceuticals in different water matrices, Applied Catalysis B: Environmental 240 (2019) 9-18. https://doi.org/10.1016/j.apcatb.2018.08.067.

[128] E. Luster, D. Avisar, I. Horovitz, L. Lozzi, M.A. Baker, R. Grilli, H. Mamane, N-Doped TiO_2-Coated Ceramic Membrane for Carbamazepine Degradation in Different Water Qualities, Nanomaterials 7 (8) (2017) 206. https://doi.org/10.3390/nano7080206.

[129] Y. Li, L. Zhu, Evaluation of the antifouling and photocatalytic properties of novel poly(vinylidene fluoride) membranes with a reduced graphene oxide–Bi_2WO_6 active layer, Journal of Applied Polymer Science 134 (42) (2017) 45426. https://doi.org/10.1002/app.45426.

[130] M.J. Arlos, M.M. Hatat-Fraile, R. Liang, L.M. Bragg, N.Y. Zhou, S.A. Andrews, M.R. Servos, Photocatalytic decomposition of organic micropollutants using immobilized TiO_2 having different isoelectric points, Water Research 101 (2016) 351-361. https://doi.org/10.1016/j.watres.2016.05.073.

[131] R. Lyubimenko, O.I. Gutierrez Cardenas, A. Turshatov, B.S. Richards, A.I. Schäfer, Photodegradation of steroid-hormone micropollutants in a flow-through membrane reactor coated with Pd(II)-porphyrin, Applied Catalysis B: Environmental 291 (2021) 120097. https://doi.org/10.1016/j.apcatb.2021.120097.

[132] S. Chakraborty, S. Loutatidou, G. Palmisano, J. Kujawa, M.O. Mavukkandy, S. Al-Gharabli, E. Curcio, H.A. Arafat, Photocatalytic hollow fiber membranes for the degradation of pharmaceutical compounds in wastewater, Journal of Environmental Chemical Engineering 5 (5) (2017) 5014-5024. https://doi.org/10.1016/j.jece.2017.09.038.

[133] R. Singh, V.S.K. Yadav, M.K. Purkait, Cu_2O photocatalyst modified antifouling polysulfone mixed matrix membrane for ultrafiltration of protein and visible light driven photocatalytic pharmaceutical removal, Separation and Purification Technology 212 (2019) 191-204. https://doi.org/10.1016/j.seppur.2018.11.029.

[134] R. Lyubimenko, B.S. Richards, A.I. Schäfer, A. Turshatov, Noble-metal-free photosensitizers for continuous-flow photochemical oxidation of steroid hormone micropollutants under sunlight, Journal of Membrane Science 642 (2022) 119981. https://doi.org/10.1016/j.memsci.2021.119981.

[135] K. Celebi, J. Buchheim, R.M. Wyss, A. Droudian, P. Gasser, I. Shorubalko, J.-I. Kye, C. Lee, H.G. Park, Ultimate Permeation Across Atomically Thin Porous Graphene, Science 344 (6181) (2014) 289-292. https://doi.org/10.1126/science.1249097.

[136] G. He, S. Huang, L.F. Villalobos, J. Zhao, M. Mensi, E. Oveisi, M. Rezaei, K.V. Agrawal, High-permeance polymer-functionalized single-layer graphene membranes that surpass the postcombustion carbon capture target, Energy & Environmental Science 12 (11) (2019) 3305-3312. https://doi.org/10.1039/C9EE01238A.

[137] X. Wang, X. Ba, N. Cui, Z. Ma, L. Wang, Z. Wang, X. Gao, Preparation, characterisation, and desalination performance study of cellulose acetate membranes with MIL-53(Fe) additive, Journal of Membrane Science 590 (2019) 1-9. https://doi.org/10.1016/j.memsci.2019.04.061.

[138] K.A. Mahmoud, B. Mansoor, A. Mansour, M. Khraisheh, Functional graphene nanosheets: The next generation membranes for water desalination, Desalination 356 (2015) 208-225. https://doi.org/10.1016/j.desal.2014.10.022.

[139] S.G. Kim, D.H. Hyeon, J.H. Chun, B.-H. Chun, S.H. Kim, Novel thin nanocomposite RO membranes for chlorine resistance, Desalination and Water Treatment 51 (31-33) (2013) 6338-6345. https://doi.org/10.1080/19443994.2013.780994.

[140] D. Cohen-Tanugi, L.-C. Lin, J.C. Grossman, Multilayer Nanoporous Graphene Membranes for Water Desalination, Nano Letters 16 (2) (2016) 1027-1033. https://doi.org/10.1021/acs.nanolett.5b04089.

[141] B.W. Reed, M.J. Semmens, E.L. Cussler, Membrane contactors, in: R.D. Noble, S.A. Stern (Eds.), Membrane Science and Technology, Elsevier 1995, pp. 467-498. https://doi.org/10.1016/S0927-5193(06)80012-4.

[142] K.K. Sirkar, Membranes, Phase Interfaces, and Separations: Novel Techniques and Membranes—An Overview, Industrial & Engineering Chemistry Research 47 (15) (2008) 5250-5266. https://doi.org/10.1021/ie8001952.

[143] S. Psaltou, A. Zouboulis, Catalytic Ozonation and Membrane Contactors—A Review Concerning Fouling Occurrence and Pollutant Removal, Water 12 (11) (2020) 2964. https://doi.org/10.3390/w12112964.

[144] S.D. Bazhenov, A.V. Bildyukevich, A.V. Volkov, Gas-Liquid Hollow Fiber Membrane Contactors for Different Applications, Fibers 6 (4) (2018) 76. https://doi.org/10.3390/fib6040076.

[145] M.H. Al-Marzouqi, S.A.M. Marzouk, N. Abdullatif, High pressure removal of acid gases using hollow fiber membrane contactors: Further characterization and long-term operational stability, Journal of Natural Gas Science and Engineering 37 (2017) 192-198. https://doi.org/10.1016/j.jngse.2016.11.039.

[146] T. My Hanh Le, R. Nuisin, R. Mongkolnavin, P. Painmanakul, S. Sairiam, Enhancing dye wastewater treatment efficiency in ozonation membrane contactors by chloro– and fluoro–organosilanes' functionality on hydrophobic PVDF membrane modification, Separation and Purification Technology 288 (2022) 120711. https://doi.org/10.1016/j.seppur.2022.120711.

[147] A. Khrueakham, J. Masomboon, J. Roongruang, S. Sairiam, Efficient reactive blue 19 decolorization by the comparison of ozonation membrane contacting process and Fenton oxidation, RSC Advances 11 (29) (2021) 17775-17788. https://doi.org/10.1039/D1RA01871J.

[148] K. Li, Y. Zhang, L. Xu, L. Liu, Z. Wang, D. Hou, Y. Wang, J. Wang, Mass transfer and interfacial reaction mechanisms in a novel electro-catalytic membrane contactor for wastewater treatment by O_3, Applied Catalysis B: Environmental 264 (2020) 118512. https://doi.org/10.1016/j.apcatb.2019.118512.

[149] C. Gottschalk, J.A. Libra, A. Saupe, Ozonation of water and waste water: A practical guide to understanding ozone and its applications, 2nd Edition, Wiley-VCH Verlag GmbH & Co. kGaA, Germany, 2010.

[150] S. Ribeirinho-Soares, N.F.F. Moreira, C. Graça, M.F.R. Pereira, A.M.T. Silva, O.C. Nunes, Overgrowth control of potentially hazardous bacteria during storage of ozone treated wastewater through natural competition, Water Research 209 (2022) 117932. https://doi.org/10.1016/j.watres.2021.117932.

[151] T. Spit, J.P. van der Hoek, C. de Jong, D. van Halem, M. de Kreuk, B.B. Perez, Removal of Antibiotic Resistance From Municipal Secondary Effluents by Ozone-Activated Carbon Filtration, Frontiers in Environmental Science 10 (2022). https://doi.org/10.3389/fenvs.2022.834577.

[152] T. Merle, W. Pronk, U. von Gunten, MEMBRO$_3$X, a Novel Combination of a Membrane Contactor with Advanced Oxidation (O_3/H_2O_2) for Simultaneous Micropollutant Abatement and Bromate Minimization, Environmental Science & Technology Letters 4 (5) (2017) 180-185. https://doi.org/10.1021/acs.estlett.7b00061.

[153] F. Smuts, C. Gaszynski, D. Ikumi, A framework to determine the optimum contact time and organic micropollutant removal efficiency of the ozone process applied in the context of Cape Flats Managed Aquifer Recharge Water Reclamation Plant, Journal of Water Process Engineering 47 (2022) 102651. https://doi.org/10.1016/j.jwpe.2022.102651.

[154] B. Mathon, M. Coquery, Z. Liu, Y. Penru, A. Guillon, M. Esperanza, C. Miège, J.M. Choubert, Ozonation of 47 organic micropollutants in secondary treated municipal effluents: Direct and indirect kinetic reaction rates and modelling, Chemosphere 262 (2021) 127969. https://doi.org/10.1016/j.chemosphere.2020.127969.

[155] Z.A. Yacouba, J. Mendret, G. Lesage, F. Zaviska, S. Brosillon, Removal of organic micropollutants from domestic wastewater: The effect of ozone-based advanced oxidation process on nanofiltration, Journal of Water Process Engineering 39 (2021) 101869. https://doi.org/10.1016/j.jwpe.2020.101869.

[156] C. Anselme, I.H. Suffet, J. Mallevialle, Effects of Ozonation on Tastes and Odors, Journal (American Water Works Association) 80 (10) (1988) 45-51.

[157] E. Bein, I. Zucker, J.E. Drewes, U. Hübner, Ozone membrane contactors for water and wastewater treatment: A critical review on materials selection, mass transfer and process design, Chemical Engineering Journal 413 (2021) 127393. https://doi.org/10.1016/j.cej.2020.127393.

[158] A.K. Pabby, A.M. Sastre, State-of-the-art review on hollow fibre contactor technology and membrane-based extraction processes, Journal of Membrane Science 430 (2013) 263-303. https://doi.org/10.1016/j.memsci.2012.11.060.

[159] A. Mansourizadeh, A.F. Ismail, Hollow fiber gas–liquid membrane contactors for acid gas capture: A review, Journal of Hazardous Materials 171 (1) (2009) 38-53. https://doi.org/10.1016/j.jhazmat.2009.06.026.

[160] K. Li, L. Xu, Y. Zhang, A. Cao, Y. Wang, H. Huang, J. Wang, A novel electro-catalytic membrane contactor for improving the efficiency of ozone on wastewater treatment, Applied Catalysis B: Environmental 249 (2019) 316-321. https://doi.org/10.1016/j.apcatb.2019.03.015.

[161] A. Schmitt, J. Mendret, M. Roustan, S. Brosillon, Ozonation using hollow fiber contactor technology and its perspectives for micropollutants removal in water: A review, Science of The Total Environment 729 (2020) 138664. https://doi.org/10.1016/j.scitotenv.2020.138664.

[162] A. Mansourizadeh, I. Rezaei, W.J. Lau, M.Q. Seah, A.F. Ismail, A review on recent progress in environmental applications of membrane contactor technology, Journal of Environmental Chemical Engineering 10 (3) (2022) 107631. https://doi.org/10.1016/j.jece.2022.107631.

[163] J. Phattaranawik, T. Leiknes, W. Pronk, Mass transfer studies in flat-sheet membrane contactor with ozonation, Journal of Membrane Science 247 (1) (2005) 153-167. https://doi.org/10.1016/j.memsci.2004.08.020.

[164] T.M. Hanh Le, S. Singto, W. Sajomsang, R. Mongkolnavin, R. Nuisin, P. Painmanakul, S. Sairiam, Hydrophobic PVDF hollow fiber membrane modified with pulse inductively coupling plasma activation and chloroalkylsilanes for efficient dye wastewater treatment by ozonation membrane contactor, Journal of Membrane Science 635 (2021) 119443. https://doi.org/10.1016/j.memsci.2021.119443.

[165] B. Wang, H. Zhang, Q. Meng, H. Ren, M. Xiong, C. Gao, The enhancement of ozone–liquid mass transfer performance in a PTFE hollow fiber membrane contactor using ultrasound as a catalyzer, RSC Advances 11 (23) (2021) 14017-14028. https://doi.org/10.1039/D1RA00452B.

[166] J. Kämmler, G.A. Zoumpouli, J. Sellmann, Y.M.J. Chew, J. Wenk, M. Ernst, Decolorization and control of bromate formation in membrane ozonation of humic-rich groundwater, Water Research 221 (2022) 118739. https://doi.org/10.1016/j.watres.2022.118739.

[167] Y. Mori, T. Oota, M. Hashino, M. Takamura, Y. Fujii, Ozone-microfiltration system, Desalination 117 (1) (1998) 211-218. https://doi.org/10.1016/S0011-9164(98)00098-8.

[168] S. Bamperng, T. Suwannachart, S. Atchariyawut, R. Jiraratananon, Ozonation of dye wastewater by membrane contactor using PVDF and PTFE membranes, Separation and Purification Technology 72 (2) (2010) 186-193. https://doi.org/10.1016/j.seppur.2010.02.006.

[169] S.K. Stylianou, I.A. Katsoyiannis, M. Mitrakas, A.I. Zouboulis, Application of a ceramic membrane contacting process for ozone and peroxone treatment of micropollutant contaminated surface

water, Journal of Hazardous Materials 358 (2018) 129-135. https://doi.org/10.1016/j.jhazmat.2018.06.060.

[170] W. Kit Chan, J. Jouët, S. Heng, K. Lun Yeung, J.-C. Schrotter, Membrane contactor/separator for an advanced ozone membrane reactor for treatment of recalcitrant organic pollutants in water, Journal of Solid State Chemistry 189 (2012) 96-100. https://doi.org/10.1016/j.jssc.2012.01.023.

[171] Y. Fang, R.M. Hozalski, L.W. Clapp, P.J. Novak, M.J. Semmens, Passive dissolution of hydrogen gas into groundwater using hollow-fiber membranes, Water Research 36 (14) (2002) 3533-3542. https://doi.org/10.1016/S0043-1354(02)00046-5.

[172] M. Kukuzaki, K. Fujimoto, S. Kai, K. Ohe, T. Oshima, Y. Baba, Ozone mass transfer in an ozone–water contacting process with Shirasu porous glass (SPG) membranes—A comparative study of hydrophilic and hydrophobic membranes, Separation and Purification Technology 72 (3) (2010) 347-356. https://doi.org/10.1016/j.seppur.2010.03.004.

[173] M. Sabelfeld, S.-U. Geißen, Effect of helical structure on ozone mass transfer in a hollow fiber membrane contactor, Journal of Membrane Science 574 (2019) 222-234. https://doi.org/10.1016/j.memsci.2018.10.056.

[174] M. Mavroudi, S.P. Kaldis, G.P. Sakellaropoulos, A study of mass transfer resistance in membrane gas–liquid contacting processes, Journal of Membrane Science 272 (1) (2006) 103-115. https://doi.org/10.1016/j.memsci.2005.07.025.

[175] P.N. Johnson, R.A. Davis, Diffusivity of Ozone in Water, Journal of Chemical & Engineering Data 41 (6) (1996) 1485-1487. https://doi.org/10.1021/je9602125.

[176] R.H.S. Jansen, J.W. de Rijk, A. Zwijnenburg, M.H.V. Mulder, M. Wessling, Hollow fiber membrane contactors—A means to study the reaction kinetics of humic substance ozonation, Journal of Membrane Science 257 (1) (2005) 48-59. https://doi.org/10.1016/j.memsci.2004.07.038.

[177] Y. Fang, P.J. Novak, R.M. Hozalski, E.L. Cussler, M.J. Semmens, Condensation studies in gas permeable membranes, Journal of Membrane Science 231 (1) (2004) 47-55. https://doi.org/10.1016/j.memsci.2003.10.039.

[178] G.T. Vladisavljević, Use of polysulfone hollow fibers for bubbleless membrane oxygenation/deoxygenation of water, Separation and Purification Technology 17 (1) (1999) 1-10. https://doi.org/10.1016/S1383-5866(99)00012-X.

[179] W. Jiao, Y. Qin, Y. Wang, L. Guo, Y. Liu, Enhancement performance of ozone mass transfer by high gravity technology, Desalination and Water Treatment 66 (2017) 195-202. https://doi.org/10.5004/dwt.2017.20210.

[180] S.K. Stylianou, M. Kostoglou, A.I. Zouboulis, Ozone Mass Transfer Studies in a Hydrophobized Ceramic Membrane Contactor: Experiments and Analysis, Industrial & Engineering Chemistry Research 55 (28) (2016) 7587-7597. https://doi.org/10.1021/acs.iecr.6b01446.

[181] R. Rosal, A. Rodríguez, M. Zerhouni, Enhancement of gas–liquid mass transfer during the unsteady-state catalytic decomposition of ozone in water, Applied Catalysis A: General 305 (2) (2006) 169-175. https://doi.org/10.1016/j.apcata.2006.02.059.

[182] B. Wang, X. Xiong, Y. Shui, Z. Huang, K. Tian, A systematic study of enhanced ozone mass transfer for ultrasonic-assisted PTFE hollow fiber membrane aeration process, Chemical Engineering Journal 357 (2019) 678-688. https://doi.org/10.1016/j.cej.2018.09.188.

[183] X. Huang, X. Quan, W. Cheng, C. Cheng, Z. Cheng, L. Yang, L. Jiang, Enhancement of Ozone Mass Transfer by Stainless Steel Wire Mesh and Its Effect on Hydroxyl Radical Generation, Ozone: Science & Engineering 42 (4) (2020) 347-356. https://doi.org/10.1080/01919512.2019.1676196.

[184] A. Al-Abduly, P. Christensen, A. Harvey, K. Zahng, Characterization and optimization of an oscillatory baffled reactor (OBR) for ozone-water mass transfer, Chemical Engineering and Processing: Process Intensification 84 (2014) 82-89. https://doi.org/10.1016/j.cep.2014.03.015.

[185] M.J. Nieves-Remacha, A.A. Kulkarni, K.F. Jensen, Gas–Liquid Flow and Mass Transfer in an Advanced-Flow Reactor, Industrial & Engineering Chemistry Research 52 (26) (2013) 8996-9010. https://doi.org/10.1021/ie4011707.

[186] J. Li, L.-P. Zhu, Y.-Y. Xu, B.-K. Zhu, Oxygen transfer characteristics of hydrophilic treated polypropylene hollow fiber membranes for bubbleless aeration, Journal of Membrane Science 362 (1) (2010) 47-57. https://doi.org/10.1016/j.memsci.2010.06.013.

[187] Y.M. Mehta, C.E. George, C.H. Kuo, Mass transfer and selectivity of ozone reactions, The Canadian Journal of Chemical Engineering 67 (1) (1989) 118-126. https://doi.org/10.1002/cjce.5450670117.

[188] H. Zhou, D.W. Smith, Ozone mass transfer in water and wastewater treatment: experimental observations using a 2D laser particle dynamics analyzer, Water Research 34 (3) (2000) 909-921. https://doi.org/10.1016/S0043-1354(99)00196-7.

[189] J.A. Roth, D.E. Sullivan, Solubility of ozone in water, Industrial & Engineering Chemistry Fundamentals 20 (2) (1981) 137-140. https://doi.org/10.1021/i100002a004.

[190] G.A. Zoumpouli, R. Baker, C.M. Taylor, M.J. Chippendale, C. Smithers, S.S.X. Ho, D. Mattia, Y.M.J. Chew, J. Wenk, A Single Tube Contactor for Testing Membrane Ozonation, Water 10 (10) (2018) 1416. https://doi.org/10.3390/w10101416.

[191] A. Schmitt, J. Mendret, S. Brosillon, Evaluation of an ozone diffusion process using a hollow fiber membrane contactor, Chemical Engineering Research and Design 177 (2022) 291-303. https://doi.org/10.1016/j.cherd.2021.11.002.

[192] Y. Li, K.L. Yeung, Polymeric catalytic membrane for ozone treatment of DEET in water, Catalysis Today 331 (2019) 53-59. https://doi.org/10.1016/j.cattod.2018.06.005.

[193] C. Mansas, L. Atfane-Karfane, E. Petit, J. Mendret, S. Brosillon, A. Ayral, Functionalized ceramic nanofilter for wastewater treatment by coupling membrane separation and catalytic ozonation, Journal of Environmental Chemical Engineering 8 (4) (2020) 104043. https://doi.org/10.1016/j.jece.2020.104043.

[194] Y. Liu, Z. Song, W. Wang, Z. Wang, Y. Zhang, C. Liu, Y. Wang, A. Li, B. Xu, F. Qi, A $CuMn_2O_4$/g-C_3N_4 catalytic ozonation membrane reactor used for water purification: Membrane fabrication and performance evaluation, Separation and Purification Technology 265 (2021) 118268. https://doi.org/10.1016/j.seppur.2020.118268.

[195] W.J. Lee, Y. Bao, A. Liangdy, X. Hu, T.-T. Lim, Insights into the synergistic role of catalytic ceramic membranes for ozone and peroxymonosulfate activation towards effective recalcitrant micropollutant degradation and mineralization, Chemical Engineering Journal 430 (2022) 132921. https://doi.org/10.1016/j.cej.2021.132921.

[196] M. Darestani, V. Haigh, S.J. Couperthwaite, G.J. Millar, L.D. Nghiem, Hollow fibre membrane contactors for ammonia recovery: Current status and future developments, Journal of Environmental Chemical Engineering 5 (2) (2017) 1349-1359. https://doi.org/10.1016/j.jece.2017.02.016.

[197] A. Diório, J. Díaz-Angulo, R.M. Castellanos, A.I. Gomes, R. Bergamasco, M.F. Vieira, M. Dezotti, M.A. Mueses, F. Machuca-Martinez, V.J.P. Vilar, A tubular ceramic membrane coated with TiO_2-P25 for radial addition of H_2O_2 towards AMX removal from synthetic solutions and secondary urban wastewater, Environmental Science and Pollution Research 29 (28) (2022) 42120-42129. https://doi.org/10.1007/s11356-021-14297-4.

[198] E. Cuervo Lumbaque, C. Sirtori, V.J.P. Vilar, Heterogeneous photocatalytic degradation of pharmaceuticals in synthetic and real matrices using a tube-in-tube membrane reactor with radial addition of H_2O_2, Science of The Total Environment 743 (2020) 140629. https://doi.org/10.1016/j.scitotenv.2020.140629.

[199] E.C. Lumbaque, D.S. Lüdtke, D.D. Dionysiou, V.J.P. Vilar, C. Sirtori, Tube-in-tube membrane photoreactor as a new technology to boost sulfate radical advanced oxidation processes, Water Research 191 (2021) 116815. https://doi.org/10.1016/j.watres.2021.116815.

[200] N. De la Cruz, L. Esquius, D. Grandjean, A. Magnet, A. Tungler, L.F. de Alencastro, C. Pulgarín, Degradation of emergent contaminants by UV, UV/H_2O_2 and neutral photo-Fenton at pilot scale in a domestic wastewater treatment plant, Water Research 47 (15) (2013) 5836-5845. https://doi.org/10.1016/j.watres.2013.07.005.

[201] S.R. Sarathy, M.I. Stefan, A. Royce, M. Mohseni, Pilot-scale UV/H_2O_2 advanced oxidation process for surface water treatment and downstream biological treatment: effects on natural organic matter characteristics and DBP formation potential, Environmental Technology 32 (15) (2011) 1709-1718. https://doi.org/10.1080/09593330.2011.553843.

[202] R.R. Giri, H. Ozaki, Y. Takayanagi, S. Taniguchi, R. Takanami, Efficacy of ultraviolet radiation and hydrogen peroxide oxidation to eliminate large number of pharmaceutical compounds in mixed solution, International Journal of Environmental Science and Technology 8 (1) (2011) 19-30. https://doi.org/10.1007/BF03326192.

[203] E.K. Schoenell, N. Otto, M.A.S. Rodrigues, J.W. Metzger, Removal of Organic Micropollutants from Treated Municipal Wastewater by O_3/UV/H_2O_2 in a UVA-LED Reactor, Ozone: Science & Engineering 44 (2) (2022) 172-181. https://doi.org/10.1080/01919512.2021.1900716.

[204] X. Cui, M.S. Mannan, B.A. Wilhite, Segregated-Feed Membrane Reactor Design for Alkylpyridine N-Oxidation: Implications for Process Safety and Intensification, Industrial & Engineering Chemistry Research 56 (14) (2017) 3822-3832. https://doi.org/10.1021/acs.iecr.7b00047.

[205] A.E. Buba, S. Koch, H. Kunz, H. Löwe, Fluorenylmethoxycarbonyl-N-methylamino Acids Synthesized in a Flow Tube-in-Tube Reactor with a Liquid–Liquid Semipermeable Membrane, European Journal of Organic Chemistry 2013 (21) (2013) 4509-4513. https://doi.org/10.1002/ejoc.201300705.

[206] United Nations, Department of Economic and Social Affairs, Population Division, World Urbanization Prospects, The 2018 Revision, 2018. https://population.un.org/wup/. (Accessed November 14th 2022).

[207] European Commission, Implementation of the Chemicals Strategy, 2021. https://ec.europa.eu/environment/strategy/chemicals-strategy/implementation_en. (Accessed November 14th 2022).

[208] European Commission, Communication from the Commission to the European Parliament, the Council, the European Economic and Social Committee and the Committee of the Regions EU Biodiversity Strategy for 2030 Bringing nature back into our lives, 2020. https://eur-lex.europa.eu/legal-content/EN/TXT/?uri=CELEX:52020DC0380. (Accessed November 14th 2022).

[209] European Commission, Urban Agenda for the EU – Multi-level governance in action (2021 Update), 2021. https://futurium.ec.europa.eu/en/urban-agenda/library/online-brochure-urban-agenda-eu-multi-level-governance-action-has-new-revised-version. (Accessed November 14th 2022).

2 Materials and Methods

This chapter presents a detailed description of all chemical reagents, analytical determinations, modelling of degradation kinetics and experimental units used throughout this thesis, as well as of the experimental procedures implemented to meet the proposed objectives. Microbiological assays, zebrafish embryonic toxicity bioassays, and actinometry measurement procedures are also described in detail. Two experimental membrane reactor units with different modes of operation were used on a laboratory scale: (i) PMP: filtration mode (the membrane acts as a filter medium and catalyst support) and (ii) MC: dosing mode (the membrane acts as an ozone injector and catalyst support).

The experimental work in Chapters 4 to 6 was mostly developed in the Laboratory of Separation and Reaction Engineering – Laboratory of Catalysis and Materials (LSRE-LCM) at the Department of Chemical Engineering, Faculty of Engineering of the University of Porto. Results reported in Chapter 3 were carried out at the Instituto Universitario de Tecnología Química (CSIC), Universitat Politècnica de València (UPV), Spain.

2.1 Chemicals and materials

Different types of membranes were selected for the development of the functionalized membranes in terms of composition and porosity, which characteristics are listed in Table 2.1. AvistaClean® P611 (Avista Technologies, United Kingdom) and HCl (Fisher Chemical™) solutions were used to clean the ceramic and the glass membranes after each experiment, respectively, according to the procedure recommended by the manufacturer.

Table 2.1. Characteristics of the selected membranes.

Information	**Ceramic membrane** 	**Glass membrane** 
Manufacturer	Inopor®	Robu®
Material	α-Al_2O_3	Borossilicato VitraPOR®
Pore size	100 nm	5 µm
Porosity (%)	40 – 55	45
Outer diameter (mm)	20	21
Internal diameter (mm)	16	10
Length (mm)	200	200
Maximum temperature (°C)	1000	500
Maximum pressure (MPa)	n.d.*	0.1

* Not determined.

Chitosan (CS) of low molecular weight and boric acid (H_3BO_3) from Sigma Aldrich (Sigma-Aldrich, St. Louis, MO, USA) were used as a precursor to graphene films (Chapters 3 and 4). In Chapter 3, potassium chloride (KCl) and sodium chloride (NaCl) salts were added in the required amount to reach a final 50 mM concentration. KCl and NaCl were obtained from Scharlau (Scharlab Chemie, S.A., Barcelona, Spain). Salt concentration was measured using a calibrated CRISON conductivity meter 524.

TiO_2 Aeroxide® P25 (Evonik, Germany, ≥ 99.5% (w/w) purity, 80% anatase and 20% rutile crystalline phases, average crystal size of 25 nm, specific surface area of 50 $m^2\ g^{-1}$, and density of 3.9 $g\ cm^{-3}$) was used as a photocatalyst (Chapters 4, 5 and 6). The surfactant Triton™ X-100 was purchased from Sigma-Aldrich and used to prepare the TiO_2-P25 suspension for membrane coating.

To evaluate the photonic flow in both membrane reactors (Chapters 4, 5 and 6), 2-Nitrobenzaldehyde-2NB (99% purity) provided by Labbox Labware, S.L and ferric chloride hexahydrate from Merck were used.

Ultrapure water (UPW; Millipore Direct-Q®, 18.2 MΩ cm^{-1} at 25 °C) was used to prepare all solutions and to simulate wastewater in Chapter 4. Demineralised water (DW; Panice®) was used in all tests in Chapter 3 and to simulate wastewater in Chapters 5 and 6.

The ozone probe was validated by the iodometric method with the use of potassium iodide (KI, Merck), sodium thiosulfate ($Na_2S_2O_3$, Pronalab) and amide (Sigma). In addition, the 2% KI solution was used to destroy any remaining ozone (O_3) in the outlet gas stream (Chapters 5 and 6). Sulfuric acid (H_2SO_4, Pronalab) and sodium hydroxide (NaOH, Merck) solutions were used to adjust the solution pH.

Table 2.2 summarizes the physicochemical properties and suppliers of the CECs used in Chapters 4, 5 and 6.

Table 2.2. List of the 20 CECs selected for testing in this thesis and respective abbreviations and chemical composition.

Contaminants Groups	Contaminants	Abbreviation	Chemical Composition	CAS	Chapter
Penicillin antibiotic	Amoxicillin	AMX	$C_{16}H_{19}N_3O_5S$	26787-78-0	4
Hormones	17-beta-estradiol	E2	$C_{18}H_{24}O_2$	50-28-2	4, 5 and 6
	17-alpha-ethynylestradiol	EE2	$C_{20}H_{24}O_2$	57-63-6	
Non-Steroidal Anti-Inflammatory Drugs	Diclofenac	DCF	$C_{14}H_{11}Cl_2NO_2$	15307-86-5	
Short-chain perfluoroalkylated substances (PFAS)	Heptafluorobutyric acid	HFBA	$C_4HF_7O_2$	375-22-4	5 and 6
	Nonafluoro-1-butanesulfonic acid	PFBS	$C_4HF_9O_3S$	29420-49-3	
	Perfluorooctanoic acid	PFOA	$C_8HF_{15}O_2$	335-67-1	
	Trifluormethanesulfonic acid	TFMS	CHF_3O_3S	1493-13-6	
Angiotensin II Receptor Blockers	Valsartan	VSTN	$C_{24}H_{29}N_5O_3$	137862-53-4	
	Irbesartan	ISTN	$C_{25}H_{28}N_6O$	138402-11-6	
	Losartan	LSTN	$C_{22}H_{23}ClN_6O$	124750-99-8	
Flame Retardant	Melamine	MLN	$C_3H_6N_6$	108-78-1	
Herbicide	Diuron	DRN	$C_9H_{10}C_{l2}N_2O$	330-54-1	
Insect Repellent	DEET	DEET	$C_{12}H_{17}NO$	134-62-3	
Artificial Sweeteners	Acesulfame	AC-K	$C_4H_4KNO_4S$	55589-62-3	
	Saccharin	SCH	$C_7H_5NO_3S$	81-07-2	
Carbamazepine and Metabolites	Carbamazepine	CBZ	$C_{15}H_{12}N_2O$	298-46-4	
	10,11 Carbamazepine-epoxide	CBZ-EPX	$C_{15}H_{12}N_2O_2$	36507-30-9	
Beta blockers	Atenolol	ATNL	$C_{14}H_{22}N_2O_3$	29122-68-7	
	Bisoprolol	BSPL	$C_{18}H_{31}NO_4$	66722-44-9	

2.2 Preparation of functionalized membranes

2.2.1 Fabrication of continuous multilayer boron, nitrogen-codoped defective graphene film on porous α-Al_2O_3 membrane

Continuous multilayer boron and nitrogen-codoped defective graphene [(B,N)G] films supported on α-Al_2O_3 membrane were prepared similarly to a previous report for (B,N)G as powders [1]. Briefly, CS (2.5 g) was dissolved in UPW (250 mL) by adding 1.7 mL of acetic acid. The viscous gel was filtered under pressure through a Nylon filter (250 µm) to remove insoluble impurities that could be present in the commercial sample. The prepared solution was used to coat the alumina membrane following a dip-coating method with 1 min of contact time. This CS film on the alumina membrane was immersed in 250 mL of 25% aqueous ammonia solution containing H_3BO_3 (1.0 g). The CS film impregnated with ammonium borate was pyrolyzed under an argon/hydrogen (5 vol% of H_2) flow (200 mL min^{-1}), increasing the temperature to 900 °C at a heating rate of 0.9 °C min^{-1}.

2.2.1.1 Characterisation techniques

Raman spectra were recorded with a Horiba Jobin YvonLabram HR UV–Visible–NIR (200–1600 nm) Raman Microscope Spectrometer, using a 632 nm laser as an excitation source. Atomic force microscopy (AFM) images were recorded with a Veeco apparatus working in tapping mode, using mica as substrate. X-ray photoelectron spectroscopy (XPS) was recorded on a SPECS spectrometer with a Phoibos 150 9 MCD detector using a non-monochromatic X-ray source (Al and Mg) operating at 200 W. For the calculation of the binding energies, the peak appearing at 284.4 eV (C1s peak) was used as a reference.

The morphology of the (B,N)G sample, film continuity and thickness were analysed by scanning electron microscopy (SEM) using a JEOL JSM 6300 apparatus equipped with an X-MAX detector of Oxford Instruments and coupled to a fast ion bombardment (FIB) technique. The crystallinity and structural ordering of the (B,N)G sample were determined by transmission electron microscopy (TEM). TEM images were recorded in a Philips CM300 FEG system with 100 kV operating voltage. TEM samples were obtained by scratching a piece of the membrane with a cutter, suspending it in ethanol by sonication. A microdrop of this suspension was cast onto a carbon-coated copper TEM grid and the solvent evaporated before introducing into the microscope.

2.2.2 Fabrication of continuous G-TiO_2 thin-films on membrane shell-side

Continuous multilayer defective G-TiO_2 thin-films over the ceramic membrane shell-side were prepared *in situ* following the procedure detailed described in *Section 2.2.1*. A CS solution was prepared

by slowly adding 5 g of CS in 250 mL of UPW acidified with acetic acid (25%). A photocatalyst aqueous suspension was prepared by adding 5 g of TiO_2-P25 powder and two drops of TritonTM X-100 in 250 mL of UPW.

G-TiO_2 nanocomposite thin films were prepared using two methods: (i) membrane A (MA): TiO_2-P25 incorporated in the G preparation stage; and membrane B (MB): TiO_2-P25 thin-film uniformly coated over the G film surface (Table 2.3). For MA, different amounts of TiO_2-P25 (1% [MA-1], 2% [MA-2] and 3% [MA-3] [w/v]) were added to the CS solution. For values higher than 4% w/v, the film was not continuous. A detachment and peeling of the resulting G-TiO_2 film from the alumina membrane were visibly observed. Hence, a maximum of 3% TiO_2 (w/v) was used in this work. Before use, the prepared suspensions were magnetically stirred for 24 h and sonicated for 15 min at 50 kHz. The suspensions were used to coat the membrane shell-side with one immersion using a dip-coating method with an immersion rate and withdrawing speed of 8 cm min^{-1} and an immersion time of 1 min (Dip-Coater RDC 15, Bungard Elektronik GmbH & Co. KG). The G-TiO_2 decorated membrane was dried by placing it in a horizontal position over a heating plate at 100 °C for 30 min, at a rotation speed of 40 rpm, followed by another 30 min in an oven at 100 °C. Subsequently, the membranes were subjected to compressed air flow (inside-outside mode) at 5 bar for 10 min, providing a physical opening of the pores. Then, the membrane with CS-TiO_2-P25 film was pyrolyzed under argon flow (300 mL min^{-1}), at a heating rate of 5 °C min^{-1} until reaching 600 °C for 4 h [2].

Table 2.3. Summary of membrane nomenclature.

Membrane*	Fabrication conditions	Nomenclature
Membrane A (MA)	CS + 1% of TiO_2-P25 + pyrolysis	MA-1
	CS + 2% of TiO_2-P25 + pyrolysis	MA-2
	CS + 3% of TiO_2-P25 + pyrolysis	MA-3
Membrane B (MB)	CS + pyrolysis + 3 coating layers (TiO_2-P25)	MB-1
	CS + pyrolysis + 6 coating layers (TiO_2-P25)	MB-2
	CS + pyrolysis + 9 coating layers (TiO_2-P25)	MB-3

Note: *MA: TiO_2-P25 incorporated in the G preparation stage; MB: TiO_2-P25 thin-film uniformly coated over the G film surface; CS – Chitosan; G – Graphene.

For the preparation of MB, the same procedure described above was repeated using a CS solution without TiO_2-P25; after which the G-decorated membrane was immersed in a TiO_2-P25 solution using the same dip-coating procedure. Following each immersion, the membrane was dried in an oven at 100 °C for about 30 min and this procedure was repeated for coating layers of 3 [MB-1], 6 [MB-2], and 9 [MB-3].

Regardless of the deposition method (A or B), the membrane functionalized with G-TiO_2 was inserted into the reactor and cleaned through the permeation of UPW for 1 h. The total mass of catalyst deposited

on the membrane was calculated by weighing the membrane prior to catalyst deposition and after the cleaning and drying process (as the procedure described above). Furthermore, the membranes before and after the reactions were weighed (dry mass) to measure the possible leaching of TiO_2, and the difference was <1% of the total mass of TiO_2. Also, the absorbance of the concentrate and permeate streams at 500 nm, characteristic of TiO_2, was negligible during the permeation studies.

2.2.2.1 Characterisation techniques

Raman spectra were recorded at room temperature with a Horiba Jobin YvonLabram HR UV–Visible–NIR (200 – 1600 nm) Raman Microscope Spectrometer, using a 632 nm laser as the excitation source. Raman spectra were recorded in random points of a 1 × 1 cm^2 film.

The morphology of the sample was analysed by SEM using a JEOL JSM 6300 apparatus equipped with an X-MAX detector of Oxford Instruments and coupled with energy dispersive X-ray (EDS) analysis. To determine the surface porosity and pore size distribution on the G-TiO_2 functionalized samples, SEM images from randomly chosen area (around 100 points) were analysed by Image Pro software. The textural properties of tested samples were analysed using liquid nitrogen porosimetry or the Brunauer-Emmett-Teller (BET) adsorption-desorption isotherms, measured by Micrometrics ASAP 2020 V 1.05H surface area analyser.

The surface morphology was investigated by AFM with NanoScope 3D (Veeco, USA) microscope operated in taping mode under ambient conditions. Etched silicon probes with spring constants 20 – 80 N m^{-1} were used. Image analysis was done by Nanoscope image processing software. The roughness surface morphology (*RSM*) is calculated as the root mean square average of height deviations taken from the mean data plane (Equation (2.1)):

$$RSM = \sqrt{\frac{\sum Z_i^2}{n}} \tag{2.1}$$

where Z_i is the maximum vertical distance between the highest and lowest data points in the image and n is the number of samples.

Fourier transform infrared spectra (FTIR) of samples were recorded on ATR-FTIR Nicolet iS10 (Thermo Scientific) spectrometer in the range 4000–500 cm^{-1} with a resolution of 4 cm^{-1} and at room temperature. The UV–Visible diffuse reflectance spectra (DRS) were recorded on a Shimadzu 2600 UV–Visible spectrometer with an integrating sphere attachment within the wavelength range from 200

to 700 nm. An Attension Theta optical tensiometer with an automated liquid pumping system was used for the contact angle measurements. UPW was used as the probe liquid.

The point of zero charge (pH_{pzc}) of the G-TiO_2 film was determined following a pH drift test as described elsewhere [3]. Briefly, an amount (5 mL) of 0.01 M NaCl solution was placed in a flask and the pH was adjusted to a value between 2 and 10 by the addition of 0.01 M HCl or 0.01 M NaOH. Then, 15 mg of G-TiO_2 film powder was added and the final pH was measured after 24 h under stirring at room temperature. After the shaking process, the final pH of the suspensions was recorded. The difference between the final and initial pH values (ΔpH) was plotted against the initial pH. The point of intersection of the resulting curve with $\Delta pH = 0$ gives the value of pH_{pzc}.

X-ray powder diffraction (XRD) data for the quantitative phase analysis were acquired on a Shimadzu XRD-7000 diffractometer with Cu Kα radiation (40 kV and 30 mA).

2.2.3 Preparation of the photocatalytic borosilicate membrane

2% (w/v) TiO_2-P25 suspension (250 mL) with two drops of TritonTM X-100 was stirred for 24 h and placed in an ultrasonic probe (Vibra-Cell^{TM} VCX 130 from Sonics) with a frequency of 20 kHz (80% amplitude) for 15 min. The prepared suspension was used to coat the external surface of the membrane following an immersion coating method, employing an automatic dip-coating unit (RDC 15 from Bungard-Elektronik) with an immersion rate of 8 cm min^{-1} and immersion time of 1 min. After each immersion, the membrane was dried in an oven at 100 ºC for 30 min. The process was repeated four times and, afterwards, the membrane decorated with TiO_2-P25 was taken for heat treatment in a furnace (up to 450 ºC for 2 h). Before its use in photocatalytic tests, the coated membrane was placed inside the reactor and UPW was recirculated throughout the system in the dark for 1 h to remove unbounded TiO_2-P25 particles. The total mass of the catalyst deposited on the membrane was calculated by weighing the membrane before catalyst deposition and after the cleaning and drying process.

2.2.3.1 Characterisation techniques

The membrane surface morphology was observed by SEM. A Jeol JSM 7401F Field Emission Scanning Electron Microscope equipped with Gentle Beam mode was employed to characterise the developed modified membranes' surface morphology. XRD patterns of the samples that performed the phase identification were recorded on a D/max 2550Pc automatic diffractometer of polycrystalline (Cu Kα radiation, Rigaku-D/MAX2500/PC, Japan) that operated at 40 keV and 100 mA over the range of $20^{\circ} < 2\theta < 90^{\circ}$ at a scanning rate of $0.02^{\circ}s^{-1}$. Mercury intrusion porosimeter equipment (PoreMaster 60, Quantachrome Inst.) was used to determine the pore size and porosity of the membrane after TiO_2-P25 deposition.

2.3 Experimental units and procedures

The various sets of experiments performed during this thesis were executed in two different membrane reactors described below. Table 2.4 assigns each reactor to the respective chapter where it was employed.

Table 2.4. List of reactors employed in each chapter.

Reactor	Description	Chapter
Pressure-driven membrane process (PMP)	Water desalination Photocatalytic membrane reactor	3 and 4
Membrane contactor (MC)	Ozone contactor	5 and 6

2.3.1 Pressure-driven membrane process

2.3.1.1 Water desalination: Permeation test and salt rejection

The experiments were conducted in a laboratory-scale cross-flow membrane filtration reactor (MFR). Figure 2.1 shows a schematic diagram of the experimental equipment. A thermostated tank (5 L capacity) was used to feed the solution into the MFR and the water temperature was maintained at 25 °C. The solution was constantly stirred magnetically at 250 rpm. During the experiment, the feed solution was pumped to the MFR using a gear pump (Tuthill Pump Group, DGS.68). The MFR comprises an inner-tubular membrane and an outer borosilicate glass tube (length: 15.5 cm; internal diameter: 6 cm; thickness: 8 mm; maximum pressure: 12.5 bar). In addition, the system has a pressure control system connected to a data collector. The MFR worked at a transmembrane pressure (*TMP*) of 5, 8 and 10 bar and a cross-flow velocity (*CFV*) of 10 cm s^{-1}. The whole system was connected by polytetrafluoroethylene (PTFE) tubes.

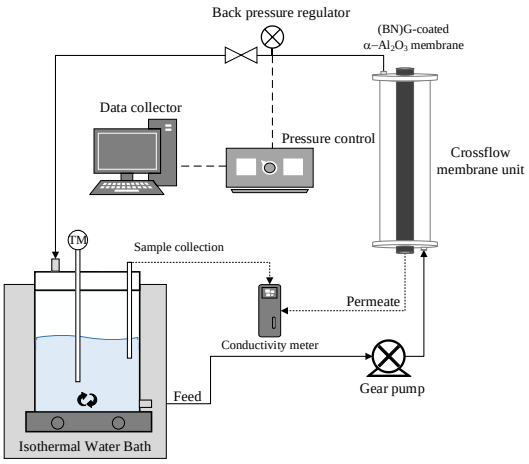

(a)

(b)

Figure 2.1. Schematic diagram of the laboratory-scale cross-flow membrane filtration unit (a) and photograph of the MFR (b). Note: TM – thermometer, (B,N)G – multilayer (B,N)G membrane (for preparation procedure of the (B,N)G membrane on porous alumina see *Section 2.2.1*).

The permeate was collected in a glass container and its conductivity was measured to determine salt concentration. Salt concentrations were confirmed by ICP analyses. The permeate flux was estimated by measuring the volume that crosses the membrane in a certain period of time. The maximum pure water flux by the MFR (without (B,N)G film coating) was 4.2, 6.8 and 8.5 $m^3\ m^{-2}h^{-1}$ for *TMP* of 5, 8 and 10 bar, respectively.

After each reaction, the MFR was washed with UPW and the system flushed for a sufficiently long period of time until the conductivity measurements did not detect the presence of salt in either the feed tank or permeate.

The desalination efficiency of the prepared membrane was evaluated by measuring water flow and salt rejection. The water flux (J; L m^{-2} h^{-1}) was determined from the volume collected through the membrane (V; L), the effective membrane area (A; m^2) and a certain experiment time (t; h) using the following Equation (2.2):

$$J = \frac{V}{A \times t} \tag{2.2}$$

The salt concentrations of the feed (C_f ; µS cm^{-1}) and the permeate (C_p; µS cm^{-1}) were determined from conductivity measurements using a calibrated plot. The salt rejection (R; %) efficiency was determined by Equation (2.3):

$$R\ (\%) = \frac{C_f - C_p}{C_f} \times 100 \tag{2.3}$$

2.3.1.2 Photocatalytic membrane reactor

Preliminary photocatalytic tests in a batch reactor

As there is an impossibility to compare G-TiO_2 membranes with a TiO_2 membrane in continuous filtration mode, since there are significant differences in size and distribution of the pores (discussed in more detail in *Section 4.3.1*), batch tests were carried out to evaluate the oxidation ability of the different catalyst thin-films over the membrane shell-side. Hence, a tubular MF membrane was cut into small pieces of 1 cm in length. G-TiO_2 and TiO_2 films were produced on the external surface of the small pieces of MF membrane using the methods described in *Section 2.2.2*. Under batch conditions, the following catalyst films/system were tested and compared towards CECs oxidation: pristine membrane piece, G membrane piece, UVA + pristine membrane piece, UVA + G membrane piece, UVA + TiO_2 membrane piece, and UVA + G-TiO_2 membrane pieces (MA or MB).

The batch experimental system was composed mainly of a 200 mL thermostatic glass vessel, a magnetic stirrer, and a UVA lamp (Philips TL 6 W, λ_{max} = 365 nm) located above the vessel. 150 mL of CECs solution prepared with UPW ($[CEC]_0$ = 500 µg L^{-1} of each; DCF, E2, EE2 and AMX) was added to the vessel (25 °C) and mixed by magnetic stirring. The MF membrane piece was inserted into the bottom of the vessel. CECs adsorption on the catalyst film was evaluated for 10 min and, immediately afterwards, the UVA lamp was switched on, starting the reaction for 180 min. CECs photolysis was evaluated in the absence of the membrane pieces. Samples were collected at a predefined series of time intervals and then analysed in terms of CECs concentration.

A pseudo-first-order model (Equation (2.4)) was fitted to experimental data of CECs oxidation in the batch system, as a simple mathematical model, using a nonlinear regression method (Fig. P software for Windows from Biosoft).

$$[CEC]_t = [CEC]_0 \times e^{-k_{CEC} \times t} \quad (2.4)$$

where $[CEC]_t$ and $[CEC]_0$ are CEC concentration (µM or µg L^{-1}) after a certain time (t) and just before reaction beginning (t = 0), respectively, and k_{CEC} (min^{-1}) is the pseudo-first-order kinetic constant. The goodness of fitting was evaluated considering the relative standard deviations, the residual variance (S^2_R) and coefficient of determination (R^2).

Photocatalytic membrane reactor's setup and experimental procedure

The lab-scale system integrates: (i) a photocatalytic membrane reactor (vertical position) equipped with four UVA lamps (Philips TL 6 W, λ_{max} = 365 nm, photonic flux of 1.19 ± 0.02 J s^{-1}) located externally to the reactor window; (ii) a 5 L feed tank (cylindrical glass vessel) coupled to a thermostatic bath

(Julabo, model F12-EH) and a magnetic stirrer (CAT, model M5); (iii) a gear pump (Tuthill Pump Group, DGS.68) to feed the membrane module; (iv) a system to control the pump, lights and flow rate; and (v) a back pressure regulator (BPR) connected to a personal computer to regulate the *TMP*. The PMR unit comprises an inner-tubular ceramic membrane and an outer borosilicate glass tube (length: 15.5 cm; internal diameter: 6 cm; thickness: 8 mm; maximum pressure: 12.5 bar), as reactor window, allowing UVA light to penetrate into the annular reaction zone until the membrane surface. Polytetrafluoroethylene (PTFE) tubes were used to connect the whole system units (Figure 2.2).

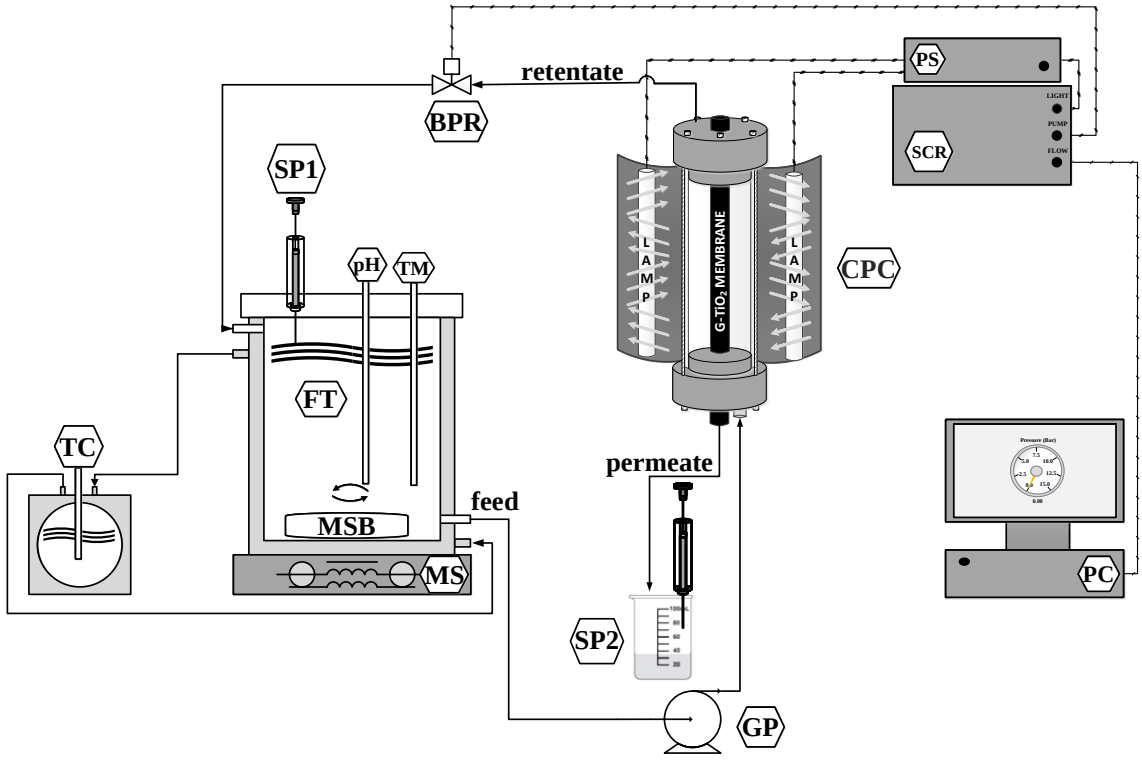

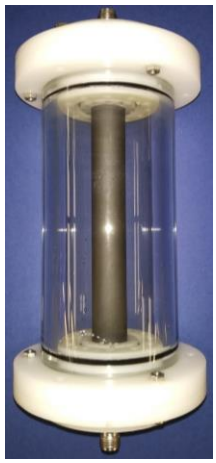

(b)

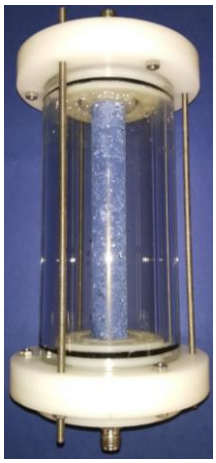

(c)

Figure 2.2. Schematic representation of laboratory-scale photocatalytic membrane reactor (a) and photograph of the reactor with membrane A (MA) (b) and membrane B (MB) (c). Note: BPR – back pressure regulator; CPC – compound parabolic collector; FT – feed tank; GP – gear pump; MS – magnetic stirrer; MSB – magnetic stirrer bar; PC – computer; pH – pH-meter; PS – power supply; SCR – system controller; SP1 – feed sampling point; SP2 – permeate sampling point; TC – temperature controller; TM – temperature meter.

First, the feed tank was filled with 5 L of CECs solution, which was maintained at 25 °C. The CECs solutions were prepared using UPW or UWW fortified with the same amount of CECs ($[CEC]_0$ = 500 µg L^{-1} of each). No pH correction was performed for the UWW fortified with CECs.

The CECs adsorption on the membrane surface was evaluated for 30 min (without permeation), in which the solution passed through the entire system in the dark (recirculation mode). Immediately, the *CFV* and the *TMP* were set to 0.01 m s^{-1} and 10 bar, respectively, and the UVA lamps were switched on, starting the reaction time. The CECs solution filtration was carried out in outside-inside mode. Before the photocatalytic experiments, all membranes were first stabilized with UPW filtration (J_0; L m^{-2} h^{-1}) water at a *TMP* of 10 bar for 1 h. The membrane's permeability was evaluated using UPW at multiple *TMP* (3, 6, 10 bar). The permeate flux (J_{CECs}; L m^{-2} h^{-1}) was determined by collecting a volume of permeate during a certain period of time. Samples were collected at predefined times (0, 15, 30, 45, 60, 90, 120, 150, 180 and 210 min). The retentate was continuously recirculated to the feed tank. Permeate samples were collected under time intervals until steady-state conditions (90 min) were achieved and then analysed in terms of CECs.

In order to investigate the antifouling properties of the G-TiO_2 membranes, the flux recovery ratio (*FRR*), the relative flux reduction ratio (*RFR*), the reversible fouling ratio (*Rr*) and the irreversible fouling ratio (*Rir*) were determined. After the experiment, the membranes were washed with UPW for 1 h to remove loosely attached organics. Then, the flux of the cleaned membrane (J_{CM}; L m^{-2} h^{-1}) was measured again at 10 bar. The *FRR* (Equation (2.5)), *RFR* (Equation (2.6)), *Rr* (Equation (2.7)) and *Rir* (Equation (2.8)) were calculated as follows [4]:

$$FRR\ (\%) = \left(\frac{J_{CM}}{J_0}\right) \times 100 \tag{2.5}$$

$$RFR\ (\%) = \left(\frac{J_0 - J_{CECs}}{J_0}\right) \times 100 \tag{2.6}$$

$$Rr\ (\%) = \left(\frac{J_{CM} - J_{CECs}}{J_0}\right) \times 100 \tag{2.7}$$

$$Rir\ (\%) = \left(\frac{J_0 - J_{CM}}{J_0}\right) \times 100 \tag{2.8}$$

The photonic flow was determined by the actinometry of 2NB (10 mM) [5]. 2 L of 2NB solution was placed in the reactor vessel, recirculated in all system for 10 min in the dark, and a control sample was taken. Then, the 4 UVA lamps were turned on and samples were collected at predefined times (0, 7.5, 15, 22.5, 30, 37.5, 45 min). The BPR was fully open, and no permeation occurred.

2.3.2 Membrane contactor

The schematic diagram of the lab-scale prototype is shown in Figure 2.3. The apparatus consists of an ozone system and an ozone membrane reactor.

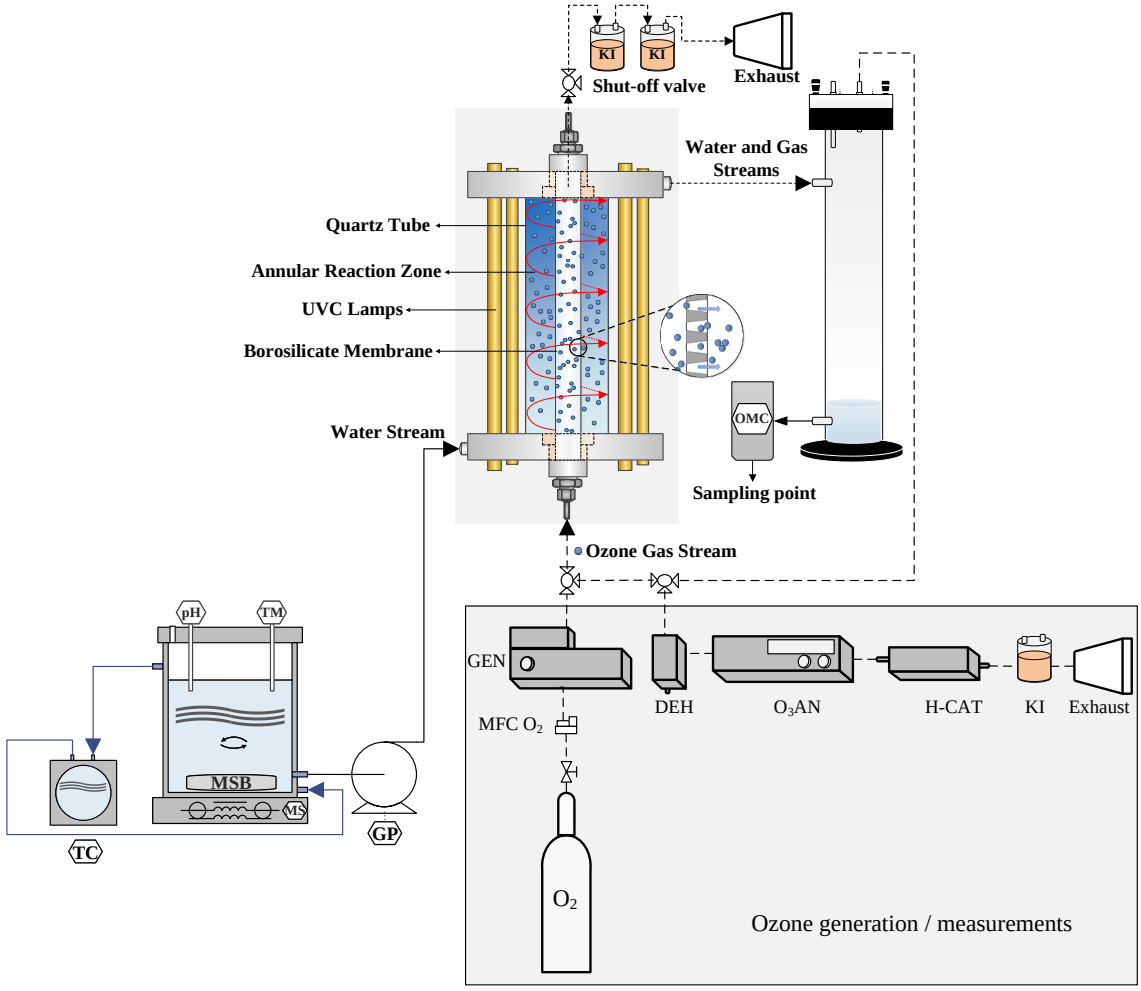

(a)

(b)

Figure 2.3. Schematic representation of laboratory-scale setup (a) and photography (b). Note: DEH – dehumidifier; GEN – ozone generator; GP – gear pump; H-CAT – heat catalyst (ozone destruction); KI – 2% KI solution; MFC – mass flow controller; MS – magnetic stirrer; MSB – magnetic stir bar; O_2 – oxygen; O_3AN – ozone analyser; OMC – ozone measuring cells; pH – pH-meter; TC – temperature controller; TM – temperature meter; Continuous lines – water; Dotted lines – water + ozone gas stream; Dashed lines – ozone gas stream.

2.3.2.1 Ozone system

O_3 was generated from oxygen (O_2, 99.995% supplied by Air Liquide) using a corona discharge generator (BMT 802 N) with a production capacity of up to 4 g O_3 h^{-1} (at 100 g Nm^{-3}, 20 ºC). The input

gas flow rate (Q_G = 0.15-1.00 $Ndm^3\ min^{-1}$) was controlled with the aid of a digital mass flow meter (Alicat Scientific). The O_3 concentration in the gas flow ($[O_3]_{G,inlet}$ = 20-200 g Nm^{-3}) was controlled by changing the power input to the O_3 generator and was monitored with an O_3 analyser (BMT 964). Before passing through the analyser, the residual O_3 leaving the reactor passes through a column to separate the liquid and gas phase. The gas phase was directed to a sample gas dehumidifier (BMT DH3b), vented through the catalytic O_3 destruction unit (Heated Catalyst BMT) and sequentially to an O_3 destroyer bottle (containing a 2% KI solution) before going into exhaustion. The concentration of O_3 in water was monitored using a measuring cell AQC-D12 with a reference electrode for ozone (Grundfos Alldos) connected to a controller Conex DIA-1 (Grundfos Alldos). According to the manufacturer's specifications, the measuring range was 0.05–50 g O_3 m^{-3}, sensitivity <0.02 g O_3 m^{-3}, and accuracy < ± 5%. The O_3 probe was calibrated using the iodometric method, based on the oxidation of iodide with O_3 and posterior evaluation of the produced iodine or its ion in solution [6, 7]. The analysis of iodine was made by titration with $Na_2S_2O_3$. The iodometric method is described in detail in *Section 2.4.1*.

2.3.2.2 Ozone membrane reactor

The ozone membrane reactor comprises an inner tubular borosilicate MF membrane (ASTM VitraPOR from ROBU; outside diameter: 20.9 mm; internal diameter: 10.5 mm; wall thickness: 5.2 mm; useful length: 174 mm; porosity: 45%; BET: 1200 $m^2\ g^{-1}$) with 5 µm pore size adequately installed in an outer quartz tube (outside diameter: 42.2 mm; internal diameter: 38.2 mm; length: 200 mm) vertically fixed in a stainless-steel structure. The borosilicate membrane and quartz tube ends were tightly sealed by two movable polypropylene flanges. The membrane outlet was connected to a shut-off valve to allow gas permeation through the porous glass membrane. In this system, the O_3 gas stream is fed by the lumen side of the membrane, while the water to be treated is introduced in the shell side of the membrane, and the gas/water contact takes place at the outer membrane surface. DW (with or without CECs) or UWW (with or without CECs) was pumped from a jacketed vessel to the annular reaction zone (ARZ) using a gear pump (ISMATEC BVP-Z pump). Viton O-rings (ozone-resistant) were used to ensure sealing conditions within the reaction module. Polytetrafluoroethylene (PTFE) and stainless-steel tubes were used to connect the liquid and gas units of the system, respectively.

To assess the effect of combining the ozonation process with photocatalysis in the removal of CECs, four UVC lamps (Philips TL 11 W, λ_{max} = 254 nm) were located externally to the reactor window. UVC radiation was chosen since it is able to effectively activate both TiO_2 and O_3. O_3 has an absorption band at 200-300 nm with a maximum at λ of 254 nm [8, 9]. A photon flow (2.89 ± 0.08 W) inside the ARZ was measured by ferrioxalate actinometry [10, 11] (Fe^{3+} = 6 × 10^{-3} M; overall quantum yield,

Φ_T = 1.39 ± 0.02; optical path length = 8.65 mm;). An aluminium shell enclosed the illuminated reactor setup to prevent light escape to the surroundings.

Ozone gas/water mass transfer was determined in continuous mode operation and the effect of water pH and temperature (T), the concentration of O_3 in the gas stream ($[O_3]_{G,inlet}$), liquid (Q_L) and gas (Q_G) flow rates in the volumetric mass transfer coefficient (K_La) were assessed. To begin the experimental trial, the borosilicate membrane was filled internally with the ozone gas stream with the shut-off valve fully open (Figure 2.3). This procedure ensures that the entire interior of the membrane was filled with the gas. The residual O_3 stream was directed to a 2% KI solution in an O_3 destroyer bottle. Subsequently, DW or UWW was pumped and the shut-off valve was immediately closed. The concentration of dissolved O_3 in the water at the reactor outlet was analysed *in situ,* and the data were collected at regular time intervals.

2.3.2.3 Gas/liquid mass transfer calculations

The two-film theory was used for the modelling of the O_3 mass transfer, typically controlled by resistance on the liquid side. As O_3 is slightly soluble in water, resistance to mass transfer is located in the liquid film [12]. Thus, the K_La can be calculated from the mass balance of O_3 in the liquid, considering plug flow conditions, and represented by Equation (2.9):

$$\frac{d[O_3]}{dt} = K_La \times ([O_3^*] - [O_3]) - k_d[O_3] \quad (2.9)$$

where, $\frac{d[O_3]}{dt}$ is the variation of dissolved O_3 concentration in water as a function of time (g m^{-3} min^{-1}), K_La is the product of the O_3 mass transfer coefficient (min^{-1}) through the liquid phase (K_L) and the interfacial area (a), $[O_3^*]$ is the O_3 saturation concentration in the liquid in equilibrium with the gas phase (g m^{-3}) at the experimental temperature and k_d is the self-decomposition constant of O_3 (min^{-1}). For a negligible self-decomposition of O_3, the integration of the Equation (2.9) leads to Equation (2.10), considering the following boundary conditions for continuous mode operation: $[O_3] = 0$ at $t = 0$; $[O_3] = [O_3]_L$ at $t = \tau$:

$$K_La = -\frac{1}{\tau} ln \left(1 - \frac{[O_3]_L}{[O_3^*]}\right) \quad (2.10)$$

where $[O_3]_L$ is the dissolved ozone concentration in the outlet liquid stream at steady-state conditions (g m^{-3}), and τ is the liquid residence time (min), calculated taking into account the gas holdup (ε_G; %).

The $[O_3^*]$ with the gas phase were experimentally determined in batch mode (Figure 2.4) with DW at water pH of 3.0 ± 0.2, T = 20 ºC, Q_G = 0.75 Ndm^3 min^{-1}, $[O_3]_{G,inlet}$ = 20 g Nm^{-3}, Q_L = 50 L h^{-1}, by recirculating the outlet gas/liquid stream to a column for 45 min.

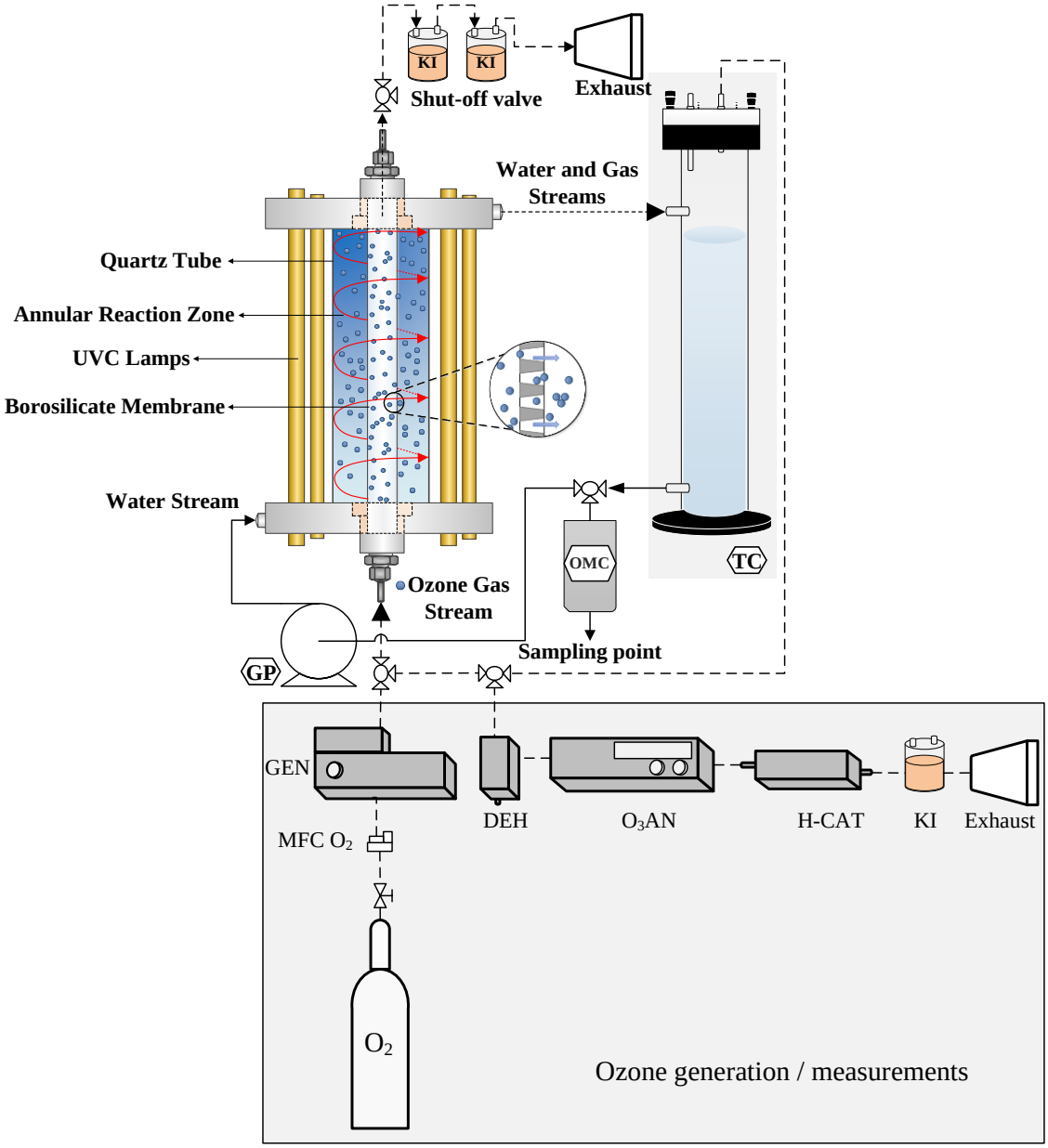

Figure 2.4. Schematic representation of laboratory-scale setup of the batch system. Note: DEH – dehumidifier; GEN – ozone generator; GP – gear pump; H-CAT – heat catalyst (ozone destruction); KI – 2% KI solution; MFC – mass flow controller; MS – magnetic stirrer; MSB – magnetic stir bar; O_2 – oxygen; O_3AN – ozone analyser; OMC – ozone measuring cells; TC – temperature controller; Continuous lines – water; Dotted lines – water + ozone gas stream; Dashed lines – ozone gas stream.

After the saturation, the injection of the ozone gas stream in the system was stopped. Then, the value of k_d was calculated by the kinetic profile of ozone concentration decay as a function of time. As reported by other authors [13-15], the decrease of ozone concentration was considered as a first-order process and the self-decomposition constant k_d could be calculated from the following equation:

$$\frac{d[O_3]}{dt} = -k_d \times [O_3] \quad (2.11)$$

Similarly, integrating Equation (2.11) gives Equation (2.12):

$$ln\frac{[O_3^*]}{[O_3]} = k_d \times t \quad (2.12)$$

The interfacial area (a; m^{-1}) is one of the essential parameters for processes involving gas-liquid mass transfer (Equation (2.13)) and requires the determination of ε_G and the Sauter mean diameter (d_{32}, mm), which can be obtained from the bubble size distribution data (Equation (2.14)).

$$a = 6\frac{\varepsilon_G}{d_{32}} \quad (2.13)$$

$$d_{32} = \frac{\sum_{i=1}^{n} n_i d_{eq}^3}{\sum_{i=1}^{n} n_i d_{eq}^2} \quad (2.14)$$

where n_i is the number of bubbles of diameter d_{eq} (mm).

Further details on bubble size distribution and mean bubble size are provided in *Section 2.3.2.4*.

In O_3 membrane contactors, the membrane creates an additional mass transfer resistance, significantly reducing process efficiency. For a conventional membrane contactor with a hydrophilic membrane, the overall mass transfer resistance ($1/K_L$) is given by Equation (1.5) [14].

In a GLMC, the resistance to mass transfer in the liquid boundary layer has already been proved to be the dominant step of overall mass transfer resistance for the case of low liquid Reynolds number and low gas solubility [16]. As a result, the simpler model can be obtained when the mass transfer resistance in the gas phase is neglected (i.e., $1/(k_G H) \cong 0$), owing to the ozone diffusion coefficient in the gas phase is 4 orders of magnitude higher than in the water [17, 18] (Equation (2.15)).

$$\frac{1}{K_L} = \frac{1}{k_M} + \frac{1}{k_L} \quad (2.15)$$

2.3.2.4 Determination of bubble size distribution, mean bubble size, gas holdup and specific interfacial area

The acquisition of bubble images was performed using a high-speed digital video camera (Photron, FASTCAM SA-Z) in three different axial zones of the reactor (top, middle and bottom), under the same conditions of $K_L a$ determinations. During image acquisition, a light source and a black sheet (behind the

reactor) were used to improve the image's quality and differentiate the boundaries of the gas bubbles. The digital camera was positioned at approximately 30 cm from the reactor wall. Thus, in the axial zone, a filming of 30 s was performed and 10 frames were taken as images (same position as the camera, but at different times of image acquisition). The best images acquired, with at least 500 marked bubbles, were treated, analysed and the results were extracted using the ImageJ software coupled with the "Analyze Particles" tool.

The numerical descriptors resulting from the software image analysis are the projected bubble area (A_p, mm^2). Considering that the bubbles are homogeneous, without deformations and symmetrical, it can be considered for the calculations that the bubbles generated by the ozone contactor are spherical. Therefore, d_{eq} can be calculated by Equation (2.16).

$$d_{eq} = \sqrt{\frac{A_p}{\pi}} \tag{2.16}$$

With the same digital images, the volume fraction of the gas phase, also known as ε_G, was calculated according to Equation (2.17). The methodology involves measuring the height of the liquid without the presence of gas (h_0, mm) and the corresponding level (h, mm) when the gas is continuously introduced into the reactor at a given flow rate. The gas-phase volume fraction was measured at least 10 times with a mean error of less than 2%.

$$\varepsilon_G = \frac{h - h_0}{h} \tag{2.17}$$

2.3.2.5 Evaluation of CECs removal

CECs removal was evaluated in continuous mode using DW or UWW contaminated with 19 CECs (10 µg L^{-1} each) and different oxidation processes: (i) ozonation (with O_3 permeation and light irradiation off); (ii) photocatalysis UVC/TiO_2 (no O_3 permeation), and (iii) photocatalytic ozonation (O_3/UVC/TiO_2). The following operational conditions were applied: CECs solution inlet flow rate (Q_L = 50-150 L h^{-1}; hydraulic residence time–τ = 3.9 – 11.6 s), O_3 concentration at the gas inlet ($[O_3]_{G,inlet}$ = 6, 20, 40, 60, 100 or 200 g Nm^{-3}), and gas flow rate (Q_G = 0.15, 0.50 or 0.75 Ndm^3 min^{-1}), corresponding to different inlet O_3 doses ($D_{A\text{-}O_3}$ = 2, 6, 12 or 18 g m^{-3}). Furthermore, the effect of increasing the contact time on CEC removal and the consumption of residual ozone in the liquid phase was evaluated using a 1.5 L retention column after the reactor (contact time = 1 min).

The ozone concentrations in the inlet and outlet of the system were monitored and the transferred ozone dose ($D_{T\text{-}O_3}$; g m^{-3}) was calculated according to Equation (2.18):

$$D_{T-O_3} = \frac{\left([O_3]_{G,inlet} - [O_3]_{G,outlet}\right) \times Q_G}{Q_L} \quad (2.18)$$

where $[O_3]_{G,outlet}$ is the O_3 concentration in the outlet gas stream (g Nm^{-3}).

The $[O_3]_L$ was measured in-line as described in *Section 2.3.2.1* to allow the assessment of consumed ozone dose ($D_{C\text{-}O_3}$, g m^{-3}) by Equation (2.19):

$$D_{C-O_3} = D_{T-O_3} - [O_3]_L \quad (2.19)$$

The samples were taken at pre-determined time intervals and the residual ozone was removed immediately by placing the samples in a water bath at 80 ºC. After each experiment, the ozone membrane contactor was washed by pumping DW through the ARZ.

2.3.2.6 Adsorption process

An adsorption step was used to complement the ozonation treatment, targeting the removal of CECs recalcitrant to ozonation and degradation by-products (Figure 2.5). The adsorption step was performed in continuous mode using a Chromaflex® jacketed column (borosilicate glass column with acrylic water jacket; internal diameter = 4.8 cm; maximum length = 30 cm; maximum pressure of 3.4 bar) with a flow adapter to adjust the bed height inside the column. The column was packed with 265 g of commercial granular activated carbon in pellets (ORNI-EX, LDA). According to the product specifications, the GAC had an appearance of a pelleted black granular solid, iodine number of 1080 mg g^{-1}, an apparent density of 0.4–0.5 kg L^{-1}, diameter with an average size of 1.5 mm and BET surface area of 1100 m^2 g^{-1}. The diameter and shape of the particles were carefully selected as these are factors that affect the phenomena of mass transfer within the particle, as well as the axial and radial dispersion within the packed bed column [19]. To avoid poor flow distribution and liquid retention, the bed length/particle diameter and the bed diameter/particle diameter ratio must be higher than 150 and 30, respectively [20]. Taking into account a coal bed height of 27 cm and an average GAC particle size of 1.5 mm, the ratios are 180 and 32, respectively. The ozonized wastewater ($D_{A\text{-}O_3}$ = 18 g m^{-3}; $[O_3]_{G,inlet}$ = 200 g Nm^{-3}) was pumped up (5 mL min^{-1}) through the column using a peristaltic pump (Gilson Minipuls 2) in upwards mode. Samples were collected regularly at the column outlet and analysed for CECs removal (*Section 2.4.3.2*) and zebrafish toxicity assays (*Section 2.4.4*).

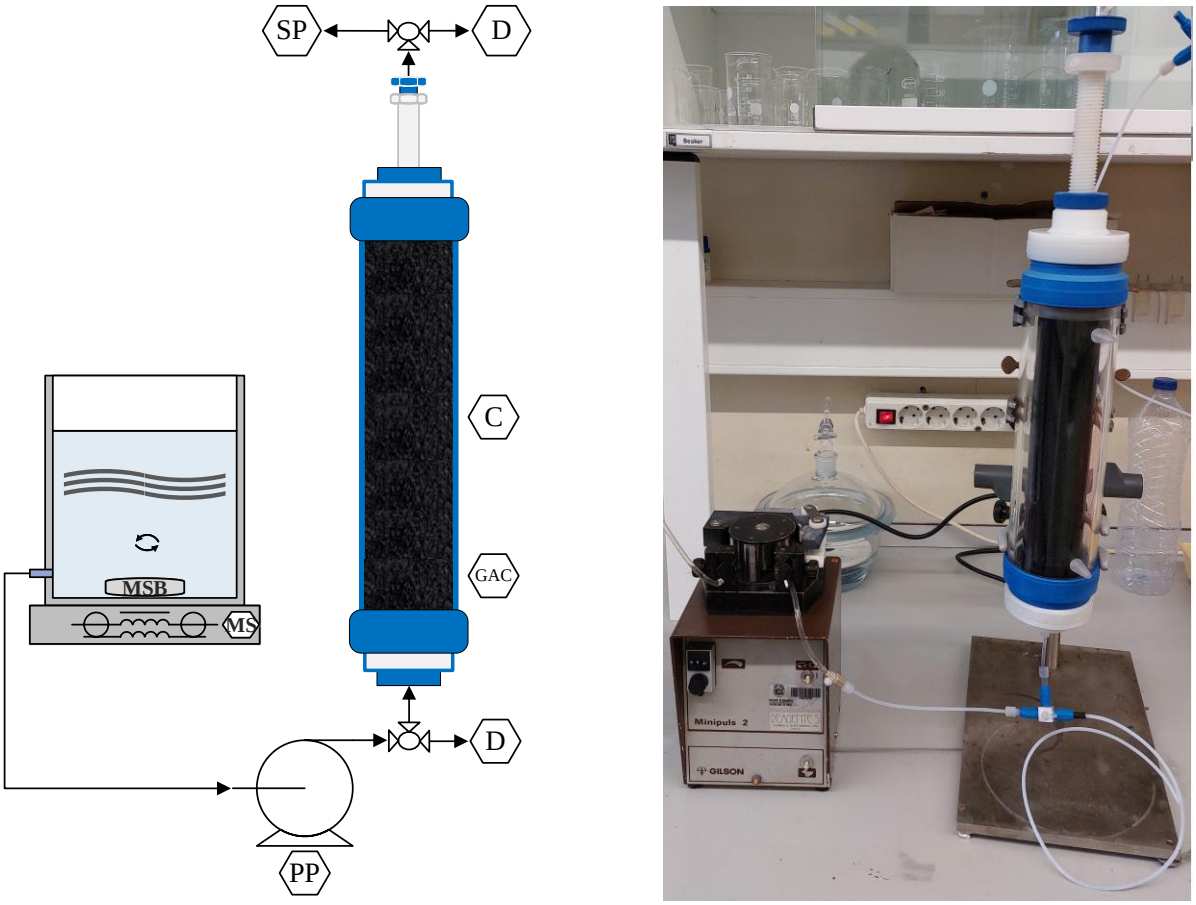

(a) **(b)**

Figure 2.5. Sketch of the continuous adsorption system (a) and photography (b). Note: C – column; D – discard; GAC – granular activated carbon; MS – magnetic stirrer; MSB – magnetic stir bar; PP – peristaltic pump; SP – sampling point.

2.4 Analytical methods

2.4.1 Iodometric method for the determination of ozone concentration in liquid phase

The O_3 probe was calibrated by the iodometric method according to the methodology adapted from American Public Health Association [6] and Birdsall et al. [7]. The principle of this method consists of the oxidation of the iodide ion in excess by O_3 to form iodine (Equations (2.20) and (2.21)) and measuring the produced iodine concentration by titration with sodium thiosulfate.

$$O_3 + 3I^- + 2H^+ \leftrightarrow O_2 + I_3^- + H_2O \quad (2.20)$$

$$I_3^- + 2S_2O_3^{2-} \leftrightarrow 3I^- + S_4O_6^{2-} \quad (2.21)$$

In order to quantify the dissolved O_3 in water, 100 mL of a liquid sample containing dissolved O_3 was added to 50 mL of the KI 2% (w/v), and then 2.5 mL of H_2SO_4 (0.5 M) was added to acidify the solution.

Subsequently, the sample of ozonised water and KI solution was immediately titrated with sodium thiosulfate, previously standardised with potassium dichromate (0.01 M). In addition, a starch indicator

solution (1% w/v) was used. The ozone mass was calculated from the amount of thiosulfate consumed in the titration (Equation (2.22)) and the ozone concentration (g O_3 m^{-3}) was calculated from the ozone mass obtained through Equation (2.23).

$$m = 0.5 \times C_{thi} \times f \times V_{thi} \times M_{O_3} \quad (2.22)$$

$$C = \frac{m}{V} \times 10^3 \quad (2.23)$$

where m is the mass of ozone (mg), C_{thi} is the nominal concentration of thiosulfate (mol L^{-1}), f is the correction factor for thiosulfate, V_{thi} is the sodium thiosulfate volume (mL), M_{O_3} is the molar mass of ozone (g mol^{-1}), C is the ozone concentration (mg L^{-1}), and V is the volume of the ozonized water sample (mL).

2.4.2 Wastewater characterisation

The UWW samples used in the advanced treatment assays were collected from a full-scale UWWTP after secondary treatment in northern Portugal. Turbidity, total nitrogen, total phosphorous, total dissolved iron, chemical oxygen demand, total suspended solids, and volatile suspended solids were determined according to the American Public Health Association [6]. The total dissolved carbon and dissolved inorganic carbon were measured in a Shimadzu TOC-V_{CSN} analyser (Shimadzu, Kyoto, Japan). pH and temperature were measured using a Hanna Instruments HI-2020 edge® hybrid. Conductivity was determined by Hanna Instruments HI9828 multiparameter meter. The absorption spectra were evaluated between 200 and 800 nm using a Merck Spectroquant® Prove 300 UV/Vis spectrophotometer. Inorganic anions were analysed by ion chromatography (Dionex ICS-2100 LC) equipped with an IonPac® AS11-HC 250 mm × 4 mm column (T = 30 °C) and an anion self-regenerating suppressor (ASRS® 300, 4 mm) under an isocratic elution of 30 mM KOH at a flow rate of 1.5 mL min^{-1}. Inorganic cations were also evaluated by ion chromatography in a Dionex DX-120 LC coupled with an IonPac® CS12A 250 mm × 4 mm column at ambient temperature and a CSRS® Ultra II cation self-regenerating suppressor (4 mm) under an isocratic elution of 20 mM methanesulfonic acid at a flow rate of 1.0 mL min^{-1}. All the effluent samples were stored at 4 °C prior to be used.

2.4.3 CECs analysis

2.4.3.1 High-performance liquid chromatography with DAD detector

AMX, DCF, E2 and EE2 concentrations were followed by a reversed-phase HPLC using a VWR Hitachi ELITE LaChrom equipped with a Merck LiChrosorb® RP-18 (5 μm) LiChroCART® 125–4 column and an L-2455 diode array detector (DAD). An isocratic elution (48:52 (v/v) acetonitrile/0.014 M oxalic

acid) was used for E2, EE2 and DCF determination. For the AMX quantification, the equipment was operated in a gradient mode using acetonitrile/methanol/0.014 M oxalic acid with ratios of 10:5:85 (v/v) from 0 to 3 min, 15:5:80 (v/v) from 3 to 5 min, 10:5:85 (v/v) from 5 to 8 min. The flow rate was set at 1.0 mL min^{-1}, the injection volume at 50 µL and DAD at 230 nm for AMX and 280 nm for E2, EE2 and DCF. The retention times for E2, EE2, DCF and AMX were 3.3 min, 4.0 min, 5.1 min and 9.4 min, giving detection limits of 10.7 µg L^{-1}, 7.86 µg L^{-1}, 18.8 µg L^{-1} and 15.2 µg L^{-1}, respectively. The 2NB concentration was determined using an isocratic elution with 60% 0.014 M oxalic acid/40% acetonitrile at a flow rate of 0.60 mL min^{-1}. The retention time and the detection limit were 7.6 min and 2.4 mg L^{-1}, respectively.

2.4.3.2 Liquid chromatography-tandem mass spectrometry (LC-MS/MS)

The analysis of the selected CECs in water/wastewater samples was performed in an Acquity UPLC® liquid chromatograph interfaced to a XEVO TQD® triple quadrupole mass spectrometer (LC-MS/MS) equipped with an electrospray interface (ESI) from Waters (Milford, MA, USA). A sample volume of 45 µL was directly injected into a Luna C18 100A column (50 mm × 2 mm, 3 µm particle size) supplied by Phenomenex (Torrance, CA, USA) maintained at a constant temperature of 30 °C and 0.2 mL min^{-1} flow rate. The quantification in UWW was performed by the standard addition method using standards prepared in UWW and direct injection of the samples. The mobile phases consisted of (A) 1 mM ammonium fluoride in UPW and (B) 1 mM ammonium fluoride in MeOH. The gradient was as follows: 0-1 min, 100% A; 1-8 min, linear gradient to 100% B; 7-13 min, 100% B and finally, 13-20 min, 100% A. Nitrogen was used as nebulizing and drying gas and Argon was used as collision gas. The analyses were determined in the ESI positive and negative polarities, and the acquisition mode was multiple-reaction monitoring (MRM). Two MRM transitions were used as a quantifier (Q) and qualifier (q) for each compound, except in the case of PFBA, where only one intense MRM transition was observed (see Table 2.5 for detailed information). The quantification was performed by the standard addition method using standards. The method performance parameters are given in Table 2.6 for DW and Table 2.7 for UWW.

Table 2.5. Instrumental LC-MS/MS parameters.

CECs	Retention time (min)	Precursor ion (m/z)	Product ion (m/z)	Cone voltage (V)	Collision energy (V)	ESI mode
CBZ	8.2	237	194 (Q) 179 (q)	40	20 38	Pos
CBZ-EPX	7.5	253	180 (Q) 210 (q)	39	25 12	Pos
DCF	9.5	294 296	250 (Q) 252 (q)	33 33	10 10	Neg
EE2	9.3	295	145 (Q) 159 (q)	60	37 33	Neg
E2	9.0	271	145 (Q) 183 (q)	65	42 38	Neg
ATNL	5.2	267	145 (Q) 190 (q)	38	30 16	Pos
BSPL	7.5	326	116 (Q) 204 (q)	45	20 18	Pos
DEET	8.5	192	119 (Q) 91 (q)	25	15 25	Pos
ISTN	9.2	434	179 (Q) 350 (q)	50	65 28	Neg
LSTN	9	421	127 (Q) 157 (q)	30	30 25	Neg
VSTN	9.3	427	193 (Q) 121(q)	35	20 25	Neg
DRN	8.6	233	72 (Q) 160 (q)	30	20 20	Pos
MLN	1.5	127	85 (Q) 69 (q)	45	15 20	Pos
AC-K	4.8	162	82 (Q) 78 (q)	30	15 30	Neg
SCH	5.7	182	42 (Q) 62 (q)	45	35 30	Neg
TFMS	2.7	149	80 (Q) 99 (q)	46	20 20	Neg
PFOA	9.7	413	369 (Q) 169 (q)	20	14 20	Neg
PFBS	8.5	299	80 (Q) 99 (q)	56	36 30	Neg
PFBA	7.5	213	169 (Q)	20	10	Neg

Note: Capillary voltages: 3.5 and 1.5 kV in positive and negative polarities, respectively. Source temperature: 350 ºC. Desolvation gas (N_2) flow: 650 L h^{-1}. Cone gas (N_2) flow: 5 L h^{-1}. Collision energy (*CE*) and cone voltage (*CV*) were adjusted for every transition. (Q) quantifier transition; (q) qualifier transition.

Table 2.6. LC-MS/MS method performance for DW.

CECs	Linearity (R^2) *LOQ**-50 µg L^{-1}	Precision *RSD** (%) 10 µg L^{-1} (n=5)	*LOQ** µg L^{-1}
CBZ	0.999	2.2	0.02
CBZ-EPX	0.999	2.8	0.02
DCF	0.997	2.3	0.18
EE2	0.996	6.5	1.50
E2	0.997	5.7	2.10
ATNL	0.995	2.6	0.15
BSPL	0.993	3.2	0.04
DEET	0.999	3.2	0.03
ISTN	0.999	3.7	0.05
LSTN	0.999	4.2	0.15
VSTN	0.999	4.3	0.28
DRN	0.999	4.0	0.07
MLN	0.998	7.1	0.58
AC-K	0.998	6.2	0.50
SCH	0.998	7.1	1.00
TFMS	0.999	6.9	1.00
PFOA	0.999	4.1	0.02
PFBS	0.999	2.9	0.09
PFBA	0.997	2.1	0.14

Note: **LOQ* - Limit of Quantification; *RSD* - Relative Standard Deviation.

Table 2.7. LC-MS/MS method performance for UWW.

CECs	Linearity (R^2) *LOQ**-50 µg L^{-1}	Precision *RSD** (%) 10 µg L^{-1} (n=5)	*LOQ** µg L^{-1}
CBZ	0.998	3.1	0.03
CBZ-EPX	0.996	2.5	0.02
DCF	0.996	3.5	0.19
EE2	0.991	8.5	2.3
E2	0.995	7.9	3.1
ATNL	0.998	3.2	0.24
BSPL	0.992	4.1	0.11
DEET	0.999	4	0.03
ISTN	0.999	6.9	0.08
LSTN	0.999	6.2	0.26
VSTN	0.999	7.1	0.44
DRN	0.999	4.6	0.07
MLN	0.998	6.8	0.75
AC-K	0.994	8	0.68
SCH	0.992	8.3	1.1
TFMS	0.999	7.2	1.2
PFOA	0.999	5.8	0.02
PFBS	0.999	3.8	0.09
PFBA	0.998	3.2	0.14

Note: **LOQ* - Limit of Quantification; *RSD* - Relative Standard Deviation.

2.4.4 Toxicity screening using zebrafish embryo bioassay

The zebrafish embryo bioassay carried out based on the OECD Fish Embryo Acute Toxicity (FET) Test 236 [21], was used to evaluate the toxicity of the water samples before and after the treatment. In Chapter 4, the zebrafish embryo bioassay was evaluated for 10 samples: synthetic matrix (dechlorinated DW - control), solvent control (acetonitrile in dechlorinated UPW; the percentage of acetonitrile is equal to the amount in the CECs working solution), real matrix (secondary-treated UWW), real matrix + acetonitrile, and CECs in UPW and real matrix before and after the treatment with the membranes. For Chapter 6, the zebrafish embryo bioassay was performed for six samples: control (dechlorinated DW), real matrix fortified with 19 target CECs before and after the ozonation treatment (UWW+CECs and UWW+CECs+O_3, respectively), and after ozonation plus GAC adsorption (UWW+CECs+O_3+GAC). Each treatment condition was tested without dilution and with dilutions factors of 2 and 4 with dechlorinated water.

2.4.4.1 *Zebrafish maintenance and eggs collection*

Adults zebrafish AB strain were kept in dechlorinated water at 28 ± 1 °C and under a photoperiod of 12:12 h (light:dark). Animals were fed ad libitum, twice a day, with commercial food Tetramin (Tetra, Melle, Germany), supplemented every two days with live *Artemia spp*. In order to induce zebrafish breeding, in the afternoon prior to the beginning of the embryo bioassay, adults in a proportion of 2:1 (male:female) were allocated in a breading box to reproduce. On the following day, 1.5 h after the beginning of the light period, newly fertilized eggs were collected and cleaned in order to start the embryo bioassay [22].

2.4.4.2 Zebrafish embryo bioassay OECD 236

The clean zebrafish eggs were observed in a magnifying glass and randomly allocated in 24-well plates (one embryo per well) previously incubated with 1.5 mL of each treatment. In each 24-well plate was assigned one treatment composed of 20 embryos divided into five replicates plus an internal plate control (4 embryos). The plates were randomly maintained in an incubator at 26 °C ± 0.5 for 96 h under the same photoperiod as the adults. The treatment solutions were renewed daily in order to maintain oxygen saturation and the integrity of the solutions. Embryos were checked every day for mortality and dead embryos were removed. Embryo development was checked under an inverted microscope (Nikon Eclipse 5100 T) coupled with a digital camera Nikon D5 – Fi2, and morphological abnormalities on the head, tail, notochord, pericardial and yolk-sac oedemas, and hatching rate were recorded as present or absent at 24, 48, 72, and 96 h post-fertilization (hpf) [22, 23]. At each observation time point, the different abnormalities were grouped and presented as total abnormalities.

2.4.4.3 *Statistical analysis*

Data obtained during the embryo bioassay were computed in Statistica 12.5 (Statsoft, USA). Data were tested for homogeneity of variances using Leven's test and transformed if required. If the homogeneity of variances was met, a one-way ANOVA followed by Fisher's least significant difference (LSD) test was performed in order to evaluate differences between the CECs in DW-UPW/real matrices and the DW-UPW/real matrices without the CECs; as well as differences between the CECs in both matrices before and after treatment. If the homogeneity of variances was not met even after data transformation, data were analysed by Kruskal–Wallis followed by Multiple Comparison Rank Test. Significant differences were set at $p < 0.05$.

2.4.5 Enumeration of culturable microorganisms

In Chapter 6, the enumeration of cultivable microorganisms was evaluated. One millilitre of serially 10-fold diluted sample, or up to 100 mL of sample, was filtered through cellulose nitrate membrane filters (0.22 μm porosity; Whatman, UK) in triplicate. Afterwards, the filtering membranes were placed onto the appropriate culture media of the target microbial group: Plate Count Agar [PCA; VWR International (Pennsylvania, USA); 30 ºC, 48 h] for culturable heterotrophs, m-Faecal Coliform Agar [mFC; Thermo Fisher Scientific (Massachusetts, USA); 37 ºC, 24 h] for enterobacteria, and Slanetz Bartley Agar (mENT; Thermo Fisher Scientific (Massachusetts, USA); 37 ºC, 48 h] for enterococci. Additionally, m-Faecal Coliform Agar supplemented with 32 mg L^{-1} amoxicillin (AMX), 4 mg L^{-1} cefotaxime (CTX) or 350 mg L^{-1} sulfamethoxazole (SUL) were used to assess resistance prevalence before and after treatment. These antibiotic concentrations were based on previous studies [24, 25]. Results were expressed as colony forming units (CFU) per 100 mL of sample.

2.5 References

[1] A. Dhakshinamoorthy, A. Primo, P. Concepcion, M. Alvaro, H. Garcia, Doped graphene as a metal-free carbocatalyst for the selective aerobic oxidation of benzylic hydrocarbons, cyclooctane and styrene, Chemistry-A European Journal 19 (23) (2013) 7547-7554. https://doi.org/10.1002/chem.201300653.

[2] A.M. Primo Arnau, H. García Gómez, E. Sánchez Cortezón, J.M. Delgado Sánchez, Method for obtaining solid graphene samples or suspensions, European Patent Office, 2015, pp. 1-15.

[3] M.A. Ferro-García, J. Rivera-Utrilla, I. Bautista-Toledo, C. Moreno-Castilla, Adsorption of Humic Substances on Activated Carbon from Aqueous Solutions and Their Effect on the Removal of Cr(III) Ions, Langmuir 14 (7) (1998) 1880-1886. https://doi.org/10.1021/la970565h.

[4] M. Shakak, R. Rezaee, A. Maleki, A. Jafari, M. Safari, B. Shahmoradi, H. Daraei, S.-M. Lee, Synthesis and characterization of nanocomposite ultrafiltration membrane (PSF/PVP/SiO_2) and performance evaluation for the removal of amoxicillin from aqueous solutions, Environmental Technology & Innovation 17 (2020) 100529. https://doi.org/10.1016/j.eti.2019.100529.

[5] E.S. Galbavy, K. Ram, C. Anastasio, 2-Nitrobenzaldehyde as a chemical actinometer for solution and ice photochemistry, Journal of Photochemistry and Photobiology A: Chemistry 209 (2) (2010) 186-192. https://doi.org/10.1016/j.jphotochem.2009.11.013.

[6] American Public Health Association, Standard methods for the examination of water and wastewater, 19th ed., American Public Health Association, Washington, D.C, 1995.

[7] C.M. Birdsall, A.C. Jenkins, E. Spadinger, Iodometric Determination of Ozone, Analytical Chemistry 24 (4) (1952) 662-664. https://doi.org/10.1021/ac60064a013.

[8] J.F.d.S. Petruci, D.N. Barreto, M.A. Dias, E.P. Felix, A.A. Cardoso, Analytical methods applied for ozone gas detection: A review, TrAC Trends in Analytical Chemistry 149 (2022) 116552. https://doi.org/10.1016/j.trac.2022.116552.

[9] M. Griggs, Absorption Coefficients of Ozone in the Ultraviolet and Visible Regions, The Journal of Chemical Physics 49 (2) (1968) 857-859. https://doi.org/10.1063/1.1670152.

[10] C.G. Hatchard, C.A. Parker, E.J. Bowen, A new sensitive chemical actinometer - II. Potassium ferrioxalate as a standard chemical actinometer, Proceedings of the Royal Society of London. Series A. Mathematical and Physical Sciences 235 (1203) (1956) 518-536. doi:10.1098/rspa.1956.0102.

[11] J. Rabani, H. Mamane, D. Pousty, J.R. Bolton, Practical Chemical Actinometry—A Review, Photochemistry and Photobiology 97 (5) (2021) 873-902. https://doi.org/10.1111/php.13429.

[12] T. Liu, D. Wang, W. Wang, Q. Liang, L. Shao, Study on the Efficient Production of Ozone Water by a Rotating Packed Bed, Industrial & Engineering Chemistry Research 58 (17) (2019) 7227-7232. https://doi.org/10.1021/acs.iecr.8b06486.

[13] M.-T. Gao, M. Hirata, H. Takanashi, T. Hano, Ozone mass transfer in a new gas–liquid contactor–Karman contactor, Separation and Purification Technology 42 (2) (2005) 145-149. https://doi.org/10.1016/j.seppur.2004.07.004.

[14] M. Kukuzaki, K. Fujimoto, S. Kai, K. Ohe, T. Oshima, Y. Baba, Ozone mass transfer in an ozone–water contacting process with Shirasu porous glass (SPG) membranes—A comparative study of

hydrophilic and hydrophobic membranes, Separation and Purification Technology 72 (3) (2010) 347-356. https://doi.org/10.1016/j.seppur.2010.03.004.

[15] J. Wang, H. Liu, D. Ma, Y. Wang, G. Yao, Q. Yue, B. Gao, S. Wang, X. Xu, Degradation of organic pollutants by ultraviolet/ozone in high salinity condition: Non-radical pathway dominated by singlet oxygen, Chemosphere 268 (2021) 128796. https://doi.org/10.1016/j.chemosphere.2020.128796.

[16] A. Gabelman, S.-T. Hwang, Hollow fiber membrane contactors, Journal of Membrane Science 159 (1) (1999) 61-106. https://doi.org/10.1016/S0376-7388(99)00040-X.

[17] P.N. Johnson, R.A. Davis, Diffusivity of Ozone in Water, Journal of Chemical & Engineering Data 41 (6) (1996) 1485-1487. https://doi.org/10.1021/je9602125.

[18] S. Bamperng, T. Suwannachart, S. Atchariyawut, R. Jiraratananon, Ozonation of dye wastewater by membrane contactor using PVDF and PTFE membranes, Separation and Purification Technology 72 (2) (2010) 186-193. https://doi.org/10.1016/j.seppur.2010.02.006.

[19] L.P. Mazur, M.A.P. Cechinel, S.M.A.G.U. de Souza, R.A.R. Boaventura, V.J.P. Vilar, Brown marine macroalgae as natural cation exchangers for toxic metal removal from industrial wastewaters: A review, Journal of Environmental Management 223 (2018) 215-253. https://doi.org/10.1016/j.jenvman.2018.05.086.

[20] V.J. Inglezakis, A. Zorpas, Fundamentals of Ion Exchange Fixed-Bed Operations, in: I. Dr, M. Luqman (Eds.), Ion Exchange Technology I: Theory and Materials, Springer Netherlands, Dordrecht, 2012, pp. 121-161. https://doi.org/10.1007/978-94-007-1700-8_4.

[21] OECD, Test No. 236: Fish Embryo Acute Toxicity (FET) Test, OECD Publishing, Paris, 2013. https://doi.org/10.1787/9789264203709-en.

[22] S. Barros, R. Montes, J.B. Quintana, R. Rodil, A. André, A. Capitão, J. Soares, M.M. Santos, T. Neuparth, Chronic environmentally relevant levels of simvastatin disrupt embryonic development, biochemical and molecular responses in zebrafish (*Danio rerio*), Aquatic Toxicology 201 (2018) 47-57. https://doi.org/10.1016/j.aquatox.2018.05.014.

[23] J.C. Espíndola, R.O. Cristóvão, S.R.F. Araújo, T. Neuparth, M.M. Santos, R. Montes, J.B. Quintana, R. Rodil, R.A.R. Boaventura, V.J.P. Vilar, An innovative photoreactor, FluHelik, to promote UVC/H_2O_2 photochemical reactions: Tertiary treatment of an urban wastewater, Science of The Total Environment 667 (2019) 197-207. https://doi.org/10.1016/j.scitotenv.2019.02.335.

[24] R.B.M. Marano, T. Fernandes, C.M. Manaia, O. Nunes, D. Morrison, T.U. Berendonk, N. Kreuzinger, T. Tenson, G. Corno, D. Fatta-Kassinos, C. Merlin, E. Topp, E. Jurkevitch, L. Henn, A. Scott, S. Heß, K. Slipko, M. Laht, V. Kisand, A. Di Cesare, P. Karaolia, S.G. Michael, A.L. Petre, R. Rosal, A. Pruden, V. Riquelme, A. Agüera, B. Esteban, A. Luczkiewicz, A. Kalinowska, A. Leonard, W.H. Gaze, A.A. Adegoke, T.A. Stenstrom, A. Pollice, C. Salerno, C.U. Schwermer, P. Krzeminski, H. Guilloteau, E. Donner, B. Drigo, G. Libralato, M. Guida, H. Bürgmann, K. Beck, H. Garelick, M. Tacão, I. Henriques, I. Martínez-Alcalá, J.M. Guillén-Navarro, M. Popowska, M. Piotrowska, M. Quintela-Baluja, J.T. Bunce, M.I. Polo-López, S. Nahim–Granados, M.-N. Pons, M. Milakovic, N. Udikovic-Kolic, J. Ory, T. Ousmane, P. Caballero, A. Oliver, S. Rodriguez-Mozaz, J.L. Balcazar, T. Jäger, T. Schwartz, Y. Yang, S. Zou, Y. Lee, Y. Yoon, B. Herzog, H. Mayrhofer, O. Prakash, Y. Nimonkar, E. Heath, A. Baraniak, J. Abreu-Silva, M. Choudhury, L.P. Munoz, S. Krizanovic, G. Brunetti, A. Maile-Moskowitz, C. Brown, E. Cytryn, A global multinational survey of cefotaxime-resistant coliforms in

urban wastewater treatment plants, Environment International 144 (2020) 106035. https://doi.org/10.1016/j.envint.2020.106035.

[25] A. Novo, S. André, P. Viana, O.C. Nunes, C.M. Manaia, Antibiotic resistance, antimicrobial residues and bacterial community composition in urban wastewater, Water Research 47 (5) (2013) 1875-1887. https://doi.org/10.1016/j.watres.2013.01.010.

3 Large Area Continuous Multilayer Graphene Membrane for Water Desalination

This chapter reports the preparation of a large area (84 cm^2) desalination membrane based on multilayers (11 nm thickness) of B,N-codoped defective graphene. The process consists of coating a porous ceramic α-Al_2O_3 support (100 nm pore size) with a continuous nanometric (50 nm) chitosan film containing adsorbed $(NH_4)_3BO_3$. Subsequent pyrolysis in the presence of hydrogen converts chitosan into multilayer defective B,N-codoped graphene. The partial removal of B and N dopant atoms by H_2 during the pyrolysis causes the generation of subnanometric pores due to atom vacancy, as determined by control experiments in the absence of this gas. NaCl and KCl removal efficiency from brackish water higher than 95% for a permeate flux of 24.3 L m^{-2} h^{-1} at 10 bar was achieved. Due to the excellent rejection rate of NaCl and KCl from brackish water and high permeate flux at lower transmembrane pressure, as well as the large area, the membrane reported herein appears to be easy to implement in water desalination. As far as we know our report describes the largest, continuous graphene membrane with subnanometric pores, where the membrane and the pores have been formed on site in a single step during the preparation process.

This chapter is based on the following research article: "Presumido, P.H., Primo, A., Vilar, V.J.P., Garcia, H. *Large area continuous multilayer graphene membrane for water desalination*, Chemical Engineering Journal, 413 (2021) 127510. DOI: 10.1016/j.cej.2020.127510".

3.1 Introduction

Global demand for fresh water has been increasing in recent years [1, 2]. Therefore, technologies aimed at the desalination of sea and brackish water are crucial for meeting future demand and improving drinking water quality [3]. In this context, it has been proposed that continuous graphene films can serve to develop the ultimate membranes, since the one-atom thickness represents the physical zero-depth limit for any membrane [4, 5].

Among the many important physical properties of ideal graphene including high electron mobility, optical transparency and remarkable mechanical resistance and elasticity [6], one of relevance for developing membranes is that ideal graphene constitutes a perfect barrier that does not allow the crossover of even the smallest atom or molecule. In particular, it has been proved that a perfect graphene layer cannot permeate He or H_2 at room temperature [7-10] only in exceptional cases where ripples, wrinkles and other defects induce a local curvature that allow the permeation of H_2 [11]. The major advantages of continuous graphene as membrane that would make its use as a disruptive technology are its high mechanical strength, high elasticity and wide range of chemical stability. Adequate porosity on the graphene sheet should allow combining a high flux due to the zero depth and high solute removal [12, 13].

The main barriers that limit the general application of desalination technologies to produce fresh water are the high pressures required to overcome osmotic pressure and low permeate fluxes, resulting in a high energy consumption. These limitations are closely related to the development of more efficient strong continuous membranes that withstands high pressures and exhibits a high salt rejection rate.

In this context, graphene materials have attractive properties for their use in water desalination and purification membranes [14-16]. However, the difficulty to obtain a large area graphene membranes on appropriate supports, together with the lack of suitable strategies to generate pores of proper dimensions to exclude small ions, such as Na^+, K^+ and Cl^-, in a pressurized filtration process are the two major limitations to be overcome for the wide use of graphene on desalination.

High quality graphene films of sufficiently large area are typically obtained by chemical vapor deposition on metal surfaces, most commonly Ni or Cu. After preparation, it is necessary to devise suitable transfer techniques to deposit this graphene film on the appropriate porous support. Subnanometric porosity must be generated by electron or ion impact [17]. Otherwise, porosity on graphene has also been generated by a two-step procedure consisting of O_2 plasma nucleation of defects and subsequent etching and expansion of defects with ozone treatment [18]. The complexity of the

process and the need for dedicated equipment reduce the attractiveness and limit the use of graphene as membrane.

To circumvent this limitation, most of the reports so far on the use of graphene and graphene derivatives in desalination membranes are employing this material as an additive, rather than as a continuous film, to improve the performance of the embedding polymeric matrix [3, 19]. Alternatively, measurements on graphene membranes have been made on films of micrometric size [14, 20] or larger areas by cumbersome transfer process of costly preformed chemical vapor deposition (CVD) graphene on flat substrates [21, 22]. Besides high-quality graphene [14, 20], other related materials that have been also employed for the preparation of desalination membranes include graphene oxide (GO) [23, 24] and boron nitrite (BN) [25-27]. In one of these examples, Kim et al. [28] deposited GO nanosheets followed by amino GO nanosheets on the surface of amino polyethersulfone (PES) membrane. The obtained membrane exhibits a good salt rejection of 98% for a water flux of 28 L m^{-2} h^{-1} at a pressure of 55 bar.

Cohen-Tanugi et al. [29] reported theoretical studies based on classical molecular dynamics simulations on the behaviour of multilayer graphene membrane for desalination. Their study on models varying the number of overlapped holey graphene layers concluded that a ~ 200 nm thick nanoporous multilayer graphene membrane should have rejection efficiency and permeate flux similar to those of a single-layer graphene membrane.

There is a clear gap in commercially producing continuous graphene membranes of large area, affordable cost and within quality assurance/quality control requisites [30]. In most of the studies in the field of membranes, graphene is previously prepared by chemical exfoliation of industrial graphite and then deposited on the support [31-33]. Briefly in this method, graphite is oxidized to graphite oxide that after neutralization is converted to GO. The product is dried to get the GO powder. Lastly, the membrane is immersed in GO solution. However, since graphite particles have, at best, a lateral dimension of a few micrometers, the membrane is constituted by the overlap of micrometric flakes, but it is not a continuous graphene film. Therefore, an innovative method of fabricating large area graphene films that can be used as membranes should be a significant step forward in the area of desalination.

3.2 Objectives

The main objective of the work presented in this chapter is to prepare a large area, continuous film of multilayer graphene membrane with subnanometric porosity for water desalination. The preparation procedure and extensive characterisation of the multilayer graphene will be correlated with its

performance in terms of water flux and salt rejection as a function of applied pressure using brackish water.

3.3 Materials and methods

All the chemicals used in this work, permeation tests, experimental units and procedures, as well as the employed analytical determinations, are depicted in *Chapter 2*. The fabrication of continuous multilayer boron, nitrogen-codoped defective graphene film on porous α-Al_2O_3 membrane is described in detail in *Section 2.2.1*. All the experimental data presented in this chapter was obtained using the MF membrane reactor, which is detailed described in *Section 2.3.1.1*, and will be designated as a membrane reactor throughout this chapter. Before submitting for filtration, KCl and NaCl salts were added in the required amount to reach a final 50 mM concentration.

3.4 Results and discussion

3.4.1 Large area graphene membrane concept and preparation

The concept of the present desalination membrane has been the preparation of a continuous film of multilayer B and N-codoped defective G on a porous (100 nm) α-Al_2O_3 membrane as support. Rigid ceramic α-Al_2O_3 membrane allows easy handling of the multilayer (B,N)G film and the design of a membrane reactor. Notice that the dimension of the cylindrical membrane is over 80 cm^2 and the procedure can be easily adapted for larger sizes. Thus, the present (B,N)G film corresponds probably to the largest example of a continuous multilayer graphene membrane for desalination ever reported that proves the efficiency of this technology. It should be noted that previous studies have determined graphene performance on micrometric membranes that were 10^{-9} times smaller than the present one [14, 20].

The thermal stability of the ceramic α-Al_2O_3 makes possible the preparation of defective multilayer (B,N)G by pyrolysis of chitosan (CS) containing adsorbed $(NH_4)_3BO_3$. CS is a soluble deacetylated derivative of chitin that is the most important waste from the fishery industry [34]. Previous studies have shown that the pyrolysis of this natural polysaccharide renders a defective N-doped G and that B and N-codoped defective G can be obtained upon pyrolysis of CS containing $(NH_4)_3BO_3$ [35]. The surface area determined by isothermal N_2 adsorption in powders gave values of about 80–150 $m^2\,g^{-1}$ with a large micropore size distribution, indicating that as a powder the material undergoes extensive stacking due to π–π interactions and van der Waals forces [35]. The success of the continuous multilayer graphene preparation process derives from the ability of CS to form conformal, continuous films on arbitrary

substrates and its subsequent transformation into defective doped G upon pyrolysis at 900 ºC [36]. Of note is that during the process of transformation of CS into (B,N)G by thermal treatment at 900 ºC, no detachment or peeling of the resulting (B,N)G from the alumina tube was observed. The good adherence of graphene film to the Al_2O_3 membrane could reflect a match of the thermal dilatation behaviour of both materials and an adequate interaction among the surface of graphene and Al_2O_3. Defects on the resulting G derived from polysaccharides are due to the presence of a residual O content on the final G and the generation of carbon vacancies on the graphene sheet [37]. In addition, the presence of N atoms in a percentage of about 5% has also been established by combustion elemental analysis [38].

The thickness of the resulting defective G layer depends on the thickness of CS precursor. It has been found that during the pyrolysis the thickness of the film decreases by a factor of 5 to 10-fold as a consequence of CS dehydration, its structural transformation and packing of the G layers. Although the formation of single layers N-doped G has been reported by pyrolysis of very thin CS films on flat substrates [38], the texture of α-Al_2O_3 characterized by a high surface roughness (see SEM images) makes it impossible the preparation of continuous CS films of the required small thickness. Continuity of the defective G film was considered a crucial parameter for the preparation of the desalination membrane, since preliminary experiments with these discontinuous defective G films showed that they do not act as barriers for alkali chlorides. For this reason, thicker CS films of 50 nm or larger were necessary to obtain, after pyrolysis, continuous G films. In this regard, it should be commented that the defective nature of the G films obtained by pyrolysis of CS makes also advisable the stacking of several layers, in a way that the defects and vacancies of one layer that would decrease the selectivity can be masked by the stacking of other layers on top of the defect.

Generation of subnanometric pores to allow water permeation was herein designed by the introduction of doping elements on the graphene sheet that subsequently could be removed by suitable chemical treatments. In this regard, it has been found that dopant B atoms on the graphene sheet can be removed either by oxidative treatment and hydrolysis [39] or by thermal hydrogenation [40]. Also, dopant N atoms are removed from the graphene sheet by thermal hydrogen treatment [37, 40]. Thus, the hypothesis of the present (B,N)G films as membrane is that by preparing doped or codoped defective multilayer graphene films, subsequent removal of the dopant elements can result, according to density functional theory (DFT) modelling of ideal and one-carbon vacancy sheets (Figure 3.1), in the generation of subnanometric pores, able to allow the permeation of H_2O (0.275 nm), but not crossover of hydrated alkali metal ions with hydrated diameters of 0.72 and 0.66 nm for Na^+ and K^+, respectively. As it will be shown below, the results of the permeation measurements of brackish water are in accordance with the above hypothesis.

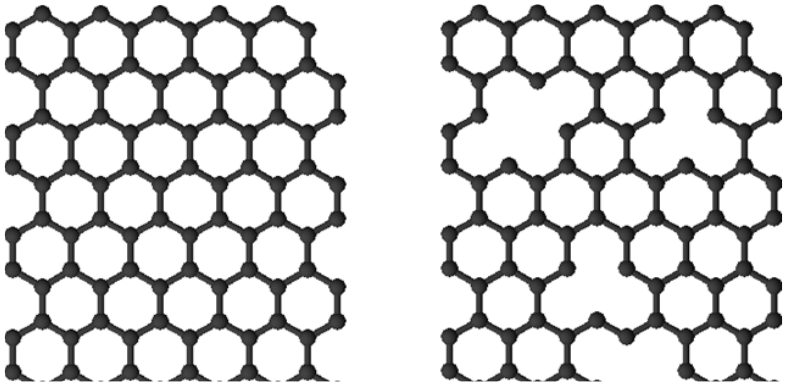

Figure 3.1. Model of an ideal graphene sheet (left) and a model graphene sheet having one or two atom carbon vacancies (right). The concept of the present (B,N)G film as desalination membrane is based on the atomic radius distances among the carbon atoms around vacancies that are about 0.36 nm, in the range wanted for selective H_2O permeation. Note that besides C atoms, defective (B,N)G film contains B, N and O heteroatoms.

3.4.2 Characterisation of multilayer (B,N)G film supported on porous α-Al_2O_3 membrane

The morphology of the α-Al_2O_3 membrane surface was studied by SEM. Figure 3.2 provides two representative images of the fresh and (B,N)G coated α-Al_2O_3 surface. It can be seen there that the fresh α-Al_2O_3 surface is typical of a ceramic material with sintered nanoparticles and significant roughness. The presence of pores in the fresh α-Al_2O_3 membrane is clearly revealed by the images. After forming the (B,N)G membrane, the images show that the whole surface has been completely coated by a conformal film, smoothing the roughness angles and covering the pores. Importantly, SEM images revealed that the film is continuous throughout the whole area.

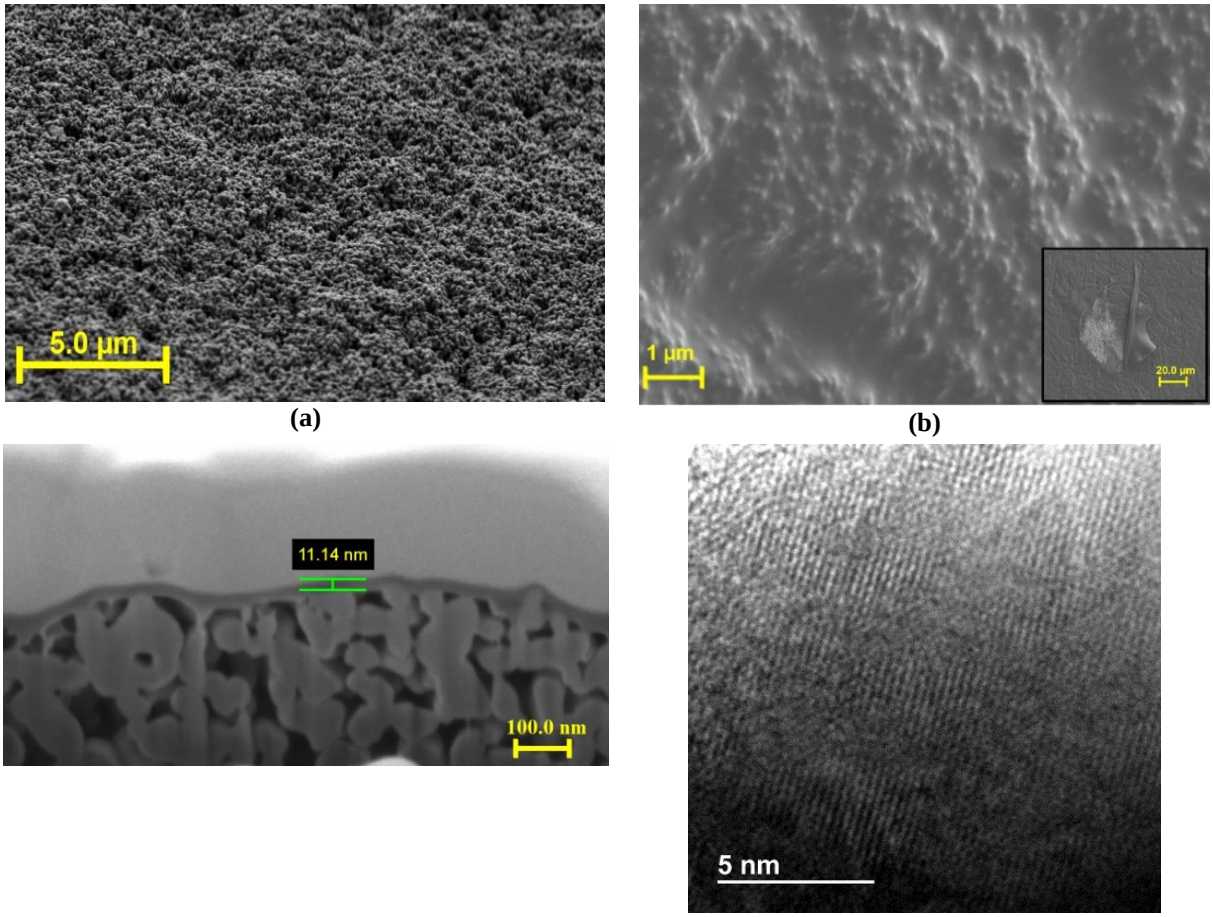

Figure 3.2. SEM image of membrane surface (a) without and (b) with (B,N)G film; (c) FIB image to measure (B,N)G film thickness indicated by green parallel lines underneath the thick layer needed for taking the image; high resolution TEM of (d) (B,N)G film. The inset of panel b shows a small debris scratched from the graphene membrane to perform the high resolution TEM images of the (B,N)G film shown in panel d.

Fast ion bombardment (FIB) can dig into the solid surface and makes it possible to obtain a cross-sectional image of the surface. A representative image is also shown in Figure 3.2c. It can be seen there that underneath the thicker layer needed for ion bombardment, there is a thin continuous (B,N)G film with a thickness of 11.14 nm (indicated by the green parallel lines). This thin continuous (B,N)G film covers the α-Al_2O_3 membrane characterized by a nanoparticulate morphology and large porosity. Regarding the number of (B,N)G layers corresponding to this thickness, it has been determined that the defective graphene layers pack somewhat more loosely than ideal graphene sheets characterized by a short interlayer distance about 0.34 nm. It has been determined that graphene oxide layer thickness is around 0.5-0.7 nm and similar values are proposed for defective N-doped graphene [41]. Therefore, the measured thickness of the multilayer (B,N)G film could correspond most probably to between 15 and 20 graphene layers. In the present case, the broadness of the XRD peaks, indicating a loose packing and low crystallinity of (B,N)G precludes an estimation of the interlayer distance. (B,N)G was obtained as powder by pyrolysis at 900 ºC under a flow (200 mL min^{-1}) of 95 vol.% Ar and 5 vol.% H_2 of an intimate mixture of chitosan and 20 wt.% NaH_2PO_4 following the pyrolysis procedure previously reported in

Dhakshinamoorthy et al. [35]. This sample is analogous to that forming the desalination membrane film coating porous alumina but can be subjected to study by XRD. Figure 3.3 presents powder XRD of (B,N)G compared to pyrolytic graphite.

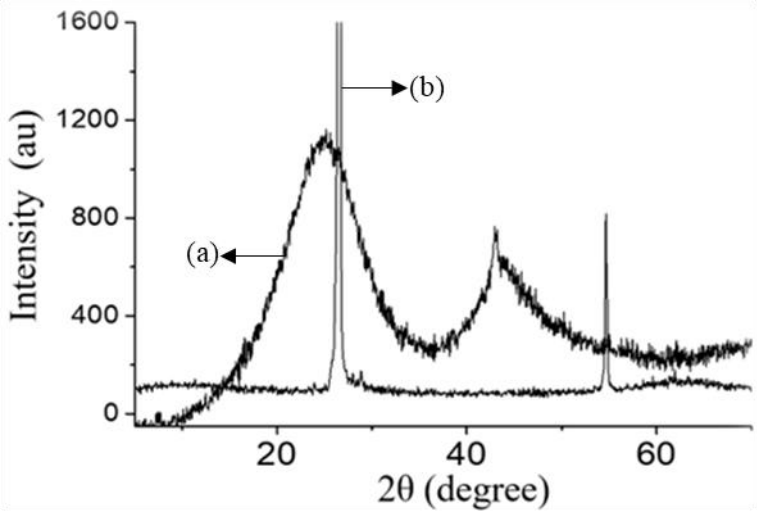

Figure 3.3. XRD of defective graphene (a) and pyrolytic graphite (b).

High-resolution TEM images of the (B,N)G film were taken upon scratching the film from the CS-coated α-Al_2O_3 membrane after pyrolysis (see inset of Figure 3.2b for an image of the (B,N)G peeling off), dispersion of the small piece in ethanol by ultrasonication and drop casting onto a TEM sample holder grid. A representative image of the (B,N)G film coating the α-Al_2O_3 membrane is also presented in Figure 3.2d. As it can be seen there, the TEM image shows the expected hexagonal structural arrangement characteristic of graphene, in accordance with the previously reported behaviour upon pyrolysis of CS at 900 ^oC [38]. In addition, the cross-sectional image shows the multilayer stacking of the graphene obtained by pyrolysis, with an interlayer spacing of about 0.38 nm corresponding to the expected distance between graphene sheets. To image the layered structure of the (B,N)G film, a small piece was scratched from the alumina membrane and analysed by TEM. Figure 3.4 shows a) a cross-section of the film in which the stacking of the layers can be clearly seen. The inset shows the interlayer distance based on the contrast change through 4.5 nm in which 12 layers can be counted, and b) high-resolution frontal view.

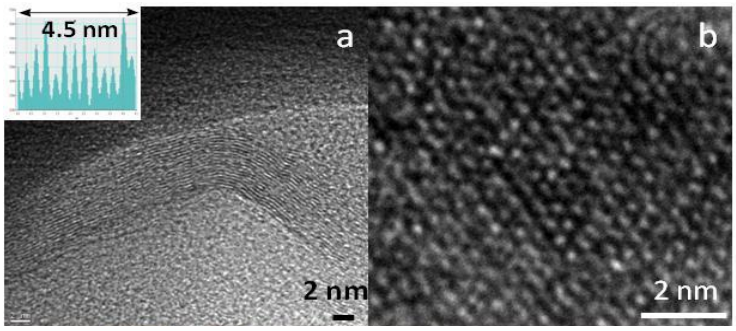

Figure 3.4. High-resolution TEM image of a) a cross-section of the (B,N)G film, and b) frontal view.

A representative AFM image of the (B,N)G-coated α-Al_2O_3 membrane is presented in Figure 3.5. The image shows a frontal view (left frame) and a 3D image (right frame) at the micrometric length scale of the (B,N)G film as a smooth surface without the presence of pinholes, cracks or pitches. The colour codes of the Figure 3.5 refer to differences in height due to the sintering of the coarse grains of micrometric size of Al_2O_3 nanoparticles constituting the substrate on which the (B,N)G film is supported. It is noteworthy that while the Al_2O_3 membrane presents apparent holes among the grains corresponding to the submicrometric membrane pores, these discontinuities are coated and not present when the (B,N)G film is on top of the membrane.

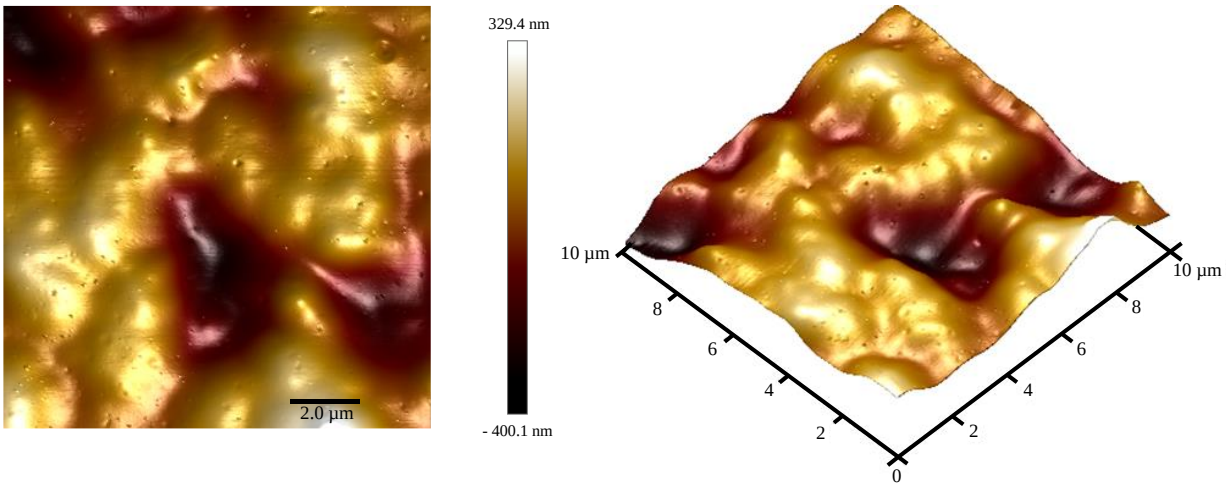

Figure 3.5. Frontal wide-field AFM image of (B,N)G-coated α-Al_2O_3 membrane with the height scale colour codes. This image shows the continuity of the (B,N)G films and the absence of cracks and pinholes on it.

Since porous alumina is not a flat surface and in order to better determine the graphene film thickness, the preparation procedure of (B,N)-codoped graphene film was also performed on a flat quartz plate. By scratching the graphene film with a cutter and measuring the height profile perpendicular to the scratch, a thickness of 10 nm was also measured for this film, in good agreement with the 11.14 nm thickness determined for the graphene film on porous alumina by FIB in SEM measurement.

XPS analysis of the (B,N)G-coated α-Al_2O_3 membrane resulting after pyrolysis at 900 ^oC revealed the presence of C, O, N and B elements. Figure 3.6 presents the high-resolution XPS signals for C1s, O1s, B1s and N1s peaks and the best fitting to individual components for each element and their relative

atomic proportion. According to XPS analysis over 85% of the atoms present in (B,N)G correspond to C atoms in three different environments, namely, graphenic, single bonded to N or O and a minor percentage of carboxylate group carbon atoms. The presence of residual O in about 10 at.% from over the 50% O content of CS precursor was also recorded, in good agreement with reported data [37]. O atoms double bonded to C (carbonyls) interrupt the graphene lattice and are located at the periphery of the sheet or at holes.

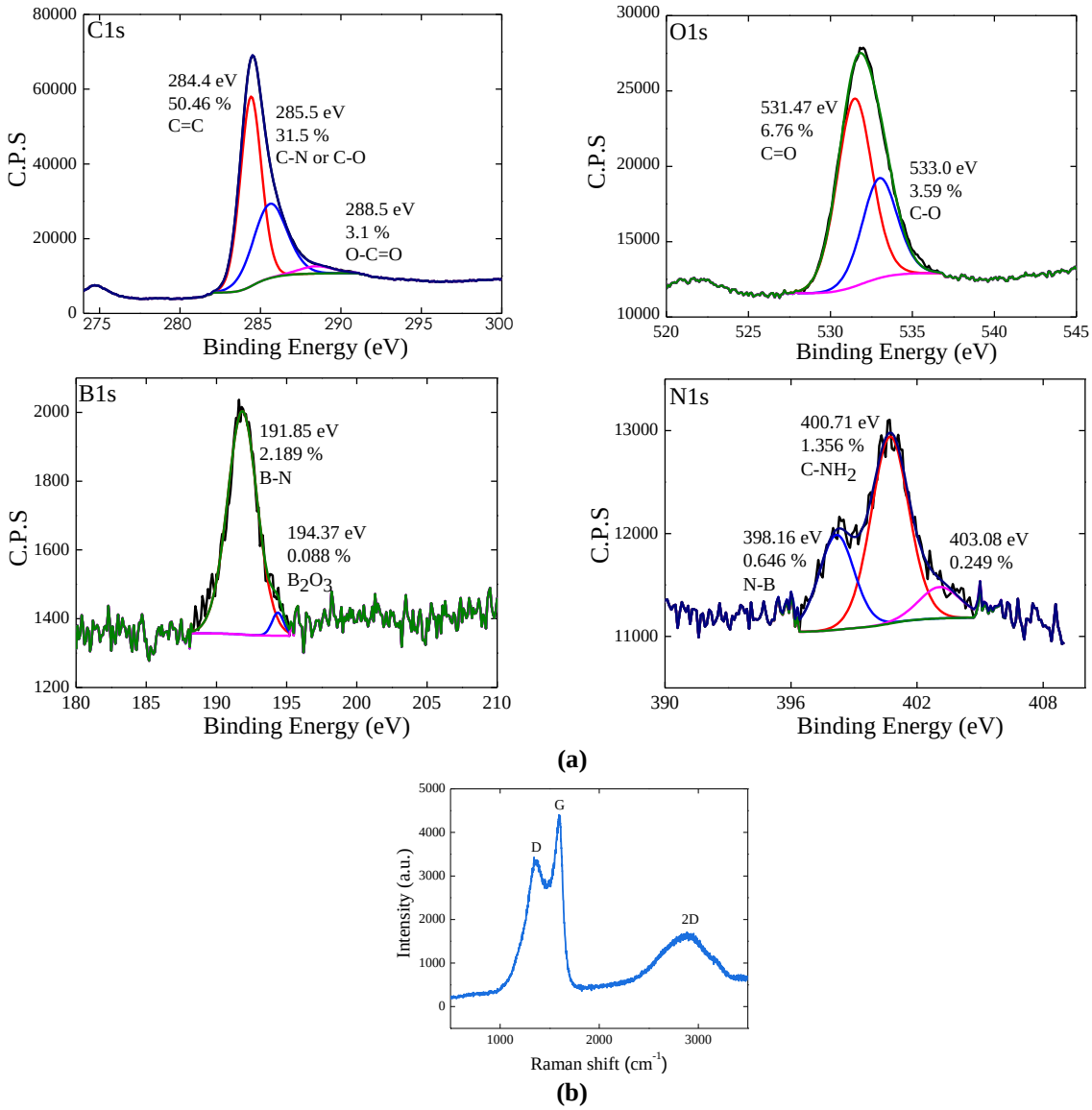

Figure 3.6. (a) High resolution XP spectra of C1s, O1s, B1s and N1s peaks, together with the best fitting to individual components, indicating their corresponding binding energy values, atomic proportion and assignment. (b) Raman spectra of (B,N)G film on α-Al_2O_3 membrane upon 632 nm excitation and the assignment of the vibrational bands.

Importantly, the presence of about 2 at.% each B and N was also detected, distributed in graphenic dopants and bonded to heteroatoms. In this regard, it has been established that the presence of 5 vol% H_2 in the flow during pyrolysis decreases the percentage of N, with respect to samples prepared following the same procedure in Ar flow that contains a N proportion of about 5% [37]. Similarly, it has

been found that H_2 at temperatures of about 300 °C removes dopant elements from graphene, this being one reason for doped graphene instability as a hydrogenation catalyst [40]. In the case of N-doped defective graphene, evolution of NH_3 was confirmed [40]. These data indicate that the B and N dopant atoms that otherwise become incorporated into the graphene basal plane are partially removed during the pyrolysis by its reaction with H_2 and subsequent evacuation in the effluent gas flushing the system, generating atom vacancies in the graphene sheet.

Figure 3.1 shows optimized DFT models of single and double atom vacancy on the graphene sheet showing the subnanometric pores generated in the process. Unfortunately, direct imaging at subnanometric resolution of the atom vacancies by high-resolution TEM is not routine due to the lack of graphene stability under high voltage electron beam. In fact, exposure to these high-energy electrons has been proposed as a way to generate nanometric pores on graphene sheet [42]. On the other hand, no evidence of larger pores can be obtained by TEM images in the present work or in the precedents that reported the transformation of polysaccharides into graphene. The importance of doping and H_2 treatment to generate subnanometric pores will be confirmed when commenting on the performance as the desalination membrane of a control membrane prepared similarly but in the absence of H_2.

Raman spectroscopy of the (B,N)G-coated α-Al_2O_3 membrane exhibit the expected G and D bands appearing at about 1590 and 1350 cm^{-1} characteristic of defective graphene, as well as a broad band from 3100 till 2500 cm^{-1}, with maximum about 2700 cm^{-1} corresponding to the 2D peak (Figure 3.6b). The broadness of this band is in agreement with the multilayer arrangement of the (B,N)G film, while the relative intensity of the G vs. the D band of 1.2 is coincident to values reported for defective graphene obtained by pyrolysis of polysaccharides. Overall the Raman spectrum signature confirms the defective graphene nature of the (B,N)G film.

3.4.3 Performance of (B,N)G films on porous α-Al_2O_3 ceramics as a desalination membrane

Preliminary experiments using multilayer N-doped G films on α-Al_2O_3 formed by pyrolysis at 900 °C under Ar (no H_2) of 50 nm CS films on α-Al_2O_3 ceramic showed no water permeation, indicating that this film behaves as a barrier. In contrast, attempts to obtain thinner CS films on α-Al_2O_3 membranes by coating porous α-Al_2O_3 support with CS aqueous solutions of half the concentration indicated in the experimental section (*Section 2.2.1*), resulted in membranes without any permeation efficiency, the reason being the lack of continuity of the resulting (B,N)G film. It was also observed that imperfect coating or damage of the coating also results in (B,N)G films without desalination efficiency. Thus, the presence of H_2 in the pyrolysis to partially remove dopant elements and the use of an optimal CS

concentration as indicated in the experimental section appear to be conditions necessary to achieve the permeation selectivity described below.

Following the preparation procedure indicated in the experimental section, the resulting (B,N)G films were able to achieve selective water transport with high salt rejection. The removal efficiency of NaCl and KCl, permeate flux and pressure effects were determined. The results are summarized in Figure 3.7.

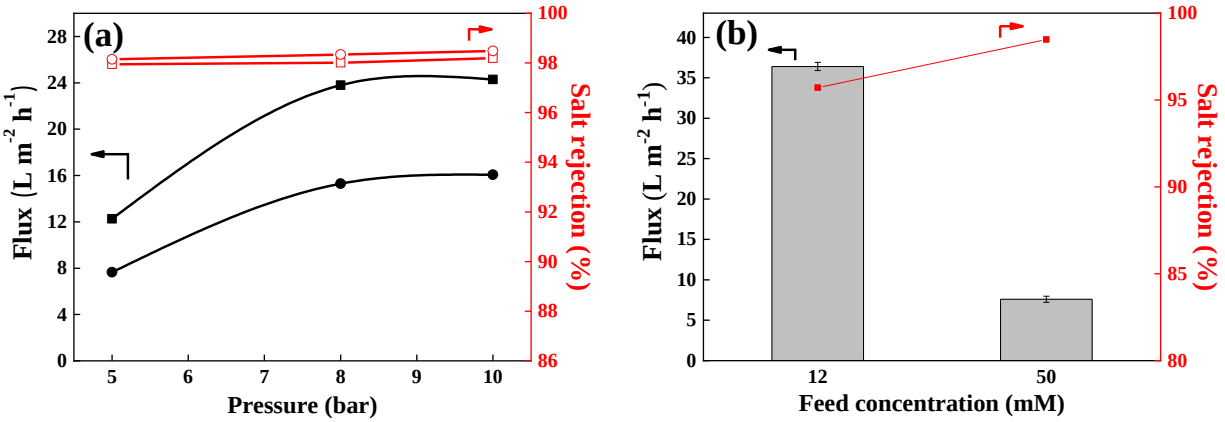

Figure 3.7. (a) Effects of transmembrane pressure on (B,N)G-coated α-Al_2O_3 membrane water flow for NaCl (●) and KCl (■) salts as well as the rejection percentage of NaCl (○) and KCl (□) ([NaCl] = [KCl] = 50 mM); (b) Effects of feed NaCl concentration on the desalination performance of the (B,N)G-coated α-Al_2O_3 membrane (Pressure = 5 bar).

One important parameter to be considered in desalination is the pressure dependency of permeate flux and salt rejection since industrial desalinization is operated at very high pressure to achieve a sufficiently high flux of purified water [43]. In desalination processes, the external pressure must be sufficiently greater than the osmotic pressure to make osmosis happen. Usually, the osmotic pressure of seawater is around 23–26 bar with a salt concentration of 32,000 mg L^{-1} [44]. On the other hand, osmotic pressures of brackish water range from 1 to 3 bar, for a concentration of 1,000–5,000 mg L^{-1} [44, 45]. Therefore, to achieve osmosis, feed pressures applied to brackish water may vary from 5 [46] to 55 bar [28]. In the present study, a concentration in the typical range of brackish waters of 50 mM was selected to prove the selectivity in salt removal. This concentration value corresponds to 2,925 and 3,725 mg L^{-1} for NaCl and KCl, respectively.

As the pressure in the membrane reactor increases, the permeate flow in the (B,N)G-coated α-Al_2O_3 membrane increases as expected according to Darcy's law. The permeation values for (B,N)G-coated α-Al_2O_3 membrane were from 12.3 and 7.6 L m^{-2} h^{-1} (5 bar) to 24.3 and 15.1 L m^{-2} h^{-1} (10 bar) for KCl and NaCl, respectively. In this pressure range (5–10 bar), the water flux varies linearly with the pressure. However, this linearity between water flux and pressure could not apply to higher pressures, since these conditions could decrease membrane permeation due to compaction and morphological changes.

The influence of increasing from 8 bar to 10 bar on the permeation flow was insignificant, with an increase of 2.1 and 5.2% for KCl and NaCl, respectively. This can be explained by assuming that once the external pressure exerted on the reactor is sufficiently high to overcome the osmotic pressure, the limiting factor is pore density on the membrane that allows the permeation to happen, approaching a plateau for the water flux with the pressure.

As it can be seen in Figure 3.7, there is a remarkable difference in the water flux as a function of the nature of the alkali metal chloride salt. The maximum difference in the water flux for the two salts can be as high as 66% larger for KCl with respect to NaCl for the 10 bar pressure measurement. The difference in water flux is proposed to be related to the difference in the size of K^+ and Na^+ ions that should be close to the effective pore size of the (B,N)G membrane. In principle, K^+ has a larger ionic radius (1.32 Å) than Na^+ (0.93 Å), because it has a larger number of atomic orbital shells and electrons surrounding the nucleus. However, Na^+ is a larger ion for hydrated ions, since its higher polarization effect determines a stronger attractive force on neighbouring water molecules. As a consequence, Na^+ (3.60 Å) has a larger hydration radius than K^+ (3.30 Å) [47]. Since the radius of hydrated ions is significantly larger than the radius of isolated water molecules passing through the membrane, a selectivity should be expected for pores of adequate dimensions as those predicted by the models in Figure 3.1. The pore sizes of the membrane are very important and critical in this case. Cohen-Tanugi et al. [29] found that a graphene membrane with a radius of 0.3 nm exhibited full salt rejection. Other authors show that most salt ions can pass through pores of a diameter above 0.55 nm [18]. Thus, the available experimental data indicates that in the case of (B,N)G films the pore radius should be around 0.3 nm, in addition to the presence of residual percentage of B, N and O heteroatoms. Under these circumstances, the interaction of hydrated Na^+ with the pore rims can result in partial dynamic clogging of the pores and, therefore, lower fluxes should be observed for Na^+, since the larger radius makes this interaction with the pore entrances much weaker. Thus, the different behaviour of NaCl and KCl constitutes indirect evidence of the effective pore diameter that should be in a narrow window close to the Na^+ ions able to discriminate in such a notable percentage between Na^+ and K^+ sizes.

As can be seen also in Figure 3.7, (B,N)G membrane exhibited high salt rejection efficiency value for both NaCl and KCl around 98.0 and 98.5% for pressures of 5, 8 and 10 bar. Commercial desalination membranes generally exhibit more than 98% NaCl rejection, but there is a relationship between water flow and salt rejection, as GO membranes with higher rejection efficiency must operate at relatively low water flux [14]. Other studies also had high salt rejection rates around 98–99%, but with higher pressures or with permeate flow smaller than the current study [48]. Thus, the (B,N)G-coated α-Al_2O_3 membrane reported here outperforms commercial and most of the previously reported graphene desalination

membranes by achieving high water flux and high salt rejection rate at pressures of 8 bar for 50 mM salt concentration.

To put the results shown in Figure 3.7 into context, Table 3.1 summarizes the performance data from other studies based on the use of graphene and graphene oxide in combination or not with a support. The performance of (B,N)G-coated α-Al_2O_3 membrane showed relatively good performance in terms of water flow as well as excellent salt rejection compared to other filtration membranes. It should be, however, stressed that the previous report on the performance of single-layer graphene refers to a measurement on a membrane of 5 μm diameter that is about 1 billion times smaller area than the one under study here.

Another factor that directly affects the permeate flux is salt concentration. In general, the water permeate flux decreases as the solute concentration increases. The same effect is also observed here for (B,N)G-coated α-Al_2O_3 membrane with a flux for 12 and 50 mM NaCl solutions of 36.4 and 7.6 L m^{-2} h^{-1}, respectively, at 5 bar pressure; the corresponding values for salt rejection were 95.7 and 98.5%, respectively (Figure 3.7b). A change in feed concentration directly affects sorption at the liquid/membrane interface. Therefore, hydrated ion concentration on the membrane near or at the pores increases with feed solution concentration, causing a decrease in the water flow [49]. Observation of the strong influence of NaCl concentration on the permeate flux is again in agreement with the previous justification of the different permeate flux between NaCl and KCl based on the assumption that the effective pore radius size of (B,N)G film should be close to the hydrated radius of the Na^+ ion, about 0.36 nm.

Table 3.1. Overview of reported data on graphene-based water desalination membranes and relevant operation conditions.

Membrane material	Preparation method	Membrane area (cm^2)	Feed concentration	Flux ($L \cdot m^{-2} \cdot h^{-1}$)	Pressure (bar)	Rejection (%)	Ref.
GO-PAN	Hummers method and vacuum filtration of GO particles	14.7	35000 ppm	14.3 - 65.1	10	99.8	[49]
GO-PTFE	CVD graphene on flat substrates and poly (methyl methacrylate) (PMMA)-assisted transfer of graphene was adopted	4	70000 ppm	50	-	99.9	[50]
GO-PA	Hummers method and coating method	9.6	2000 ppm	59.4	20	94	[51]
GO-PSF	Brodie method and layer-by-layer method	12.56	300 ppm	28	55	98	[28]
rGO/TiO_2-PSF	Hummers method and phase inversion method	36	2000 ppm	51.3	15	99.45	[32]
GO-PES	Hummers method and the precursor solution were filtered through the membrane	14.6	2000 ppm	35.6	10	98.5	[46]
GO-PSF	Brodie's method and phase inversion method	19.6	1000 ppm	10	4	40-60	[52]
GO-PVDF	Hummers method and pressure-assisted self-assembly	4.8	2000 ppm	73.2	15	95.6	[33]
(B,N)G	CS film impregnated in the membrane with ammonium borate was pyrolyzed	84	50 mM (± 3725 ppm)	24.3	10	98.5	This work

Note: GO – graphene oxide; PAN – polyacrylonitrile; PTFE – polytetrafluoroethylene; PA – Polyamide; PSF – polysulfone; PES - poly(ether sulfones); PVDF – polyvinylidene fluoride; CVD – Chemical vapour deposition; (B,N)G – graphene-boron nitride.

Regarding the filtration mechanism, it is important to rule out that the selectivity of the salt retention is not due to the adsorption of the salt on the graphene. Considering the theoretical graphene density of 2.26 g cm^{-3}, the area (84 cm^2) and the average thickness (11 nm), the graphene mass in the membrane is estimated as 0.2 mg, while the total amount of NaCl flushed through the membrane in 5 h at 10 bar is 18.90 mol, corresponding to 1098.8 g. To further determine the adsorption capacity of (B,N)G for NaCl, 50 mg of (B,N)G (about 250 times higher amount than the amount of (B,N)G on the alumina membrane) was added to 25 mL of a 50 mM aqueous solution of NaCl (same concentration as in the permeation measurements), observing a negligible decrease in NaCl concentration. Figure 3.8 provides the temporal profile of the isothermal NaCl adsorption.

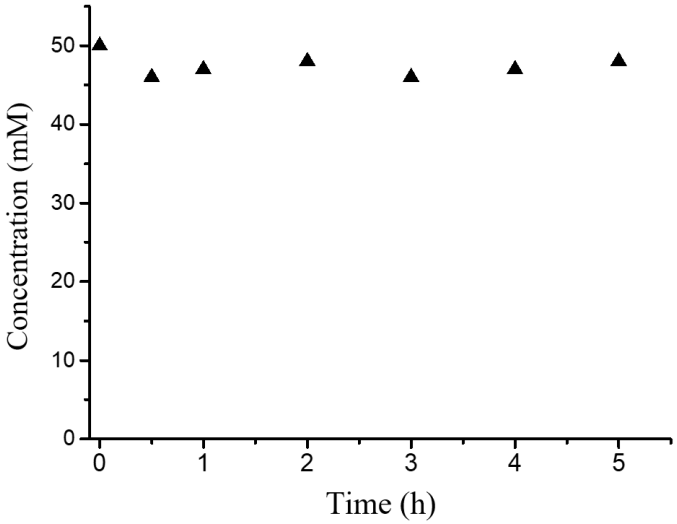

Figure 3.8. NaCl concentration profile over time on (B,N)G film.

3.5 Conclusions

The present study reports a new concept for the preparation of large area desalination membranes based *on site* formation of multilayer defective graphene with subnanometric pores. The process derives from the ability of chitosan to form conformal nanometric films that can be subsequently transformed into multilayer doped defective graphene. The pyrolysis conditions can be adapted to form atom vacancies on the graphene sample. The (B,N)G membrane exhibits a remarkable permeation selectivity. Thus, the present report may constitute a significant advance in desalination technology providing a suitable preparation procedure not only on flat but also on curved supports. It can also be anticipated that the procedure can be easily adapted to obtain analogous membranes based on defective graphene with controlled pore sizes for different applications.

3.6 References

[1] P.H. Gleick, Global freshwater resources: soft-path solutions for the 21st century, Science 302 (5650) (2003) 1524-1528. https://doi.org/10.1126/science.1089967.

[2] P.H. Gleick, The human right to water, Water Policy 1 (5) (1998) 487-503.

[3] J.R. Werber, C.O. Osuji, M. Elimelech, Materials for next-generation desalination and water purification membranes, Nature Reviews Materials 1 (2016) 1-15. https://doi.org/10.1038/natrevmats.2016.18.

[4] K. Celebi, J. Buchheim, R.M. Wyss, A. Droudian, P. Gasser, I. Shorubalko, J.-I. Kye, C. Lee, H.G. Park, Ultimate Permeation Across Atomically Thin Porous Graphene, Science 344 (6181) (2014) 289-292. https://doi.org/10.1126/science.1249097.

[5] G. He, S. Huang, L.F. Villalobos, J. Zhao, M. Mensi, E. Oveisi, M. Rezaei, K.V. Agrawal, High-permeance polymer-functionalized single-layer graphene membranes that surpass the postcombustion carbon capture target, Energy & Environmental Science 12 (11) (2019) 3305-3312. https://doi.org/10.1039/C9EE01238A.

[6] A.K. Geim, K.S. Novoselov, The rise of graphene, Nanoscience and technology: a collection of reviews from nature journals, 6 (3) (2007) 183–191.

[7] J.S. Bunch, S.S. Verbridge, J.S. Alden, A.M. Van Der Zande, J.M. Parpia, H.G. Craighead, P.L. McEuen, Impermeable atomic membranes from graphene sheets, Nano Letters 8 (8) (2008) 2458-2462. https://doi.org/10.1021/nl801457b.

[8] F. Guo, G. Silverberg, S. Bowers, S.-P. Kim, D. Datta, V. Shenoy, R.H. Hurt, Graphene-based environmental barriers, Environmental Science & Technology 46 (14) (2012) 7717-7724. https://doi.org/10.1021/es301377y.

[9] M.-S. Cao, X.-X. Wang, W.-Q. Cao, J. Yuan, Ultrathin graphene: electrical properties and highly efficient electromagnetic interference shielding, Journal of Materials Chemistry C 3 (26) (2015) 6589-6599. https://doi.org/10.1039/C5TC01354B.

[10] V. Berry, Impermeability of graphene and its applications, Carbon 62 (2013) 1-10. https://doi.org/10.1016/j.carbon.2013.05.052.

[11] P.Z. Sun, Q. Yang, W.J. Kuang, Y.V. Stebunov, W.Q. Xiong, J. Yu, R.R. Nair, M.I. Katsnelson, S.J. Yuan, I.V. Grigorieva, M. Lozada-Hidalgo, F.C. Wang, A.K. Geim, Limits on gas impermeability of graphene, Nature 579 (7798) (2020) 229-232. https://doi.org/10.1038/s41586-020-2070-x.

[12] X. Wang, X. Ba, N. Cui, Z. Ma, L. Wang, Z. Wang, X. Gao, Preparation, characterisation, and desalination performance study of cellulose acetate membranes with MIL-53(Fe) additive, Journal of Membrane Science 590 (2019) 1-9. https://doi.org/10.1016/j.memsci.2019.04.061.

[13] K.A. Mahmoud, B. Mansoor, A. Mansour, M. Khraisheh, Functional graphene nanosheets: The next generation membranes for water desalination, Desalination 356 (2015) 208-225. https://doi.org/10.1016/j.desal.2014.10.022.

[14] S.P. Surwade, S.N. Smirnov, I.V. Vlassiouk, R.R. Unocic, G.M. Veith, S. Dai, S.M. Mahurin, Water desalination using nanoporous single-layer graphene, Nature Nanotechnology 10 (5) (2015) 459-464. https://doi.org/10.1038/nnano.2015.37.

[15] D. Cohen-Tanugi, J.C. Grossman, Mechanical strength of nanoporous graphene as a desalination membrane, Nano Letters 14 (11) (2014) 6171-6178. https://doi.org/10.1021/nl502399y.

[16] E.N. Wang, R. Karnik, Water desalination: Graphene cleans up water, Nature Nanotechnology 7 (9) (2012) 552-554. https://www.nature.com/articles/am2017135.

[17] H.W. Yoon, Y.H. Cho, H.B. Park, Graphene-based membranes: status and prospects, Philosophical Transactions of the Royal Society A 374 (2060) (2016) 1-23. https://doi.org/10.1098/rsta.2015.0024.

[18] J. Zhao, G. He, S. Huang, L.F. Villalobos, M. Dakhchoune, H. Bassas, K.V. Agrawal, Etching gas-sieving nanopores in single-layer graphene with an angstrom precision for high-performance gas mixture separation, Science Advances 5 (1) (2019) eaav1851. https://doi.org/10.1126/sciadv.aav1851.

[19] M.E. Ali, L. Wang, X. Wang, X. Feng, Thin film composite membranes embedded with graphene oxide for water desalination, Desalination 386 (2016) 67-76. https://doi.org/10.1016/j.desal.2016.02.034.

[20] S.C. O'Hern, M.S.H. Boutilier, J.-C. Idrobo, Y. Song, J. Kong, T. Laoui, M. Atieh, R. Karnik, Selective Ionic Transport through Tunable Subnanometer Pores in Single-Layer Graphene Membranes, Nano Letters 14 (3) (2014) 1234-1241. https://doi.org/10.1021/nl404118f.

[21] P.R. Kidambi, D. Jang, J.-C. Idrobo, M.S.H. Boutilier, L. Wang, J. Kong, R. Karnik, Nanoporous Atomically Thin Graphene Membranes for Desalting and Dialysis Applications, Advanced Materials 29 (33) (2017) 1700277. https://doi.org/10.1002/adma.201700277.

[22] F.M. Kafiah, Z. Khan, A. Ibrahim, R. Karnik, M. Atieh, T. Laoui, Monolayer graphene transfer onto polypropylene and polyvinylidenedifluoride microfiltration membranes for water desalination, Desalination 388 (2016) 29-37. https://doi.org/10.1016/j.desal.2016.02.027.

[23] J. Abraham, K.S. Vasu, C.D. Williams, K. Gopinadhan, Y. Su, C.T. Cherian, J. Dix, E. Prestat, S.J. Haigh, I.V. Grigorieva, P. Carbone, A.K. Geim, R.R. Nair, Tunable sieving of ions using graphene oxide membranes, Nature Nanotechnology 12 (2017) 1-6. http://dx.doi.org/10.1038/nnano.2017.21.

[24] R. Mukherjee, P. Bhunia, S. De, Nanofiltration range desalination by high flux graphene oxide impregnated ultrafiltration hollow fiber mixed matrix membrane, Journal of Cleaner Production 213 (2019) 393-405. https://doi.org/10.1016/j.jclepro.2018.12.162.

[25] J. Azamat, A. Khataee, Molecular dynamics simulations of removal of cyanide from aqueous solution using boron nitride nanotubes, Computational Materials Science 128 (2017) 8-14. https://doi.org/10.1016/j.commatsci.2016.10.040.

[26] J. Azamat, A. Khataee, Removal of nitrate ion from water using boron nitride nanotubes: Insights from molecular dynamics simulations, Computational and Theoretical Chemistry 1098 (2016) 56-62. https://doi.org/10.1016/j.comptc.2016.11.002.

[27] L. Zhang, L. Jia, J. Zhang, J. Li, L. Liang, Z. Kong, J.-W. Shen, X. Wang, W. Zhang, H. Wang, Understanding the effect of chemical modification on water desalination in boron nitride nanotubes via molecular dynamics simulation, Desalination 464 (2019) 84-93. https://doi.org/10.1016/j.desal.2019.03.014.

[28] S.G. Kim, D.H. Hyeon, J.H. Chun, B.-H. Chun, S.H. Kim, Novel thin nanocomposite RO membranes for chlorine resistance, Desalination and Water Treatment 51 (31-33) (2013) 6338-6345. https://doi.org/10.1080/19443994.2013.780994.

[29] D. Cohen-Tanugi, L.-C. Lin, J.C. Grossman, Multilayer Nanoporous Graphene Membranes for Water Desalination, Nano Letters 16 (2) (2016) 1027-1033. https://doi.org/10.1021/acs.nanolett.5b04089.

[30] A. Boretti, S. Al-Zubaidy, M. Vaclavikova, M. Al-Abri, S. Castelletto, S. Mikhalovsky, Outlook for graphene-based desalination membranes, npj Clean Water 1 (1) (2018) 1-11. https://doi.org/10.1038/s41545-018-0004-z.

[31] H.-H. Huang, R.K. Joshi, K.K.H. De Silva, R. Badam, M. Yoshimura, Fabrication of reduced graphene oxide membranes for water desalination, Journal of Membrane Science 572 (2019) 12-19. https://doi.org/10.1016/j.memsci.2018.10.085.

[32] M. Safarpour, A. Khataee, V. Vatanpour, Thin film nanocomposite reverse osmosis membrane modified by reduced graphene oxide/TiO_2 with improved desalination performance, Journal of Membrane Science 489 (2015) 43-54. https://doi.org/10.1016/j.memsci.2015.04.010.

[33] H. Khorramdel, E. Dabiri, F.F. Tabrizi, M. Galehdari, Synthesis and characterization of graphene acid membrane with ultrafast and selective water transport channels, Separation and Purification Technology 212 (2019) 497-504. https://doi.org/10.1016/j.seppur.2018.11.044.

[34] D. Elieh-Ali-Komi, M.R. Hamblin, Chitin and chitosan: production and application of versatile biomedical nanomaterials, International Journal of Advanced Research 4 (3) (2016) 411-427. https://pubmed.ncbi.nlm.nih.gov/27819009/.

[35] A. Dhakshinamoorthy, A. Primo, P. Concepcion, M. Alvaro, H. Garcia, Doped graphene as a metal-free carbocatalyst for the selective aerobic oxidation of benzylic hydrocarbons, cyclooctane and styrene, Chemistry-A European Journal 19 (23) (2013) 7547-7554. https://doi.org/10.1002/chem.201300653.

[36] J. Niu, A. Domenech-Carbó, A. Primo, H. Garcia, Uniform nanoporous graphene sponge from natural polysaccharides as a metal-free electrocatalyst for hydrogen generation, RSC Advances 9 (1) (2019) 99-106. https://doi.org/10.1039/C8RA08745H.

[37] J. He, A. Anouar, A. Primo, H. García, Quality Improvement of Few-Layers Defective Graphene from Biomass and Application for H_2 Generation, Nanomaterials 9 (6) (2019) 1-15. https://doi.org/10.3390/nano9060895.

[38] A. Primo, P. Atienzar, E. Sanchez, J.M. Delgado, H. García, From biomass wastes to large-area, high-quality, N-doped graphene: catalyst-free carbonization of chitosan coatings on arbitrary substrates, Chemical Communications 48 (74) (2012) 9254-9256. https://doi.org/10.1039/C2CC34978G.

[39] J.C. Espinosa, S. Navalón, A. Primo, M. Moral, J.F. Sanz, M. Álvaro, H. García, Graphenes as Efficient Metal-Free Fenton Catalysts, Chemistry-A European Journal 21 (34) (2015) 11966-11971. https://doi.org/10.1002/chem.201501533.

[40] A. Primo, F. Neatu, M. Florea, V. Parvulescu, H. Garcia, Graphenes in the absence of metals as carbocatalysts for selective acetylene hydrogenation and alkene hydrogenation, Nature Communications 5 (2014) 1-9. https://doi.org/10.1038/ncomms6291.

[41] P. Solís-Fernández, J.I. Paredes, S. Villar-Rodil, A. Martínez-Alonso, J.M.D. Tascón, Determining the thickness of chemically modified graphenes by scanning probe microscopy, Carbon 48 (9) (2010) 2657-2660. https://doi.org/10.1016/j.carbon.2010.03.033.

[42] H.W. Yoon, Y.H. Cho, H.B. Park, Graphene-based membranes: status and prospects, Philosophical Transactions of the Royal Society A: Mathematical, Physical and Engineering Sciences 374 (2060) (2016) 20150024. https://doi.org/10.1098/rsta.2015.0024.

[43] K.P. Lee, T.C. Arnot, D. Mattia, A review of reverse osmosis membrane materials for desalination—Development to date and future potential, Journal of Membrane Science 370 (1) (2011) 1-22. https://doi.org/10.1016/j.memsci.2010.12.036.

[44] A. Sagle, B. Freeman, Fundamentals of Membranes for Water Treatment in: J.A. Arroyo (Ed.), The Future of Desalination in Texas, Texas Water Development Board, Austin, TX, 2004.

[45] C. Fritzmann, J. Löwenberg, T. Wintgens, T. Melin, State-of-the-art of reverse osmosis desalination, Desalination 216 (1) (2007) 1-76. https://doi.org/10.1016/j.desal.2006.12.009.

[46] S. Kim, R. Ou, Y. Hu, X. Li, H. Zhang, G.P. Simon, H. Wang, Non-swelling graphene oxide-polymer nanocomposite membrane for reverse osmosis desalination, Journal of Membrane Science 562 (2018) 47-55. https://doi.org/10.1016/j.memsci.2018.05.029.

[47] L.B. Railsback, Some Fundamentals of Mineralogy and Geochemistry, Department of Geology, University of Georgia, Athens, Georgia, 2006.

[48] M. Akhavan, J. Schofield, S. Jalili, Water transport and desalination through double-layer graphyne membranes, Physical Chemistry Chemical Physics 20 (19) (2018) 13607-13615. http://dx.doi.org/10.1039/C8CP02076K.

[49] B. Liang, W. Zhan, G. Qi, S. Lin, Q. Nan, Y. Liu, B. Cao, K. Pan, High performance graphene oxide/polyacrylonitrile composite pervaporation membranes for desalination applications, Journal of Materials Chemistry A 3 (9) (2015) 5140-5147. https://doi.org/10.1039/C4TA06573E.

[50] D.H. Seo, S. Pineda, Y.C. Woo, M. Xie, A.T. Murdock, E.Y.M. Ang, Y. Jiao, M.J. Park, S.I. Lim, M. Lawn, F.F. Borghi, Z.J. Han, S. Gray, G. Millar, A. Du, H.K. Shon, T.Y. Ng, K. Ostrikov, Anti-fouling graphene-based membranes for effective water desalination, Nature Communications 9 (1) (2018) 683. https://doi.org/10.1038/s41467-018-02871-3.

[51] J. Yin, G. Zhu, B. Deng, Graphene oxide (GO) enhanced polyamide (PA) thin-film nanocomposite (TFN) membrane for water purification, Desalination 379 (2016) 93-101. https://doi.org/10.1016/j.desal.2015.11.001.

[52] B.M. Ganesh, A.M. Isloor, A.F. Ismail, Enhanced hydrophilicity and salt rejection study of graphene oxide-polysulfone mixed matrix membrane, Desalination 313 (2013) 199-207. https://doi.org/10.1016/j.desal.2012.11.037.

4 A Novel Ceramic Tubular Membrane Coated with a Continuous Graphene-TiO_2 Nanocomposite Thin-film for CECs Mitigation

This chapter reports a ceramic tubular membrane coated with a continuous graphene-TiO_2 nanocomposite thin-film for CECs removal from UPW and real matrix in single-pass flow-through operation. Microfiltration ceramic membranes were coated in situ with graphene (G)-TiO_2-P25 nano-composite using two different methods: Membrane A (MA) - TiO_2-P25 incorporated in the G preparation stage (1% [MA-1], 2% [MA-2] and 3% [MA-3] [w/v]), and Membrane B (MB) - TiO_2-P25 thin-film uniformly coated over the G film surface (coating layers: 3 [MB-1], 6 [MB-2], and 9 [MB-3]). After the catalyst deposition and before the pyrolysis step, air was forced to pass through the membranes pores (inside-outside mode), providing a porous film. The CECs solution (diclofenac-DCF, 17β-estradiol-E2, 17α-ethinylestradiol-EE2 and amoxicillin-AMX) was prepared using UPW or UWW fortified with 500 µg L^{-1} of each CEC. Membranes were characterized by the following techniques: Scanning Electron Microscopy (SEM), Atomic Force Microscopy (AFM), Fourier-Transform Infrared spectroscopy (FTIR), Diffuse Reflectance UV-Visible spectroscopy (DR UV-Vis) and Raman spectroscopy. The membranes coated with MA-3 and MB-2 catalyst films, irradiated by UVA light, showed the highest ability for CECs removal. Furthermore, the relative flux reduction ratio (RFR) decreased by around 45% in the absence of UVA light, owing to membrane fouling. The combination of filtration and oxidation (G-TiO_2-UVA) provided a permeate with higher quality and minimized membrane fouling. Although MB allowed for a permeate with higher quality, MA provided a higher permeate flux.

This chapter is based on the following research article: "Presumido, P.H., Santos, L.F. dos, Neuparth, T., Santos, M.M., Feliciano, M., Primo, A., Garcia, H., Đolić, M.B., Vilar, V.J.P. *A Novel ceramic tubular membrane coated with a continuous graphene-TiO_2 nanocomposite thin-film for CECs mitigation*, Chemical Engineering Journal, 430 (2022) 132639. DOI: 10.1016/j.cej.2021.132639".

4.1 Objectives

Graphene (G)-TiO_2 composites have been prepared through various techniques using more than one stage without achieving a continuous G layer in membrane supports [1-3]. Moreover, most of them have several limitations, either in the membrane area or in the need to prepare highly expensive chemical vapor deposition (CVD) graphene and subsequent transfer graphene to the membrane surface [4]. Therefore, the method of preparing graphene-based membranes is the key to the large-scale fabrication of nanosheet membranes on tubular substrates for industrial applications.

The main objective of this chapter is the preparation of a ceramic tubular membrane coated with a continuous G-TiO_2 nanocomposite thin-film for CECs removal from UPW and real matrix in single-pass flow-through operation. The functionalization of the MF membranes was optimized using two different methods to verify which is the best option regarding the quality and quantity of the permeate: membrane A (MA) - TiO_2-P25 incorporated in the preparation stage of graphene-G, and membrane B (MB) - TiO_2-P25 deposited over the G layer. The photocatalytic membranes were assembled in a photocatalytic membrane reactor, having an outer borosilicate tube as the reactor window, and UVA lamps located around the window, and further tested for the removal of a mixture of four CECs (diclofenac-DCF, 17β-estradiol-E2, 17α-ethinylestradiol-EE2 and amoxicillin-AMX) using UPW or UWW after secondary treatment from UWWTPs, as reaction matrices.

4.2 Materials and methods

All the chemicals used in this work, modelling of degradation kinetics, permeation tests, experimental units and procedures, as well as the employed analytical determinations are described in *Chapter 2*. The fabrication of continuous G-TiO_2 thin-films on α-Al_2O_3 membrane shell-side is described in detail in *Section 2.2.2*. All the experimental data presented in this chapter was obtained using the membrane reactor, which is detailed described in *Section 2.3.1.2*, and will be designated as photocatalytic membrane reactor or PMR during this entire chapter. Before submitting to treatment, the UPW and the secondary UWW were fortified with 500 μg L^{-1} of each CEC (DCF, E2, EE2 and AMX).

4.3 Results and discussion

The best G-TiO_2 functionalized membranes towards CECs rejection and permeate quantity were MA-3 (membrane A) and MB-2 (membrane B) (see *Section 4.3.2.2*). Therefore, the discussion on membrane

characteristics and results is based on these two samples and compared to their respective controls - in the absence of light (MA-3_{UVAoff} and MB-2_{UVAoff}).

4.3.1 Characterisation of the catalyst film immobilized on the porous membrane

The G-TiO_2 nanocomposite films were obtained through a facile and single-step method in which CS was used as a precursor to G production. The surface of the ceramic membrane modified with G-TiO_2 was wholly covered by a continuous film without the apparent presence of pinholes or cracks (Figure 4.1). The preparation method for MA-3 resulted in a continuous film of G interspersed with aggregates of TiO_2, creating a discontinuity in the G layer, which allows more defects in the catalyst film (Figure 4.1a). The image also shows that TiO_2 was bound together with G at the time of its formation by pyrolysis in an oxygen-free atmosphere. On the other hand, Figure 4.1d (MB-2) shows a continuous G layer covered by TiO_2 nanoparticles. The surface morphology itself presented a slight agglomeration caused by the deposition of the photocatalyst over the G layer (Figure 4.1d). Figure 4.1a shows debris scratched from the G membrane to visually show a comparison between two different zones of the MA-3 film. From the analysis of EDS (Figure 4.1b and Figure 4.1e), the two different zones of the manufactured membranes indicate the presence of carbon, titanium and alumina, describing the materials of the G film, TiO_2 film and the ceramic membrane (α-Al_2O_3), respectively. The EDS results show the presence of carbon on the entire surface of the MA-3, even when zone Z2 is analysed, which shows strong signs of the presence of both titanium and carbon. This indicates that G and TiO_2 are incorporated into each other. In contrast, for the manufacturing method of MB-2, the G film was coated with a TiO_2 layer. In zone Z2, where titanium is the predominant element, the TiO_2 film covers the G signal (Figure 4.1e).

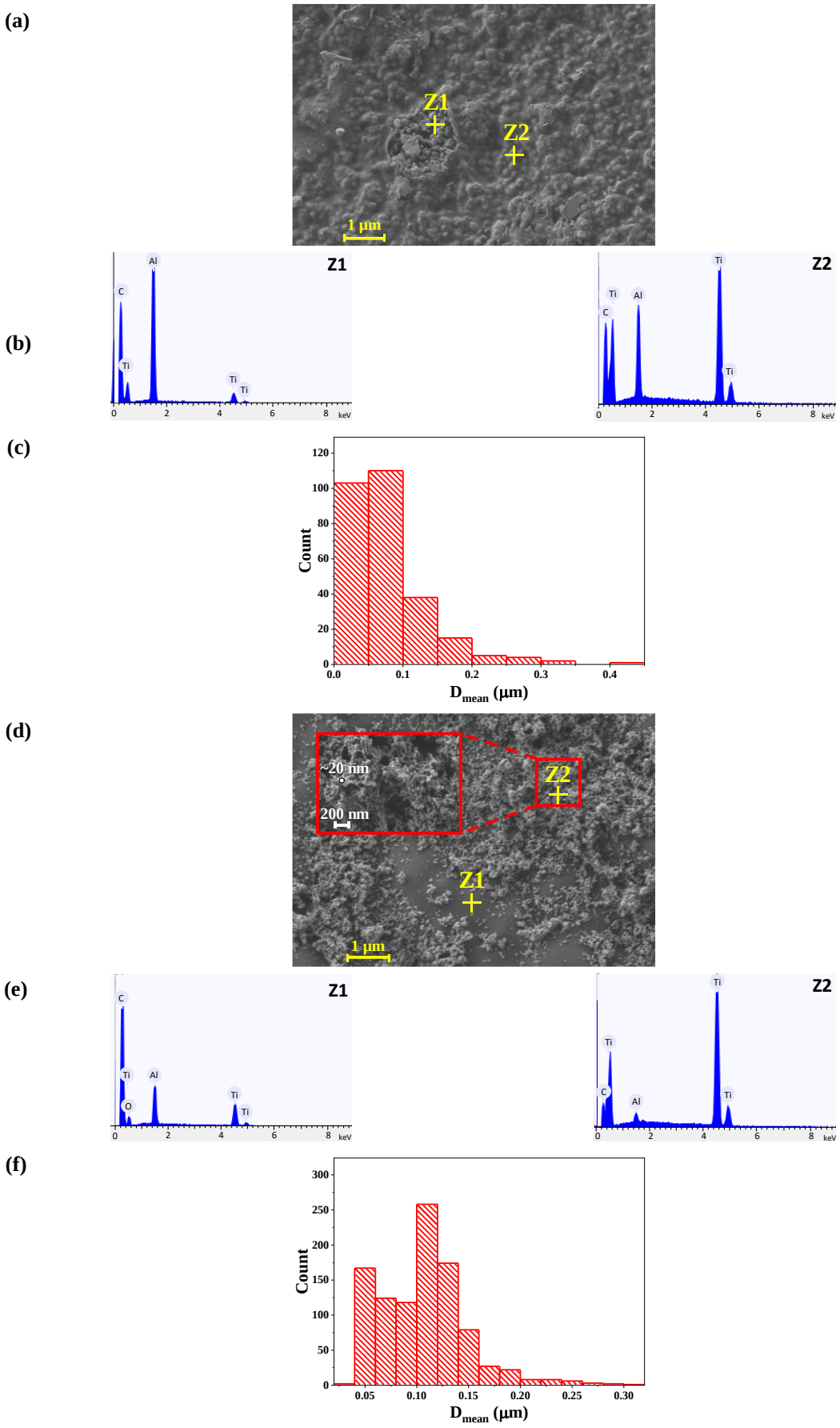

Figure 4.1. SEM images of the top surface of the MA-3 (a) and MB-2 (d) modified membranes with the expected EDS spectra (b, e) and surface pore size distribution (c, f).

Hence, SEM analysis provides strong evidence that the G-TiO_2 was successfully prepared, in which the TiO_2 was bonded together with G film or coated over the G layer. This structure is beneficial for membrane fabrication as G can enhance the connection with TiO_2 and improve the strength of the membrane to be used as a barrier for the retention of CECs. In addition, the contact between G film and TiO_2 nanoparticles minimizes charge recombination, enhancing photocatalytic activity (see *Section 4.3.2.1*).

The comparison of the surface porosity and pore size distribution between the TiO_2-functionalized G samples (Figure 4.1c and Figure 4.1f) are set up to the following values: 1) the sample MA-3 showed a mean pore size of 67.3 nm with an average film porosity of 13.3%; and 2) the sample MB-2 presents a mean pore size of 48.4 nm with an average film porosity of 12.1%. Although the sample MB-2 presents a narrow pore size distribution than MA-3, both are classified as UF membranes. In general, several ranges of G-TiO_2 micropores have been measured in the sample MB-2, making the catalyst surface more accessible/available for the solid–liquid interactions (i.e., the tendency of higher membrane fouling). The accumulation of the nanoparticles over the G film increases the surface roughness of MB and subsequently reduces membrane fouling resistance.

The surface profile at the nanometer scale was effectively presented by the AFM technique. The top view image displays the selected image from a top-down perspective, where the height information is represented by the colour at a given scale from 0.0 to 1200.0 nm, indicating generally low roughness of the sample MA-3 (Figure 4.2a) and sample MB-2 (Figure 4.2c). Surface plot image displays the selected image with colour-coded height information in a three-dimensional perspective (Figure 4.2b and Figure 4.2d). The roughness surface morphology (*RSM*) for the sample MA-3 has shown higher homogeneity of the surface, with similar *RSM* values for the sections of 5 µm × 5 µm × 800 nm ($RSM_{1\_5\mu m}$ = 52.9 nm, Figure 4.2b) and 10 µm × 10 µm × 1500 nm ($RSM_{1\_10\mu m}$ = 75.39 nm – data not showed). The sample MB-2 has shown slightly higher roughness ($RSM_{2\_5\mu m}$ = 56.38 nm, Figure 4.2d and $RSM_{2\_5\mu m}$ = 82.21 nm – data not shown). Additionally, the analytical AFM performance for the sample MB-2 was much more time/accuracy demanding, also indicating the higher roughness of the membrane surface.

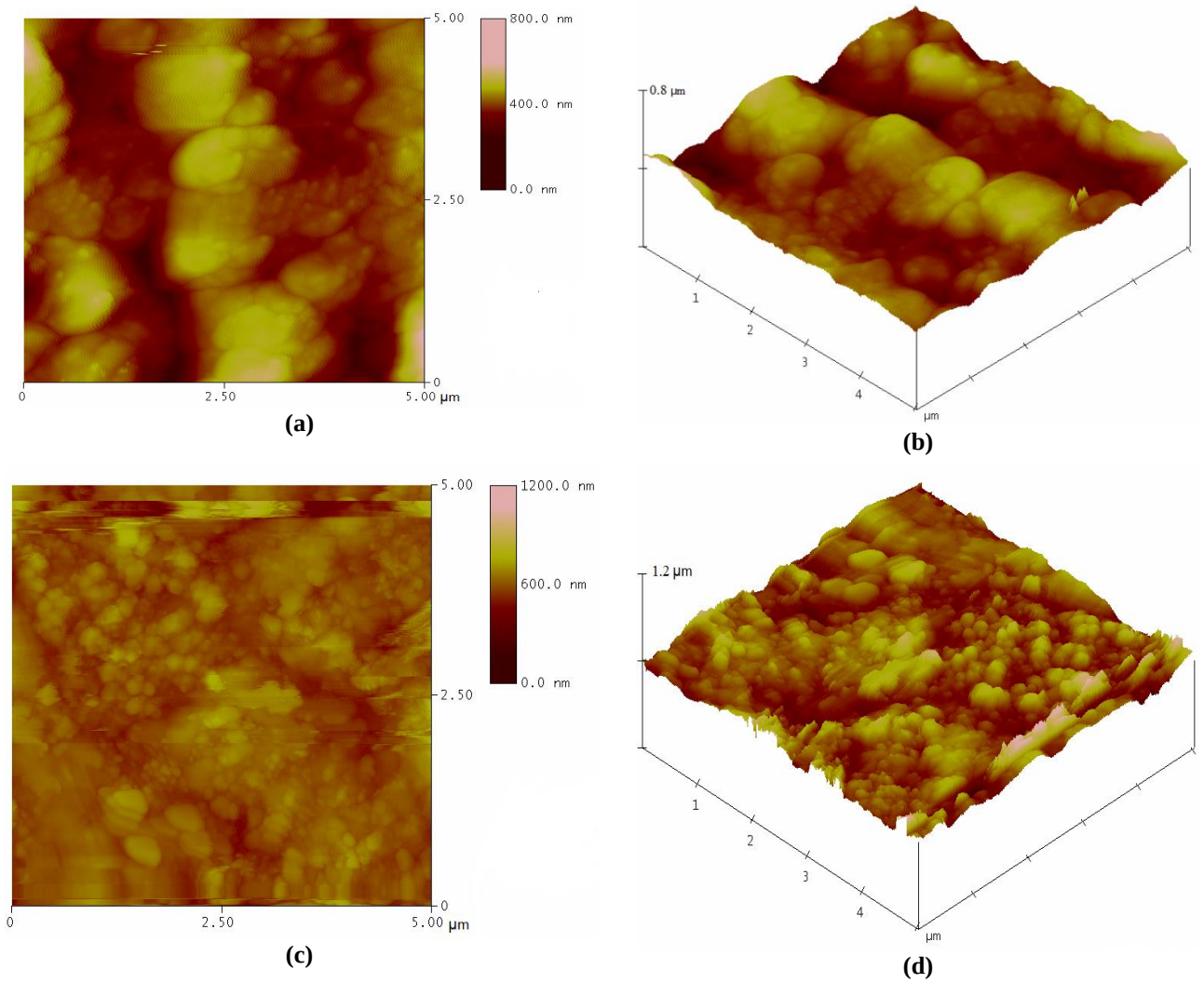

Figure 4.2. Tapping mode AFM image of the sample MA-3: section 5 µm × 5 µm × 800 nm - top view image (a) and surface plot image (b); and the sample MB-2: section: 5 µm × 5 µm × 1200 nm - top view image (c) and surface plot image (d).

Similar values of surface porosity and roughness of the tested materials (MA-3 and MB-2) are directly reflected in their analytical performances – both membranes resulted in a stable structure with enhanced photocatalytic activity (*Section 4.3.2*). The major difference in membranes' fabrication procedures is further demonstrated by the higher accessibility/availability of the TiO_2 active sites – manifesting the higher CECs abatement of the MB-2 sample (with TiO_2 thin-film layer).

The FTIR spectra of G and G-TiO_2-functionalized samples (Figure 4.3a) show the corresponding peaks at 1055 cm^{-1} (C-O), 1067 cm^{-1}(C-O), 1085 cm^{-1} (C-O), 1137 cm^{-1} (C-OH), 1207 cm^{-1} (C-OH), 1236 cm^{-1} (C-OH) and 1597 cm^{-1} (C = C) [5-7]. The surface oxygen-containing functional groups render the possibility of covalent linkage of TiO_2 onto the G surface [8]. The intensities of those peaks are low for the MA-3 sample due to the influence of TiO_2 incorporated into CS before pyrolysis and, therefore, less exposure of the photocatalyst on the membrane surface. The peak at 3390 cm^{-1} originates from the hydroxyl group of water [5], which also demonstrates the hydrophilic surface of the MB-2 sample [9].

The bands at 2961, 2926 and 2854 cm^{-1} correspond to the C–H stretch vibrations of the methylene group [10]. The slight difference detected in the peak position for the tested samples is due to the difference in the degree of hydrogen bonding and other interactions [11]. The low peak of the lattice vibration of TiO_2 (Ti-O-Ti stretching) has been recorded in the wavelength of 703 cm^{-1} [6] and 1400 cm^{-1} [5] for the MB-2 sample. Moreover, Ti-O-C bond has been detected at a wavelength of 1096 cm^{-1} (MA-3) and 1085 cm^{-1} (MB-2) demonstrating an interaction between TiO_2 and G [7]; the Ti-element was dominantly present on the MB-2 surface of the membrane (previously confirmed by the EDS technique).

The UV-Vis absorption spectra were measured in the diffuse reflection mode to access the optical absorption of composite material (Figure 4.3b). An enhanced absorption capacity of the G-TiO_2 composites in the range of 200–700 nm is shown, and the absorption region is extended to the near-infrared region. The enhanced absorption of the G-TiO_2 composites is attributed to the presence of the Ti–C and Ti–O–C bonds. The characteristic absorption band of the graphene centred at 264 nm is attributed to the $\pi \rightarrow \pi^*$ transition of aromatic C–C bonds [12]. The shoulder present in the G-TiO_2-functionalized samples at 298 nm corresponds to the $n \rightarrow \pi^*$ transition of C–O bonds. The adsorption peak at 315 nm and 385 nm indicates the formation of continuous G-TiO_2 nanofilm [9, 13]. It was observed that the peak position for the G-TiO_2-functionalized composites at 315 nm slightly shifted to 318 nm compared to the G. This redshift (of 3 nm) results from charge-transfer interactions between G and TiO_2, which is also confirmed by enhancing the Raman signal [14]. The bandgap energies, Eg (eV) of the MA-3 and MB-2 samples obtained from the Tauc Plot method [15], are 2.36 and 2.65 eV, respectively, much lower than that of the pure TiO_2 – 3.36 eV (mostly in the range of 3.1–3.4 eV) [16]. After the interaction of G with TiO_2, the Eg is narrowed, and the light absorption range of TiO_2 can be extended into the visible region. The unique structure of the MA-3 facilitates the electron transfer due to the less exposed TiO_2 particles (i.e., graphene is providing the space separation of photoelectron and hole pairs in rapid electron transfer units), leading to the inhibition of the recombination of the e^-–h^+ pairs [9, 17].

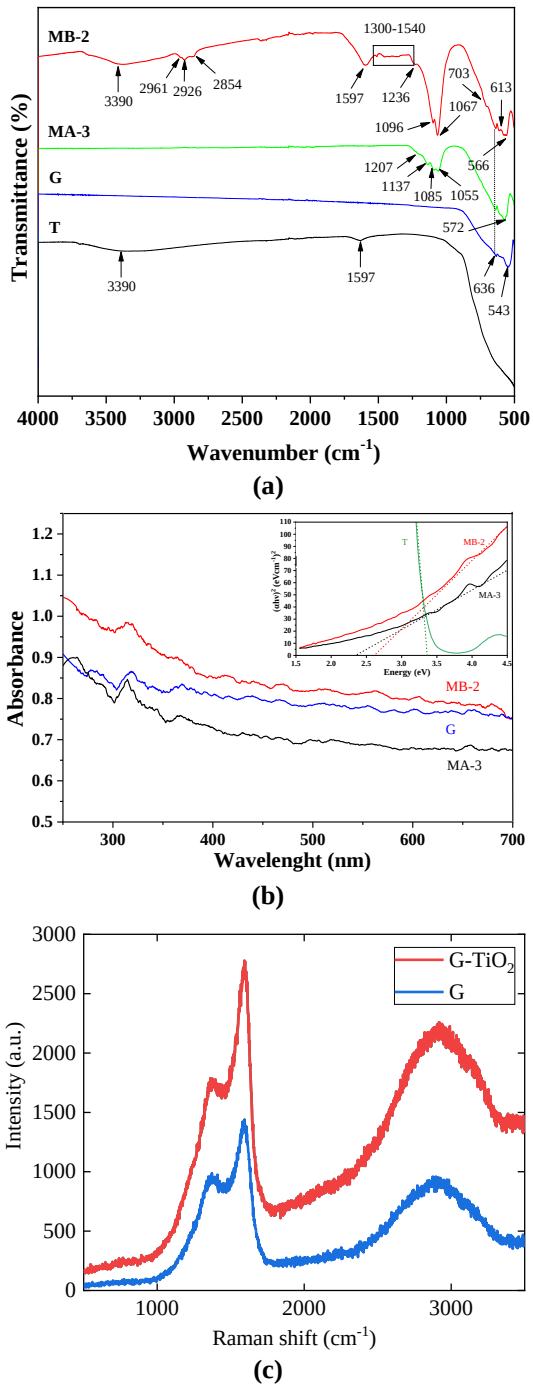

Figure 4.3. (a) The FTIR spectra of graphene (G), TiO_2-P25 (T) and G-TiO_2-functionalized samples (MA-3 and MB-2); (b) The UV-Vis spectra of graphene (G) and G-TiO_2-functionalized samples (MA-3 and MB-2); the inset of panel (b) shows the bandgap energies of graphene (G), TiO_2-P25 (T) and G-TiO_2-functionalized samples (MA-3 and MB-2) (Tauc Plot method); (c) The Raman spectra of graphene and G-TiO_2-functionalized sample (MA-3).

Raman spectroscopy was applied to determine the crystalline quality of the composite with continuous G-TiO_2 film – MA-3 (Figure 4.3c). Two sharp picks have been detected for the G and G-TiO_2-functionalized sample: 1360 cm^{-1} for the D band (disorder carbon) and 1594 cm^{-1} for the G band (graphene carbon) [18]. D-band corresponds to the structural carbon disorders [6], while the G-band can be attributed to the first-order scattering of E_{2g} proton of sp^2 carbon atoms of graphene [19]. The crystal

structure, disorder and defects may be further determined by the relative intensity of D and G peaks. The position of D- and G-band (Figure 4.3c) is the same for both samples, where the higher intensity of peaks implies the density of structural defects in the G-TiO_2 sample (MA-3). The G band in thermally reduced TiO_2-sample slightly shifts to the lower frequencies, showing the broader peaks with higher intensities [10]. The intensity ratio ID/IG of the G sample (0.64) increased for the MA-3 sample (0.69) due to the removal of oxygenated groups after the thermal treatment (reestablishment of conjugated graphene network) [18]. Further analysis showed marginal G-band shift (~ 5 cm^{-1}) to a lower frequency at 1589 cm^{-1} (from 1594 cm^{-1}), which confirms the interaction (charge transfer) between graphene and TiO_2 [5]. The broad 2D peak at 2960 cm^{-1} is typically present in the graphene spectra, indicating the possible formation of the multi-layer structure and the presence of the amorphous carbon phase [9, 19].

The phase structures of the TiO_2-P25 samples after pyrolysis were confirmed by XRD and compared to pure TiO_2-P25, as shown in Figure 4.4. The characteristic diffraction peaks appear at 2θ = 25.3 and 2θ = 27.4 diffraction planes for the anatase and rutile, respectively [20]. The results before and after pyrolysis at 600 °C are similar. Kim et al. [21] reported that the anatase-rutile phase transformation occurred at temperatures above 600 °C. Therefore, the characterisation data indicated that the thermal treatment did not affect the TiO_2 crystallinity.

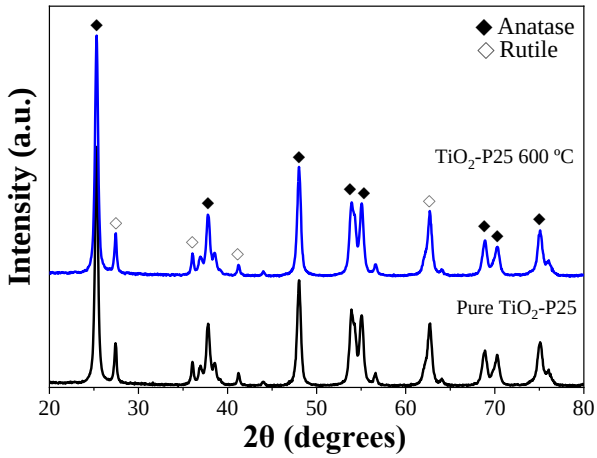

Figure 4.4. XRD patterns of pure TiO_2-P25 before and after pyrolysis at 600 ºC.

4.3.2 Performance of the photocatalytic membranes

4.3.2.1 Batch tests

Preliminary CECs removal experiments using small membrane pieces were carried out in a batch reactor. All these experiments are laid out in Table 4.1. Experiments with a pristine membrane showed negligible CECs removal, indicating insignificant i) photoactivity of the membrane material and ii) photolysis of CECs in the presence of UVA light. Furthermore, the membrane coated with TiO_2 and G-TiO_2 thin-films showed negligible CECs adsorption.

However, the functionalized membranes boosted the CECs removal, where G-TiO_2 thin-films performed better than TiO_2 thin-film, indicating that the incorporation of TiO_2 nanoparticles on G nanosheets can improve the photocatalytic activity of the membrane surface. MB showed better results than MA (a 1.3-fold increase on k_{CEC}, #C11 and #D11) due to the better exposure of the TiO_2 nanoparticles to the UVA light. Although the increment in the amount of photocatalyst deposited on the membrane showed a positive effect on CECs oxidation, the reaction rate will reach a maximum value with further film thickness increase, as it will be discussed in the following sections [22].

Table 4.1. Pseudo-first-order kinetic constants for CEC removal (k_{CEC}) along with the corresponding residual variance (S^2_R) and coefficient of determination (R^2).

#	Fabrication conditions [a]	UVA	CEC	Removal (%)	k_{CEC} (10^{-4} min^{-1})	S^2_R (μg^2 L^{-2})	R^2
A.1	Pristine membrane	Off	DCF	1.4	0.82 ± 0.04	6.0×10^{-8}	0.993
A.2			AMX	1.3	0.63 ± 0.08	3.5×10^{-7}	0.933
A.3			E2	1.0	1.2 ± 0.3	1.3×10^{-7}	0.999
A.4			EE2	0.8	1.5 ± 0.4	4.0×10^{-6}	0.894
A.5	Graphene membrane	Off	DCF	4.4	2.4 ± 0.5	9.4×10^{-6}	0.875
A.6			AMX	4.9	2.9 ± 0.2	1.6×10^{-6}	0.984
A.7			E2	4.2	2.2 ± 0.8	3.2×10^{-5}	0.721
A.8			EE2	1.7	1.2 ± 0.2	2.7×10^{-6}	0.864
A.9	Pristine membrane	On	DCF	5.8	3.5 ± 0.3	5.3×10^{-6}	0.958
A.10			AMX	4.8	2.7 ± 0.3	3.2×10^{-6}	0.974
A.11			E2	1.9	1.0 ± 0.3	7.8×10^{-6}	0.823
A.12			EE2	0.8	0.6 ± 0.1	6.5×10^{-5}	0.748
A.13	Graphene membrane	On	DCF	5.6	3.4 ± 0.3	6.6×10^{-6}	0.948
A.14			AMX	5.2	4.3 ± 0.9	4.9×10^{-5}	0.781
A.15			E2	2.3	4.8 ± 0.3	6.5×10^{-6}	0.839
A.16			EE2	3.1	4.4 ± 0.5	7.4×10^{-6}	0.797
B.1	MT-1[a]	On	DCF	10.6	10.4 ± 0.6	1.8×10^{-5}	0.977
B.2			AMX	15.0	12.3 ± 0.7	2.3×10^{-5}	0.978
B.3			E2	19.1	14.1 ± 1.5	1.2×10^{-4}	0.922
B.4			EE2	17.6	14.9 ± 1.0	5.7×10^{-5}	0.964
B.5	MT-2[a]	On	DCF	23.6	14.6 ± 0.5	1.2×10^{-5}	0.992
B.6			AMX	23.8	14.6 ± 1.3	8.5×10^{-5}	0.939
B.7			E2	27.4	17.9 ± 1.1	7.7×10^{-5}	0.970
B.8			EE2	26.4	15.9 ± 1.0	5.4×10^{-5}	0.970
B.9	MT-3[a]	On	DCF	27.8	19.1 ± 0.5	1.5×10^{-5}	0.995
B.10			AMX	28.8	18.0 ± 1.5	1.3×10^{-4}	0.947
B.11			E2	31.4	19.4 ± 1.0	5.7×10^{-5}	0.980
B.12			EE2	30.0	19.2 ± 1.0	5.0×10^{-5}	0.980

Table 4.1. Pseudo-first-order kinetic constants for CEC removal (k_{CEC}) along with the corresponding residual variance (S^2_R) and coefficient of determination (R^2) (continued).

#	Fabrication conditions [a]	UVA	CEC	Removal (%)	k_{CEC} (10^{-4} min^{-1})	S^2_R (μg^2 L^{-2})	R^2
C.1	MA-1[b]	On	DCF	22.8	14.3 ± 0.7	3.0×10^{-5}	0.982
C.2			AMX	23.7	14.3 ± 0.7	3.2×10^{-5}	0.981
C.3			E2	27.9	18.1 ± 0.8	3.5×10^{-5}	0.987
C.4			EE2	27.3	17.6 ± 0.3	4.0×10^{-6}	0.998
C.5	MA-2[b]	On	DCF	27.6	16.2 ± 3.8	6.5×10^{-4}	0.813
C.6			AMX	29.6	20.0 ± 1.4	9.6×10^{-5}	0.972
C.7			E2	32.9	23.0 ± 1.8	2.5×10^{-4}	0.961
C.8			EE2	31.7	21.9 ± 1.9	2.2×10^{-4}	0.953
C.9	MA-3[b]	On	DCF	30.2	20.0 ± 0.9	5.1×10^{-5}	0.984
C.10			AMX	30.0	18.1 ± 1.8	1.7×10^{-4}	0.932
C.11			E2	34.3	22.5 ± 0.7	3.5×10^{-5}	0.992
C.12			EE2	32.8	20.1 ± 1.1	6.5×10^{-5}	0.977
D.1	MB-1[c]	On	DCF	23.6	14.4 ± 0.7	2.9×10^{-5}	0.985
D.2			AMX	25.0	16.6 ± 0.4	1.0×10^{-5}	0.995
D.3			E2	28.2	17.6 ± 0.7	4.3×10^{-5}	0.987
D.4			EE2	26.3	16.1 ± 1.6	1.4×10^{-4}	0.926
D.5	MB-2[c]	On	DCF	28.8	19.3 ± 0.7	2.9×10^{-5}	0.990
D.6			AMX	31.6	20.1 ± 0.6	8.8×10^{-6}	0.994
D.7			E2	36.3	24.9 ± 1.9	2.0×10^{-4}	0.960
D.8			EE2	37.3	27.6 ± 1.3	8.5×10^{-5}	0.983
D.9	MB-3[c]	On	DCF	32.4	22.2 ± 0.8	3.7×10^{-5}	0.991
D.10			AMX	35.8	24.0 ± 0.5	4.7×10^{-6}	0.997
D.11			E2	42.1	31.6 ± 2.2	2.5×10^{-4}	0.965
D.12			EE2	40.3	28.0 ± 2.0	1.9×10^{-4}	0.961

[a]Membrane with TiO_2: 2 wt.% of TiO_2-P25 powder + two drops of TritonTM X-100 (500 mL) + 3 (MT-1), 6 (MT-2) or 9 (MT-3) coating layers.
[b]Membrane A: CS + 1 (MA-1), 2 (MA-1) or 3% (MA-1) of TiO_2 + pyrolysis.
[c]Membrane B: CS + pyrolysis + 3 (MB-1), 6 (MB-2) or 9 (MB-3) coating layers.

4.3.2.2 PMR tests using synthetic CECs solutions

Prior to CEC oxidation experiments, the hydraulic permeability of each membrane was evaluated by the slope of the straight line obtained by plotting the water flux (J, L m^{-2} h^{-1}) values, measured in fixed conditions of temperature (25 °C), as a function of the transmembrane pressure (TMP =3, 5 and 10 bar), according to Darcy's law (Figure 4.5). The hydraulic permeability computed from the slope flux for MA-3 and MB-2 were 7.8 ± 0.3 L m^{-2} h^{-1} bar^{-1} and 2.6 ± 0.1 L m^{-2} h^{-1} bar^{-1}, respectively.

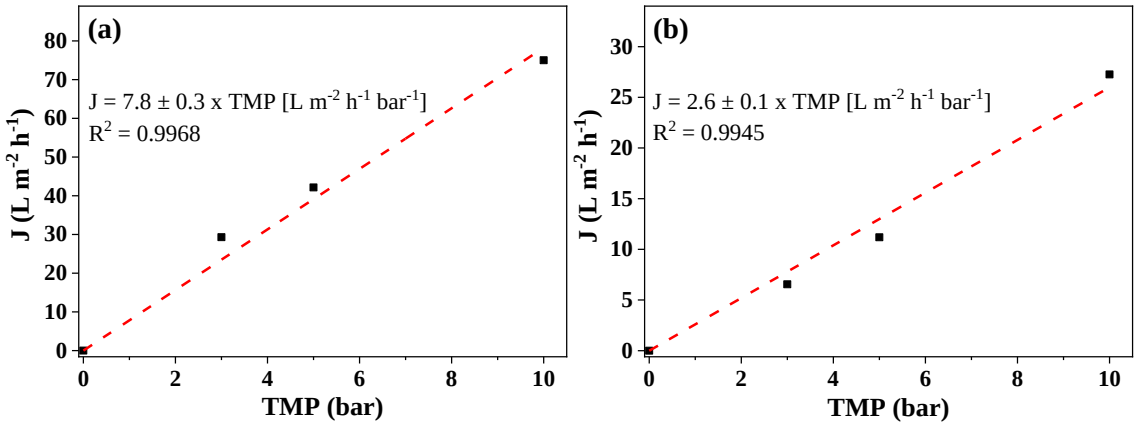

Figure 4.5. Hydraulic permeability of membranes MA-3 (a) and MB-2 (b) obtained by plotting the water flux values as a function of the *TMP* computed from Darcy's law. Note: Experimental data = symbols; Slope flux = dashed line.

The membrane hydrophilicity or wetting capacity is one of the most important factors for improving the pure water flux and reducing fouling. The membrane with less water-contact angle has better hydrophilicity properties [23]. The addition of TiO_2 nanoparticles on the membrane surface decreased the contact angle for MA-3 and reached a value of zero for MB-2 (Table 4.2). This can be attributed to the presence of TiO_2 hydrophilic nanoparticles in the upper layer of MB-2. The presence of TiO_2 nanoparticles containing a large number of hydrophilic hydroxyl groups on the surface of the membrane increases its hydrophilicity [24]. The outermost surface of MB has a layer of TiO_2, which is highly wettable. However, below the layer of TiO_2, there is a layer of graphene that has hydrophobic characteristics. Although MB-2 has a smaller apparent contact angle than MA-3, the high TiO_2 content on the surface of MB caused a high decrease in the permeate flux. This permeate flux decline could be attributed to pore blocking by the TiO_2 nanoparticles, correlated with the reduction in porosity and mean pore radius (see Figure 4.1c and Figure 4.1f).

Table 4.2. Contact angle and zeta potential of membranes.

Membrane	Contact angle (º)	Zeta potential (mV)
Pristine membrane	0	0
G membrane	83.6 ± 0.4	- 17.3
MA-3	62.6 ± 0.8	
MB-2	The drop is immediately absorbed by the surface of the material	- 10.6

In continuous-flow experiments using PMR, the pristine/commercial MF membrane could not reject CECs molecules due to its larger pore size when compared with the diameter of the target organic compounds and its non-photoactive characteristic. Furthermore, tests were carried out with the BPR fully open (no permeation) in the absence of light, in order to evaluate the possible adsorption of the CECs in the experimental setup. CECs adsorption on the membrane with and without a catalyst thin-

film was negligible (<1%). However, in the presence of light and catalyst thin-film, CECs rejection achieved maximum values of nearly 60% (Figure 4.6a and Figure 4.6c).

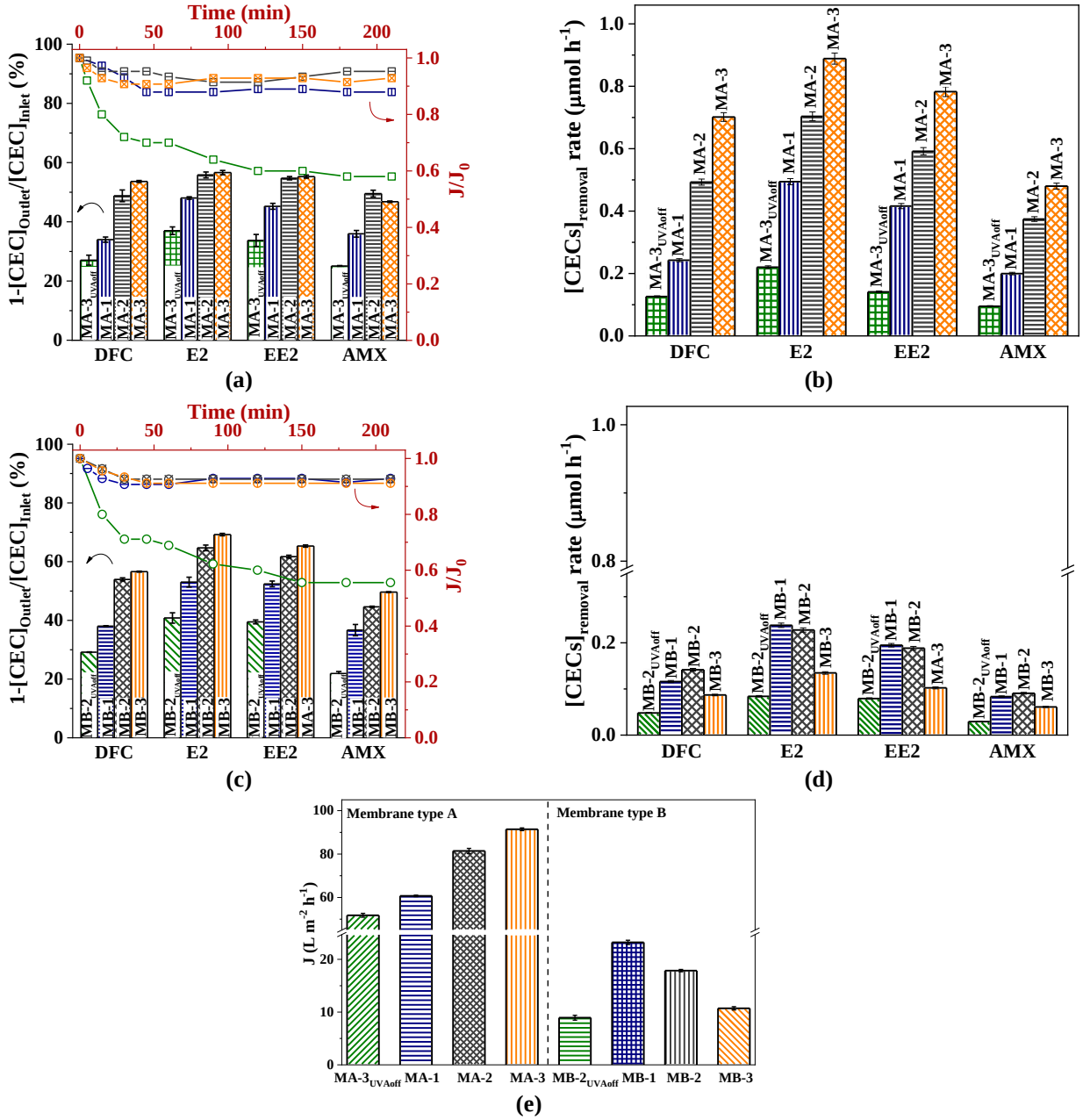

Figure 4.6. CECs removal efficiency (a) and removal rate in μmol h^{-1} (b) from an UPW and, permeate flux as a function of the reaction time for the different catalyst films using membrane A: MA-3_{UVAoff} (▦; −□−), MA-1 (▥;−▣−), MA-2 (▤;−⊟−) and, MA-3 (▨; −⊠−); CECs removal efficiency (c) and removal rate in μmol h^{-1} (d) from an UPW and, permeate flux as a function of the reaction time for the different catalyst films using membrane B: MB-2_{UVAoff} (▧; −○−), MB-1 (▥; −⊖−), MB-2 (▩; −⊗−) and MB-3 (▥; −◍−); e) Permeate flux in L m^{-2} h^{-1} after 210 min of reaction (J_{210}). Conditions: $[CEC]_0$ = 500 μg L^{-1}; T = 25 ºC; Cross Flow Velocity (*CFV*) = 0.01 m s^{-1}; *TMP* = 10 bar.

The membranes coated with multi-layer G-TiO_2 films (A or B) without physical treatment showed no water permeation (maximum pressure of 10 bar), confirming the hypothesis that the pores were created by the passage of an air stream through the membrane (inside-outside mode). This procedure creates nanogaps in the CS film after the catalyst deposition and before the pyrolysis step. The success of the

pore preparation process in multi-layer graphene membrane derives from the ability of CS to form conformal, continuous films on arbitrary substrates and its subsequent transformation into defective doped G upon pyrolysis at 600 °C. Pyrolysis causes a profound structural change of the polysaccharide forming doped G even after physical treatment. The goal was to achieve a membrane able to reject CECs and allow the permeation of nutrients, producing a safe and nutrient-rich permeate for irrigation in agriculture [25]. For example, recent experimental investigations using a MF membrane proved that physical opening methods using an electron beam or a laser could be an excellent approach to create variable-sized graphene nanopores to tune selectivity and molecular diffusivity [26].

As expected, in the presence of UVA light, the functionalized membranes exhibit an improvement in the membrane permeate flux and quality and reduced membrane fouling (Figure 4.6), due to the synergetic functions for CECs oxidation and self-cleaning process. Maximum CECs rejection coupling continuous filtration with photocatalysis were as follows: (i) 48 and 53% (DFC); (ii) 56 and 65% (E2); (iii) 54 and 62% (EE2); 49 and 45% (AMX) for membranes MA-3 and MB-2, respectively. MB enables a slightly higher CECs rejection than MA, which can be explained mainly by the better exposure of the photocatalyst to light. As the preparation method of MB only inserts TiO_2 after the formation of the G layer in the membrane shell-side, a greater amount of catalyst is susceptible to being activated by UVA light. Although an increment on the catalyst film thickness improved the CECs rejection efficiency, permeate flux declined (Figure 4.6c, to be further discussed below), leading to a maximum CECs removal rate ($\mu mol\ h^{-1}$) (Figure 4.6d) for the catalyst film with 6 layers.

For MA, CECs removal efficiency (Figure 4.6a), permeate flux (Figure 4.6e) and consequently, CECs removal rate (Figure 4.6b) increased with the increment on TiO_2 mass (1, 2 and 3% w/v) used in the preparation of the CS solution (before pyrolysis). For values higher than 4% w/v, the film was not continuous and for that reason, 3% w/v was considered the optimum concentration of TiO_2.

According to the data presented in Figure 4.6b and 4d, the CECs removal rate followed the sequence E2 > EE2 > DCF > AMX. CECs have starkly different chemical properties, and their particle size can vary [27-29]. Under the experimental conditions (pH = 6.9), DCF and AMX are both negatively charged molecules. Also, the pH_{pzc} for the G-TiO_2 film powder, for both fabrication conditions, was found to be 6.4 (Figure 4.7). As the solution pH is higher than the catalyst zero-point charge, the surface of the G-TiO_2 film is negatively charged, providing selective rejection of the negatively charged CECs. These results were confirmed by the zeta potential analyses (Table 4.2). Regarding hormones, neutral molecules for the pH working conditions, their rejections positively correlated with their larger

molecular dimension (size exclusion) and fairly hydrophobic characteristics (log K_{OW} = 4.01 and log K_{OW} = 3.67, respectively).

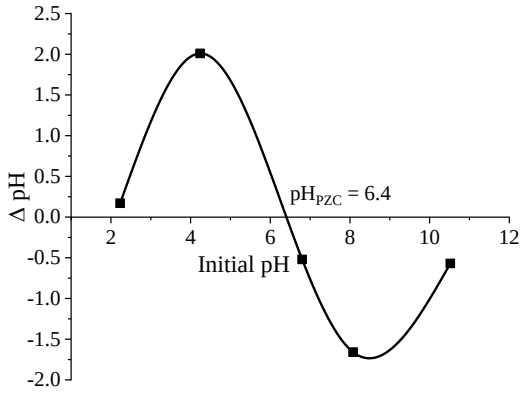

Figure 4.7. Zero-point charge of G-TiO_2 powder.

In the presence of light, the CECs rejection can be correlated with its reactivity towards hydroxyl radicals (E2 - $k_{\bullet OH}$ = (1.2 ± 0.3) × 10^{10} M^{-1} s^{-1}; EE2 - $k_{\bullet OH}$ = (1.5 ± 0.2) × 10^{10} M^{-1} s^{-1}); DCF - $k_{\bullet OH}$ = (9.29 ± 0.11) × 10^{9} M^{-1} s^{-1}; AMX - $k_{\bullet OH}$ = (3.93–7.95) × 10^{9} M^{-1} s^{-1}) [30-33] and higher driving force for the catalyst surface ($[E2]_{feed}$ = 2.1 ± 0.2 mM > $[EE2]_{feed}$ = 1.8 ± 0.1 mM > $[DCF]_{feed}$ = 1.64 ± 0.09 mM > $[AMX]_{feed}$ = 1.29 ± 0.08 mM). During the usual membrane filtration process, solutes are transported from the surface of the membrane ($C_{surface}$) to the bulk crossflow by convective transport ($J_{Convection}$) as a part of the permeate flow. Solutes that are rejected accumulate (C_{bulk}) near the surface, forming either deposits or a gelatinous-type layer (fouling). This solute build-up will cause a steep concentration gradient within the boundary layer, causing a back-transport of solute into the bulk stream due to diffusion ($J_{diffusion}$) [34]. Consequently, there is an exponential increase in the concentration of organic compounds near the membrane surface (Figure 4.8), which are oxidized by the action of reactive species, such as superoxide radicals ($O_2^{-\bullet}$), photogenerated holes (h^+), and hydroxyl radicals ($OH^\bullet$), generated when the G-TiO_2 film is exposed to light (UVA) [2]. Therefore, a hybrid system that couples membrane filtration and photocatalytic processes appear to be an alternative pathway to preclude fouling and improve CECs removal.

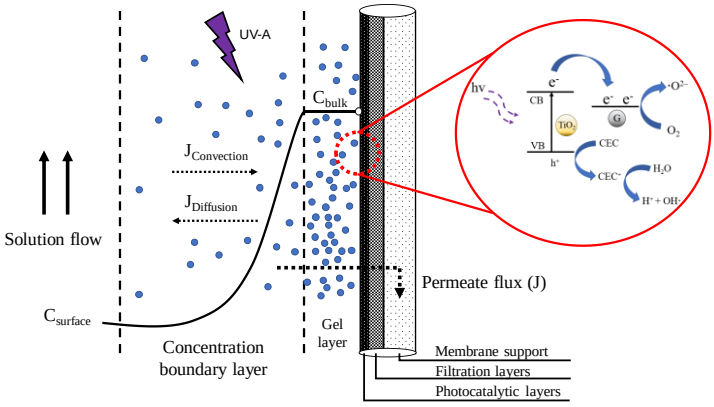

Figure 4.8. Schematic illustration of the proposed photocatalytic mechanism of G-TiO_2 membrane under UVA irradiation.

In this study, the permeate flux changes were monitored for 210 min where the starting point of the reaction was carried out by permeation of UPW and the following points were accomplished with a CEC solution. The permeability performance of G-TiO_2 membranes was investigated and presented in Figure 4.6a and Figure 4.6c. As can be seen, the highest permeate flux decline was observed at the beginning of the experiments and after 30 min of reaction time, the permeate flux achieved steady-state conditions in the presence of UVA light (MA-1, MA-2, MA-3, MB-1, MB-2 and MB-3). In the absence of UVA light (MA-3_{UVAoff} and MB-2_{UVAoff}), the decline in the permeate flux was continuous and did not reach a steady-state condition even after 210 min of reaction. Generally, the reduction in permeate flow is attributed to the fouling phenomenon in which size exclusion, hydrophobic interaction and electrostatic repulsion are the mechanisms responsible for the fouling of the membrane surface [35]. In the absence of UVA light, the *RFR* of MA-3 or MB-2 membranes decreased by 40 and 45% owing to membrane fouling, respectively.

As shown in Figure 4.9, the G-TiO_2-UVA system (MA-3 and MB-2) has a lower *RFR* and higher *FRR* than the G-TiO_2 system (MA-3_{UVAoff} and MB-2_{UVAoff}). Generally, lower *RFR* and higher *FRR* values indicate better membrane antifouling properties. Additionally, fouling can be divided into reversible (*Rr*) and irreversible (*Rir*) fouling. *Rr* is a fouling that could be cleaned by re-washing and is caused by the rejected contaminant molecules adsorbed or deposited on the surface of the membrane. *Rir* fouling is mainly removed by chemical washing or enzymatic degradation and is formed by various compounds that strongly bind with the membrane. Figure 4.9 shows that both *Rr* and *Rir* fouling strongly decreased with the use of the G-TiO_2-UVA system. For example, *Rir* decreased from 42.3 and 46.6% for MA-3_{UVAoff} and MB-2_{UVAoff} to 5.7 and 9.2% for MA-3 or MB-2, respectively. The G-TiO_2 membranes have not only a lower *RFR* value but also a lower *Rir* value, which indicates a higher longevity of the fabricated membranes. Similar results were also obtained by Xu et al. [36], using a PVDF UF membranes based on the synergy of GO and TiO_2.

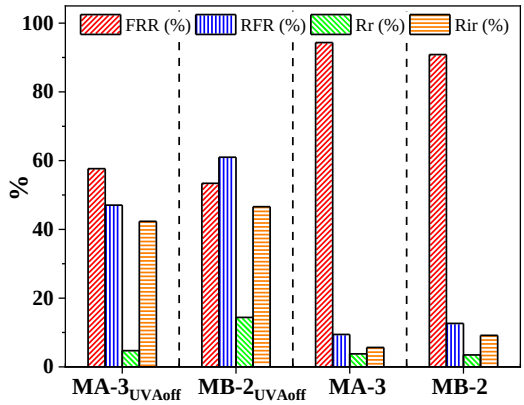

Figure 4.9. Flux recovery ratio (*FRR*), relative flux reduction ratio (*RFR*), reversible fouling ratio (*Rr*) and irreversible fouling ratio (*Rir*) to assess antifouling performance of G-TiO_2 membranes with (MA-2 and MB-3) and without (MA-3_{UVAoff} and MB-2_{UVAoff}) UVA irradiation. Conditions: $[CEC]_0$ = 500 µg L^{-1}; T = 25 ºC; CFV = 0.01 m s^{-1}; TMP = 10 bar.

Hence, the G-TiO_2-UVA system presents a better permeability and antifouling properties when compared to the system in the absence of light. Figure 4.6e also presents the permeate flux during the filtration of CECs solution through the examined membranes. After 210 min, the permeate flux reached maximum values of 91 L m^{-2} h^{-1} and 23 L m^{-2} h^{-1} for the MA-3 and MB-2 membranes, respectively. MA shows the highest water permeability, which may be attributed to the pyrolysis of the CS with TiO_2 nanoparticles, resulting in more defects in the continuous G film. The results showed that the permeability of MA increased according to the concentration of TiO_2 nanoparticles up to 3% [w/v], when the film started to create gaps in the continuous film. On the other hand, when the photocatalyst was added over the G film (MB), there was a significant decrease in the permeate flux after 210 min (J_{210}) for increasing amounts of TiO_2 ($J_{210\text{-}MB\text{-}1}$ = 23 L m^{-2} h^{-1}; $J_{210\text{-}MB\text{-}2}$ = 18 L m^{-2} h^{-1}; $J_{210\text{-}MB\text{-}3}$ = 11 L m^{-2} h^{-1}). Therefore, the accumulation of nanoparticles may lead to porosity reduction, which affects the flux through the membrane.

The long-term stability of the G-TiO_2 nanocomposite thin-film was evaluated for an operation period of 12 h. The relative permeate flux (J_{CECs}/J_0) of MA and MB with/without UVA radiation (MA-3_{UVAoff}, MB-2_{UVAoff}, MA-3 and MB-2) versus time is displayed in Figure 4.10. The obtained results reveal that a considerable flux decline for all membranes is observed during the first minutes of operation. However, after 60 min of filtration, the membranes with UVA radiation reached an almost constant flux, and the membranes without UVA radiation had a steep slope up to approximately 60% within 300 min. Moreover, although all the membranes showed a flux decline during the filtration process, at the end of the 12-hour filtration, MA-3 and MB-2 membranes in the presence of UVA light reveal about 40 and 50% higher permeate flux than the respective membranes without UVA radiation, suggesting the superior potential of membranes with catalyst activation. The stability of catalyst films was also evaluated based on the CECs removal for a period of 12 h. Figure 4.10b shows the treatment level

achieved for each CEC throughout the experiment. In general, the CECs removal percentage level was stable throughout the monitored period, with no evident trends of decreased treatment performance. Mean levels of treatment ranged from 45% removal for AMX to 65% removal for E2 using the G-TiO_2-UVA systems.

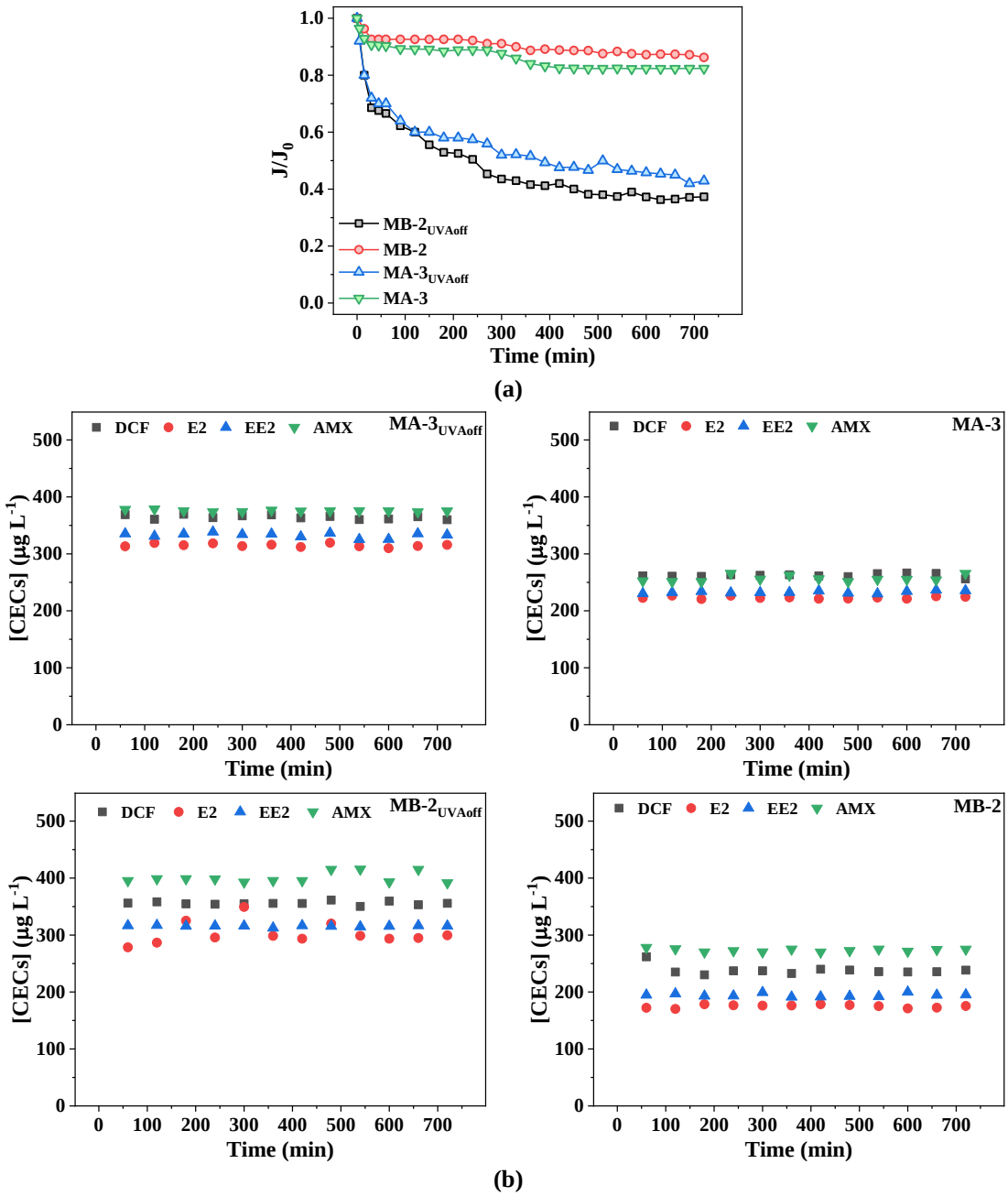

Figure 4.10. Long-term stability of the G-TiO_2 nanocomposite thin-films of both membranes types based on the permeate decline (a) and CECs concentration in the permeate (b) as a function of reaction time. Conditions: $[CEC]_0$ = 500 µg L^{-1}; T = 25 ºC; CFV = 0.01 m s^{-1}; TMP = 10 bar.

4.3.2.3 PMR tests using UWW matrix fortified with CECs

The effectiveness of the PMR system, using MA-3 and MB-2 membranes, was evaluated towards CECs removal from a secondary effluent from an UWWTP fortified with 500 μg L^{-1} of each CEC (Figure 4.11). The main characteristics of the UWW sample are presented in Table 4.3.

Table 4.3. Main physicochemical characteristics of the urban wastewater (UWW) collected after secondary treatment from an UWWTP (Northern Portugal).

Parameter (units)	Values
Colour	Pale yellow
pH	7.2
Temperature (ºC)	16.7
Conductivity (μS cm^{-1})	198
Turbidity (NTU)	0.9
Absorbance at 254 nm (AU)	0.15
Transmittance at 254 nm (%)	70.8
Dissolved organic carbon (mg L^{-1})	6.2
Dissolved inorganic carbon (mg L^{-1})	2.9
Specific UV Absorbance (SUVA) at 254 nm (L mg^{-1} m^{-1})	2.4
Chemical oxygen demand (mg O_2 L^{-1})	26
Total dissolved iron (mg L^{-1})	0.2
Total suspended solids (mg L^{-1})	1.5
Volatile suspended solids (mg L^{-1})	0.5
Total nitrogen (mg L^{-1})	35
Total phosphorous (mg L^{-1})	1.9
Nitrite – N-NO_3^- (mg L^{-1})	0.1
Sulfate – SO_4^{2-} (mg L^{-1})	19.0
Chloride – Cl^- (mg L^{-1})	17.4
Bromide – Br^- (mg L^{-1})	< 0.08[a]
Fluoride – F^- (mg L^{-1})	< 0.03[a]
Phosphate – PO_4^{3-} (mg L^{-1})	<0.5[b]
Sodium – Na^+ (mg L^{-1})	0.93
Ammonium – NH_4^+ (mg L^{-1})	< 0.02[a]
Potassium – K^+ (mg L^{-1})	5.2
Magnesium – Mg^{2+} (mg L^{-1})	1.7
Calcium – Ca^{2+} (mg L^{-1})	15.4

Note: [a]Limit of detection; [b]Limit of quantification

Figure 4.11b and Figure 4.11c show high *RFR* values of 70–75%, using the UWW matrix, nearly 12 times higher than when using synthetic CECs solutions. This is associated with the presence of organic matter in the UWW, resulting in the formation of a dense cake layer around the membrane shell-side, contributing to a rapid deterioration of the permeate flux. UWW components include a broad range of organic (e.g., natural organic matter composed of humic and fulvic acids, carbohydrates, proteins) and inorganic species (e.g., carbonate, bicarbonate, nitrite, sulphate, chloride), which react with $OH^{\bullet}$ and $O_2^{-\bullet}$ radicals, either competing with CECs for oxidation or forming the respective radicals with lower oxidation potential [37, 38]. Moreover, the presence of cation ions (Ca^{2+}, Mg^{2+} and K^+) in the UWW solutions (Table 4.3), might lead to a less negative G-TiO_2 membrane surface due to charge shielding and chemical adsorption [39]. As expected, in the presence of the UVA light, pollutants are oxidized on

the membrane surface, showing a lower decline in the permeate flux when compared with the system in the absence of UVA light (*RFR* higher than 90%) (Figure 4.11b and Figure 4.11c). Regarding the permeate flux, as observed during the filtration of a pure synthetic CECs solution, MA-3 presents higher values than MB-2 (inset graphics of Figure 4.11b and Figure 4.11c).

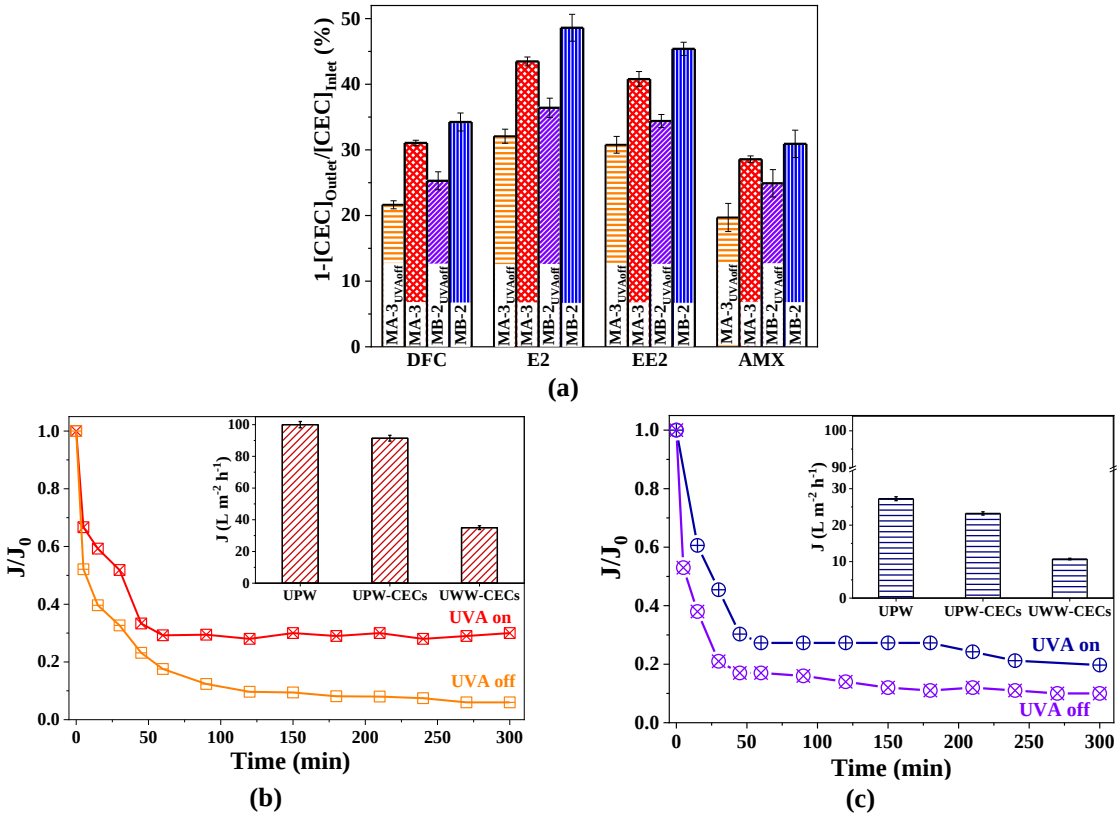

Figure 4.11. a) CECs removal from an UWW and permeate flux as a function of the reaction time for the best catalyst conditions using membrane A (b): MA-3_{UVAoff} (▨, ⊟); MA-3 (▩, ⊠); and membrane B (c): MB-2_{UVAoff} (▨, ⊗), MB-2 (▥, ⊕). Conditions: $[CEC]_0$ = 500 µg L^{-1}; *T* = 25 ºC; pH = 6.7; *CFV* = 0.01 m s^{-1}; *TMP* = 10 bar.

Although the UWW matrix negatively affects the permeate flux, CECs rejection was not significantly impaired, achieving maximum values of: (i) 31 and 34% (DFC); (ii) 43 and 49% (E2); (iii) 41 and 45% (EE2); and 29 and 31% (AMX), respectively for MA-3 and MB-2 membranes irradiated by UVA light (Figure 4.11a). The decline in CECs rejection can be associated with: (i) the existing contaminants (organic and inorganic matter) in the UWW matrix that are capable of inhibiting the rate of CECs removal; (ii) the deposited/adsorbed pollutants onto the catalyst's film, preventing the catalyst contact with light, oxygen and water, hindering the photocatalytic activity.

As in the CECs synthetic solution studies, MB-2 behaves better than MA-3, considering the CECs removal. The well-controlled morphology (the pore exposure/accessibility, the functionality/hydrophilicity of the surface), efficient TiO_2 interactions with the graphene and good material stability disclose the role of multicomponent hybrid photocatalytic-membrane system.

4.3.3 Toxicity

The zebrafish embryo bioassays met the OECD FET test 236 criteria: overall survival and hatching rate in control and solvent control at the end of the 96 h exposure were ≥ 90% and 80%, respectively. Moreover, no significant differences were observed between the control and solvent control.

Mortality, total abnormalities, and hatching rate observed on zebrafish embryos exposed to the CECs in UPW or real matrices before and after the treatment using MA-3 or MB-2 are presented in Table 4.4. A significant increase of total abnormalities (sum of pericardial and yolk-sac oedemas and notochord malformation) was observed in embryos exposed to the CECs plus UPW or real matrices when compared with both matrices without CECs. After 48 h of exposure to CECs in the real matrix, 100% of the embryos showed pericardial and yolk sac oedemas, and abnormalities in the notochord (Table 4.4, Figure 4.12) compared with 5% abnormalities in the real matrix. At 72 and 96 h, 35 and 100% of embryos died, respectively, in the real matrix with CECs. Similarly, although less severe, the embryos exposed to CECs in the UPW matrix also presented a significant increase of abnormalities (88.3%) at 96 h (Table 4.4, Figure 4.12) compared with no abnormalities recorded in the UPW matrix alone at this time point. The mortality rate for the CECs plus UPW matrix reached 15% at 72 h and 20% at 96 h compared to 2.1% in the UPW matrix alone in these time points. With regard to the hatching rate, no embryos hatched after exposition to CECs in the real matrix and all of them died at 96 h. The hatching rate for the embryos exposed to CECs in the UPW matrix was significantly reduced at 96 h with only 10% of the embryos hatched, compared to 97.9% in the UPW matrix alone.

The abnormalities and mortality reported for the CECs in both matrices were significantly reduced after the treatment using MA-3 or MB-2 with values similar to the UPW and real matrices ($p > 0.05$) (Table 4.4, Figure 4.12). The same effect was observed for the endpoint hatching rate that was significantly increased after the treatment using both types of membranes. It is evident that the filtration + oxidation treatment process increased the fitness of zebrafish embryos and led to a significant decrease in the toxicity produced by CECs present in the UPW and real matrices.

Table 4.4. Toxicological effects observed in zebrafish embryos exposed to the CECs, in ultrapure water (UPW) and real matrix (dechlorinated UPW and UWWTP secondary effluent, respectively) before and after the treatment with the functionalized ceramic membranes MA-3 and MB-2.

Hours post fertilization (hpf)	Treatment	Endpoints		
		Mortality (%)	Total abnormalities (%)	Hatching (%)
24	Synthetic matrix (dechlorinated UPW - control)	2.1 ± 0.6	0 ± 0	0 ± 0
	Synthetic matrix + acetonitrile (sol. control)	5 ± 5	0 ± 0	0 ± 0
	Synthetic matrix + CECs	15 ± 6 *	0 ± 0	0 ± 0
	Synthetic matrix + CECs + MA-3	10 ± 6	0 ± 0	0 ± 0
	Synthetic matrix + CECs + MB-2	5 ± 5	0 ± 0	0 ± 0
	Real matrix (secondary-treated UWW)	5 ± 5	0 ± 0	0 ± 0
	Real matrix + acetonitrile	5 ± 5	0 ± 0	0 ± 0
	Real matrix + CECs	5 ± 5	10 ± 6	0 ± 0
	Real matrix + CECs + MA-3	5 ± 5	0 ± 0	0 ± 0
	Real matrix + CECs + MB-2	5 ± 5	0 ± 0	0 ± 0
48	Synthetic matrix (dechlorinated UPW - control)	2.1 ± 0.6	0 ± 0	0 ± 0
	Synthetic matrix + acetonitrile (sol. control)	5 ± 5	0 ± 0	0 ± 0
	Synthetic matrix + CECs	15 ± 6 *	7 ± 7	0 ± 0
	Synthetic matrix + CECs + MA-3	10 ± 6	5 ± 5	0 ± 0
	Synthetic matrix + CECs + MB-2	5 ± 5	0 ± 0	0 ± 0
	Real matrix (secondary-treated UWW)	5 ± 5	0 ± 0	0 ± 0
	Real matrix + acetonitrile	5 ± 5	0 ± 0	0 ± 0
	Real matrix + CECs	5 ± 5	100 ± 0 * # &	0 ± 0
	Real matrix + CECs + MA-3	5 ± 5	0 ± 0	0 ± 0
	Real matrix + CECs + MB-2	5 ± 5	0 ± 0	0 ± 0
72	Synthetic matrix (dechlorinated UPW – control)	2.1 ± 0.6	0 ± 0	17 ± 2
	Synthetic matrix + acetonitrile (sol. control)	5 ± 5	0 ± 0	$(3\pm1) \times 10^1$
	Synthetic matrix + CECs	15 ± 6 *	27 ± 2 * # &	0 ± 0 #
	Synthetic matrix + CECs + MA-3	10 ± 6	0 ± 0	$(4 \pm 1) \times 10^1$
	Synthetic matrix + CECs + MB-2	5 ± 5	5 ± 5	10 ± 6
	Real matrix (secondary-treated UWW)	5 ± 5	5 ± 5	$(6 \pm2) \times 10^1$
	Real matrix + acetonitrile	5 ± 5	0 ± 0	$(4 \pm 1) \times 10^1$
	Real matrix + CECs	$(4 \pm 1) \times 10^1$ * # &	100 ± 0 * # &	0 ± 0 *
	Real matrix + CECs + MA-3	5 ± 5	0 ± 0	$(2 \pm 1) \times 10^1$
	Real matrix + CECs + MB-2	5 ± 5	5 ± 5	10 ± 6

Table 4.4. Toxicological effects observed in zebrafish embryos exposed to the CECs, in ultrapure water (UPW) and real matrix (dechlorinated UPW and UWWTP secondary effluent, respectively) before and after the treatment with the functionalized ceramic membranes MA-3 and MB-2 (continued).

Hours post fertilization (hpf)	Treatment	Endpoints		
		Mortality (%)	Total abnormalities (%)	Hatching (%)
96	Synthetic matrix (dechlorinated UPW - control)	2.1 ± 0.6	2.1 ± 0.6	97.9 ± 0.6
	Synthetic matrix + acetonitrile (sol. control)	5 ± 5	10 ± 6	95 ± 5
	Synthetic matrix + CECs	20 ± 5 * &	88 ± 7 * # &	10 ± 6 * # &
	Synthetic matrix + CECs + MA-3	10 ± 6	5 ± 5	90 ± 6
	Synthetic matrix + CECs + MB-2	5 ± 5	5 ± 5	95 ± 5
	Real matrix (secondary-treated UWW)	5 ± 5	5 ± 5	95 ± 5
	Real matrix + acetonitrile	5 ± 5	5 ± 5	95 ± 5
	Real matrix + CECs	100 ± 0 * # &	a	a
	Real matrix + CECs + MA-3	5 ± 5	0 ± 0	100 ± 0
	Real matrix + CECs + MB-2	5 ± 5	5 ± 5	80 ± 9

"*" indicates significant differences ($p < 0.05$) between CECs in UPW or in real matrix and control or UWWTP; "#" and "&" indicate significant differences between treated and non-treated groups (i.e., CECs in UPW or real matrices before and after the treatments with the MA-3 and MB-2, respectively); a – not measured because all embryos died. Data are expressed as mean ± standard error (N = 10 for control; N = 5 for the other treatments).

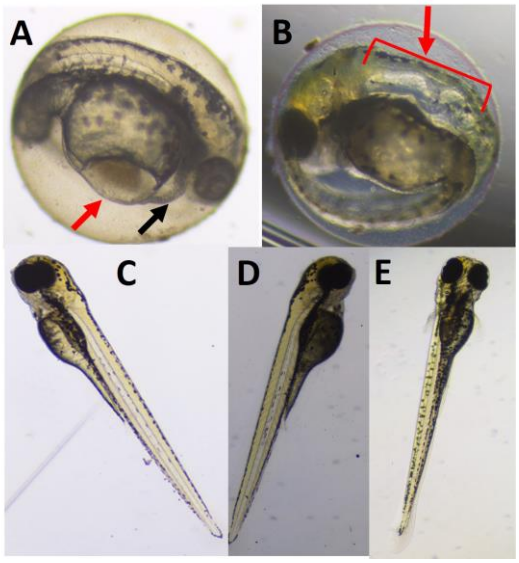

Figure 4.12. Abnormalities observed in the zebrafish embryo bioassay: Pericardial oedema – black arrow; yolk sac oedema – red arrow at 48 hpf exposition to CECs + real matrix (A); Abnormal notochord formation at 96 hpf exposition to CECs + UPW matrix (B); normal development at 96 hpf recorded in CECs + real matrix + MA-3 (C), CECs + real matrix + MB-2 (D) and control – UPW (E).

4.4 Conclusions

The PMR with the functionalized membranes, activated by UVA light, operated in a single-pass flow-through mode for the treatment of synthetic CECs solutions, exhibits a substantial improvement in the membrane permeate quality and quantity compared to its performance in the absence of light. The G-TiO_2-UVA systems present high stability for at least 12 h of continuous operation and reduced reversible and irreversible fouling due to the synergetic functions for CECs oxidation and self-cleaning process. Overall, the results in this study indicate that the G-TiO_2-UVA systems investigated achieved good removal of CECs and could effectively reduce toxicity to zebrafish embryos. MB enables a slightly higher CECs rejection than MA, which can be explained mainly by the better exposure of the photocatalyst to light. However, the accumulation of the nanoparticles over the G film increases the surface roughness of membrane MB-2, confirmed by AFM analysis, reducing its resistance to fouling compared to membrane MA-3. Although the UWW matrix showed a significant negative effect on permeate flux when compared to UPW, mainly due to the presence of substances that may deposit or adsorb onto the membrane's surface (blocking the membrane pores), the CECs rejection was similar to the one obtained with UPW.

4.5 References

[1] Y. Gao, M. Hu, B. Mi, Membrane surface modification with TiO_2–graphene oxide for enhanced photocatalytic performance, Journal of Membrane Science 455 (2014) 349-356. https://doi.org/10.1016/j.memsci.2014.01.011.

[2] P. Gao, Z. Liu, M. Tai, D.D. Sun, W. Ng, Multifunctional graphene oxide–TiO_2 microsphere hierarchical membrane for clean water production, Applied Catalysis B: Environmental 138-139 (2013) 17-25. https://doi.org/10.1016/j.apcatb.2013.01.014.

[3] S.G.S. Santos, L.O. Paulista, T.F.C.V. Silva, M.M. Dias, J.C.B. Lopes, R.A.R. Boaventura, V.J.P. Vilar, Intensifying heterogeneous TiO_2 photocatalysis for bromate reduction using the NETmix photoreactor, Science of the Total Environment 664 (2019) 805-816. https://doi.org/10.1016/j.scitotenv.2019.02.045.

[4] P.R. Kidambi, D. Jang, J.-C. Idrobo, M.S.H. Boutilier, L. Wang, J. Kong, R. Karnik, Nanoporous Atomically Thin Graphene Membranes for Desalting and Dialysis Applications, Advanced Materials 29 (33) (2017) 1700277. https://doi.org/10.1002/adma.201700277.

[5] E.H. Alsharaeh, T. Bora, A. Soliman, F. Ahmed, G. Bharath, M.G. Ghoniem, K.M. Abu-Salah, J. Dutta, Sol-Gel-Assisted Microwave-Derived Synthesis of Anatase Ag/TiO_2/GO Nanohybrids toward Efficient Visible Light Phenol Degradation, Catalysts 7 (5) (2017) 1-10. https://doi.org/10.3390/catal7050133.

[6] P. Benjwal, M. Kumar, P. Chamoli, K.K. Kar, Enhanced photocatalytic degradation of methylene blue and adsorption of arsenic(iii) by reduced graphene oxide (rGO)–metal oxide (TiO_2/Fe_3O_4) based nanocomposites, RSC Advances 5 (89) (2015) 73249-73260. https://doi.org/10.1039/C5RA13689J.

[7] P.T. Tuoi, N.N. Anh, B.H. Thang, P.V. Trinh, C.T. Thanh, D.N. Minh, N.V. Hung, N.V. Chuc, N.C. Khang, P.N. Minh, P.N. Hong, Optical and photocatalytic property of nanocomposite based functionalized graphene and TiO_2, The 8th International Workshop on Advanced Materials Science and Nanotechnology (IWAMSN2016), Ha Long City, Vietnam, 2016, pp. 398-404.

[8] N.R. Khalid, E. Ahmed, Z. Hong, Y. Zhang, M. Ahmad, Nitrogen doped TiO_2 nanoparticles decorated on graphene sheets for photocatalysis applications, Current Applied Physics 12 (6) (2012) 1485-1492. https://doi.org/10.1016/j.cap.2012.04.019.

[9] W. Zhou, Y. Liu, Y. Zhang, G. Yang, S. Deng, F. Shen, H. Peng, L. Wang, Novel multi-layer cross-linked TiO_2/C nanosheets and their photocatalytic properties, New Journal of Chemistry 38 (4) (2014) 1647-1654. https://doi.org/10.1039/C3NJ01342A.

[10] M. Naebe, J. Wang, A. Amini, H. Khayyam, N. Hameed, L.H. Li, Y. Chen, B. Fox, Mechanical Property and Structure of Covalent Functionalised Graphene/Epoxy Nanocomposites, Scientific Reports 4 (1) (2014) 4375. https://doi.org/10.1038/srep04375.

[11] C.H. Manoratne, S.R.D. Rosa, I.R.M. Kottegoda, XRD-HTA, UV visible, FTIR and SEM interpretation of reduced graphene oxide synthesized from high purity vein graphite, Material Science Research India 14 (1) (2017) 19-30. http://dx.doi.org/10.13005/msri/140104.

[12] Z. Çiplak, N. Yildiz, A. Çalimli, Investigation of Graphene/Ag Nanocomposites Synthesis Parameters for Two Different Synthesis Methods, Fullerenes, Nanotubes and Carbon Nanostructures 23 (4) (2015) 361-370. https://doi.org/10.1080/1536383X.2014.894025.

[13] G. Rao, Q. Zhang, H. Zhao, J. Chen, Y. Li, Novel titanium dioxide/iron (III) oxide/graphene oxide photocatalytic membrane for enhanced humic acid removal from water, Chemical Engineering Journal 302 (2016) 633-640. https://doi.org/10.1016/j.cej.2016.05.095.

[14] Z. Xu, H. Gao, H. Guoxin, Solution-based synthesis and characterization of a silver nanoparticle–graphene hybrid film, Carbon 49 (14) (2011) 4731-4738. https://doi.org/10.1016/j.carbon.2011.06.078.

[15] V. Koutu, R. Dhakar, P. Ojha, L. Shastri, M.M. Malik, Structural and optical studies of TiO_2:Ag_2O nanocomposite by sol-gel method, Materials Science-Poland 38 (2) (2020) 263-270. https://doi.org/10.2478/msp-2020-0036.

[16] R. López, R. Gómez, Band-gap energy estimation from diffuse reflectance measurements on sol–gel and commercial TiO_2: a comparative study, Journal of Sol-Gel Science and Technology 61 (1) (2012) 1-7. https://doi.org/10.1007/s10971-011-2582-9.

[17] Y. Wang, J. Yu, W. Xiao, Q. Li, Microwave-assisted hydrothermal synthesis of graphene based Au–TiO_2 photocatalysts for efficient visible-light hydrogen production, Journal of Materials Chemistry A 2 (11) (2014) 3847-3855. https://doi.org/10.1039/C3TA14908K.

[18] K.H. Leong, L.C. Sim, D. Bahnemann, M. Jang, S. Ibrahim, P. Saravanan, Reduced graphene oxide and Ag wrapped TiO_2 photocatalyst for enhanced visible light photocatalysis, APL Materials 3 (10) (2015) 104503. https://doi.org/10.1063/1.4926454.

[19] I. Childres, L.A. Jauregui, W. Park, H. Cao, Y.P. Chen, Raman spectroscopy of graphene and related materials, in: J.I. Jang (Ed.), New Developments in Photon and Materials Research, Nova Science, New York, 2013, pp. 1-20.

[20] J. Mani, H. Sakeek, S. Habouti, M. Dietze, M. Es-Souni, Macro–meso-porous TiO_2, ZnO and ZnO–TiO_2-composite thick films. Properties and application to photocatalysis, Catalysis Science & Technology 2 (2) (2012) 379-385. https://doi.org/10.1039/C1CY00302J.

[21] D.J. Kim, S.H. Hahn, S.H. Oh, E.J. Kim, Influence of calcination temperature on structural and optical properties of TiO_2 thin films prepared by sol–gel dip coating, Materials Letters 57 (2) (2002) 355-360. https://doi.org/10.1016/S0167-577X(02)00790-5.

[22] D. Chen, F. Li, A.K. Ray, External and internal mass transfer effect on photocatalytic degradation, Catalysis Today 66 (2) (2001) 475-485. https://doi.org/10.1016/S0920-5861(01)00256-5.

[23] Y. Zhang, F. Liu, Y. Lu, L. Zhao, L. Song, Investigation of phosphorylated TiO_2–SiO_2 particles/polysulfone composite membrane for wastewater treatment, Desalination 324 (2013) 118-126. https://doi.org/10.1016/j.desal.2013.06.007.

[24] M. Safarpour, A. Khataee, V. Vatanpour, Preparation of a Novel Polyvinylidene Fluoride (PVDF) Ultrafiltration Membrane Modified with Reduced Graphene Oxide/Titanium Dioxide (TiO_2) Nanocomposite with Enhanced Hydrophilicity and Antifouling Properties, Industrial & Engineering Chemistry Research 53 (34) (2014) 13370-13382. https://doi.org/10.1021/ie502407g.

[25] A. Nahrstedt, A. Gaba, B. Zimmermann, T. Jentzsch, K. Kroemer, Y. Tiemann, L. Harsanyi, P. Buchta, U. Doelchow, J. Lipnizki, K. Mende, T. Koch, A. Rohn, Reuse of municipal wastewater for

different purposes based on a modular treatment concept, Journal of Water Reuse and Desalination 10 (4) (2020) 301-316. https://doi.org/10.2166/wrd.2020.040.

[26] T. Uragami, Science and technology of separation membranes, Wiley Online Library, 2017.

[27] J.C. Birnbaum, T.O. Danby, T.J. Johnson, M.R.K. Kelly-Gorham, R. Lindenmaier, T.L. Myers, PNNL Solid Phase IR Spectra, Pacific Northwest National Laboratory (PNNL) (2017).

[28] A.Z. Hezave, F. Esmaeilzadeh, The effects of RESS parameters on the diclofenac particle size, Advanced Powder Technology 22 (5) (2011) 587-595. https://doi.org/10.1016/j.apt.2010.08.010.

[29] J.W. Groenendaal, E.J.A.M. Leenderts, T. Van Der Does, Crystalline amoxicillin trihydrate powder, Google Patents, 2009.

[30] S.P. Mezyk, E.M. Abud, K.L. Swancutt, G. McKay, D.D. Dionysiou, Removing Steroids from Contaminated Waters Using Radical Reactions, Contaminants of Emerging Concern in the Environment: Ecological and Human Health Considerations, American Chemical Society, 2010, pp. 213-225. https://doi.org/10.1021/bk-2010-1048.ch009.

[31] H. Yu, E. Nie, J. Xu, S. Yan, W.J. Cooper, W. Song, Degradation of Diclofenac by Advanced Oxidation and Reduction Processes: Kinetic Studies, Degradation Pathways and Toxicity Assessments, Water Research 47 (5) (2013) 1909-1918. https://doi.org/10.1016/j.watres.2013.01.016.

[32] R. Andreozzi, M. Canterino, R. Marotta, N. Paxeus, Antibiotic removal from wastewaters: The ozonation of amoxicillin, Journal of Hazardous Materials 122 (3) (2005) 243-250. https://doi.org/10.1016/j.jhazmat.2005.03.004.

[33] F.J. Benitez, F.J. Real, J.L. Acero, G. Roldan, Removal of selected pharmaceuticals in waters by photochemical processes, Journal of Chemical Technology & Biotechnology 84 (8) (2009) 1186-1195. https://doi.org/10.1002/jctb.2156.

[34] M. Cheryan, Membrane Separations: Mechanisms and Models, in: R.P. Singh, A.G. Medina (Eds.), Food Properties and Computer-Aided Engineering of Food Processing Systems, Springer Netherlands, Dordrecht, 1989, pp. 367-391. https://doi.org/10.1007/978-94-009-2370-6_31.

[35] K.H. Chu, M. Fathizadeh, M. Yu, J.R.V. Flora, A. Jang, M. Jang, C.M. Park, S.S. Yoo, N. Her, Y. Yoon, Evaluation of Removal Mechanisms in a Graphene Oxide-Coated Ceramic Ultrafiltration Membrane for Retention of Natural Organic Matter, Pharmaceuticals, and Inorganic Salts, ACS Applied Materials & Interfaces 9 (46) (2017) 40369-40377. https://doi.org/10.1021/acsami.7b14217.

[36] Z. Xu, T. Wu, J. Shi, K. Teng, W. Wang, M. Ma, J. Li, X. Qian, C. Li, J. Fan, Photocatalytic antifouling PVDF ultrafiltration membranes based on synergy of graphene oxide and TiO_2 for water treatment, Journal of Membrane Science 520 (2016) 281-293. https://doi.org/10.1016/j.memsci.2016.07.060.

[37] I. Michael-Kordatou, C. Michael, X. Duan, X. He, D.D. Dionysiou, M.A. Mills, D. Fatta-Kassinos, Dissolved effluent organic matter: Characteristics and potential implications in wastewater treatment and reuse applications, Water Research 77 (2015) 213-248. https://doi.org/10.1016/j.watres.2015.03.011.

[38] I. Michael, E. Hapeshi, V. Osorio, S. Perez, M. Petrovic, A. Zapata, S. Malato, D. Barceló, D. Fatta-Kassinos, Solar photocatalytic treatment of trimethoprim in four environmental matrices at a pilot scale:

Transformation products and ecotoxicity evaluation, Science of The Total Environment 430 (2012) 167-173. https://doi.org/10.1016/j.scitotenv.2012.05.003.

[39] A. Azaïs, J. Mendret, E. Petit, S. Brosillon, Evidence of solute-solute interactions and cake enhanced concentration polarization during removal of pharmaceuticals from urban wastewater by nanofiltration, Water Research 104 (2016) 156-167. https://doi.org/10.1016/j.watres.2016.08.014.

5 Ozone Membrane Contactor to Intensify Gas/liquid Mass Transfer and Contaminants of Emerging Concern Oxidation

In this chapter, a tubular porous borosilicate membrane contactor was investigated for ozone gas/water mass transfer and the removal of CECs in water. Ozone gas/water contact occurs on the membrane shell-side, which is coated with a photocatalyst (TiO_2-P25), as the ozone gas stream is fed from the lumen side and permeates through the pores generating micro-sized ozone bubbles pseudo-uniformly delivered to the annular reaction zone where the contaminated water to be treated flows. Under continuous flow, water pH at 3.0 and temperature at 20 ºC, the volumetric mass transfer coefficient (K_La) ranged from 3.5 to 9.0 min^{-1} and improved with the increase of gas flow rate (Q_G, 1.5-fold from 0.15 to 1.0 Ndm^3 min^{-1}) and liquid flow rate (Q_L, 2.0-fold from 20 to 50 L h^{-1}), due to enhanced turbulence on the membrane shell-side and annular zone. The main resistances to ozone transfer were in the water phase boundary layer (53–76%) and in the membrane (24–47%; $k_M = (1.14 \pm 0.01) \times 10^{-4}$ m s^{-1}). For an ozone dose of 12 g m^{-3} and residence time of 3.9 s, removals ≥ 80% were achieved for 13 of 19 CECs spiked in DW (each 10 µg L^{-1}), demonstrating the applicability of this membrane contactor for ozonation treatment. Photocatalytic ozonation (O_3/UVC/TiO_2) did not significantly improve the treatment performance due to the low residence time inside the contactor.

This chapter is based on the following research article: "Presumido, P.H., Montes, R., Quintana, J.B., Rodil, R., Feliciano, M., Li-Puma, G., Gomes, A.I., Vilar, V.J.P. *Ozone membrane contactor to intensify gas/liquid mass transfer and contaminants of emerging concern oxidation*, Journal of Environmental Chemical Engineering, 10, 6 (2022), 108671. DOI: 10.1016/j.jece.2022.108671"

5.1 Objectives

In this chapter, a novel ozone membrane contactor is proposed to intensify ozone gas/water mass transfer and, simultaneously, allow the use of light and catalyst to activate ozone in a single unit. In the tubular porous borosilicate membrane distributor, the O_3 stream is fed by the lumen side and quickly delivered to the liquid through virtually unlimited dosing points along the membrane length. An outer quartz tube allows light penetration through the annular reaction zone (ARZ), where the membrane shell-side is coated with titanium dioxide (TiO_2-P25). The increased performance of the proposed membrane contactor was assessed by measuring the volumetric mass transfer coefficient (K_La), determined in continuous mode from a mass balance for O_3 in the gas and the liquid phases, considering the water pH and temperature (T), the O_3 concentration in the gas phase ($[O_3]_{G,inlet}$), the liquid (Q_L) and gas (Q_G) flow rates. Furthermore, the mass transfer efficiency (*MTE*), i.e., the fraction of O_3 that dissolves into the aqueous solution, was also determined. Lastly, also in continuous mode, the ozone membrane contactor was applied to treat a mixture of 19 CECs spiked in DW at low concentrations (10 μg L^{-1}) to simulate the concentrations and the range of contaminants typically found in water and wastewater. The primary aim was to determine CECs degradation efficiency envisaging its application in water/wastewater treatment.

5.2 Materials and methods

All the chemicals used in this work, gas/liquid mass transfer modelling, experimental units and procedures, as well as the employed analytical determinations, are described in *Chapter 2*. The preparation of the photocatalytic membrane on a tubular borosilicate membrane shell-side is described in detail in *Section 2.2.3*. All the experimental data presented in this chapter (Table 5.1) was obtained using the membrane contactor, which is detailed described in *Section 2.3.2.2*. Before submitting to treatment, the DW was fortified with 10 μg L^{-1} of each 19 CECs. The CECs were selected within the scope of the NOR-WATER project (http://nor-water.eu/pt/home/), according to their occurrence and persistence in the river basins and UWWTP effluents located in Northern Portugal and Galicia. The target CECs include four short-chain perfluorinated compounds-PFAS (HFBA, PFBS, PFOA, TFMS), three angiotensin II receptor blockers (VSTN, ISTN, LSTN), two beta-blockers (ATNL and BSPL), two hormones (E2 and EE2), an anti-inflammatory (DCF), two artificial sweeteners (AC-K and SCH), a flame retardant (MLN), an herbicide (DRN), an insect repellent (DEET), carbamazepine (CBZ) and its metabolite (CBZ-EPX).

Table 5.1. Experimental conditions employed in all ozone mass transfer tests.

Q_G ($Ndm^3\ min^{-1}$)	$[O_3]_{G,inlet}$ ($g\ Nm^{-3}$)	Q_L ($L\ h^{-1}$)	τ (s)	pH	Temperature (ºC)	$[O_3^*]^a$ ($g\ m^{-3}$)	$[O_3]_L{}^a$ ($g\ m^{-3}$)	K_La^a (min^{-1})
Effect of pH								
0.75	21.0	50	10.1	3.28	20	4.65 ± 0.07	3.18 ± 0.05	6.86 ± 0.03
0.75	21.6	50	10.1	5.00	20	3.02 ± 0.02	1.86 ± 0.01	5.70 ± 0.08
0.75	20.8	50	10.1	6.96	20	2.55 ± 0.01	1.39 ± 0.01	4.69 ± 0.07
0.75	20.6	50	10.1	9.00	20	1.16 ± 0.05	0.58 ± 0.02	4.13 ± 0.04
Effect of Temperature								
0.75	21.4	50	10.1	3.28	15	4.8 ± 0.1	3.54 ± 0.04	8.02 ± 0.08
0.75	21.0	50	10.1	3.28	20	4.65 ± 0.07	3.18 ± 0.05	6.86 ± 0.03
0.75	21.2	50	10.1	3.29	25	4.5 ± 0.1	3.02 ± 0.03	6.59 ± 0.05
Effect of Q_L								
0.75	20.3	20	25.2	3.28	20	4.65 ± 0.07	3.57 ± 0.04	3.51 ± 0.01
0.75	20.3	30	16.8	3.21	20	4.65 ± 0.07	3.42 ± 0.03	4.79 ± 0.02
0.75	20.1	35	14.4	3.14	20	4.65 ± 0.07	3.28 ± 0.09	5.13 ± 0.03
0.75	20.0	40	12.6	3.24	20	4.65 ± 0.07	3.20 ± 0.04	5.59 ± 0.05
0.75	21.0	50	10.1	3.28	20	4.65 ± 0.07	3.18 ± 0.05	6.86 ± 0.03
0.75	20.0	60	8.4	3.20	20	4.65 ± 0.07	2.81 ± 0.07	6.83 ± 0.02
0.75	20.1	150	3.4	3.12	20	4.65 ± 0.07	1.36 ± 0.02	6.18 ± 0.06
Effect of $[O_3]_{G,inlet}$								
0.75	21.0	50	10.1	3.28	20	4.65 ± 0.07	3.18 ± 0.05	6.86 ± 0.03
0.75	40.0	50	10.1	3.20	20	11.15 ± 0.06	8.06 ± 0.07	7.64 ± 0.02
0.75	60.3	50	10.1	3.14	20	21.14 ± 0.08	14.8 ± 0.1	7.12 ± 0.08
0.75	80.3	50	10.1	3.08	20	30.7 ± 0.2	22.3 ± 0.1	7.7 ± 0.2
Effect of Q_G								
0.15	80.8	50	10.1	3.21	20	30.7 ± 0.2	19.3 ± 0.2	5.9 ± 0.1
0.30	81.8	50	10.1	3.17	20	30.7 ± 0.2	19.7 ± 0.2	6.1 ± 0.1
0.50	80.0	50	10.1	3.09	20	30.7 ± 0.2	21.2 ± 0.9	7.0 ± 0.2
0.75	80.3	50	10.1	3.08	20	30.7 ± 0.2	22.3 ± 0.1	7.7 ± 0.2
0.75	21.0	50	10.1	3.28	20	4.65 ± 0.07	3.18 ± 0.05	6.86 ± 0.03
0.85	23.0	50	10.1	3.30	20	4.65 ± 0.07	3.45 ± 0.03	8.1 ± 0.7
1.00	22.0	50	10.1	2.90	20	4.65 ± 0.07	3.63 ± 0.04	9.0 ± 0.4

Note: [a]Standard Error

5.3 Results and discussion

5.3.1 Characterisation of TiO_2 coated borosilicate membrane

The membrane prior to and after catalyst immobilization was examined using the SEM technique (Figure 5.1). The fresh borosilicate surface (Figure 5.1a) is typical of a silica-based material with the presence of nanoparticles and significant roughness. On the other hand, the surface of the membrane with TiO_2-P25 composite (Figure 5.1b) became more uniform and presented fewer imperfections and roughness compared to the unmodified membrane. Uniform deposition of c.a. 623 mg of TiO_2-P25 over the entire membrane was obtained after 4 immersions in the catalyst suspension, which allowed not only the occurrence of thin-films of the catalyst on the membrane surface but also an accumulation of large amounts of TiO_2-P25 particles in the membrane pores (not attained with fewer immersions).

TiO_2-P25 films deposited on the membrane surface were subjected to thermal treatment (at 450 ºC) to stabilize the catalyst on the membrane surface. The XRD pattern of the material before and after thermal treatment (Figure 5.1c) confirmed a mixed anatase crystal structure (JCPDS file No.73–1764) and rutile crystal structure (JCPDS file No.78–1510). The distinct diffraction peaks observed in the 2θ values of 25.3 º, 37.8 º, 48.0 º, 54.0 º, 55.1 º, 68.9 º, 70.3 º, and 75.0 º correspond to (101), (004), (200), (211), (105), (204), (116), (220) and (215) of the anatase crystal planes. The distinct diffraction peaks for rutile are observed at 27.5 º, 36.1 º, and 41.3 º, corresponding to the (110), (101), and (111) planes, respectively. Consequently, the expected photocatalytic activity of the TiO_2-450ºC immobilised on the membrane surface is very similar to TiO_2-P25.

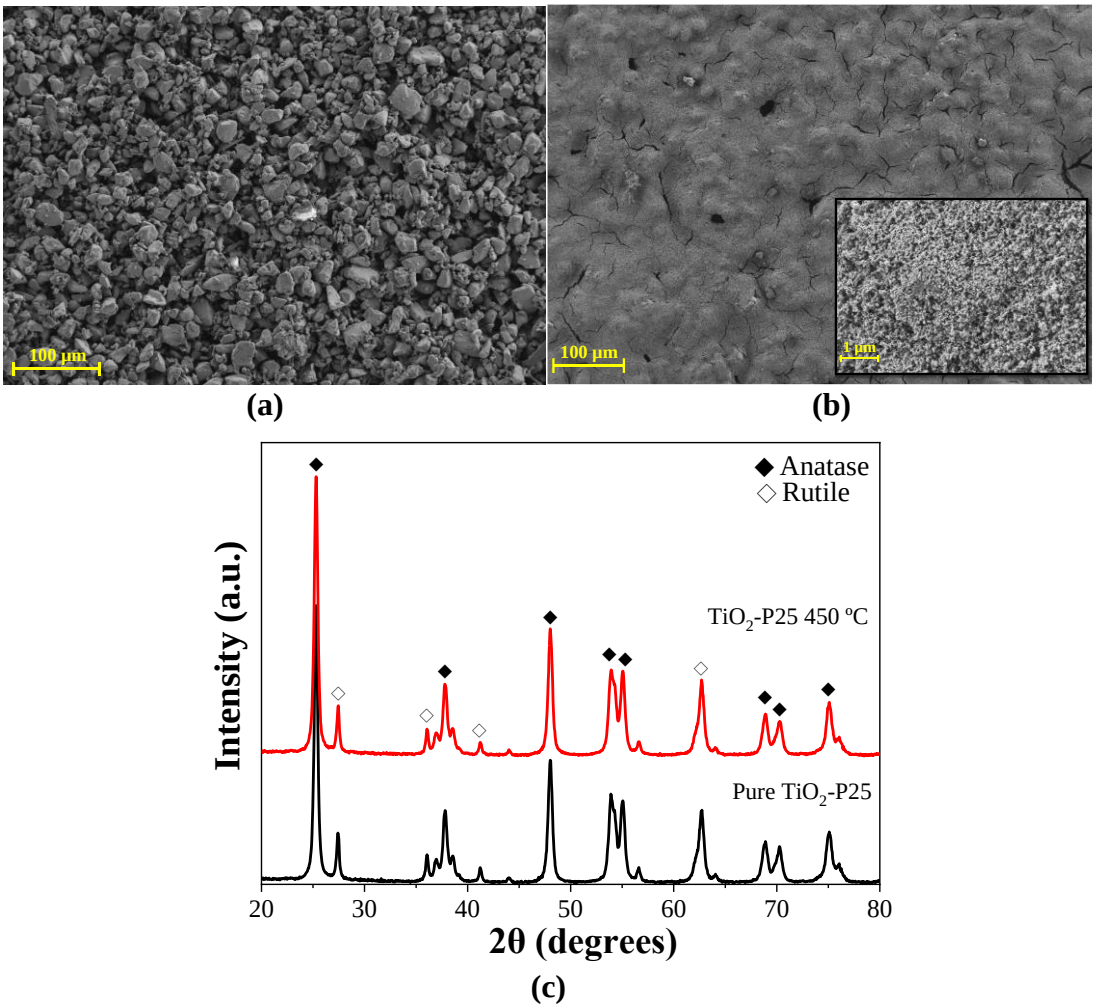

Figure 5.1. SEM images of the (a) unmodified borosilicate membrane, (b) borosilicate membrane after deposition of TiO_2-P25 (2% w/v), and (c) XDR patterns of pure TiO_2-P25 and after thermal treatment.

5.3.2 Determination of bubble size distribution, mean bubble size, gas holdup and specific interfacial area

After the addition of the TiO_2 surface layer, the membrane showed a pore size of 3.8 µm, meaning a decrease in the initial pore size of the pristine membrane (5 µm). This allows reducing the size of the

O_3 bubbles generated by the contact between the membrane surface and the liquid phase. Figure 5.2a shows the average distribution of equivalent bubble diameters. The bubble diameter distribution is detailed using histograms with 5 classes. The first frequency peak appears with bubbles <0.1 mm (representing more than 60% of the bubble size) and the second between 0.1 and 0.3 mm (>30%). The average size of the ozone bubbles formed by the new ozone membrane contactor is approximately 0.20 ± 0.04 mm (Conditions: Q_L = 150 L h^{-1}; Q_G = 0.75 Ndm^3 min^{-1}; T = 20 ºC). The average bubble diameter for the bubble column can vary between 2 and 4 mm [1].

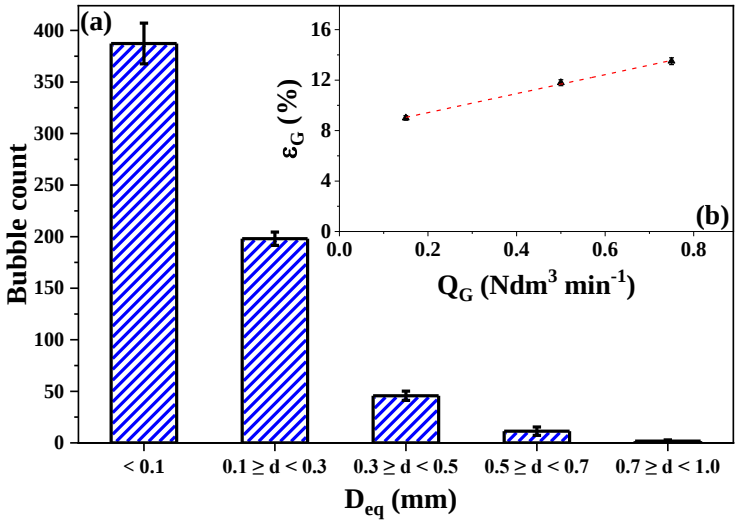

Figure 5.2. a) Bubble size distribution in the tubular porous borosilicate membrane contactor. Conditions: Q_L = 150 L h^{-1}; Q_G = 0.75 Ndm^3 min^{-1}; T = 20 ºC. b) Influence of the gas flow rate (Q_G) on the gas holdup ε_G (%).

The volume fraction of the gas phase, also known as gas holdup (ε_G), was calculated according to Equation (2.17) and values between 9.0 and 13.5% were obtained (Figure 5.2b). Finally, images obtained allowed the determination of the bubble size distribution and mean bubble size (Conditions: Q_L = 150 L h^{-1}; Q_G = 0.75 Ndm^3 min^{-1}; T = 20 ºC), corresponding to Sauter mean diameter (d_{32} = 0.38 mm), gas holdup (ε_G = 13.5%) and specific interfacial area (a = 2131.6 m^{-1}).

5.3.3 Determination of self-decomposition constant of O_3 and dissolved O_3 concentration at saturation

The experiments to determine the self-decomposition constant of O_3 were carried out, in batch mode, with DW at water pH of 3.0 ± 0.2, T = 20 ºC, Q_G = 0.75 Ndm^3 min^{-1}, $[O_3]_{G,inlet}$ = 20 g Nm^{-3}, Q_L = 50 L h^{-1} (Figure 5.3). A plot of $\ln([O_3\infty]/[O_3])$ versus t for the self-decomposition data in Figure 5.3 yielded a straight line (R^2 = 0.9850) with a slope of k_d of (131 ± 7) ×10^{-4} min^{-1}, which was close to the literature values [2, 3]. The K_La value is notably more significant than the k_d value (K_La = 0.53 ± 0.02 min^{-1} >> k_d = (131 ± 7) ×10^{-4} min^{-1}; more than 40 times higher). Thus, the k_d value

can be considered negligible for these experimental conditions. This means that the mass balance of O_3 in the liquid (Equation (2.9)) can be converted into Equation (5.1):

$$\frac{d[O_3]}{dt} = K_L a \times ([O_3^*] - [O_3]) \quad (5.1)$$

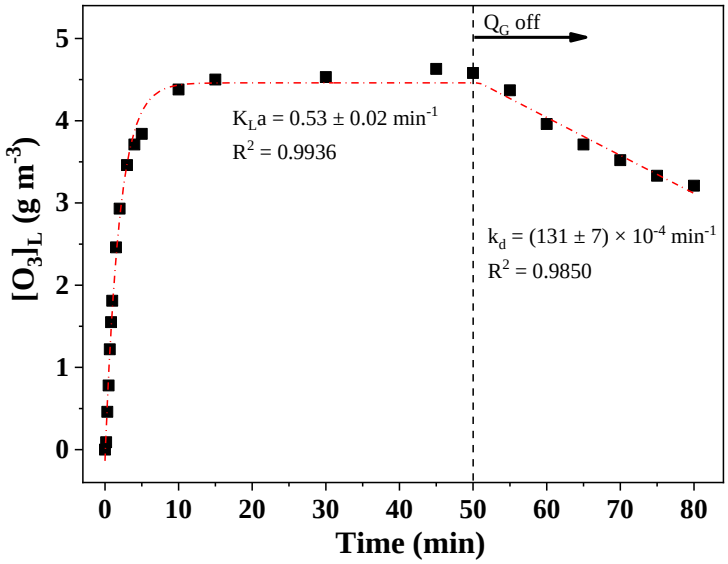

Figure 5.3. Time course of ozone dissolution in water and ozone self-decomposition using the tubular porous borosilicate membrane contactor. Conditions: Q_L = 50 L h^{-1}; Q_G = 0.75 Ndm^3 min^{-1}; $[O_3]_{G,inlet}$ = 20.0 ±1.0 g Nm^{-3}; T = 20 ºC; pH = 3; batch mode.

The ozone concentration at saturation $[O_3^*]$ was 4.65 ± 0.07 g Nm^{-3} (Figure 5.4) for the following operating conditions: $[O_3]_{G,inlet}$ = 20 g Nm^{-3}; Q_G = 0.75 Ndm^3 min^{-1}; T = 20 ºC; pH = 3; batch mode. The ozone saturated value in water is close to the theoretical value found by Henry's law [4].

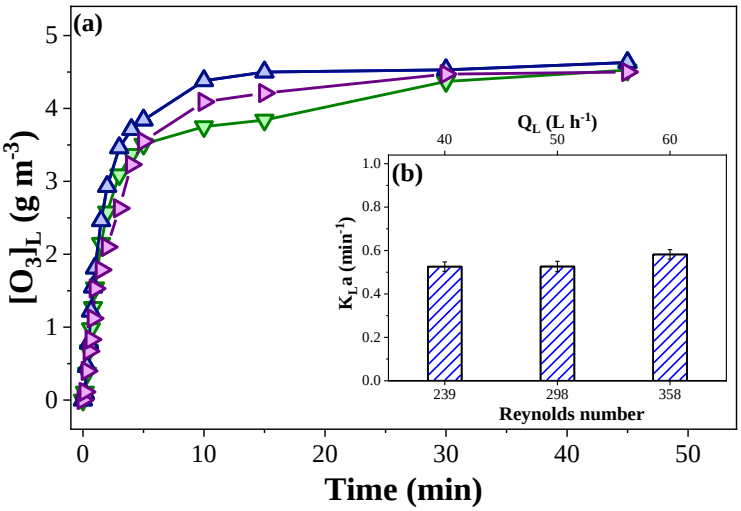

Figure 5.4. Dissolved ozone concentration in the liquid phase as a function of time (a), and the effect of liquid flow rate and Reynolds number on the K_La value (b). Note: 50 (▽); 60 (▷); and 150 (△) L h^{-1}. Conditions: Q_G = 0.75 Ndm^3 min^{-1}; $[O_3]_{G,inlet}$ = 20.0 ±1.0 g Nm^{-3}; T = 20 ºC; pH = 3; batch mode.

5.3.4 Effect of operating parameters on K_La using the ozone membrane contactor under continuous mode

5.3.4.1 Water pH and temperature

The increase in the water pH (from 3 to 9) negatively influenced K_La values (Table 5.1 and Figure 5.5), as reported by Roth and Sullivan [4], who point to a decrease in Henry's constant for O_3 in water as the pH drops. According to the authors, a lower value of Henry's constant leads to a higher value of solubility and, consequently, of K_La. Thus, the concentration of O_3 in water ($[O_3]_L$) increased gradually as the pH dropped (Table 5.1 and Figure 5.5), with $[O_3]_L$ at pH 3 around 3 times higher than at pH 7. Decreasing the pH of the solution can help reduce O_3 self-decomposition (since hydroxide ions act as reaction initiators, Equations (1.9) and (1.10) [5-7]) and promote the dissolution of O_3 in the liquid phase. Therefore, for better gas-liquid mass transfer results and increased O_3 concentration in the water, the pH of the solution must be reduced to create an acidic environment minimising the presence of hydroxide ions. Thus, to avoid the decomposition of the molecular ozone into hydroxyl radicals, all the tests to assess mass transfer were carried out at a pH value of 3.

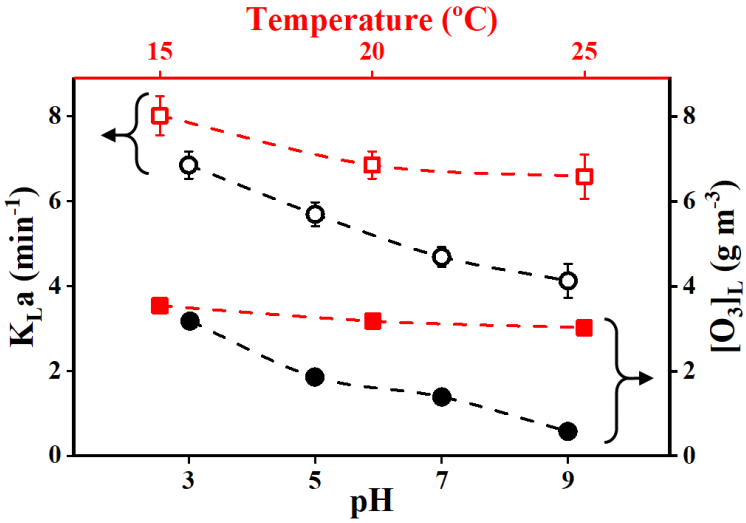

Figure 5.5. Effect of water pH value (–○–; –●–) and operating temperature (–□–; –■–) on K_La value (open symbols) and on ozone solubility in the liquid-phase-$[O_3]_L$ (closed symbols). Conditions: $Q_L = 50$ L h^{-1}; $[O_3]_{G,inlet} = 20$ g Nm^{-3}; $Q_G = 0.75$ Ndm^3 min^{-1}.

According to Henry's law, the solubility and half-life of the O_3 molecule can be directly affected by the liquid temperature. The water temperature was shown to be inversely proportional to the O_3 concentration in the liquid-phase (Table 5.1 and Figure 5.5). Therefore, by increasing the temperature: (i) the O_3 decomposition was accelerated and the stability of O_3 in water decreased, thus reducing the $[O_3]_L$ [8]; (ii) specific properties of the liquid were changed, such as lower surface tension and viscosity, increasing the transfer resistance through the liquid-phase due to the reduction of cavitation intensity [9]. As can be seen in Figure 5.5, the K_La value reached a maximum reduction of

approximately 20% at a 10 ºC increase in temperature (15 ºC to 25 ºC) and the amount of O_3 in the water showed a small tendency to fall with the increase of the operational temperature. The small difference in the K_La value between 20 ºC and 25 ºC may be related to the fact that this parameter involves two opposite contributions. On the one hand, Henry's constant decreases as the temperature increases, leading to lower O_3 solubility. On the other hand, the Arrhenius equation predicts an increase in the reaction rate of ozonation with temperature [10]. Despite this, ozonation has the advantage of taking place under normal conditions of temperature, thus minimising the need to heat the reactor, which is economically preferable. Thus, hereafter only data taken at 20 ºC will be analysed.

5.3.4.2 Liquid flow rate

For different liquid flow rates (Q_L = 20–150 L h^{-1}), it can be seen (Figure 5.6a) that the K_La value increased up to Q_L of 50 L h^{-1} and after that remained constant. A possible reason for this phenomenon is that with increasing Q_L there is more significant liquid turbulence, i.e., a higher Reynolds number, resulting in the formation of smaller gas bubbles or thinner liquid films, with a consequent increase in the interfacial area and reducing the resistance to O_3 transfer in the water phase boundary layer. Furthermore, hydrodynamics studies of tubular photoreactors with a tangential position of inlet/outlet pipes have shown that these reactors tend to exhibit turbulent flow patterns even at low Reynolds numbers [11] and a longer effective flow path (i.e., longer contact time) due to the helical motion of the water around the inner tube [12]. Another reason for this phenomenon is that the shear rate on the membrane surface increases as the flow rate increases. Therefore, the microbubbles attached by surface tension to the membrane surface are removed faster. It is worth remembering that when the reactor works in continuous mode, there is a direct interference between the liquid velocity and the residence time. Therefore, with the increase in the liquid flow, inversely occurs the reduction of the concentration of O_3 in the water at steady-state (Figure 5.6b). Thus, the $[O_3]_L$ decreased from 3.6 g m^{-3} to 1.4 g m^{-3} when Q_L increased from 20 L h^{-1} to 150 L h^{-1}.

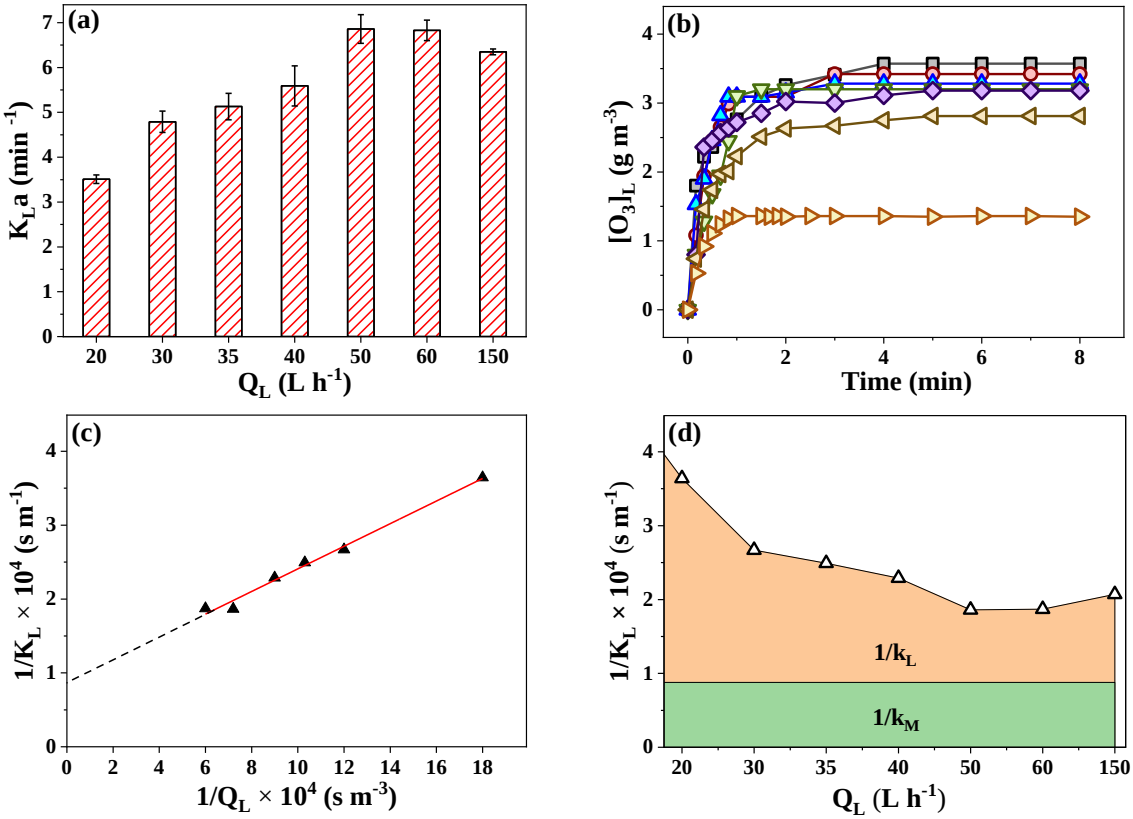

Figure 5.6. Effect of liquid flow rates (a) on K_La value and (b) on dissolved ozone concentration over time; (c) "Wilson plots" for volumetric mass transfer coefficient and water flow, and (d) mass transfer resistances in the water phase boundary layer ($1/k_L$) and in the membrane ($1/k_M$) as a function of water flow rate (Q_L = 20 (—□—), 30 (—○—); 35 (—△—); 40 (—▽—); 50 (—◇—); 60 (—◁—); 150 (—▷—) L h^{-1}). Conditions: Q_G = 0.75 Ndm^3 min^{-1}; $[O_3]_{G,inlet}$ = 20 g Nm^{-3}; T = 20 ºC; pH = 3.

The membrane mass transfer coefficient (k_M) was obtained from "Wilson plot", whereby the values of $1/K_L$ were plotted against $1/Q_L$ (Figure 5.6c). Thus, the mass transfer resistance in the membrane ($1/k_M$) was determined by extrapolating the linear fit of the data to $1/Q_L = 0$, implying $Q_L \rightarrow \infty$ and thus $1/k_L \approx 0$ (see Equation ((2.15))). The same linear trend has been reported in other studies combining membranes with O_3 [2] and O_2 [13]. A least-squares regression analysis of the data in Figure 5.6c gave a value of $1/k_M = (8.8 \pm 0.1) \times 10^3$ s m^{-1} for the tubular porous borosilicate membrane, which corresponds to the k_M value of $(1.14 \pm 0.01) \times 10^{-4}$ m s^{-1}. The resistance in the membrane matrix is affected by pore size, membrane thickness and hydrophobicity. Membranes with smaller pores, larger thicknesses and lower hydrophobicity present greater resistance to O_3 mass transfer [14]. This emphasizes the importance of the structural material used. The mass transfer coefficient in the membrane can be also calculated from the structural properties of the membrane by Equation (1.6) [13]. Where D_M is the effective diffusion coefficient of ozone in the membrane (m^2 s^{-1}), ε is the porosity of the membrane (45%), τ_p is the pore tortuosity and Δx is the membrane thickness (5.2 mm). The τ_p was estimated by the porosity-tortuosity relationship defined by Iversen et al. [15] ($\tau_p = (2 - \varepsilon)^2 / \varepsilon$). Inside the membrane pores, the gas can flow by molecular diffusion and Knudsen diffusion (D_K). D_M can therefore be expressed as Equation (1.7)

and D_K is defined by $D_K = \frac{d_{pore}}{3} \times \sqrt{\frac{8 \times R \times T}{\pi \times M}}$. Therefore, Equation (1.7) can be rewritten as Equation (5.2).

$$D_M = \frac{1}{\frac{1}{D_{O_3}} + \frac{1}{\frac{d_{pore}}{3} \times \sqrt{\frac{8 \times R \times T}{\pi \times M}}}} \tag{5.2}$$

where D_{O_3} is the diffusion coefficient of ozone in the gas phase (2×10^{-5} m^2 s^{-1} at 20 ºC [17]), T is the temperature (293.15 K), M is the molar mass of ozone (47.998 g mol^{-1}), R is the ideal gas constant (8.3145 J K^{-1} mol^{-1}), and d_{pore} is the mean pore diameter (3.8×10^{-6} m). Substituting the terms in Equation (1.6) gives $k_M = 1.4 \times 10^{-4}$ m s^{-1} which is slightly higher than the experimental k_M value of $(1.14 \pm 0.01) \times 10^{-4}$ m s^{-1}. This shows the consistency of the experimental results obtained. Moreover, using Equation (2.15) and the experimental values K_L and k_M, the liquid-phase mass transfer coefficient (k_L) can be obtained by the following equation (Equation (5.3)).

$$k_L = \left(\frac{1}{K_L} + \frac{1}{k_M}\right)^{-1} \tag{5.3}$$

The results of individual mass-transfer resistances for O_3 dissolution in water are shown in Figure 5.6d. The resistance to diffusion through the water phase boundary layer ($1/k_L$) is the main resistance to ozone transfer providing 53–76% of the total mass transfer resistance, while the contribution of the membrane phase varies between 24% and 47%. In the present study, the membrane was doped with TiO_2, which has a superhydrophilic character. Kukuzaki et al. [2] reported the main resistances to ozone transfer for hydrophilic and hydrophobic membranes and showed that the individual mass transfer coefficient for membrane and water phase were higher when using a hydrophobic membrane. This is a consequence of the liquid penetration into the pores, which over time makes the resistance in the membrane more significant and closer to the liquid phase resistance [18]. Hence, it is assumed that the membrane pores were partially wetted, leading to a higher membrane resistance than the non-wetted pores. The reduction in resistance to diffusion through the water phase boundary as the flow rate increased (Figure 5.6d) resulted from higher shear over the membrane, which favoured faster removal of the microbubbles attached by surface tension to the membrane surface.

5.3.4.3 Applied ozone concentration

The effect of O_3 concentration in the inlet gas stream ($[O_3]_{G,inlet}$) on the values of $[O_3]_L$ and on K_La are summarised in Table 5.1 and Figure 5.7. Note that when $[O_3]_{G,inlet}$ increases 4 times (from 20 g Nm^{-3} to

80 g Nm^{-3}), $[O_3]_L$ raises ~7 times (from 3.18 g m^{-3} to 22.3 g m^{-3}) (Figure 5.7a). The relationship between O_3 in the gas-phase and soluble O_3 in the liquid-phase can be represented by Henry's law. The concentration of dissolved O_3 in water at steady-state increases with the enhancement of equilibrium pressure and O_3 gas concentration due to the higher O_3 diffusion rate [2]. Therefore, by increasing the $[O_3]_{G,inlet}$, more O_3 molecules are available in the liquid-phase, improving O_3 concentration (driving force). In turn, the K_La values for the different initial $[O_3]_{G,inlet}$ were almost constant and independent (Figure 5.7b), which shows the stability of the ozone mass transfer device in good agreement with those observed by other studies [2, 19, 20]. The mass transfer rate is controlled by the degree of turbulence and shear in the shell side of the membrane.

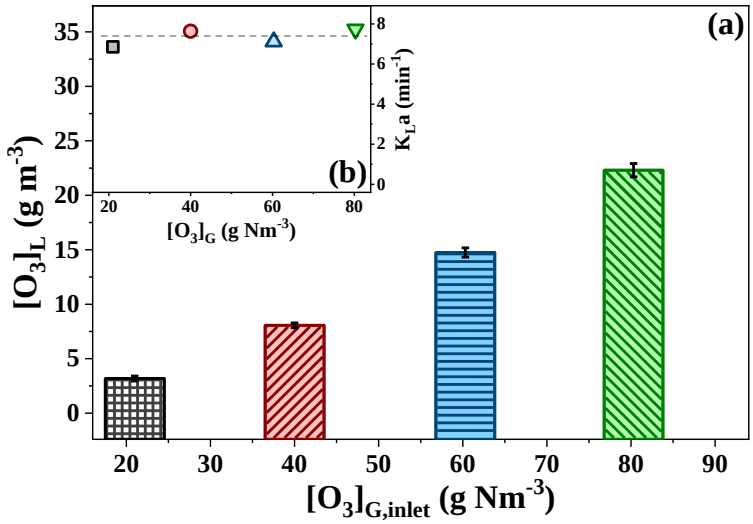

Figure 5.7. Effect of applied ozone concentration on ozone solubility in the liquid-phase (a) for ozone concentrations of 20 (▦), 40 (▨), 60 (▭) and 80 (▨) g Nm^{-3} *a*nd (b) the respective K_La values. Conditions: Q_L = 50 L h^{-1}; Q_G = 0.75 Ndm^3 min^{-1}; T = 20 ºC; pH = 3.

5.3.4.4 Inlet ozone gas flow rate

The mass transfer results (Figure 5.8) indicate that a higher ozone gas flow rate (Q_G) decreases the required time to reach the dissolved O_3 equilibrium in the reactor and slightly improves the equilibrium concentration. With the increase in Q_G, the amount of O_3 injected per unit of time increases and, thereby, accelerates the dissolution rate of O_3 until equilibrium (Figure 5.8a). Additionally, an increase in the gas flow rate enhances the turbulence in the gas-liquid interface [2] and, therefore, improves the number/velocity of the generated bubbles and disperses the liquid better, resulting in a higher gas-liquid interface area and enabling a higher mass transfer (Figure 5.8b). Moreover, the liquid is fed tangentially to the inner surface of the outer tube, inducing a helical motion of the water that provides additional gas mixing. It reduces local points near the external membrane surface where greater O_3 concentrations are observed, enhancing the mass transfer. A pressure differential between the gas and water phases can enable larger O_3 dosages and control the amount of O_3 delivered to the water.

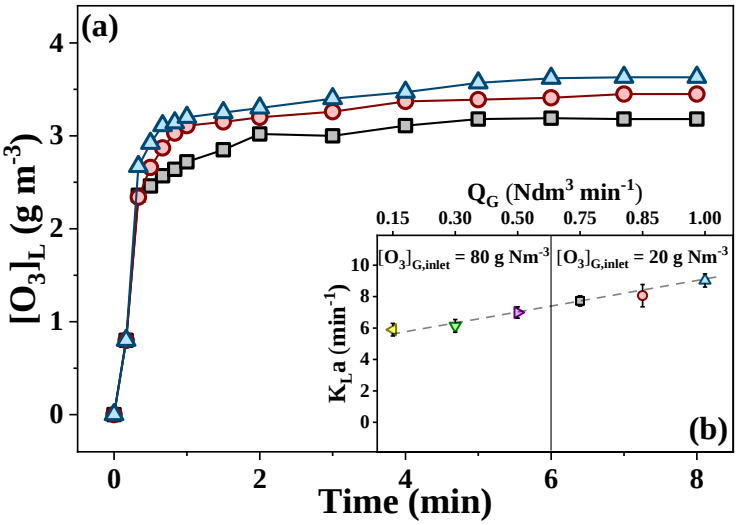

Figure 5.8. Effect of inlet ozone gas flow rate (a) on ozone solubility in the liquid-phase for gas flow of 0.75 (—■—), 0.85 (—○—) and 1.00 (—△—) Ndm^3 min^{-1} and (b) in the respective K_La values. Conditions: Q_L = 50 L h^{-1}; $[O_3]_{G,inlet}$ = 20 g Nm^{-3}; T = 20ºC; pH = 3.

In continuous mode, raising the gas velocity from 0.75 to 1.00 Ndm^3 min^{-1}, K_La increased 1.3-fold, presenting its highest value in DW with no reaction (9.0 ± 0.4 min^{-1}, Table 5.1). Considering that in conventional ozonation processes, $K_La \cong k_L$a, the intensified volumetric mass transfer coefficients obtained in this work is higher than in bubble columns [21] and comparable to highly optimized venturi injectors [22] and static mixers [23] (Table 5.2). Moreover, membrane contactors have further advantages over conventional injectors. Membrane length can be quickly increased, meaning even more O_3 "dosing" points, which is not possible for conventional single-point injection systems like the venturi tube and static mixer. In addition, functionalized membranes can be applied to enhance the performance of the ozonation system, either for O_3/O_2 separation to obtain an O_3-enriched gas stream or for promoting synergetic catalytic effects with O_3. Compared with other membrane contactors (Table 5.2), the present study enabled higher mass transfer coefficients (K_La and K_L - from 2 to 30 times higher, except for the study of Pines et al. [24]), as allows the use of a functionalised membrane to promote synergistic effects between photocatalysis and ozonation for water/wastewater treatment purposes.

Table 5.2. Characteristics of ozone-liquid contacting systems.

Type of contactor		Liquid flow ($L\ h^{-1}$)	Gas flow ($Ndm^3\ min^{-1}$)	K_La (min^{-1}) / K_L ($m\ s^{-1}$)	Reference
Conventional	Static mixers	90–138	0.4–0.8	6–18 min^{-1}	[23]
	Venturi injectors	1080–6336	3–24	4.2–18 min^{-1}	[22]
	Bubble column	100–450	5–20	0.18–1.2 min^{-1}	[21]
Membrane	Non-porous tubular polydimethylsiloxane (PDMS)	0.3–1.2	0.1	2.4×10^{-6} m s^{-1}	[25]
	Tubular Shirasu porous glass (SPG)	72–480	0.2	1.2×10^{-5} m s^{-1}	[2]
	Polytetrafluorethylene (PTFE) hollow fibre membrane	100–500	-	0.438 min^{-1}	[9]
	Flat porous and non-porous Teflon membranes	1.5–120	0.10–0.11	7.6×10^{-5} m s^{-1}	[24]
	Polytetrafluoroethylene (PTFE) hollow fibre membrane	100–500	-	0.7858 min^{-1}	[26]
	Tubular porous borosilicate	20–150	0.15–1.00	3.5–9.0 min^{-1} / 2.7–5.4×10^{-5} m s^{-1}	This work

5.3.5 Mass transfer efficiency (*MTE*)

The mass transfer efficiency (*MTE*) is defined as the portion of applied O_3 that goes into the solution and is calculated from the mass of applied O_3 and the mass of O_3 in the liquid-phase as follows (Equation (5.4)):

$$MTE\ (\%) = \frac{Q_L \times [O_3]_L}{Q_G \times [O_3]_G} \times 100 \qquad (5.4)$$

For a fixed Q_L of 50 L h^{-1} (Figure 5.9), a slight increase in *MTE* was observed with the decrease in the Q_G, mainly associated with a higher contact time between both phases. On the other hand, for a fixed Q_G of 0.75 Ndm^3 min^{-1}, it can be seen that the *MTE* increased proportionally with the water flow (Figure 5.9). This indicates the ability to work with low gas/liquid volumetric ratios, which is an appealing feature when considering the treatment of large volumes of wastewaters, such as secondary effluents from UWWTPs. For the operational conditions tested, the highest mass transfer efficiency of 23% was obtained by applying the lowest input Q_G, 0.75 Ndm^3 min^{-1}, and the highest Q_L, 150 L h^{-1}. Other contacting devices, such as multi-orifice oscillatory baffled columns, can achieve higher rates of *MTE*, although the equipment involved may require higher power input [27]. Therefore, these conditions were selected for the following ozonation tests to assess the membrane contactor application for the removal of a mixture of CECs in water.

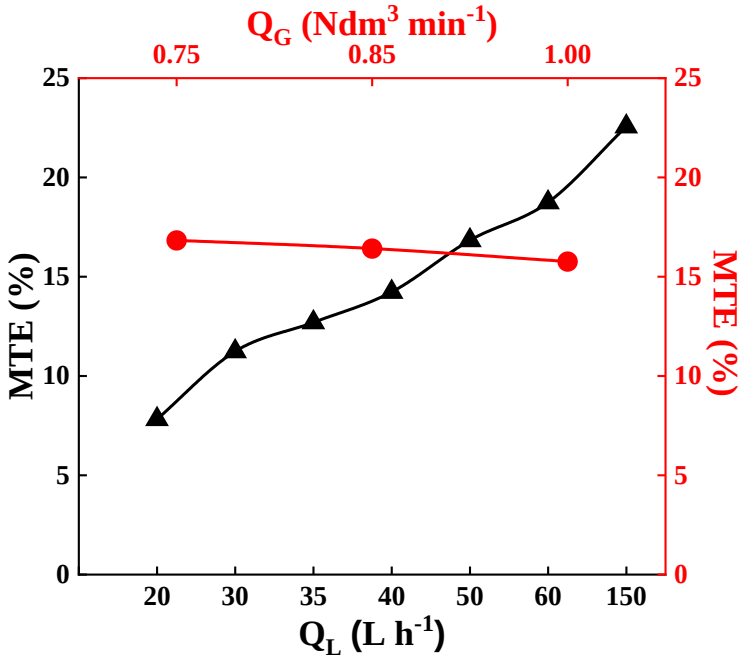

Figure 5.9. Ozone mass transfer efficiency (*MTE* %) as a function of water (—▲—) and inlet gas (—●—) flow rates obtained using the ozone membrane contactor. Conditions: $[O_3]_{G,inlet}$ = 20 g Nm^{-3}; T = 20 ºC; pH = 3; fixed Q_L = 50 L h^{-1} or fixed Q_G = 0.75 Ndm^3 min^{-1}.

5.3.6 Ozone membrane contactor for the degradation of CECs

The effectiveness of the ozone membrane contactor was evaluated by targeting the removal of 19 CECs in DW at natural pH of 6.5. The CECs were selected based on their occurrence in the water cycle, persistence during treatment and potential toxicity to health and the environment, according to the results obtained in several screening campaigns conducted under the NOR-WATER project (http://nor-water.eu/en/home/). CECs in water can react simultaneously with ozone (direct reaction) and hydroxyl radicals (indirect reaction) at different rates depending on the water pH. The underlying mechanisms for in situ formation of hydroxyl radicals by oxidation of water with O_3 at pH 7–9 have been extensively described in the literature [5, 17, 28, 29].

As shown in Figure 5.10a, the ozonation showed satisfactory degradation (>80% for 13 out of the 19 CECs) applying an ozone dose of 12 g m^{-3} ($D_{T\text{-}O_3}$ = 4.3 g m^{-3}) and a Q_L of 150 L h^{-1}. The greater removal of CECs as a function of O_3 dosage (Figure 5.10a) can be related to the higher rate of O_3 mass transfer in the membrane ozonation reactor [30]. The highly stable organic compound MLN and PFAS (PFBA, PFOA, PFBS, TFMS) showed a low reactivity with ozone even at higher ozone doses ($D_{A\text{-}O_3}$ = 18 g m^{-3}; $D_{T\text{-}O_3}$ = 7.1 g m^{-3}). Studies on the degradation of the MLN compound are still lacking, especially with O_3. Maurino et al. [31] tested several advanced oxidation processes to remove MLN and concluded that only photocatalysis and the generation of $SO_4^{\bullet-}$ are capable of transforming MLN. They indicated that the primary photocatalytic event is the oxidation of the amino group, which reacts slowly with O_3 [32]. A possible explanation for the poor removal of PFAS may be the low reactivity with O_3, indicating that large amounts of energy are required for their degradation [33]. The recalcitrance of PFAS towards ozonation is due to their strong carbon–fluorine bonds that make this compound a very stable and resistant pollutant. Other authors have also reported that ozonation has been shown to be relatively ineffective for PFAS destruction, even with a long residence time [34-36]. As the membrane contactor was designed to evaluate the interaction of the photocatalytic ozonation process, the O_3/UVC/TiO_2 process was also performed to promote the generation of hydroxyl radical species (Figure 5.10b). Nonetheless, the removal of MLN or PFAS was not improved. The low residence time (3.9 s) and UVC fluence (50 mJ cm^{-2}) applied in this treatment, resulting in a considerably lower UV dose than those normally used in UWWTPs [37], may be acting as limiting factors for the effective oxidation of these compounds. This is underlined by the experiment without ozone (photocatalysis, UVC/TiO_2), where negligible removals (<10%) for all CECs were obtained. On the other hand, O_3/UVC/TiO_2 process had a slightly better removal efficiency than the ozonation for SCH (from 44% to 62%), which can be related to the greater amount of hydroxyl radicals available in the medium, since SCH shows high reactivity with this radical [38].

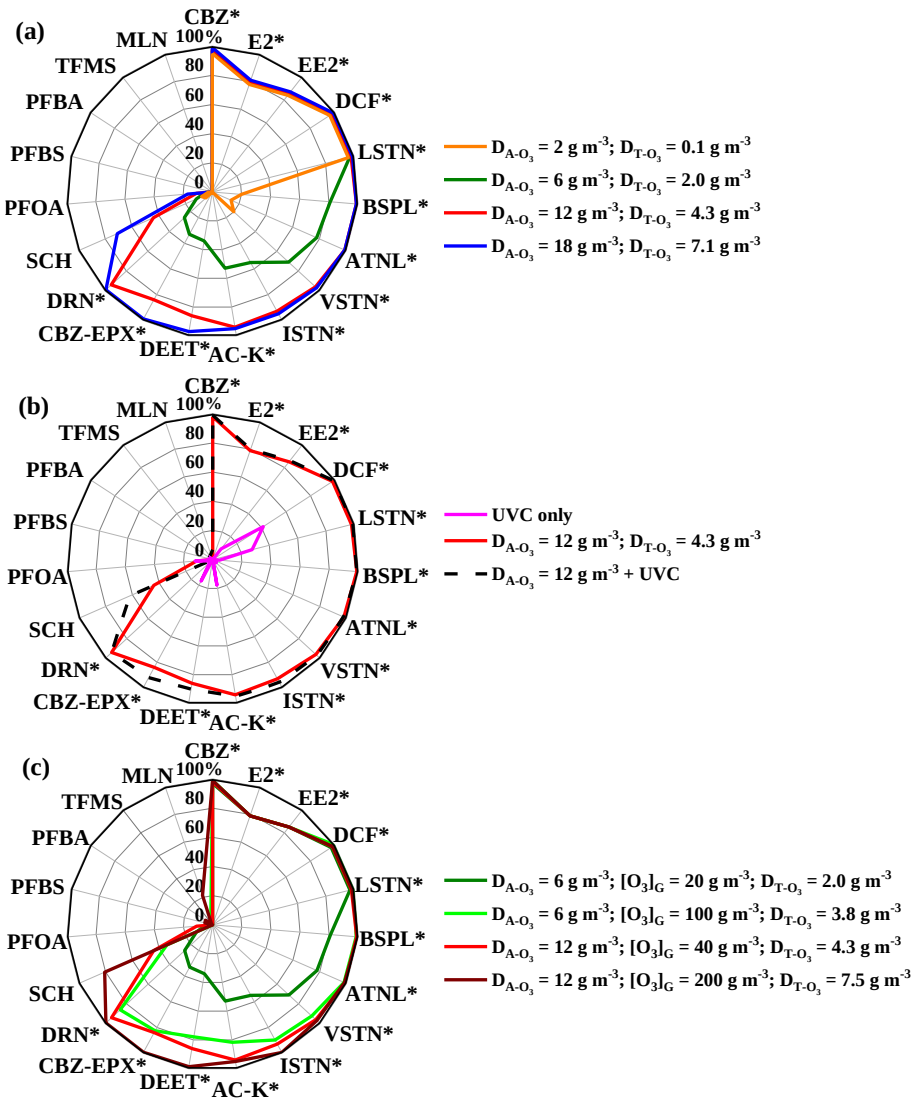

Figure 5.10. CECs removal in continuous mode: effect of (a) ozone dosage, (b) UVC/TiO_2 process and (c) inlet ozone concentration in the gas stream. Conditions: DW spiked with CECs (10 µg L^{-1} of each CEC); T = 20 ºC; pH = 6.5; Q_G = 0.15 and 0.75 Ndm^3 min^{-1}; Q_L = 150 L h^{-1}; $[O_3]_{G,inlet}$ = 20, 40, 100 and 200 g Nm^{-3}. *The removal values are presented as the maximum percentage that can be determined, taking into account the limits of quantification of the analytical method (Table 2.6).

To further assess the ozonation treatment, tests were carried out for two O_3 doses ($D_{A\text{-}O_3}$ of 6 or 12 g m^{-3}) and for each two O_3-gas flow rates (Q_G of 0.15 or 0.75 L min^{-1}) (Figure 5.10c). For the same $D_{A\text{-}O_3}$ it is advantageous to reduce the Q_G while increasing the ozone-gas concentration applied to the treatment. Since the main driving force for ozone mass transfer is the concentration difference in the gas–liquid two-phase. This indicates that more O_3 is being transferred from the gaseous to the liquid phase as a result of the increase in $[O_3]_{G,inlet}$ [39] and, consequently, the degradation rate of CECs is promoted (Figure 5.10c).

Another important factor in the interpretation of results is the determination of the Hatta number (*Ha*), a recognized necessary standard that provides information about the competition between reaction

kinetics and the rate of mass transfer [40]. As seen previously (*Section 5.3.4.2*), the mass transfer mechanism in the ozone membrane contactor can be divided into three regions (gaseous phase, membrane, and liquid phase). Therefore, *Ha* is the criterion for determining where the reaction occurs. In the present study, the data required to calculate this number can only be obtained for 13 of the 19 CECs, i.e., those that were effectively removed with ozonation (for $D_{A\text{-}O_3}$ = 12 g m^{-3}, Q_G = 0.75 Ndm^3 min^{-1}; Q_L = 150 L h^{-1}). These 13 CECs were divided into 8 groups due to their similarity. To identify the reaction regime and place during the reaction between CECs and dissolved ozone, the *Ha* is given by (Equation (5.5)) [41]:

$$Ha = \frac{\sqrt{k_{O_3} \times Dw_{O_3} \times [CECs]_0}}{k_L} \tag{5.5}$$

where k_{O_3} is the rate constant of the direct reaction between ozone and the pollutant (M^{-1} s^{-1}), Dw_{O_3} is the diffusivity of ozone in water (1.76×10^{-9} m^2 s^{-1}) [42], $[CECs]_0$ is the CECs concentration in the feed liquid stream (M) and k_L is the ozone mass transfer coefficient to the liquid (K_L cannot be considered due to the high mass transfer resistance in the membrane – *Section 5.3.4.2*). Since the reaction is with a mixture of 13 CECs, the k_{O_3} value adopted for each group was that of the chemical with the lowest rate constant, as it will limit the overall reaction rate (see Table 5.3). The k_L of 4.8×10^{-5} m s^{-1} was calculated considering the value of K_La obtained in our study for the experimental conditions used in the CECs ozonation. The *Ha* values obtained for the studied compounds were below 0.5 (Table 5.3). According to Charpentier [43], this corresponds to a moderate reaction, which occurs both in the liquid film and in the liquid bulk. The most recommended reactors to promote this type of reaction have high interfacial area and high liquid retention time. In the present study, the tubular porous borosilicate membrane contactor gave a high interfacial area (2131.6 m^{-1}) and a short liquid retention time (3.9 s), an advantageous feature when treating effluents with high flow rates, such as UWW.

Table 5.3. Hatta number values for the studied compounds.

CECs	$[CECs]_0$ (M)	Sum $[CECs]_0$ (M)	k_{O_3} (M^{-1} s^{-1})	Lowest k_{O_3} (M^{-1} s^{-1})	Hatta number (*Ha*)
CBZ	4.23×10^{-8}	8.20×10^{-8}	3.0×10^{5} [44]	3.0×10^{5}	0.14
CBZ-EPX	3.96×10^{-8}		unknown		
DCF	3.38×10^{-8}	3.38×10^{-8}	1.0×10^{6} [44]	1.0×10^{6}	0.16
EE2	3.37×10^{-8}	7.04×10^{-8}	3.0×10^{6} [44]	1.7×10^{6}	0.30
E2	3.67×10^{-8}		1.7×10^{6} [44]		
ATNL	3.75×10^{-8}	6.83×10^{-8}	6.3×10^{5} [45]	1.8×10^{4}	0.03
BSPL	3.07×10^{-8}		1.8×10^{4} [46]		
DEET	5.23×10^{-8}	5.23×10^{-8}	0.1 [45]	1.0×10^{-1}	0.0001
ISTN	2.33×10^{-8}	6.99×10^{-8}	23 [45]	2.3×10^{1}	0.0011
LSTN	2.36×10^{-8}		2.1×10^{5} [45]		
VSTN	2.30×10^{-8}		38 [45]		
DRN	4.29×10^{-8}	4.29×10^{-8}	13.3 [44]	1.3×10^{1}	0.0007
AC-K	4.97×10^{-8}	1.04×10^{-7}	88 [45]	8.8×10^{1}	0.003
SCH	5.46×10^{-8}		unknown		

5.4 Conclusions

This study has proven the viability of using a tubular porous borosilicate membrane contactor for radial delivery of O_3, promoting intensification of ozone mass transfer in a compact device and this was applied for the removal of CECs in water. The pseudo-uniform feed distribution of O_3 along the length of an annular membrane creates innumerable micro-sized bubbles, increasing the surface area of the O_3 bubble in contact with the liquid allowing for a controlled dosing of O_3 to the water-side.

Operating in continuous mode and under atmospheric pressure, the K_La values for this membrane reactor (3.5–9.0 min^{-1}) were comparable to that of a venturi injector and were superior to other membrane contactors reported in the literature. The significant enhancements obtained for K_La and *MTE* using this ozone membrane contactor with low gas/liquid volumetric ratios make this type of contactor highly effective for ozone gas/water mass transfer in water treatment.

This ozone membrane contactor was also proven to perform effectively for the removal of CECs by ozone-based processes and removals above 80% were achieved for 13 of the 19 selected CECs when using DW. In this case, the application of photocatalytic ozonation (O_3/UVC/TiO_2) did not significantly improve the removal of CECs. Notwithstanding, the versatility of this setup, allowing the membrane to be doped with a catalyst and operated under UVC radiation, may prove advantageous when treating complex wastewater matrices.

5.5 References

[1] M. Sommerfeld, D. Bröder, Analysis of Hydrodynamics and Microstructure in a Bubble Column by Planar Shadow Image Velocimetry, Industrial & Engineering Chemistry Research 48 (1) (2009) 330-340. https://doi.org/10.1021/ie800838u.

[2] M. Kukuzaki, K. Fujimoto, S. Kai, K. Ohe, T. Oshima, Y. Baba, Ozone mass transfer in an ozone–water contacting process with Shirasu porous glass (SPG) membranes—A comparative study of hydrophilic and hydrophobic membranes, Separation and Purification Technology 72 (3) (2010) 347-356. https://doi.org/10.1016/j.seppur.2010.03.004.

[3] J.C. Achar, G. Nam, J. Jung, H. Klammler, M.M. Mohamed, Microbubble ozonation of the antioxidant butylated hydroxytoluene: Degradation kinetics and toxicity reduction, Environmental Research 186 (2020) 109496. https://doi.org/10.1016/j.envres.2020.109496.

[4] J.A. Roth, D.E. Sullivan, Solubility of ozone in water, Industrial & Engineering Chemistry Fundamentals 20 (2) (1981) 137-140. https://doi.org/10.1021/i100002a004.

[5] H. Tomiyasu, H. Fukutomi, G. Gordon, Kinetics and mechanism of ozone decomposition in basic aqueous solution, Inorganic Chemistry 24 (19) (1985) 2962-2966. https://doi.org/10.1021/ic00213a018.

[6] Y. Jung, E. Hong, M. Kwon, J.-W. Kang, A kinetic study of ozone decay and bromine formation in saltwater ozonation: Effect of O_3 dose, salinity, pH, and temperature, Chemical Engineering Journal 312 (2017) 30-38. https://doi.org/10.1016/j.cej.2016.11.113.

[7] U. von Gunten, Ozonation of drinking water: Part I. Oxidation kinetics and product formation, Water Research 37 (7) (2003) 1443-1467. https://doi.org/10.1016/S0043-1354(02)00457-8.

[8] R. Rosal, A. Rodríguez, M. Zerhouni, Enhancement of gas–liquid mass transfer during the unsteady-state catalytic decomposition of ozone in water, Applied Catalysis A: General 305 (2) (2006) 169-175. https://doi.org/10.1016/j.apcata.2006.02.059.

[9] B. Wang, X. Xiong, Y. Shui, Z. Huang, K. Tian, A systematic study of enhanced ozone mass transfer for ultrasonic-assisted PTFE hollow fiber membrane aeration process, Chemical Engineering Journal 357 (2019) 678-688. https://doi.org/10.1016/j.cej.2018.09.188.

[10] R.C. Martins, R.J.G. Lopes, R.M. Quinta-Ferreira, Lumped kinetic models for single ozonation of phenolic effluents, Chemical Engineering Journal 165 (2) (2010) 678-685. https://doi.org/10.1016/j.cej.2010.09.060.

[11] J.C.G. Peres, U.d. Silvio, A.C.S.C. Teixeira, R. Guardani, A.d.S.V. Jr., Study of an Annular Photoreactor with Tangential Inlet and Outlet: I. Fluid Dynamics, Chemical Engineering & Technology 38 (2) (2015) 311-318. https://doi.org/10.1002/ceat.201400186.

[12] F.C. Moreira, E. Bocos, A.G.F. Faria, J.B.L. Pereira, C.P. Fonte, R.J. Santos, J.C.B. Lopes, M.M. Dias, M.A. Sanromán, M. Pazos, R.A.R. Boaventura, V.J.P. Vilar, Selecting the best piping arrangement for scaling-up an annular channel reactor: An experimental and computational fluid dynamics study, Science of The Total Environment 667 (2019) 821-832. https://doi.org/10.1016/j.scitotenv.2019.02.260.

[13] G.T. Vladisavljević, Use of polysulfone hollow fibers for bubbleless membrane oxygenation/deoxygenation of water, Separation and Purification Technology 17 (1) (1999) 1-10. https://doi.org/10.1016/S1383-5866(99)00012-X.

[14] K. Li, Y. Zhang, L. Xu, L. Liu, Z. Wang, D. Hou, Y. Wang, J. Wang, Mass transfer and interfacial reaction mechanisms in a novel electro-catalytic membrane contactor for wastewater treatment by O_3, Applied Catalysis B: Environmental 264 (2020) 118512. https://doi.org/10.1016/j.apcatb.2019.118512.

[15] S.B. Iversen, V.K. Bhatia, K. Dam-Johansen, G. Jonsson, Characterization of microporous membranes for use in membrane contactors, Journal of Membrane Science 130 (1) (1997) 205-217. https://doi.org/10.1016/S0376-7388(97)00026-4.

[16] R.H.S. Jansen, J.W. de Rijk, A. Zwijnenburg, M.H.V. Mulder, M. Wessling, Hollow fiber membrane contactors—A means to study the reaction kinetics of humic substance ozonation, Journal of Membrane Science 257 (1) (2005) 48-59. https://doi.org/10.1016/j.memsci.2004.07.038.

[17] S. Bamperng, T. Suwannachart, S. Atchariyawut, R. Jiraratananon, Ozonation of dye wastewater by membrane contactor using PVDF and PTFE membranes, Separation and Purification Technology 72 (2) (2010) 186-193. https://doi.org/10.1016/j.seppur.2010.02.006.

[18] M. Mavroudi, S.P. Kaldis, G.P. Sakellaropoulos, A study of mass transfer resistance in membrane gas–liquid contacting processes, Journal of Membrane Science 272 (1) (2006) 103-115. https://doi.org/10.1016/j.memsci.2005.07.025.

[19] A. Al-Abduly, P. Christensen, A. Harvey, K. Zahng, Characterization and optimization of an oscillatory baffled reactor (OBR) for ozone-water mass transfer, Chemical Engineering and Processing: Process Intensification 84 (2014) 82-89. https://doi.org/10.1016/j.cep.2014.03.015.

[20] X. Huang, X. Quan, W. Cheng, C. Cheng, Z. Cheng, L. Yang, L. Jiang, Enhancement of Ozone Mass Transfer by Stainless Steel Wire Mesh and Its Effect on Hydroxyl Radical Generation, Ozone: Science & Engineering 42 (4) (2020) 347-356. https://doi.org/10.1080/01919512.2019.1676196.

[21] A.K. Bin, B. Duczmal, P. Machniewski, Hydrodynamics and ozone mass transfer in a tall bubble column, Chemical Engineering Science 56 (21) (2001) 6233-6240. https://doi.org/10.1016/S0009-2509(01)00213-5.

[22] M.S. Baawain, M. Gamal El-Din, D.W. Smith, A. Mazzei, Hydrodynamic Characterization and Mass Transfer Analysis of an In-Line Multi-Jets Ozone Contactor, Ozone: Science & Engineering 33 (6) (2011) 449-462. https://doi.org/10.1080/01919512.2011.622705.

[23] C. Tizaoui, Y. Zhang, The modelling of ozone mass transfer in static mixers using Back Flow Cell Model, Chemical Engineering Journal 162 (2) (2010) 557-564. https://doi.org/10.1016/j.cej.2010.05.061.

[24] D.S. Pines, K.-N. Min, S.J. Ergas, D.A. Reckhow, Investigation of an Ozone Membrane Contactor System, Ozone: Science & Engineering 27 (3) (2005) 209-217. https://doi.org/10.1080/01919510590945750.

[25] G.A. Zoumpouli, R. Baker, C.M. Taylor, M.J. Chippendale, C. Smithers, S.S.X. Ho, D. Mattia, Y.M.J. Chew, J. Wenk, A Single Tube Contactor for Testing Membrane Ozonation, Water 10 (10) (2018) 1416. https://doi.org/10.3390/w10101416.

[26] B. Wang, H. Zhang, Q. Meng, H. Ren, M. Xiong, C. Gao, The enhancement of ozone–liquid mass transfer performance in a PTFE hollow fiber membrane contactor using ultrasound as a catalyzer, RSC Advances 11 (23) (2021) 14017-14028. https://doi.org/10.1039/D1RA00452B.

[27] M.S. Lucas, N.M. Reis, G. Li Puma, Intensification of ozonation processes in a novel, compact, multi-orifice oscillatory baffled column, Chemical Engineering Journal 296 (2016) 335-339. https://doi.org/10.1016/j.cej.2016.03.050.

[28] X. Liu, X. Su, S. Tian, Y. Li, R. Yuan, Mechanisms for simultaneous ozonation of sulfamethoxazole and natural organic matters in secondary effluent from sewage treatment plant, Frontiers of Environmental Science & Engineering 15 (4) (2020) 75. https://doi.org/10.1007/s11783-020-1368-0.

[29] J. Wang, H. Chen, Catalytic ozonation for water and wastewater treatment: Recent advances and perspective, Science of The Total Environment 704 (2020) 135249. https://doi.org/10.1016/j.scitotenv.2019.135249.

[30] K. Yaghmaeian, G. Moussavi, A. Mashayekh-Salehi, A. Mohseni-Bandpei, M. Satari, Oxidation of acetaminophen in the ozonation process catalyzed with modified MgO nanoparticles: Effect of operational variables and cytotoxicity assessment, Process Safety and Environmental Protection 109 (2017) 520-528. https://doi.org/10.1016/j.psep.2017.04.020.

[31] V. Maurino, M. Minella, F. Sordello, C. Minero, A proof of the direct hole transfer in photocatalysis: The case of melamine, Applied Catalysis A: General 521 (2016) 57-67. https://doi.org/10.1016/j.apcata.2015.11.012.

[32] W.A. Pryor, D.H. Giamalva, D.F. Church, Kinetics of ozonation. 2. Amino acids and model compounds in water and comparisons to rates in nonpolar solvents, Journal of the American Chemical Society 106 (23) (1984) 7094-7100. https://doi.org/10.1021/ja00335a038.

[33] M. Alameddine, A. Siraki, L. Tonoyan, M. Gamal El-Din, Treatment of a mixture of pharmaceuticals, herbicides and perfluorinated compounds by powdered activated carbon and ozone: Synergy, catalysis and insights into non-free OH contingent mechanisms, Science of The Total Environment 777 (2021) 146138. https://doi.org/10.1016/j.scitotenv.2021.146138.

[34] V. Franke, M.D. Schäfers, J. Joos Lindberg, L. Ahrens, Removal of per- and polyfluoroalkyl substances (PFASs) from tap water using heterogeneously catalyzed ozonation, Environmental Science: Water Research & Technology 5 (11) (2019) 1887-1896. https://doi.org/10.1039/C9EW00339H.

[35] H.F. Schröder, R.J.W. Meesters, Stability of fluorinated surfactants in advanced oxidation processes—A follow up of degradation products using flow injection–mass spectrometry, liquid chromatography–mass spectrometry and liquid chromatography–multiple stage mass spectrometry, Journal of Chromatography A 1082 (1) (2005) 110-119. https://doi.org/10.1016/j.chroma.2005.02.070.

[36] C.D. Vecitis, H. Park, J. Cheng, B.T. Mader, M.R. Hoffmann, Treatment technologies for aqueous perfluorooctanesulfonate (PFOS) and perfluorooctanoate (PFOA), Frontiers of Environmental Science & Engineering in China 3 (2) (2009) 129-151. https://doi.org/10.1007/s11783-009-0022-7.

[37] C.P. James, E. Germain, S. Judd, Micropollutant removal by advanced oxidation of microfiltered secondary effluent for water reuse, Separation and Purification Technology 127 (2014) 77-83. https://doi.org/10.1016/j.seppur.2014.02.016.

[38] C. Ye, X. Ma, J. Deng, X. Li, Q. Li, A.M. Dietrich, Degradation of saccharin by UV/H_2O_2 and UV/PS processes: A comparative study, Chemosphere 288 (2022) 132337. https://doi.org/10.1016/j.chemosphere.2021.132337.

[39] J. Ren, S. He, C. Ye, G. Chen, C. Sun, The ozone mass transfer characteristics and ozonation of pentachlorophenol in a novel microchannel reactor, Chemical Engineering Journal 210 (2012) 374-384. https://doi.org/10.1016/j.cej.2012.09.011.

[40] M.S. Lucas, J.A. Peres, B.Y. Lan, G. Li Puma, Ozonation kinetics of winery wastewater in a pilot-scale bubble column reactor, Water Research 43 (6) (2009) 1523-1532. https://doi.org/10.1016/j.watres.2008.12.036.

[41] H. Benbelkacem, H. Cano, S. Mathe, H. Debellefontaine, Maleic Acid Ozonation: Reactor Modeling and Rate Constants Determination, Ozone: Science & Engineering 25 (1) (2003) 13-24. https://doi.org/10.1080/713610647.

[42] P.N. Johnson, R.A. Davis, Diffusivity of Ozone in Water, Journal of Chemical & Engineering Data 41 (6) (1997) 1485-1487. https://doi.org/10.1021/je9602125.

[43] J.-C. Charpentier, Mass-Transfer Rates in Gas-Liquid Absorbers and Reactors, in: T.B. Drew, G.R. Cokelet, J.W. Hoopes, T. Vermeulen (Eds.), Advances in Chemical Engineering, Academic Press, 1981, pp. 1-133. https://doi.org/10.1016/S0065-2377(08)60025-3.

[44] F.J. Beltrán, A. Rey, Free Radical and Direct Ozone Reaction Competition to Remove Priority and Pharmaceutical Water Contaminants with Single and Hydrogen Peroxide Ozonation Systems, Ozone: Science & Engineering 40 (4) (2018) 251-265. https://doi.org/10.1080/01919512.2018.1431521.

[45] M. Bourgin, B. Beck, M. Boehler, E. Borowska, J. Fleiner, E. Salhi, R. Teichler, U. von Gunten, H. Siegrist, C.S. McArdell, Evaluation of a full-scale wastewater treatment plant upgraded with ozonation and biological post-treatments: Abatement of micropollutants, formation of transformation products and oxidation by-products, Water Research 129 (2018) 486-498. https://doi.org/10.1016/j.watres.2017.10.036.

[46] M. Mustafa. Removal of Micropollutants from Wastewater : evaluation of effect of upgrading ozonation to electro-peroxone. (Doctoral thesis). Umeå University, Umeå, Sweden (2020). Retrieved from http://urn.kb.se/resolve?urn=urn:nbn:se:umu:diva-176567 DiVA database.

6 Ozone Membrane Contactor for Tertiary Treatment of Urban Wastewater: Chemical, Microbial and Toxicological Assessment

This chapter reports the application of the ozone membrane contactor, described in Chapter 5, to promote the tertiary treatment of UWW, targeting the removal of CECs, bacterial disinfection and toxicity reduction. The membrane is also coated with titanium dioxide (TiO_2-P25) and radiation can be externally supplied via four UV lamps. The ozonation tests were carried out with secondary-treated UWW collected in different seasons (winter and summer) and spiked with a mix of 19 CECs (10 µg L^{-1} each). For an O_3 dose of 18 g m^{-3}, the best performance was obtained by increasing the O_3 concentration (maximum $[O_3]_{G,inlet}$ of 200 g Nm^{-3}) and decreasing the gas flow rate (minimum Q_G of 0.15 Ndm^3 min^{-1}), providing the highest ozone transfer yield (88%) and, thus higher specific ozone dose (g O_3 per g dissolved organic carbon). Under these conditions, removals >80% or concentrations below the limit of quantification were obtained for up to 13 of the 19 CECs and reductions up to 5 log units for total heterotrophs and below the limit of detection for enterobacteria and enterococci. Tests including a UVC dose of 0.10 kJ L^{-1} enhanced disinfection ability but had no impact on CECs oxidation. After ozonation, the abundance of antibiotic resistant bacteria was reduced but not eliminated and microbial regrowth after 3-day storage was observed. No toxic effect was detected on zebrafish embryos using a dilution factor of 4 for the ozonized UWW and when granular activated carbon adsorption was subsequently applied the dilution factor decreased to 2.

This chapter is based on the following research article: "Presumido, P.H., Ribeirinho-Soares, S., Montes, R., Quintana, J.B., Rodil, R., Ribeiro, M., Neuparth, T., Santos, M.M., Feliciano, M., Nunes, O.C., Gomes, A.I., Vilar, V.J.P. *Ozone membrane contactor for tertiary treatment of urban wastewater: Chemical, microbial and toxicological assessment*, Science of the Total Environment, 892, (2023), 164492. DOI: https://doi.org/10.1016/j.scitotenv.2023.164492.

6.1 Objectives

This work intends to deepen the application of the tubular ozone membrane contactor, reported in *Chapter 5*, to promote the tertiary treatment of UWW, jointly considering the removal of CECs, disinfection, and the reduction of toxicity. The efficiency of ozonation was assessed for the simultaneous removal of 19 CECs spiked in secondary-treated UWW and microbial inactivation (heterotrophs, enterobacteria and enterococci), including the removal of ARBs (amoxicillin (AMX), cefotaxime (CTX) and sulfamethoxazole (SUL)). The influence of different experimental parameters on CECs removal and disinfection, i.e., O_3 dose ($D_{A\text{-}O_3}$), O_3 concentration in the gas phase ($[O_3]_{G,inlet}$) and gas flow rate (Q_G), wastewater pH, and UVC radiation was examined. Furthermore, the effect of effluent quality due to seasonal fluctuations (winter-UWW1 and summer-UWW2) on ozonation efficiency, as well as microbial regrowth due to storage of the treated UWW (for reuse purposes), were also evaluated. Finally, using bioassays with zebrafish embryos, the toxicity of the effluent was assessed before and after ozonation and also after adsorption by granular activated carbon (GAC).

6.2 Materials and Methods

All the chemicals used in this work, experimental units and procedures, as well as the employed analytical determinations used for CECs, microbiology and toxicity are described in *Chapter 2*. The tubular borosilicate membrane employed in this *Chapter* is the same as the membrane used in *Chapter 5*. Therefore, the procedure used for the preparation of the photocatalytic membrane is described in detail in *Section 2.2.3*. The operational details for all ozonation experiments are summarized in Table 6.1 and further information on the procedure and reactor properties can be found in *Section 2.3.2.2*. The procedure for the adsorption column with GAC is described in *Section 2.3.2.6*. Before submitting to treatment, the UWW was fortified with 10 μg L^{-1} of each 19 CECs. The target CECs are the same as those used in *Chapter 5*. The target CECs were selected within the scope of the NOR-WATER project (http://nor-water.eu/en/home/), according to their occurrence and persistence in the river basins and UWWTP effluents located in Northern Portugal and Galicia, therefore including some highly persistent and mobile chemicals.

Table 6.1. Experimental conditions employed for each test.

Matrix[a]	#	Q_L (L h^{-1})	τ (s)	Q_G (Ndm^3 min^{-1})	$[O_3]_{G,inlet}$ (g Nm^{-3})	$D_{A\text{-}O_3}$ (g m^{-3})	$D_{T\text{-}O_3}$ (g m^{-3})	$D_{C\text{-}O_3}$ (g m^{-3})	Radiation[d]	Evaluated parameters[e]				
										CECs	M	MR	ARB	T
UWW1	1	100	5.8	0.75	14	6	2.4	2.3	-	×	-	-	-	-
UWW1	2	100	5.8	0.75	26	12	4.5	4.1	-	×	-	-	-	-
UWW1	3	100	5.8	0.75	34	15	4.8	4.3	-	×	-	-	-	-
UWW1	4	100	5.8	0.75	40	18	6.8	5.6	-	×	×	-	-	-
UWW1	5	100	60	0.75	26	12	4.6	4.6	-	×	-	-	-	-
UWW1	6	100	60	0.75	40	18	5.9	5.8	-	×	-	-	-	-
UWW1	7[b]	100	5.8	0.75	40	18	5.8	5.7	-	×	×	-	-	-
UWW1	8[c]	100	5.8	0.75	40	18	6.8	6.8	-	×	×	-	-	-
UWW1	9	100	5.8	1.00	30	18	4.8	3.4	-	×	×	-	-	-
UWW1	10	100	5.8	0.15	200	18	15.8	6.8	-	×	×	-	-	-
UWW1	11	100	5.8	0.75	40	18	5.9	5.7	UVC	×	×	-	-	-
UWW1	12	100	5.8	0.15	200	18	15.8	6.8	UVC	×	-	-	-	-
UWW2	13	100	5.8	1.00	30	18	6.6	4.2	-	×	×	×	×	-
UWW2	14	100	5.8	0.75	40	18	8.0	6.3	-	×	×	×	×	-
UWW2	15	100	5.8	0.15	200	18	16.0	8.6	-	×	×	×	×	×

[a]Wastewater collected in the winter (UWW1) and summer (UWW2) period.
[b]Adjusted pH to 5.0 ± 0.2.
[c]Adjusted pH to 9.0 ± 0.2.
[d]Photonic flux of 2.89 ± 0.08 W.
[e]CECs – CECs removal; M – enumeration of culturable microorganisms; MR – microbiological regrowth; ARB – antibiotic-resistant bacteria; T – toxicity screening with zebrafish embryo bioassays.

6.3 Results and discussion

6.3.1 Efficiency of the ozone membrane contactor for CECs removal

6.3.1.1 Effect of ozone dose and residence time

The efficiency of tertiary treatment applying the ozone membrane contactor was first evaluated for UWW1 spiked with the 19 target CECs. As expected, the application of higher doses of O_3 (tests #1 to #4, with $D_{A\text{-}O_3}$ of 6, 12, 15 and 18 g m^{-3}) increased the removal of the target CECs, either in the number of compounds presenting some level of degradation (>10%) or in their removal percentage (Figure 6.1a). The higher specific O_3 dose, ranging from 0.18 to 0.44 g O_3 g^{-1} DOC in these tests, explains these results. The target CECs also showed different levels of degradation, which is related to the reactivity of the compound to the oxidizing species present, given by second-order rate constants with O_3 (k_{O_3}) and $OH^{\bullet}$ ($k_{HO\bullet}$). According to Hollender et al. [1], compounds with k_{O_3} greater than 10^4 M^{-1} s^{-1} require low O_3 doses (easily degraded). CECs with k_{O_3} <10^4 M^{-1} s^{-1} are more persistent to treatment with O_3 and their degradation can occur mainly by reaction with $OH^{\bullet}$. For $D_{A\text{-}O_3}$ > 12 g m^{-3} (or > 0.34 g O_3 g^{-1} DOC), it was observed (Figure 6.1a) that compounds highly reactive with O_3, such as CBZ, E2, EE2, DCF and LSTN ($k_{O_3} \geq 10^5$ M^{-1} s^{-1}, Table 6.2), reached removal values below the *LOQ*. These compounds are known to contain functional groups that react quickly with O_3, such as aniline (e.g., DCF), olefins (e.g., CBZ), phenol (e.g., E2, EE2), and benzene ring (e.g., CBZ, LSTN) [2]. In contrast, beta-blockers ATNL and BSPL (with $10^3 \leq k_{O_3} \leq 10^4$ M^{-1} s^{-1}, Table 6.2), as well as ISTN and DRN (both with $k_{O_3} = 10^1$ M^{-1} s^{-1}, Table 6.2) presented removal levels between 60% and 80% only for the highest O_3 dose (test #4, $D_{A\text{-}O_3}$ of 18 g m^{-3} and specific dose of 0.44 g O_3 g^{-1} DOC), while the remaining target CECs (with $k_{O_3} \leq 10^1$ M^{-1} s^{-1}, Table 6.2) had low or null removals (Figure 6.1a). Levels of oxidation >90% for CBZ, CBZ-EPX and DCF (in common with the present study) were also reported for full-scale ozonation plants in Sweden and Denmark [3] applying a $D_{A\text{-}O_3}$ between 4 and 28.6 g m^{-3} and a residence time between 10 and 30 min. Other pertinent works [4-6], with $D_{A\text{-}O_3}$ ranging from 3-8 g m^{-3} and residence times from 4 to 15 min, also observed high removal efficiencies (>80%) for several CECs, including CBZ, DCF, PFOA, ATNL, DEET.

Table 6.2. List of the 19 CECs selected for testing and respective group, abbreviations, chemical composition, and rate constants for the reactions with ozone (k_{O_3}) and the hydroxyl radical ($k_{HO\bullet}$).

Contaminants group	Contaminants	Abbreviation	Chemical Composition	k_{O_3} (M^{-1} s^{-1})	$k_{HO\bullet}$ (M^{-1} s^{-1})
Carbamazepine and Metabolites	Carbamazepine	CBZ	$C_{15}H_{12}N_2O$	3×10^5 [7]	8.8×10^9 [7]
	10,11 Carbamazepine-epoxide	CBZ-EPX	$C_{15}H_{12}N_2O_2$	Low* [8]	Low* [8]
Non-Steroidal Anti-Inflammatory Drugs	Diclofenac	DCF	$C_{14}H_{11}Cl_2NO_2$	1×10^6 [9]	7.5×10^9 [9]
Hormones	17β-Estradiol	E2	$C_{18}H_{24}O_2$	2.2×10^5 [10]	5.12×10^9 [11]
	17α-Ethynylestradiol	EE2	$C_{20}H_{24}O_2$	3×10^6 [7]	9.8×10^9 [7]
Beta blockers	Atenolol	ATNL	$C_{14}H_{22}N_2O_3$	1.7×10^3 [12]	8×10^9 [13]
	Bisoprolol	BSPL	$C_{18}H_{31}NO_4$	1.83×10^4 [14]	unknown
Insect Repellent	Diethyltoluamide	DEET	$C_{12}H_{17}NO$	0.1 [15]	4.95×10^9 [16]
Angiotensin II Receptor Blockers	Valsartan	VSTN	$C_{24}H_{29}N_5O_3$	38 [13]	1×10^{10} [17]
	Irbesartan	ISTN	$C_{25}H_{28}N_6O$	23 [18]	1×10^{10} [18]
	Losartan	LSTN	$C_{22}H_{23}ClN_6O$	2.1×10^5 [18]	unknown
Herbicide	Diuron	DRN	$C_9H_{10}C_{l2}N_2O$	13.3 [19]	6.6×10^9 [20]
Flame Retardant	Melamine	MLN	$C_3H_6N_6$	unknown	1×10^4 [21] **
Artificial Sweeteners	Acesulfame K	AC-K	$C_4H_4KNO_4S$	88 [22]	4.55×10^9 [22]
	Saccharin	SCH	$C_7H_5NO_3S$	unknown	1.56×10^9 [23]
Short-chain perfluoroalkyl substances (PFAS)	Heptafluorobutyric acid	PFBA	$C_4HF_7O_2$	unknown	Low*,**
	Nonafluoro-1-butanesulfonic acid	PFBS	$C_4HF_9O_3S$	unknown	Low*,**
	Pentadecafluorooctanoic acid	PFOA	$C_8HF_{15}O_2$	unknown	$< 1 \times 10^5$ [24]
	Trifluoromethanesulfonic acid	TFMS	CHF_3O_3S	unknown	$< 1 \times 10^5$ [25]

Note: *Estimated reactivity; **Some authors express that radical $OH^{\bullet}$ cannot directly oxidize PFAS and MLN [21, 26].

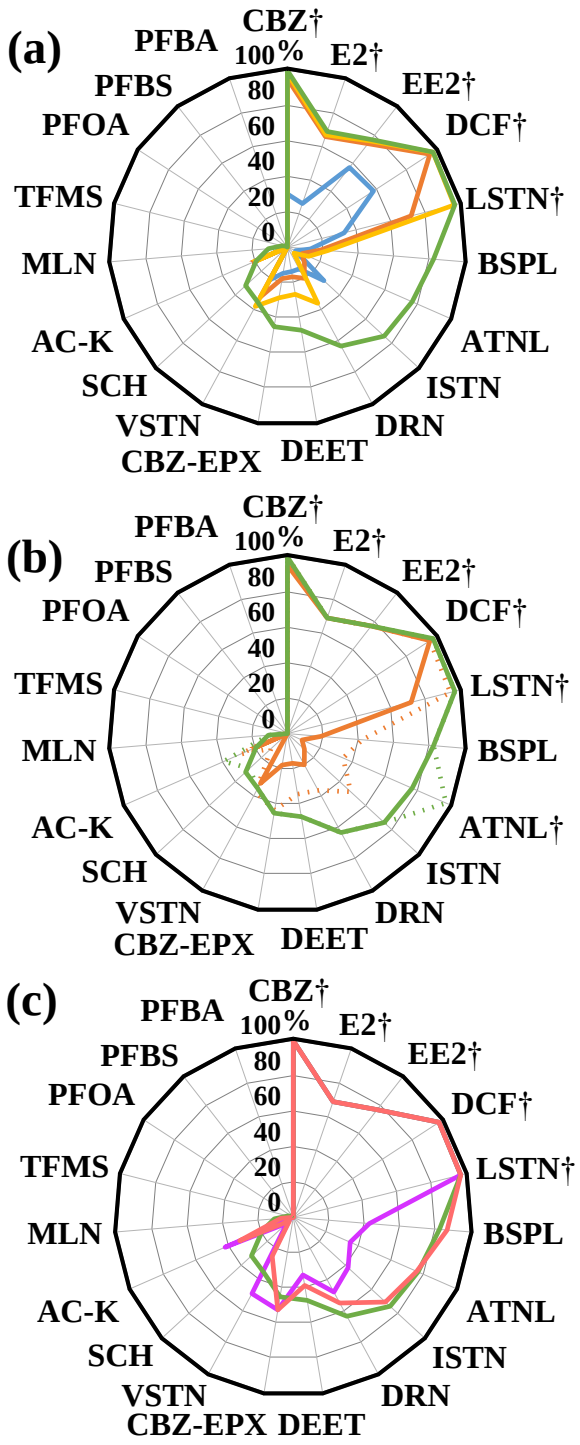

Figure 6.1. Removal efficiency (%) of the 19 target CECs spiked in UWW1 ($[CECs]_0$ = 10 µg L^{-1}) after a treatment time of 5.8 s under different (a) ozone doses (——) $D_{A\text{-}O_3}$ = 6 g m^{-3} (test #1), (——) $D_{A\text{-}O_3}$ = 12 g m^{-3} (test #2), (——) $D_{A\text{-}O_3}$ = 15 g m^{-3} (test #3), and (——) $D_{A\text{-}O_3}$ = 18 g m^{-3} (test #4); (b) contact time of 60 s (·····) $D_{A\text{-}O_3}$ = 12 g m^{-3} (test #5) and (·····) $D_{A\text{-}O_3}$ = 18 g m^{-3} (test #6); and (c) pH values (——) pH = 5.0 ± 0.2 (test #7), (——) pH = 7.7 ± 0.3 (test #4) and (——) pH = 9.0 ± 0.2 (test #8). Note: For details on the operational conditions of each test, please refer to Table 6.1. †The removal values are presented as the maximum percentage that can be determined, taking into account the limits of quantification of the analytical method (Table 2.7).

Considering the short residence time applied in these tests (Q_L of 100 L h^{-1}, corresponding to 5.8 s), and that most of the ozonation treatments applying similar $D_{A\text{-}O_3}$ are carried out with residence times of a

few minutes (from 4 to 30 min) [5, 27], tests with $D_{A\text{-}O_3}$ of 12 and 18 g m^{-3} were performed for a residence time of 60 s (tests #5 and #6, Table 6.1). In these tests, to keep the other operating conditions unchanged while increasing the residence time, a tank was coupled downstream of the membrane contacting system. Improvements in the removal efficiency of several CECs were evidenced for $D_{A\text{-}O_3}$ of 12 g m^{-3} (Figure 6.1b), with increases of 1.3-fold for LSTN, VSTN and AC-K, ~2-fold for DRN, DEET, BSPL and CBZ-EPX, and 3.8-times for ATNL and ISTN. These better results are related to the total consumption of dissolved O_3 verified in test #5 ($D_{T\text{-}O_3} = D_{C\text{-}O_3}$ = 4.6 g m^{-3}, Table 6.1), which did not occur when the contact time was only 5.8 s ($D_{T\text{-}O_3} > D_{C\text{-}O_3}$ = 4.1 g m^{-3}, Table 6.1). In turn, for a $D_{A\text{-}O_3}$ of 18 g m^{-3}, the difference between the O_3 consumed for the tests with 5.8 s and 60 s was smaller ($D_{C\text{-}O_3}$ of 5.6 and 5.8 g m^{-3}, respectively, Table 6.1), so improvements were verified only for ATNL (1.3-fold) and AC-K (2-fold) (Figure 6.1).

6.3.1.2 Effect of wastewater pH

The O_3 stability in water strongly depends on the pH value, while under acidic conditions, the rate of O_3 self-decomposition is slow (higher O_3 concentration in the liquid phase), alkaline conditions promote O_3 decay reactions (and the generation of $OH^{\bullet}$) [28]. This is in line with the observed drop in dissolved O_3 concentration (from 3.2 g m^{-3} to 0.6 g m^{-3}) when the pH value was increased (from 3 to 9) in the ozone mass transfer assays reported in *Chapter 5*, indicating greater O_3 decomposition at higher pH values. Taking this, when operating under acidic conditions, the main oxidation pathway for CECs is expected to be the direct reaction with dissolved O_3, whereas under alkaline conditions, the indirect oxidation pathway (i.e., CECs reacting with $OH^{\bullet}$) becomes predominant. In this way, for the ozonation treatment at pH 5.0 (test #7, Table 6.1), the target CECs with $k_{O_3} \geq 10^5$ M^{-1} s^{-1} maintained high levels of oxidation and reached concentrations below the *LOQ* (Figure 6.1c). On the other hand, when compared to ozonation at the natural pH of the UWW1 (test #4, pH of 7.7), the lower $OH^{\bullet}$ generation at pH 5.0 led to a decrease in the removal of several CECs such as DRN and DEET (~1.4 times lower) and BSPL, ATNL and ISTN (~2 times lower). This result shows the importance of the indirect reaction pathway for those CECs that react poorly with O_3 ($k_{O_3} \leq 10^5$ M^{-1} s^{-1}). In turn, no significant differences in performance were observed between ozonation at pH 7.7 and 9.0 (tests #4 *vs*. #8, Figure 6.1c). The lack of improvement in oxidation ability at pH 9.0 may be related to inorganic species associated with the alkalinity of the effluent (carbonates/bicarbonates) that are affected by pH adjustment, which act as $OH^{\bullet}$ scavengers and inhibitors of the chain reaction of O_3 decomposition. This was also observed in other studies [5, 29] and perceived by the increase in the concentration of inorganic carbon when the pH of

the UWW1 was adjusted to 9.0 (from 46.7 mg L^{-1} to 66.7 mg L^{-1}). The opposite trend was also observed, with decreasing concentration of inorganic carbon in the UWW when the pH was adjusted to 5.0.

6.3.1.3 Effect of ozone inlet concentration and flow rate

Keeping the natural pH, a $D_{A\text{-}O_3}$ of 18 g m^{-3} and a residence time of 5.8 s (selected according to the results presented above), the $[O_3]_{G,inlet}$ was then varied (tests #4, #9 and #10, Table 6.1). A substantial improvement in the CECs removal was observed for the highest $[O_3]_{G,inlet}$ (test #10; 200 g Nm^{-3}), with 13 of the 19 CECs removed >80% or below the *LOQ* and one CEC >50% (SCH) (Figure 6.2). These results can be explained by the ozone transfer yield observed in these experiments (Figure 6.2a inset), while only 30% ± 3% of the delivered O_3 was effectively transferred in tests #4 and #9 ($[O_3]_{G,inlet}$ of 40 and 30 g Nm^{-3}, respectively), this value increased to 88% in test #10 ($[O_3]_{G,inlet}$ of 200 g Nm^{-3}). This is consistent with the mass-transfer theory, where for increasing O_3 concentrations in the gas phase (driving force) a higher O_3 diffusion rate is expected, thus more O_3 is transferred from the gas to the liquid phase [30, 31] and available to react with the target CECs. Furthermore, to keep the hydrodynamic conditions and attain the same $D_{A\text{-}O_3}$ while increasing the $[O_3]_{G,inlet}$ for test #10, it was required to decrease the inlet gas flow rate (see Table 6.1). For this ozone membrane contactor, it was verified that for the same liquid flow rate, mass transfer efficiency increases with the decrease in the gas flow rate, due to the higher contact time between the gas and the liquid phase (as reported in *Chapter 5*). Therefore, although the same $D_{A\text{-}O_3}$ was applied in tests #4, #9 and #10, the ozone transfer yield increased and, consequently, the specific ozone dose obtained for test #10 was ~3-fold higher than for tests #4 and #9 (1.17 *vs.* 0.44 and 0.36 g O_3 g^{-1} DOC, respectively, Figure 6.2a inset).

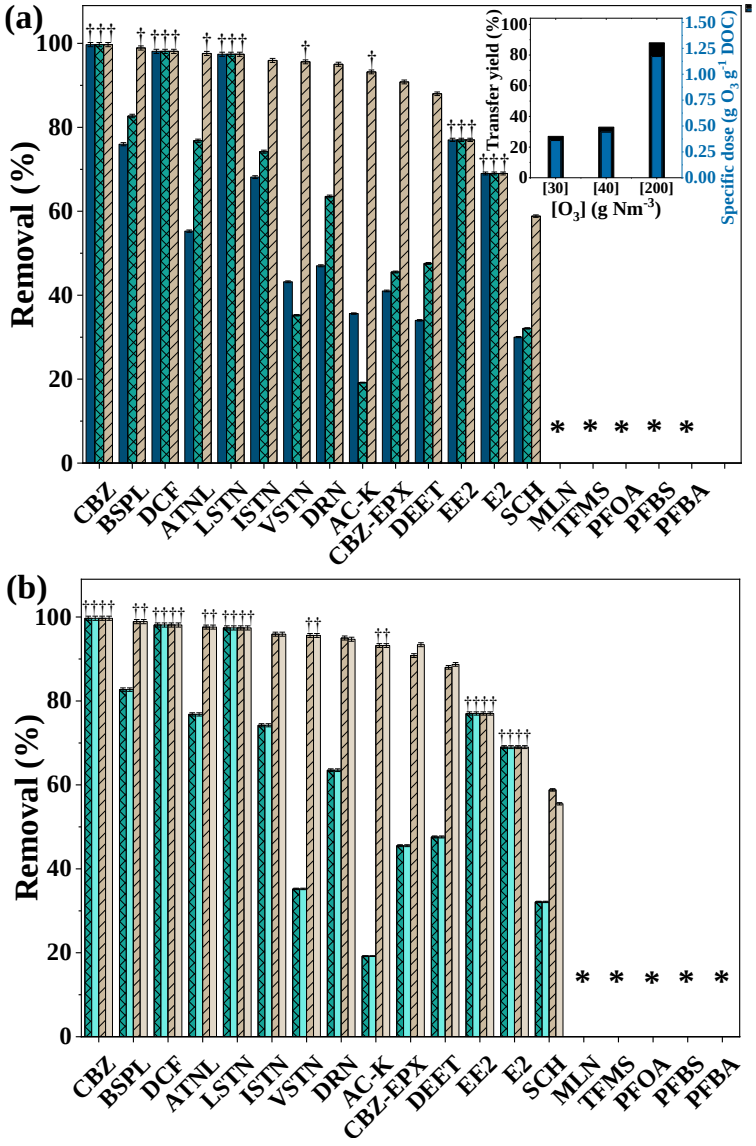

Figure 6.2. Removal efficiency (%) of the 19 target CECs spiked in UWW1 ($[CECs]_0$ = 10 µg L^{-1}) applying a $D_{A\text{-}O_3}$ of 18 g m^{-3} under (a) different ozone inlet concentrations (■) $[O_3]_{G,inlet}$ = 30 g Nm^{-3} (test #9), (▩) $[O_3]_{G,inlet}$ = 40 g Nm^{-3} (test #4) and (▨) $[O_3]_{G,inlet}$ = 200 g Nm^{-3} (test #10); and (b) photocatalytic ozonation of (▭) $[O_3]_{G,inlet}$ = 40 g Nm^{-3} + UVC/TiO_2 (test #11) and (▭) $[O_3]_{G,inlet}$ = 200 g Nm^{-3} + UVC/TiO_2 (test #12). The inset of Figure 6.2a shows the ozone transfer yield (%) and specific ozone dose (g O_3 g^{-1} DOC) employed. Note: For details on operational conditions of each test, please refer to Table 6.1. †The removal values are presented as the maximum percentage that can be determined, taking into account the limits of quantification of the analytical method (Table 2.7). *No removal.

Beyond the expected good removal performance for the CECs with $k_{O_3} \geq 10^5$ M^{-1} s^{-1}, very interesting removals (58–96%) were also observed in test #10 for compounds with low ozone reactivity, as CBZ-EPX, DEET, VSTN, ISTN, DRN, and AC-K, which can be ascribed as a result of their oxidation by the $OH^{\bullet}$ radical ($k_{HO^{\bullet}} > 10^9$ M^{-1} s^{-1}, Table 6.2) produced by ozone's decomposition. The only CECs that persisted without any sign of oxidation, even when applying the highest $[O_3]_{G,inlet}$, were the four PFAS and MLN (Figure 6.2a). These organic compounds are highly stable and expected to be resistant to degradation by both O_3 and $OH^{\bullet}$ radical (k_{O_3} unknown and $k_{HO^{\bullet}} < 10^5$ M^{-1} s^{-1}, Table 6.2). A possible

explanation for the non-removal of PFAS with O_3 may be the presence of strong and stable carbon-fluorine bonds in the alkyl carbon chain, which agrees with other studies [26, 32, 33]. Regarding MLN, a previous study has demonstrated that a $D_{A\text{-}O_3}$ of 10 g m^{-3} and a reaction time of 20 min was required to achieve ~65% removal [34]. Maurino et al. [21] also indicated that among the oxidative processes, only photocatalysis and the generation of sulphate radicals ($SO_4^{\bullet -}$) were able to transform MLN efficiently.

6.3.1.4 Photocatalytic ozonation

Literature reports a synergy in the combination of ozonation and photocatalysis for water treatment [35]. Therefore, aiming at the removal of MLN and the four PFAS compounds, the combined O_3/UVC/TiO_2 process was evaluated for an $[O_3]_{G,inlet}$ of 40 and 200 g Nm^{-3} (tests #11 and #12, from Table 6.1). For both cases, photocatalytic ozonation showed no significant differences in the removal efficiency of the target CECs when compared to ozonation treatments under similar operational conditions (tests #4 *vs* #11 and #10 *vs* #12, Figure 6.2b). An explanation for these results may be the low UVC dose provided (0.10 kJ L^{-1}) due to the short residence time (5.8 s) of the treatment tests. This hypothesis is supported by the lack of significant removal of the 19 CECs in the UVC/TiO_2 test (<10% for all targets, data not shown).

6.3.1.5 Effect of wastewater characteristics

To represent typical variations observed in the main traditional characteristics of effluent quality, that are known to occur due to seasonal fluctuations, secondary-treated UWW2 was collected in the summer period, contrary to UWW1, which was collected in the winter. For a better insight into the ozonation efficiency, three treatments were selected for UWW2 (tests #13 to #15, Table 6.1), repeating operational conditions used for UWW1 (tests #4, #9 and #10, Table 6.1). Apart from the CECs highly reactive with O_3 ($k_{O_3} \geq 10^5$ M^{-1} s^{-1}, Table 6.2), which presented concentrations below the *LOQ* for the two treated wastewaters (Figure 6.3), the removal of target CECs for UWW2 was globally lower for all compounds. Collected in the dry season, UWW2 presented a higher organic and inorganic load compared to UWW1 (Table 6.3), which can be verified by the higher values for COD (2.1-fold), DOC (1.7-fold), DIC (1.5-fold) and TSS (5.1-fold).

Table 6.3. Main physicochemical characteristics of the two wastewater samples collected after secondary treatment in an UWWTP (UWW1, Winter and UWW2, Summer), after ozonation and after ozonation followed by adsorption with granular activated carbon (GAC).

Parameter	UWW1	$O_{3\text{-}WW1}$	UWW2	$O_{3\text{-}WW2}$	$O_{3\text{-}WW2}$+GAC
pH	7.5	7.2	7.8	7.5	7.6
Temperature (ºC)	15.7	16.4	23.4	21.4	22.4
Conductivity (µS cm^{-1})	202	195	1442	1328	1030
Turbidity (NTU)	0.6	0.25	15	3.6	2.6
Absorbance at 254 nm (AU)	0.208	0.039	0.320	0.096	0.017
Transmittance at 254 nm (%)	62	91	48	80	96
Dissolved organic carbon (mg L^{-1})	13.5	10.1	22.9	15.8	7.0
Dissolved inorganic carbon (mg L^{-1})	46.5	45.9	70.8	74.3	38.9
Specific Ultraviolet Absorbance ($SUVA_{254}$, L mg^{-1} m^{-1})	1.5	0.39	1.4	0.61	0.24
Chemical oxygen demand (mg O_2 L^{-1})	38.3	21.9	79.5	35.3	14
Total suspended solids (mg L^{-1})	7.0	3.6	35.7	12.2	3.4
Sodium – Na^+ (mg L^{-1})	100	101	105	104	107
Ammonium – NH_4^+ (mg L^{-1})	1.2	0.9	62.5	35.8	30.2
Potassium – K^+ (mg L^{-1})	23.5	27.1	26.2	23.8	25.0
Magnesium – Mg^{2+} (mg L^{-1})	6.4	7.2	6.9	6.4	6.6
Calcium – Ca^{2+} (mg L^{-1})	30.6	26.2	33.0	24.9	14.4
Fluoride – F^- (mg L^{-1})	0.1	0.1	0.2	0.1	<0.01
Chloride – Cl^- (mg L^{-1})	130	137	132	134	54
Sulphate – SO_4^{2-} (mg L^{-1})	54.0	59.1	65.3	65.8	14.7
Nitrite – NO_2^- (mg L^{-1})	<0.04[a]	<0.04[a]	<0.04[a]	<0.04[a]	<0.04[a]
Nitrate – NO_3^- (mg L^{-1})	1.9	2.4	4.5	16.2	1.4
Phosphate – PO_4^{3-} (mg L^{-1})	4.0	6.1	17.6	13.6	5.0

[a]Limit of quantification

Thus, despite the operational conditions being similar to those previously applied for UWW1, a considerable decrease in the specific ozone dose for the treatments with UWW2 affected the CECs abatement. The specific ozone doses for UWW2 were 0.29, 0.35 and 0.70 g O_3 g^{-1} DOC (tests #13, #14 and #15, respectively), which in relation to analogous tests with UWW1 represents a decrease of about 20% for tests with $[O_3]_{G,inlet}$ of 30 and 40 g Nm^{-3} and 40% for $[O_3]_{G,inlet}$ of 200 g Nm^{-3}. Typically, the specific ozone dose used in UWWTPs is between 0.1 and 1.7 g O_3 g^{-1} DOC [3] which is within the range of doses applied for both wastewaters tested in this work.

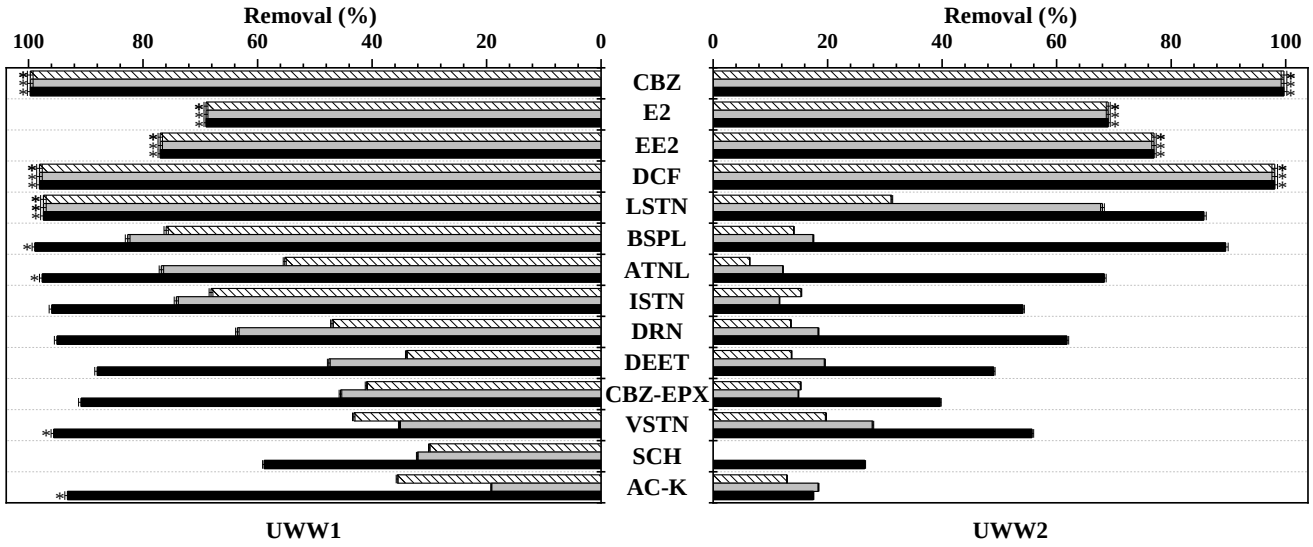

Figure 6.3. Removal efficiency (%) of the 19 target CECs spiked ($[CECs]_0$ = 10 µg L^{-1}) in UWW1 and UWW2 applying a $D_{A\text{-}O_3}$ of 18 g m^{-3} and different ozone inlet concentrations (■) $[O_3]_{G,inlet}$ = 30 g Nm^{-3} (test #9 and #13), (▒) $[O_3]_{G,inlet}$ = 40 g Nm^{-3} (test #4 and #14) and (▨) $[O_3]_{G,inlet}$ = 200 g Nm^{-3} (test #10 and #15). Note: For details on operational conditions of each test, please refer to Table 6.1. *The removal values are presented as the maximum percentage that can be determined, taking into account the limits of quantification of the analytical method (Table 2.7).

After ozonation, some physicochemical parameters of UWW1 and UWW2 were also improved (Table 6.3). DOC was reduced by 25% and 31%, COD by 43% and 56%, and TSS by 49% and 66%, for UWW1 (1.17 g O_3 g^{-1} DOC) and UWW2 (0.70 g O_3 g^{-1} DOC), respectively. In this regard, von Gunten [36] indicates that the NOM is usually the main consumer of O_3 in wastewater, which justifies the differences between the results obtained for the two UWWs. However, the DOC removal and the modification of chemical structures by ozonation greatly depend on the composition of the NOM [37], but generically results in NOM becoming more bioavailable and that can be subsequently biodegraded or removed by a simpler process, such as sand filters or activated carbon [38]. The mineralization degree obtained in this work was higher than that indicated by Sauter et al. [17], with DOC decreasing around 5% when applying 0.65 g O_3 g^{-1} DOC, and Nöthe et al. [39], who showed an average DOC decrease between 4 and 10% after ozonation with 0.4-0.8 g O_3 g^{-1} DOC.

Differences in the wastewater matrices can lead to variations in the mineralization degree, since it will influence the amount of $OH^{\bullet}$ produced by the reaction of O_3 with the naturally present electron-rich compounds, particularly amines, phenols and alkoxylate aromatics.

Among the micronutrients analysed (Table 6.3), the vast majority had concentrations similar to those found before the ozonation treatment. For UWW2, it was possible to observe that ozonation promoted a decrease in the ammonia concentration and a concomitant increase in nitrate concentration (Table 6.3). According to Singer and Zilli [40], ammonia is oxidized completely to nitrate by ozone ($NH_3 + 4O_3 \rightarrow$

$NO_3^- + 4O_2 + H_2O + H^+$). The oxidation process is first-order in terms of ammonia concentration, and the rate increases with pH in the pH 7-9 range. [40]. Furthermore, several studies on ammonia oxidation by ozone microbubbles have also been published [41, 42] and concluded that the increase in nitrate concentration is related to the ozonation oxidation of ammonia.

6.3.2 Efficiency of ozone membrane contactor for microbiological inactivation

6.3.2.1 Total heterotrophs, enterobacteria and enterococci

The performance of ozonation in terms of bacterial inactivation greatly depends on the susceptibility of the target bacterium to O_3, the O_3 concentration, wastewater pH and NOM content [43]. Therefore, the total heterotrophs, enterobacteria and enterococci were enumerated before and immediately after some selected ozonation (standalone process) treatments for UWW1 (tests #4, #7 to #11, Figure 6.4a) and UWW2 (tests #13 to #15, Figure 6.4b). All the selected tests applied a $D_{A\text{-}O_3}$ of 18 g m^{-3}, which is in line with the $D_{A\text{-}O_3}$ between 1 and 35 g m^{-3} used in UWWTPs for disinfection purposes [44]. There was no need to enrich the wastewater with microorganisms, as the original untreated UWW samples showed the presence of target bacteria at quantifiable levels: UWW1 (Log_{10} CFU/100 mL) – 6.93 ± 0.02, 6.45 ± 0.02, 1.71 ± 0.02, and UWW2 (Log_{10} CFU/100 mL) – 8.33 ± 0.03, 6.01 ± 0.08, 4.96 ± 0.02, for total heterotrophs, enterobacteria and enterococci, respectively.

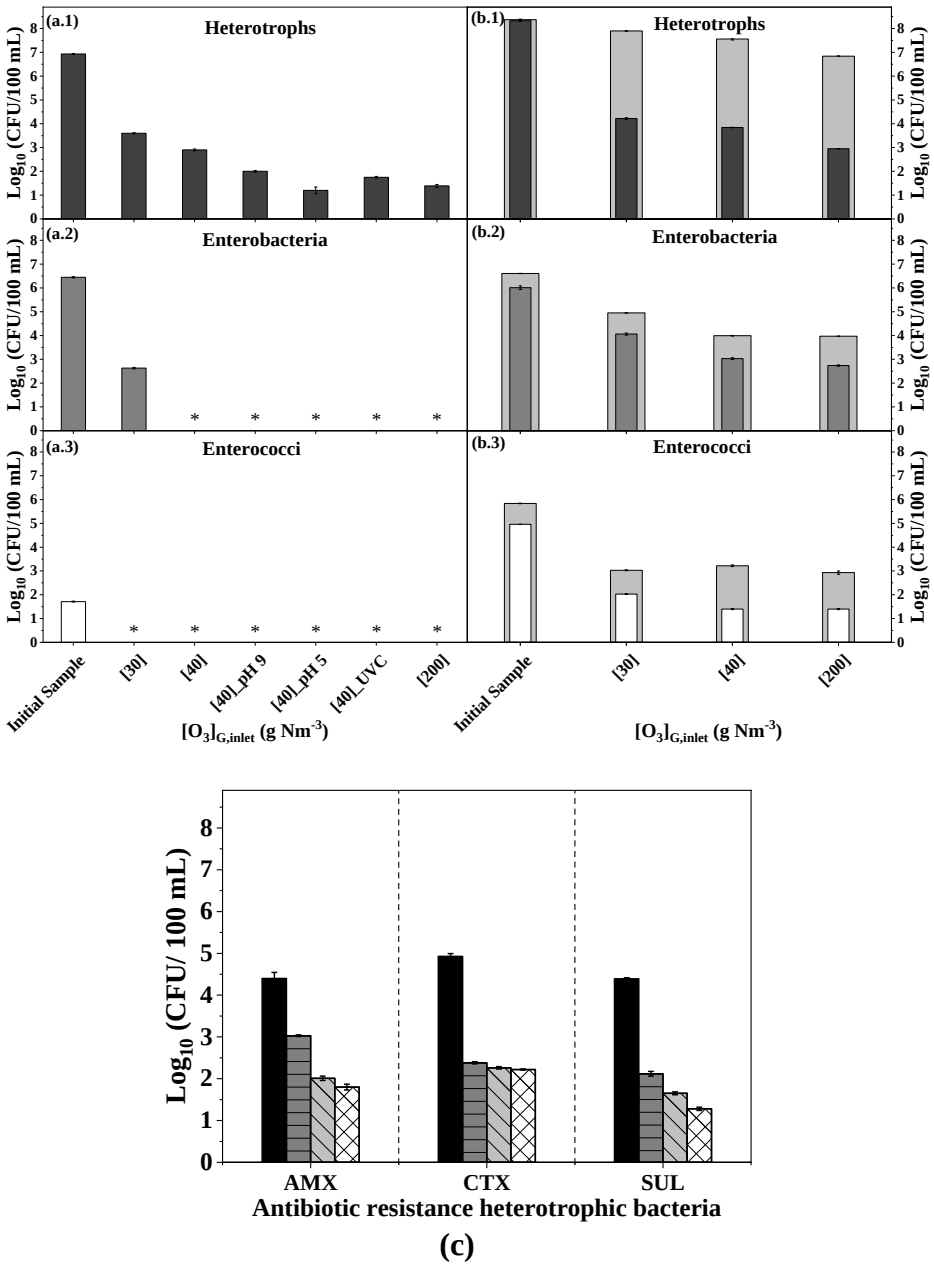

Figure 6.4. Quantification in (a) UWW1 and (b) UWW2 of total heterotrophs (.1), enterobacteria (.2) and enterococci (.3), before and after selected ozonation tests, and (c) quantification of antibiotic resistant enterobacteria (AMX – Amoxicillin; CTX – Cefotaxime; SUL – Sulfamethoxazole) for ozonation tests with UWW2 (■ - initial sample) applying a $D_{A\text{-}O_3}$ of 18 g m^{-3} and different ozone inlet concentrations (▤) $[O_3]_{G,inlet}$ = 30 g Nm^{-3} (test #13), (▨) $[O_3]_{G,inlet}$ = 40 g Nm^{-3} (test #14) and (▩) $[O_3]_{G,inlet}$ = 200 g Nm^{-3} (test #15). In graph (b) the bar in the background refer to the regrowth test. *Below the detection limit (3.3 × 10^{-3} CFU mL^{-1}).

For UWW1, good removal of the target bacterial groups was globally observed after ozonation (Figure 6.4a), with log reductions > 4 units for total heterotrophs (test #10, $[O_3]_{G,inlet}$ of 200 g Nm^{-3}) and values below the limit of detection (*LOD* of 0.33 × 10^{-2} CFU mL^{-1}) for enterobacteria (from $[O_3]_{G,inlet} \geq$ 40 g Nm^{-3}; test #4) and enterococci (from $[O_3]_{G,inlet} \geq$ 30 g Nm^{-3}; test #9). The total heterotrophs were not completely removed even when the highest $[O_3]_{G,inlet}$ was applied (Figure 6.4a.1), being quantified at approximately 10^3 CFU 100 mL^{-1} (10 CFU mL^{-1}). However, this value is below the maximum recommendable of 20 CFU mL^{-1} for the quality of water intended for human consumption [45].

Enterobacteria is a large family of gram-negative bacteria, including the well-known *Escherichia coli*, which includes both commensals and pathogenic strains. In this sense, and according to the EU Regulation 2020/741 of the European Parliament and of the Council of 25 May 2020 on minimum requirements for water reuse, the effluent after ozonation with $[O_3]_{G,inlet} \geq 40$ g Nm^{-3} (specific dose ≥ 0.44 g O_3 g^{-1} DOC) could be considered for reclaimed water quality class A (*E. coli* ≥ 5 log reduction), considering the parameter *E. coli* [46].

Several studies have regarded pH as the main effective parameter of O_3 efficiency for microorganisms inactivation [47]. It is well-known that the effect of pH on the disinfection performance of O_3 is multifaceted, as the influence of pH is a trade-off status [48]; high pH values reduce the concentration of O_3, but on the other hand, it generates more $OH^{\bullet}$ radical species. The present study observed that the lower the pH, the greater the removal efficiency of total heterotrophs (test #7, Figure 6.4a.1). It suggests that ozonation is efficient against total heterotrophs inactivation at low pH conditions (pH = 5.0) where molecular O_3 is the predominant species. In another study, Zuma et al. [49] described that the kinetics of *E. coli* removal occurred twice as fast at acidic pH (pH 4.9) than at basic pH (pH 9.2). Also, Pak et al. [48] reported that the ARB removal efficiencies at pH 6 were higher than those at pH 9. It is possible to hypothesize that $OH^{\bullet}$ scavengers, such as bicarbonate ions in microbial cells, may quench the free radical reaction [49].

The inactivation of microorganisms can be further enhanced using the synergic effect of O_3 and UVC. This was verified in test #11, where the addition of UVC radiation led to a further ~1.3 log decrease in the concentration of the total heterotrophs (Figure 6.4a.1). Microbial inactivation depends on the effect of irradiation and the interaction of the oxidant with the carbohydrates present in the cell tissue of the microorganism [50]. Furthermore, the germicidal effects of UVC are related to DNA damage, and UVC wavelength in the range of 260-270 nm is sufficient for the inactivation of the microorganism even at low residence times [50]. Although there was no improvement regarding the removal of the target CECs for test #11 (as discussed in *Section 6.3.1.4*), a clear enhancement of disinfection ability was observed, even with a low residence time and UVC dose.

For UWW2, the highest inactivation values were obtained by applying a $[O_3]_{G,inlet}$ of 200 g Nm^{-3} (test #15), where heterotrophs were reduced > 5 log units, enterobacteria and enterococci reduced > 3 log units (Figure 6.4b). As mentioned previously, for similar operational conditions, the specific ozone dose applied in UWW2 was lower than when treating UWW1, globally hindering the treatment efficiency. Furthermore, the microbial load before ozonation was considerably higher for UWW2 when compared to UWW1.

6.3.2.2 Microbiological regrowth and antibiotic resistance

Another important indicator to assess the efficiency of wastewater disinfection is the regrowth of microorganisms, which is particularly relevant for cases where the treated UWW is stored until reuse. Due to the distinct characteristics of the studied wastewaters and from a conservative perspective, UWW2 was chosen to be tested for microbial regrowth. In agreement with other works [51, 52], the storage for 3 days of O_3-treated UWW2 (from test #15) promoted regrowth (Figure 6.4b), with a decrease in the regrowth rate with increasing $[O_3]_{G,inlet}$. This result is justified, as disinfection is a process that eliminates only part of the microorganisms or harms some cells, allowing later regrowth. In the case of ozonation, may be mainly due to the availability of assimilable organic carbon resulting from the partial degradation of complex organic compounds [53]. Indeed, in stored O_3-treated UWW2, total heterotrophs, enterobacteria and enterococci density was similar to- or above the pre-treatment levels. This reflects the inability of ozone to provide a residual disinfection effect, which is paramount when reuse for agricultural purposes is intended.

The removal of enterobacteria harbouring resistance to three antibiotics (amoxicillin (AMX), cefotaxime (CTX) and sulfamethoxazole (SUL)) was observed immediately after treatment for the tested O_3 concentrations, with log reduction values ranging from 2.6 for AMX to 3.1 for SUL (Figure 6.4c). Other studies have observed that the inactivation of the examined ARB to values below the *LOD* would require higher treatment times (≥15 min) [43, 54].

6.3.3 Toxicity screening with zebrafish embryo bioassays

All the zebrafish embryo bioassays met the OECD FET test 236 criteria: overall survival and hatching rate, in the control at 96 hpf, were ≥ 90% [55]. Mortality, total abnormalities, and heart rate were determined in zebrafish embryos exposed to the three conditions – UWW2 fortified with the 19 CECs before ozonation (UWW+CECs), after ozonation test #15 (UWW+CECs+O_3) and after ozonation test #15 followed by GAC (UWW+CECs+O_3+GAC) - with undiluted samples (Table 6.4) and with dilution factors of 2 and 4 (Figure 6.5).

Table 6.4. Toxicological effects observed in zebrafish embryos exposed to the conditions without dilutions: UWW2 fortified with the 19 CECs before and after the ozonation process (UWW+CECs and UWW+CECs+O_3, respectively), and after ozonation plus GAC adsorption process (UWW+CECs+O_3+GAC).

Hours post fertilization (hpf)	Treatment without dilution	Endpoints	
		Mortality (%)	Total abnormalities (%)
24	Control	2 ± 2	0 ± 0
	UWW+CECs	0 ± 0	0 ± 0
	UWW+CECs+O_3	5 ± 5	7 ± 7
	UWW+CECs+O_3+GAC	0 ± 0	8 ± 4
48	Control	2 ± 2	4 ± 2
	UWW+CECs	95 ± 5*	β
	UWW+CECs+O_3	25 ± 8*	95 ± 5*
	UWW+CECs+O_3+GAC	5 ± 3	$(3 \pm 1) \times 10^1$
72	Control	2 ± 2	4 ± 2
	UWW+CECs	100 ± 0*	β
	UWW+CECs+O_3	100 ± 0*	β
	UWW+CECs+O_3+GAC	85 ± 7*	β
96	Control	2.1 ± 2.1	8 ± 3
	UWW+CECs	100 ± 0*	β
	UWW+CECs+O_3	100 ± 0*	β
	UWW+CECs+O_3+GAC	90 ± 5*	β

Note: *indicates significant differences ($p < 0.05$); data expressed as mean ± standard error; β – not measured because all embryos died, n = 10 for the control and n = 5 for the other treatments.

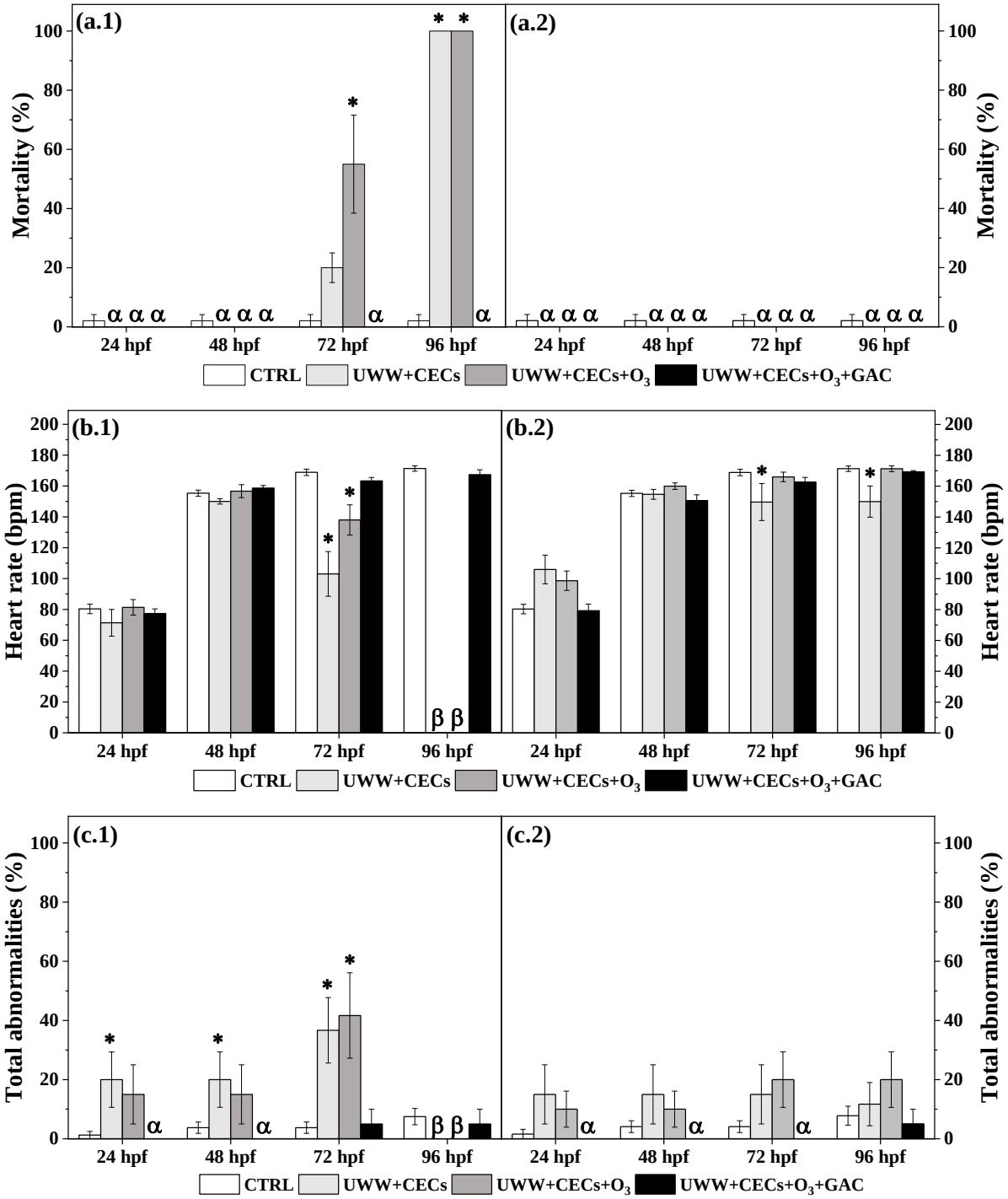

Figure 6.5. Toxicological effects observed in zebrafish embryos exposed to three conditions with a dilution factor of 2 (.1) and 4 (.2): UWW2 fortified with 19 CECs before and after the ozonation process (UWW+CECs and UWW+CECs+O_3, respectively), and UWW+CECs after ozonation plus GAC adsorption process (UWW+CECs+O_3+GAC). (a) Mortality (%), (b) Total abnormalities (%) and (c) Heart rate (bpm). Significant differences from control ($p \leq 0.05$) are marked with a symbol (*). The symbol β was used to indicate 100% mortality (so it was not possible to determine abnormalities) and α to indicate 0% mortality. Results are expresses as mean ± standard error (n = 10 for the control and n = 5 for the other treatments).

The undiluted samples showed high toxicity to zebrafish embryos with significant mortality and total abnormalities observed in all three conditions (Table 6.4). In the case of the samples with the dilution factor of 2, significant mortality and a significant decrease in the heart rate were observed in

UWW+CECs and UWW+CECs+O_3 treatments after 72 hpf exposure. Moreover, a significant increase in total abnormalities was recorded for the UWW+CECs and UWW+CECs+O_3 treatments from 24 hpf and 72 hpf of exposure, respectively (Figure 6.5b.1). Even though the ozonation process was effective in eliminating the parental compounds added to the effluent, as described in *Section 6.3.1*, the toxicity observed in the UWW+CECs+O_3 treatment is potentially related to the generation of toxic transformation products resulting from the degradation of the CECs. Regarding dilution factor 4, the toxicity was substantially reduced in all conditions, only the UWW+CECs condition showed a significant decrease in heart rate at 72 and 96 hpf (Figure 6.5b.2). It should be mentioned that a fixed standard dilution factor of 10 is frequently used in risk assessment studies for effluents entering in the receiving waters [56]. Notwithstanding, it has been verified that this may not be the case for many locations, so the chosen dilution factor in bioassays can many times lead to the underestimation of environmental risks, especially during low flow conditions of receiving water [57].

Considering that in UWWTPs a post-treatment stage is currently applied after ozonation [58], an adsorption step with GAC was used to complement the ozonation treatment (Figure 2.5), targeting the removal of CECs recalcitrant to ozonation, degradation by-products and subsequent decrease of the effluent toxicity. As expected, all CECs after ozonation and GAC adsorption showed concentration values below the *LOQ* (Table 2.7). The characterisation of the ozonated UWW2 after GAC also shows a good reduction in the organic load (Table 6.3; 56% for DOC, 61% for $SUVA_{254}$, 80% for COD, 72% for TSS compared to UWW2 after ozonation). Regarding the toxicity results, all the endpoints mentioned above returned to control levels after the ozonation was coupled with the GAC adsorption process, so no significant differences were observed between the control and the UWW+CECs+O_3+GAC treatment in all observation time points (Figure 6.5). Therefore, ozonation coupled with GAC adsorption increased the fitness of zebrafish embryos leading to a significant decrease in toxicity.

6.4 Conclusions

A novel ozone membrane contactor, operated in continuous mode, was applied for the tertiary treatment of UWW and demonstrated the ability to significantly reduce CECs and bacterial contamination, improving the overall physicochemical quality of the effluent. The best performance for this system was obtained for the highest O_3 concentration in the gas and lowest gas/liquid volumetric ratio, providing the highest ozone transfer yield (88%) and, thus higher specific ozone dose (g O_3 per g dissolved organic carbon) boosting the oxidation of the target CECs and disinfection. The seasonal fluctuation of the wastewater characteristics has shown to have an impact on the ozonation treatment efficiency, indicating the importance of adjusting the specific transfer ozone dose, as it considers the organic load of the effluent. Of the 19 target CECs, the four PFAS and melamine proved to be highly resistant to ozonation. The inclusion of a small dose of UVC radiation (0.10 kJ L^{-1}) showed no impact on the oxidation of CECs but led to improvements in the reduction of microbial contamination. Despite the high reductions in total heterotrophs, enterobacteria and enterococci, this effect was transient and cells that survived ozonation were able to regrowth back to their initial concentrations, hindering the possible reuse of the O_3-treated UWW for irrigation purposes. Ozonation with the present membrane contactor also reduced the abundance but not the presence of ARB in the effluent immediately after treatment. After ozonation, a dilution factor of 4 was shown to be required for no toxic effects to occur on zebrafish embryos, being reduced to a dilution factor of 2 if a post-treatment by GAC adsorption is coupled. Future studies are still in demand to establish the cost and life cycle assessment associated with this membrane ozonation system and the best strategy to ensure long-term disinfection. Finally, this ozone membrane reactor allows for the use of other catalysts, including those that can be photo- or ozone-activated to enhance photocatalytic activity.

6.5 References

[1] J. Hollender, S.G. Zimmermann, S. Koepke, M. Krauss, C.S. McArdell, C. Ort, H. Singer, U. von Gunten, H. Siegrist, Elimination of Organic Micropollutants in a Municipal Wastewater Treatment Plant Upgraded with a Full-Scale Post-Ozonation Followed by Sand Filtration, Environmental Science & Technology 43 (20) (2009) 7862-7869. https://doi.org/10.1021/es9014629.

[2] J. Li, S.-Y. Pang, Z. Wang, Q. Guo, J. Duan, S. Sun, L. Wang, Y. Cao, J. Jiang, Oxidative transformation of emerging organic contaminants by aqueous permanganate: Kinetics, products, toxicity changes, and effects of manganese products, Water Research 203 (2021) 117513. https://doi.org/10.1016/j.watres.2021.117513.

[3] S. Kharel, M. Stapf, U. Miehe, M. Ekblad, M. Cimbritz, P. Falås, J. Nilsson, R. Sehlén, J. Bregendahl, K. Bester, Removal of pharmaceutical metabolites in wastewater ozonation including their fate in different post-treatments, Science of The Total Environment 759 (2021) 143989. https://doi.org/10.1016/j.scitotenv.2020.143989.

[4] A.M. Gorito, J.F.J.R. Pesqueira, N.F.F. Moreira, A.R. Ribeiro, M.F.R. Pereira, O.C. Nunes, C.M.R. Almeida, A.M.T. Silva, Ozone-based water treatment (O_3, O_3/UV, O_3/H_2O_2) for removal of organic micropollutants, bacteria inactivation and regrowth prevention, Journal of Environmental Chemical Engineering 9 (4) (2021) 105315. https://doi.org/10.1016/j.jece.2021.105315.

[5] S. Dogruel, Z. Cetinkaya Atesci, E. Aydin, E. Pehlivanoglu-Mantas, Ozonation in advanced treatment of secondary municipal wastewater effluents for the removal of micropollutants, Environmental Science and Pollution Research 27 (36) (2020) 45460-45475. https://doi.org/10.1007/s11356-020-10339-5.

[6] C.O. Lee, K.J. Howe, B.M. Thomson, Ozone and biofiltration as an alternative to reverse osmosis for removing PPCPs and micropollutants from treated wastewater, Water Research 46 (4) (2012) 1005-1014. https://doi.org/10.1016/j.watres.2011.11.069.

[7] M.M. Huber, S. Canonica, G.-Y. Park, U. von Gunten, Oxidation of Pharmaceuticals during Ozonation and Advanced Oxidation Processes, Environmental Science & Technology 37 (5) (2003) 1016-1024. https://doi.org/10.1021/es025896h.

[8] R. Rosal, A. Rodríguez, J.A. Perdigón-Melón, A. Petre, E. García-Calvo, M.J. Gómez, A. Agüera, A.R. Fernández-Alba, Occurrence of emerging pollutants in urban wastewater and their removal through biological treatment followed by ozonation, Water Research 44 (2) (2010) 578-588. https://doi.org/10.1016/j.watres.2009.07.004.

[9] F.J. Beltrán, A. Rey, Free Radical and Direct Ozone Reaction Competition to Remove Priority and Pharmaceutical Water Contaminants with Single and Hydrogen Peroxide Ozonation Systems, Ozone: Science & Engineering 40 (4) (2018) 251-265. https://doi.org/10.1080/01919512.2018.1431521.

[10] M. Deborde, S. Rabouan, J.-P. Duguet, B. Legube, Kinetics of Aqueous Ozone-Induced Oxidation of Some Endocrine Disruptors, Environmental Science & Technology 39 (16) (2005) 6086-6092. https://doi.org/10.1021/es0501619.

[11] I. Naimi, N. Bellakhal, Removal of 17β-Estradiol by Electro-Fenton Process, Materials Sciences and Applications 3 (12) (2012) 7. https://doi.org/10.4236/msa.2012.312128.

[12] J. Benner, E. Salhi, T. Ternes, U. von Gunten, Ozonation of reverse osmosis concentrate: Kinetics and efficiency of beta blocker oxidation, Water Research 42 (12) (2008) 3003-3012. https://doi.org/10.1016/j.watres.2008.04.002.

[13] Y. Lee, L. Kovalova, C.S. McArdell, U. von Gunten, Prediction of micropollutant elimination during ozonation of a hospital wastewater effluent, Water Research 64 (2014) 134-148. https://doi.org/10.1016/j.watres.2014.06.027.

[14] M. Mustafa. Removal of Micropollutants from Wastewater : evaluation of effect of upgrading ozonation to electro-peroxone. (Doctoral thesis). Umeå University, Umeå, Sweden (2020). Retrieved from http://urn.kb.se/resolve?urn=urn:nbn:se:umu:diva-176567 DiVA database.

[15] F.J. Benitez, J.L. Acero, J.F. Garcia-Reyes, F.J. Real, G. Roldan, E. Rodriguez, A. Molina-Díaz, Determination of the Reaction Rate Constants and Decomposition Mechanisms of Ozone with Two Model Emerging Contaminants: DEET and Nortriptyline, Industrial & Engineering Chemistry Research 52 (48) (2013) 17064-17073. https://doi.org/10.1021/ie402916u.

[16] W. Song, W.J. Cooper, B.M. Peake, S.P. Mezyk, M.G. Nickelsen, K.E. O'Shea, Free-radical-induced oxidative and reductive degradation of N,N′-diethyl-m-toluamide (DEET): Kinetic studies and degradation pathway, Water Research 43 (3) (2009) 635-642. https://doi.org/10.1016/j.watres.2008.11.018.

[17] D. Sauter, A. Dąbrowska, R. Bloch, M. Stapf, U. Miehe, A. Sperlich, R. Gnirss, T. Wintgens, Deep-bed filters as post-treatment for ozonation in tertiary municipal wastewater treatment: impact of design and operation on treatment goals, Environmental Science: Water Research & Technology 7 (1) (2021) 197-211. https://doi.org/10.1039/D0EW00684J.

[18] M. Bourgin, B. Beck, M. Boehler, E. Borowska, J. Fleiner, E. Salhi, R. Teichler, U. von Gunten, H. Siegrist, C.S. McArdell, Evaluation of a full-scale wastewater treatment plant upgraded with ozonation and biological post-treatments: Abatement of micropollutants, formation of transformation products and oxidation by-products, Water Research 129 (2018) 486-498. https://doi.org/10.1016/j.watres.2017.10.036.

[19] W.R. Chen, C. Wu, M.S. Elovitz, K.G. Linden, I.H. Suffet, Reactions of thiocarbamate, triazine and urea herbicides, RDX and benzenes on EPA Contaminant Candidate List with ozone and with hydroxyl radicals, Water Research 42 (1) (2008) 137-144. https://doi.org/10.1016/j.watres.2007.07.037.

[20] F.J. Benitez, F.J. Real, J.L. Acero, C. Garcia, Kinetics of the transformation of phenyl-urea herbicides during ozonation of natural waters: Rate constants and model predictions, Water Research 41 (18) (2007) 4073-4084. https://doi.org/10.1016/j.watres.2007.05.041.

[21] V. Maurino, M. Minella, F. Sordello, C. Minero, A proof of the direct hole transfer in photocatalysis: The case of melamine, Applied Catalysis A: General 521 (2016) 57-67. https://doi.org/10.1016/j.apcata.2015.11.012.

[22] H.-P. Kaiser, O. Köster, M. Gresch, P.M.J. Périsset, P. Jäggi, E. Salhi, U. von Gunten, Process Control For Ozonation Systems: A Novel Real-Time Approach, Ozone: Science & Engineering 35 (3) (2013) 168-185. https://doi.org/10.1080/01919512.2013.772007.

[23] C. Ye, X. Ma, J. Deng, X. Li, Q. Li, A.M. Dietrich, Degradation of saccharin by UV/H_2O_2 and UV/PS processes: A comparative study, Chemosphere 288 (2022) 132337. https://doi.org/10.1016/j.chemosphere.2021.132337.

[24] M. Umar, Reductive and Oxidative UV Degradation of PFAS—Status, Needs and Future Perspectives, Water 13 (22) (2021) 3185. https://doi.org/10.3390/w13223185.

[25] A.M. Dreizler, E. Roduner, Reaction Kinetics of Hydroxyl Radicals with Model Compounds of Fuel Cell Polymer Membranes, Fuel Cells 12 (1) (2012) 132-140. https://doi.org/10.1002/fuce.201100157.

[26] M. Trojanowicz, A. Bojanowska-Czajka, I. Bartosiewicz, K. Kulisa, Advanced Oxidation/Reduction Processes treatment for aqueous perfluorooctanoate (PFOA) and perfluorooctanesulfonate (PFOS) – A review of recent advances, Chemical Engineering Journal 336 (2018) 170-199. https://doi.org/10.1016/j.cej.2017.10.153.

[27] R. Ashauer, Post-ozonation in a municipal wastewater treatment plant improves water quality in the receiving stream, Environmental Sciences Europe 28 (1) (2016) 1. https://doi.org/10.1186/s12302-015-0068-z.

[28] Y. Ling, G. Liao, P. Xu, L. Li, Fast mineralization of acetaminophen by highly dispersed Ag-g-C_3N_4 hybrid assisted photocatalytic ozonation, Separation and Purification Technology 216 (2019) 1-8. https://doi.org/10.1016/j.seppur.2019.01.057.

[29] E. Cuervo Lumbaque, C. Sirtori, V.J.P. Vilar, Heterogeneous photocatalytic degradation of pharmaceuticals in synthetic and real matrices using a tube-in-tube membrane reactor with radial addition of H2O2, Science of The Total Environment 743 (2020) 140629. https://doi.org/10.1016/j.scitotenv.2020.140629.

[30] T.M. Hanh Le, S. Singto, W. Sajomsang, R. Mongkolnavin, R. Nuisin, P. Painmanakul, S. Sairiam, Hydrophobic PVDF hollow fiber membrane modified with pulse inductively coupling plasma activation and chloroalkylsilanes for efficient dye wastewater treatment by ozonation membrane contactor, Journal of Membrane Science 635 (2021) 119443. https://doi.org/10.1016/j.memsci.2021.119443.

[31] J. Ren, S. He, C. Ye, G. Chen, C. Sun, The ozone mass transfer characteristics and ozonation of pentachlorophenol in a novel microchannel reactor, Chemical Engineering Journal 210 (2012) 374-384. https://doi.org/10.1016/j.cej.2012.09.011.

[32] A.-M. Kaiser, E. Saracevic, H.P. Schaar, S. Weiss, R. Hornek-Gausterer, Ozone as oxidizing agent for the total oxidizable precursor (TOP) assay and as a preceding step for activated carbon treatments concerning per- and polyfluoroalkyl substance removal, Journal of Environmental Management 300 (2021) 113692. https://doi.org/10.1016/j.jenvman.2021.113692.

[33] V. Franke, M.D. Schäfers, J. Joos Lindberg, L. Ahrens, Removal of per- and polyfluoroalkyl substances (PFASs) from tap water using heterogeneously catalyzed ozonation, Environmental Science: Water Research & Technology 5 (11) (2019) 1887-1896. https://doi.org/10.1039/C9EW00339H.

[34] L. Sangjung, H. Ihnsup, The analysis of melamine and the removal efficiencies in the advanced oxidation process (AOP) and granular activated carbon (GAC) processes, Desalination and Water Treatment 53 (6) (2015) 1565-1577. https://doi.org/10.1080/19443994.2013.855665.

[35] M. Mehrjouei, S. Müller, D. Möller, A review on photocatalytic ozonation used for the treatment of water and wastewater, Chemical Engineering Journal 263 (2015) 209-219. https://doi.org/10.1016/j.cej.2014.10.112.

[36] U. von Gunten, Oxidation Processes in Water Treatment: Are We on Track?, Environmental Science & Technology 52 (9) (2018) 5062-5075. https://doi.org/10.1021/acs.est.8b00586.

[37] L.T. Phan, H. Schaar, E. Saracevic, J. Krampe, N. Kreuzinger, Effect of ozonation on the biodegradability of urban wastewater treatment plant effluent, Science of The Total Environment 812 (2022) 152466. https://doi.org/10.1016/j.scitotenv.2021.152466.

[38] L. Zhang, Y. Peng, J. Yang, Transformation of dissolved organic matter during advanced coal liquefaction wastewater treatment and analysis of its molecular characteristics, Science of The Total Environment 658 (2019) 1334-1343. https://doi.org/10.1016/j.scitotenv.2018.12.218.

[39] T. Nöthe, H. Fahlenkamp, C.v. Sonntag, Ozonation of Wastewater: Rate of Ozone Consumption and Hydroxyl Radical Yield, Environmental Science & Technology 43 (15) (2009) 5990-5995. https://doi.org/10.1021/es900825f.

[40] P.C. Singer, W.B. Zilli, Ozonation of ammonia in wastewater, Water Research 9 (2) (1975) 127-134. https://doi.org/10.1016/0043-1354(75)90001-9.

[41] M. Yang, K. Uesugi, H. Myoga, Ammonia removal in bubble column by ozonation in the presence of bromide, Water Research 33 (8) (1999) 1911-1917. https://doi.org/10.1016/S0043-1354(98)00364-9.

[42] G.A. de Vera, W. Gernjak, H. Weinberg, M.J. Farré, J. Keller, U. von Gunten, Kinetics and mechanisms of nitrate and ammonium formation during ozonation of dissolved organic nitrogen, Water Research 108 (2017) 451-461. https://doi.org/10.1016/j.watres.2016.10.021.

[43] I.C. Iakovides, K. Manoli, P. Karaolia, I. Michael-Kordatou, C.M. Manaia, D. Fatta-Kassinos, Reduction of antibiotic resistance determinants in urban wastewater by ozone: Emphasis on the impact of wastewater matrix towards the inactivation kinetics, toxicity and bacterial regrowth, Journal of Hazardous Materials 420 (2021) 126527. https://doi.org/10.1016/j.jhazmat.2021.126527.

[44] P. Xu, M.-L. Janex, P. Savoye, A. Cockx, V. Lazarova, Wastewater disinfection by ozone: main parameters for process design, Water Research 36 (4) (2002) 1043-1055. https://doi.org/10.1016/S0043-1354(01)00298-6.

[45] J. Bartram, J. Cotruvo, M. Exner, C. Fricker, A. Glasmacher, Heterotrophic plate counts and drinking-water safety, IWA publishing, 2003.

[46] Regulation (EU) 2020/741 of the European Parliament and of the Council of 25 May 2020 on minimum requirements for water reuse, Official Journal of the European Union, 2020, p. L 177/32.

[47] M. Foroughi, M. Khiadani, S. Kakhki, V. Kholghi, K. Naderi, S. Yektay, Effect of ozonation-based disinfection methods on the removal of antibiotic resistant bacteria and resistance genes (ARB/ARGs) in water and wastewater treatment: a systematic review, Science of The Total Environment 811 (2022) 151404. https://doi.org/10.1016/j.scitotenv.2021.151404.

[48] G. Pak, D.E. Salcedo, H. Lee, J. Oh, S.K. Maeng, K.G. Song, S.W. Hong, H.-C. Kim, K. Chandran, S. Kim, Comparison of Antibiotic Resistance Removal Efficiencies Using Ozone Disinfection under Different pH and Suspended Solids and Humic Substance Concentrations, Environmental Science & Technology 50 (14) (2016) 7590-7600. https://doi.org/10.1021/acs.est.6b01340.

[49] F. Zuma, J. Lin, S.B. Jonnalagadda, Ozone-initiated disinfection kinetics of *Escherichia coli* in water, Journal of Environmental Science and Health, Part A 44 (1) (2009) 48-56. https://doi.org/10.1080/10934520802515335.

[50] M. Yadav, V.L. Gole, J. Sharma, R.K. Yadav, Biologically treated industrial wastewater disinfection using synergy of US, LED-UVS, and oxidants, Chemical Engineering and Processing - Process Intensification 169 (2021) 108646. https://doi.org/10.1016/j.cep.2021.108646.

[51] N.F.F. Moreira, S. Ribeirinho-Soares, A.T. Viana, C.A.L. Graça, A.R.L. Ribeiro, N. Castelhano, C. Egas, M.F.R. Pereira, A.M.T. Silva, O.C. Nunes, Rethinking water treatment targets: Bacteria regrowth under unprovable conditions, Water Research 201 (2021) 117374. https://doi.org/10.1016/j.watres.2021.117374.

[52] S. Ribeirinho-Soares, N.F.F. Moreira, C. Graça, M.F.R. Pereira, A.M.T. Silva, O.C. Nunes, Overgrowth control of potentially hazardous bacteria during storage of ozone treated wastewater through natural competition, Water Research 209 (2022) 117932. https://doi.org/10.1016/j.watres.2021.117932.

[53] J.M. Sousa, G. Macedo, M. Pedrosa, C. Becerra-Castro, S. Castro-Silva, M.F.R. Pereira, A.M.T. Silva, O.C. Nunes, C.M. Manaia, Ozonation and UV_{254nm} radiation for the removal of microorganisms and antibiotic resistance genes from urban wastewater, Journal of Hazardous Materials 323 (2017) 434-441. https://doi.org/10.1016/j.jhazmat.2016.03.096.

[54] N. Czekalski, S. Imminger, E. Salhi, M. Veljkovic, K. Kleffel, D. Drissner, F. Hammes, H. Bürgmann, U. von Gunten, Inactivation of Antibiotic Resistant Bacteria and Resistance Genes by Ozone: From Laboratory Experiments to Full-Scale Wastewater Treatment, Environmental Science & Technology 50 (21) (2016) 11862-11871. https://doi.org/10.1021/acs.est.6b02640.

[55] OECD, Test No. 236: Fish Embryo Acute Toxicity (FET) Test, 2013. https://doi.org/10.1787/9789264203709-en.

[56] European Chemicals Bureau, Technical Guidance Document on Risk Assessment Part II, 2003. https://echa.europa.eu/documents/10162/987906/tgdpart2_2ed_en.pdf/138b7b71-a069-428e-9036-62f4300b752f.

[57] M. Link, P.C. von der Ohe, K. Voß, R.B. Schäfer, Comparison of dilution factors for German wastewater treatment plant effluents in receiving streams to the fixed dilution factor from chemical risk assessment, Science of The Total Environment 598 (2017) 805-813. https://doi.org/10.1016/j.scitotenv.2017.04.180.

[58] C. Kienle, I. Werner, S. Fischer, C. Lüthi, A. Schifferli, H. Besselink, M. Langer, C.S. McArdell, E.L.M. Vermeirssen, Evaluation of a full-scale wastewater treatment plant with ozonation and different post-treatments using a broad range of in vitro and in vivo bioassays, Water Research 212 (2022) 118084. https://doi.org/10.1016/j.watres.2022.118084.

7 Conclusions and Future Work

This final chapter presents the most relevant results and conclusions stated in the previous chapters, complemented with some suggestions for future work.

7.1 Conclusions

The main goal of the present thesis was to design and evaluate two membrane reactors using functionalized membranes for water purification. The results presented in *Chapters 3 and 4* showed the possibility of manufacturing continuous multilayer graphene and graphene-TiO_2 nanocomposite (in a simple preparation process) to be applied in a pressure-driven membrane process for water desalination and removal of 4 CECs in wastewater, respectively. *Chapter 5* presented the results of the characterisation of an ozone membrane contactor and removal of 19 CECs in DW, while *Chapter 6* focused on applying this technology in UWW after secondary treatment. The main conclusions are divided into three sections: (i) membrane filtration systems for water desalination; (ii) PMR for CECs removal; and (iii) ozone MC to intensify gas/liquid mass transfer and tertiary treatment of UWW.

7.1.1 Graphene film in membrane filtration systems for water desalination

A new concept for preparing large-area desalination membranes based *on site* formation of multilayer defective graphene with subnanometric pores, presented in *Chapter 3*, was successfully achieved. The most relevant conclusions were:

- A continuous multilayer graphene has been prepared on a ceramic microporous support. The thermal stability of the ceramic α-Al_2O_3 makes possible the preparation of defective multilayer (B,N)G by pyrolysis of CS containing adsorbed $(NH_4)_3BO_3$.
- Subnanometric pores have been formed by B and N doping and removal by H_2. The generation of subnanometric pores to allow water permeation was herein designed by introducing doping elements on the graphene sheet that could subsequently be removed by suitable chemical treatments. This hypothesis was confirmed by the removal of B and N atoms by thermal hydrogenation.
- A NaCl and KCl removal efficiency from brackish water higher than 95% was achieved. The (B,N)G membrane exhibits a remarkable permeation selectivity. Thus, these results may constitute a significant advance in desalination technology, providing suitable preparation procedures not only on flat but also in curved supports. It can also be anticipated that the procedure can be easily adapted to obtain analogous membranes based on defective graphene with controlled pore sizes for different applications.

7.1.2 Photocatalytic membrane reactor (PMR) for CECs removal

A ceramic tubular membrane coated with a continuous G-TiO_2 nanocomposite thin-film showed promising results in the removal of CECs from UPW and real matrices in single-pass flow-through operation, as presented in *Chapter 4*. The most significant conclusions were:

- A novel continuous catalyst thin-film of G-TiO_2 was deposited on a ceramic membrane. The PMR with the functionalized membranes, activated by UVA light, operated in a single-pass flow-through mode for the treatment of synthetic CECs solutions, exhibits a substantial improvement in the membrane permeate quality and quantity compared to its performance in the absence of light.
- G thin-film structure is beneficial for membrane fabrication as G can enhance the connection with TiO_2 and improve the strength of the membrane to be used as a barrier for the retention of CECs. In addition, the contact between G film and TiO_2 nanoparticles minimizes charge recombination, enhancing photocatalytic activity.
- The membrane fouling was reduced by the G-TiO_2-UVA photocatalytic action. The G-TiO_2-UVA systems present high stability for at least 12 h of continuous operation and reduced reversible and irreversible fouling due to the synergetic functions for CECs oxidation and self-cleaning process.
- CECs rejection achieved values near 60% in continuous flow mode operation. Membrane B enables a slightly higher CECs rejection than membrane A, which can be explained mainly by the better exposure of the photocatalyst to light. However, the accumulation of the nanoparticles over the G film increases the surface roughness of membrane MB-2, reducing its resistance to fouling compared to membrane MA-3. Overall, the results in this study indicate that the G-TiO_2-UVA systems investigated achieve good removal of CECs and effectively reduce toxicity to zebrafish embryos.
- The rejection of CECs in the UWW matrix was comparable to that obtained with UPW, although it had a significant negative impact on permeate flux when compared to UPW, mainly due to the presence of substances that deposited or were adsorbed on the surface of the membrane, blocking its pores.

7.1.3 Ozone membrane contactor (MC) to intensify gas/liquid mass transfer and tertiary treatment of urban wastewater

As demonstrated in *Chapters 5 and 6*, a tubular porous borosilicate membrane contactor was developed for radial delivery of O_3, promoting the intensification of (i) ozone mass transfer in a compact device

and (ii) tertiary treatment of UWW, targeting CECs removal and disinfection. The membrane acts as photocatalyst support and O_3-catalyst/water contactor. The most significant conclusions were:

- Micro-sized ozone bubbles were pseudo-uniformly delivered throughout the reactor length. The feed distribution of O_3 along the length of an annular membrane creates innumerable micro-sized bubbles, increasing the surface area of the O_3 bubble in contact with the liquid allowing for a controlled dosing of O_3 to the water/wastewater-side.
- The membrane contactor showed a high interfacial area and low gas/liquid volumetric ratio. Operating in continuous mode and under atmospheric pressure, the K_La values for this membrane reactor (3.5–9.0 min^{-1}) were comparable to that of a venturi injector and were superior to other membrane contactors reported in the literature. The significant enhancements obtained for K_La and *MTE* using this ozone membrane contactor with low gas/liquid volumetric ratios make this type of contactor highly effective for ozone gas/water mass transfer in water treatment.
- The ozone membrane contactor demonstrated the ability to significantly reduce CECs and bacterial contamination from secondary effluent of UWWTP, improving the overall physicochemical quality of the effluent and reducing toxicity. The seasonal fluctuation of the wastewater characteristics has shown to have an impact on the ozonation treatment efficiency, indicating the importance of adjusting the specific transfer ozone dose, as it considers the organic load of the effluent. Of the 19 target CECs, the four perfluoroalkyl substances and melamine proved to be highly resistant to ozonation.
- Ozonation with the present membrane contactor also reduced the abundance but not the presence of antibiotic-resistant bacteria in the effluent immediately after treatment.
- Photocatalytic ozonation (O_3/UVC/TiO_2) did not significantly improve the removal of CECs. Notwithstanding, the versatility of this setup, allowing the membrane to be doped with a catalyst and operated under UVC radiation, may prove advantageous when treating complex wastewater matrices. The inclusion of a small dose of UVC radiation (0.10 kJ L^{-1}) showed no impact on the oxidation of CECs but led to improvements in the reduction of microbial contamination.
- After ozonation, a dilution factor of 4 was shown to be required for no toxic effects to occur on zebrafish embryos, being reduced to a dilution factor of 2 if a post-treatment by GAC adsorption is coupled.

7.2 Suggestions for future work

The results attained showed that the innovative membrane reactors present a high potential for the removal of organic contaminants from water/wastewater. Nevertheless, improvements in treatment processes and further investigation can be carried out in order to bring these technologies closer to a potential industrial approach:

- Once it was noticed that the PMR using a G-TiO_2 membrane was shown to overcome the main limitation of the reactor performance (fouling phenomenon) for a synthetic effluent, but with low permeate fluxes for UWW after secondary treatment, tests with other catalysts or coupling of other processes (ozonation, electrocatalytic membranes) could lead to higher permeate fluxes with better CEC removal rates.
- A major challenge to be overcome for ozone MCs will be the development of a more efficient membrane material. More studies should be directed towards the fabrication of hydrophobic membranes with coating techniques to minimize the impact on the membrane mass transfer resistance ($1/k_M$). The ozonation treatment process has a well-established link with increased toxicity. As a result, it is imperative to carry out additional studies to investigate the main transformation products of the CECs analysed in this thesis.
- The process of scaling up one of the treatment options presented in this thesis can be expensive both in implementation and maintenance. Therefore, it is crucial to conduct a cost-effectiveness analysis and life cycle evaluation for these processes using a shared baseline for comparison. For the cost assessment of a commercial real-scale unit, a market placement study will be crucial in determining the market acceptance and economic viability of the chosen treatment method. A benchmark assessment of the innovative technology's effectiveness, cost, and application should be carried out, using currently in use conventional solutions as a comparison. Furthermore, a more in-depth study on the energy dissipation of the fluid (pressure drop) when using more than one reactor or reactor in larger dimensions could be interesting. Computational fluid dynamics (CFD) could be used as a tool for this analysis.

Scientific Outputs

Here is a brief description of the activities and scientific outputs, developed under the Doctoral Programme in Environmental Engineering at the Associate Laboratory in Chemical Engineering (ALiCE) and Laboratory of Separation and Reaction Processes-Laboratory of Catalysis and Materials (LSRE-LCM), Department of Chemical Engineering, Faculty of Engineering, University of Porto, *supported by Fundação para a Ciência e a Tecnologia (FCT) under the references SFRH/BD/138756/2018 and COVID/BD/152947/2022.*

Activity 1: Internship at *Instituto Universitario de Tecnología Química (CSIC-UPV)*, Valencia, Spain

Four-month internship at *Instituto Universitario de Tecnología Química (CSIC-UPV)*, Valencia, Spain, under the supervision of Prof. Dr. Hermenegildo Garcia for the development of graphene membranes for application in membrane technologies. Subsequently, the graphene membrane was used for CECs removal.

Scientific Outputs

Research article: Presumido, P.H., Primo, A., Vilar, V.J.P., Garcia, H. Large area continuous multilayer graphene membrane for water desalination, Chemical Engineering Journal, 413 (2021) 127510. DOI: https://doi.org/10.1016/j.cej.2020.127510.

Activity 2: Development of a ceramic tubular membrane coated with a continuous G-TiO_2 for CECs mitigation

This activity presented a ceramic tubular membrane coated with a continuous G-TiO_2 nanocomposite thin-film for CECs removal from synthetic and real matrices in single-pass flow-through operation. The G-TiO_2 film was prepared *in situ* based on the membrane developed in Activity 1. The CECs solution (diclofenac-DCF, 17β-estradiol-E2, 17α-ethinylestradiol-EE2 and amoxicillin-AMX) was prepared using UPW or UWW after secondary treatment fortified with 500 µg L^{-1} of each CEC.

Scientific Outputs

Research article: Presumido, P.H., Santos, L.F. dos, Neuparth, T., Santos, M.M., Feliciano, M., Primo, A., Garcia, H., Đolić, M.B., Vilar, V.J.P. A Novel ceramic tubular membrane coated with a continuous graphene-TiO_2 nanocomposite thin-film for CECs mitigation, Chemical Engineering Journal, 430 (2022) 132639. DOI: https://doi.org/10.1016/j.cej.2021.132639.

Poster presentation: Presumido, P.H., Santos, L.F. dos, Feliciano, M., Primo, A., Garcia, H., Vilar, V.J.P. A novel continuous graphene-TiO_2 nanocomposite thin film to improve CECs removal in photocatalytic membrane reactors. 4th Doctoral Congress in Engineering, 28-29th of June 2021, Porto, Portugal.

Activity 3: Testing of ozone membrane contactor to intensify gas/liquid mass transfer and CECs oxidation

A tubular porous borosilicate membrane contactor was investigated for ozone gas/water mass transfer (K_La) and the removal of CECs in water. Ozone gas/water contact occurs on the membrane shell-side, which is coated with a photocatalyst (TiO_2-P25), as the ozone gas stream is fed from the lumen side and permeates through the pores generating micro-sized ozone bubbles pseudo-uniformly delivered to the annular reaction zone where the contaminated water to be treated flows. External radiation can be administered through the use of four UVC lamps.

Scientific Outputs

Research article: Presumido, P.H., Montes, R., Quintana, J.B., Rodil, R., Feliciano, M., LiPuma, G., Gomes, A.I., Vilar, V.J.P. Ozone membrane contactor to intensify gas/liquid mass transfer and contaminants of emerging concern oxidation, Journal of Environmental Chemical Engineering, 10, 6 (2022), 108671. DOI: https://doi.org/10.1016/j.jece.2022.108671.

Poster presentation: Presumido, P.H., Montes, R., Rodil, R., Quintana, J.B., Feliciano, M., Gomes, A.I., Vilar, V.J.P. Ozone mass transfer in a tubular porous borosilicate membrane contactor for CECs removal. 12th Micropol & Ecohazard Conference, 6-10th of June 2022, Santiago de Compostela, Spain.

Activity 4: Testing of ozone membrane contactor for tertiary treatment of urban wastewater: evaluation of the removal of CECs, bacterial disinfection and toxicity

The membrane ozone contactor used in Activity 3 was applied to promote the tertiary treatment of UWW, targeting the removal of CECs, bacterial disinfection and toxicity reduction. This system relies on the homogeneous radial distribution of O_3 in the reaction zone by dosing through a microfiltration borosilicate tubular membrane, while the UWW swirls around the membrane and drags the generated O_3 microbubbles. The membrane is also coated with titanium dioxide (TiO_2-P25) and radiation can be externally supplied via four UVC lamps.

Scientific Outputs

Research article: Presumido, P.H., Ribeirinho-Soares, S., Montes, R., Quintana, J.B., Rodil, R., Ribeiro, M., Neuparth, T., Santos, M.M., Feliciano, M., Nunes, O.C., Gomes, A.I., Vilar, V.J.P. Ozone membrane contactor for tertiary treatment of urban wastewater: Chemical, microbial and toxicological assessment, Science of the Total Environment, 892, (2023), 164492. DOI: https://doi.org/10.1016/j.scitotenv.2023.164492.

Poster presentation: Presumido, P.H., Ribeirinho-Soares, S., Montes, R., Rodil, R., Quintana, J.B., Feliciano, M., Gomes, A.I., Nunes, O.C., Vilar, V.J.P. Innovative ozone membrane contactor for tertiary treatment of urban wastewater: disinfection and CECs removal. 12th Micropol & Ecohazard Conference, 6-10th of June 2022, Santiago de Compostela, Spain.

Activity 5: Other activities within the scope of the Doctoral Program in Environmental Engineering

Scientific Outputs

Research article: Castellanos, R.M., Presumido, P.H., Dezotti, M., Vilar, V.J.P. Ultrafiltration ceramic membrane as oxidant-catalyst/water contactor to promote sulfate radical AOPs: a case study on 17β-estradiol and 17α-ethinylestradiol removal. Environmental Science and Pollution Research, 29, 42157–42167 (2022). DOI: https://doi.org/10.1007/s11356-021-14806-5

Research article: Vazquez, L., Gomes, L.M.M.T., Presumido, P.H., Rocca, D.G.D., Moreira, R.F.P.M., Dagnac, T., Llompart, M., Gomes, A.I., Vilar, V.J.P. Tubular membrane photoreactor for the tertiary treatment of urban wastewater towards antibiotics removal: application of different photocatalyst/oxidant combinations and ozonation. Journal of Environmental Chemical Engineering, 109766 (2023). DOI: https://doi.org/10.1016/j.jece.2023.109766

Oral presentation: Prada, M.A., Presumido, P.H., Pituco, M.M., Gomes, A.I., Cardona Gallo, S.A., Botero-Coy, A.M., Hernandez, F., Torres Palma, R.A., Vilar, V.J.P. A novel ozone membrane contactor for the removal of CECs from secondary effluent of municipal wastewater and reverse osmosis concentrate. 5th Iberoamerican Conference on Advanced Oxidation Technologies (V CIPOA), 7th to 11th November 2022, Cusco, Peru.

Poster presentation: Vazquez, L., Gomes, L.M.M.T., Gomes, A.I., Presumido, P.H., Dagnac, T., Llompart, M., Vilar, V.J.P. Optimization of the operational conditions of an ultrafiltration tube-in-tube membrane reactor for the removal of CECs in urban wastewaters. 23rd International Symposium on Advances in Extraction Technologies, 30th of June to 2nd of July, 2021, Alicante, Spain.

Poster presentation: Gomes, L.M.M.T., Presumido, P.H., Rocca, D.G.D., Moreira, R.F.P.M., Montes, R., Rodil, R., Quintana, J.B., Gomes, A.I., Vilar, V.J.P. Tube-in-tube membrane photocatalytic reactor for the treatment of urban wastewater after secondary treatment targeting 19 CECs selected in NOR-WATER project. 1st International FibEnTech Congress (FibEnTech21) – New Opportunities for Fibrous Materials in the Ecological Transition, 9th–10th of December 2021, Covilhã, Portugal.

Poster presentation: Prada, M.A., Presumido, P.H., Pituco, M.M., Caixeta, M.P., Cardona Gallo, S.A., Torres Palma, R.A., Vilar, V.J.P. Evaluation of ozone mass transfer in a tubular porous stainless steel membrane contactor. 5th Iberoamerican Conference on Advanced Oxidation Technologies (V CIPOA), 7th to 11th November 2022, Cusco, Peru.